ANALYSIS OF DENSE COLLOIDAL DISPERSIONS WITH MULTIWAVELENGTH FREQUENCY DOMAIN PHOTON MIGRATION MEASUREMENTS

A Dissertation

by

SARABJYOT SINGH DALI

Submitted to the Office of Graduate Studies of
Texas A&M University
in partial fulfillment of the requirements for the degree of

DOCTOR OF PHILOSOPHY

August 2006

Major Subject: Chemical Engineering

ANALYSIS OF DENSE COLLOIDAL DISPERSIONS WITH MULTIWAVELENGTH FREQUENCY DOMAIN PHOTON MIGRATION MEASUREMENTS

A Dissertation

by

SARABJYOT SINGH DALI

Submitted to the Office of Graduate Studies of
Texas A&M University
in partial fulfillment of the requirements for the degree of

DOCTOR OF PHILOSOPHY

Approved by:

Chair of Committee,	Eva M. Sevick-Muraca
Committee Members,	Michael A. Bevan
	David M. Ford
	Lihong Wang
Head of Department,	Kenneth R. Hall

August 2006

Major Subject: Chemical Engineering

ABSTRACT

Analysis of Dense Colloidal Dispersions with Multiwavelength
Frequency Domain Photon Migration Measurements. (August 2006)
Sarabjyot Singh Dali, B.Tech., Indian Institute of Technology, Kharagpur (India)
Chair of Advisory Committee: Dr. Eva M. Sevick-Muraca

Frequency domain photon migration (FDPM) measurements are used to study the properties of dense colloidal dispersions with hard sphere and electrostatic interactions, which are otherwise difficult to analyze due to multiple scattering effects.

Hard sphere interactions were studied using a theoretical model based upon a polydisperse mixture of particles using the hard sphere Percus Yevick theory. The particle size distribution and volume fraction were recovered by solving a non linear inverse problem using genetic algorithms. The mean sizes of the particles of 144 and 223 nm diameter were recovered within an error range of 0-15.53% of the mean diameters determined from dynamic light scattering measurements. The volume fraction was recovered within an error range of 0-24% of the experimentally determined volume fractions.

At ionic strengths varying between 0.5 and 4 mM, multiple wavelength (660, 685, 785 and 828 nm) FDPM measurements of isotropic scattering coefficients were made of 144 and 223 nm diameter, monodisperse dispersions varying between 15% - 22% volume fraction, as well as of bidisperse mixtures of 144 and 223 nm diameter latex particles in 1:3, 1:1 and 3:1 mixtures varying between volume fractions of 15% - 24%. Structure factor models with Yukawa potential were computed by Monte Carlo (MC) simulations and numerical solution of the coupled Ornstein Zernike equations.

In monodisperse dispersions of particle diameter 144 nm the isotropic scattering

coefficient versus ionic strength show an increase with increasing ionic strength consistent with model predictions, whereas there was a reversal of trends and fluctuations for the particle diameter of 223 nm.

In bidisperse mixtures for the case of maximum number of smaller particles, the isotropic scattering coefficient increased with increasing ionic strength and the trends were in conformity with MC simulations of binary Yukawa potential models. As the number of larger diameter particles increased in the dispersions, the isotropic scattering coefficients depicted fluctuations, and no match was found between the models and measurements for a number ratio of 1:3.

The research lays the foundation for the determination of particle size distribution, volume fractions and an estimate of effective charge for high density of particles.

To my parents

ACKNOWLEDGMENTS

I would like to thank the photon migration laboratories where I have learned and worked with the most blessed minds. I would like to thank my advisor Dr. Eva M. Sevick-Muraca for her constant guidance and encouragement throughout my research, whose help has made this dissertation possible. I would like to thank my committee members, Dr. Michael Bevan, Dr. David M. Ford and Dr. Lihong Wang, whose suggestions have helped in the direction of my research. I would like to thank the National Science Foundation and Malvern Instruments, Ltd. for funding this research work.

I am very grateful to Dr.Yingqing Huang, for his help from learning in the laboratories to simulations and modeling. This dissertation would not have been possible without his help. I would also like to thank Dr. Amit Joshi and Dr. Tianshu Pan for the wonderful informational sessions, which have been mentally invigorating and a much needed supply of knowledge and ideas.

I deeply appreciate the help provided by my batch mates and colleagues Dr. Ranadhir Roy, Dr. Jessica P. Houston, John Rasmussen, Feng Liang, Kildong Hwang, Amit K. Sahu, Sunkuk Kwon, Ruchi Sharma, and Lakshmi Sampath in the laboratories. My deepest regards to past group members Dr. Zhigang Sun, Dr. Alan B.Thompson, Dr. Michael Gurfinkel, Dr. Anuradha Godavarty, Dr. Eddy Kuwana, and Sharnay Torrance.

My deepest regards for my parents Amarjit, Pritpal Kaur, my sister Amandeep and her husband Jagjit Singh Choudhary, for being there for me throughout this study. Also my sincere thanks to all those friends at College Station, for the most wonderful and cheerful experience, which has made this stay enjoyable.

NOMENCLATURE

English Symbols:

c	Velocity of light in the medium
c_{salt}	Concentration of ions in the dispersion
$c(r)$	Direct correlation function
C_{scat}	Scattering Cross-Section
C_{abs}	Absorption Cross-Section
C_{ext}	Extinction Cross-Section
D	Diffusion Coefficient
F_{ij}	Binary form factor for two particles of different size
$f(x)$	Particle Size Distribution
$f_{SB}(x)$	Johnson's SB function
$f(x_i)$	Volume based particle size distribution of particle i
$f(x_j)$	Volume based particle size distribution of particle j
$f_{1,i}, f_{2,i}$	scattering amplitudes in two orthogonal polarization states
$f^*_{1,j}, f^*_{2,j}$	complex conjugates of the scattering amplitudes in two orthogonal polarization states
g	average of the cosine of the scattering angle
$g(r)$	Radial distribution function
$h(r)$	Total correlation function
k	wave number in vacuum
m	refractive index of the surrounding medium
n, n_p	refractive index of the particle suspended in the medium.
Q_{scat}	Scattering Efficiency
Q_{abs}	Absorption Efficiency
Q_{ext}	Extinction Efficiency
Q	scattering vector
r	Distance between the source and detector fibers
$S(\bar{r}, \omega)$	isotropic source term
$S_{ij}(Q)$	Partial Static Structure factor
T	Temperature
t	time
Z_p	Particle Charge

Greek Symbols:

ϕ	total volume fraction of particles
$\bar{\sigma}$	Spread of the Gaussian distribution
$\bar{X}$	Mean particle size from the Gaussian distribution
χ^2	Chi Square minimization function
μ_s'	isotropic scattering coefficient
μ_s	scattering coefficient
$\mu_s'^c$	isotropic scattering coefficient calculated from the forward model
$\mu_s'^e$	isotropic scattering coefficient obtained from experiment
μ_a	Absorption coefficient of the medium
Φ	Complex Fluence
λ	wavelength of light in the medium
ω	Angular Modulation Frequency
ρ	Total number density of the particles
ρ_{ij}	Number density for a mixture of particles
$\gamma(r)$	Indirect correlation function
$\phi(r)$	Interaction Potential
θ	scattering angle
σ_c	Particle charge density
k_B	Boltzmann Constant
κ	Debye Huckel Parameter
ϵ_o	Perimittivity of vacuum
ϵ	Relative Permittivity of the medium
λ_B	Bjerrum Length
x_{num}	Number ratio of the larger size particle to the total number of particles in the mixture
α	The ratio of the diameters of the smaller sized particle to the larger sized particle
σ_i, x_i	Diameter of particle i
σ_j, x_j	Diameter of particle j

Abbreviations :

ALS	Angular light scattering
AS	Acoustic Spectroscopy
AC	The Alternating Current generated at the photo multiplier tube of the reference light or the light from the sample.
DC	The magnitude of Direct Current generated at the photo multiplier tube of the reference light or the light from the sample
DLS	Dynamic light scattering
DLVO	Derjaguin Landau Verwey Overbeeks potential
DTS	Diffusing transmission spectroscopy
DWS	Diffusing wave spectroscopy
FDPM	Frequency Domain Photon Migration
GA	Genetic algorithms
HSPY	Hard Sphere Percus Yevick approximation of the static structure factor model
HNC	Hypernetted Chain Closure
HSY	Hard Sphere Yukawa
MSA	Mean Spherical Approximation
OZ	Ornstein Zernike Equation
PMT	Photo Multiplier Tube
PS	Phase Shift
QP	Quadratic Programming
RY	Rogers Young Closure
SQP	Sequential Quadratic Programming
SNR	Signal to noise ratio
SANS	Small Angle Neutron Scattering
SAXS	Small Angle X-ray Scattering

TABLE OF CONTENTS

CHAPTER Page

CHAPTER Page

CHAPTER Page

LIST OF TABLES

LIST OF FIGURES

FIGURE Page

FIGURE Page

FIGURE Page

FIGURE Page

FIGURE Page

FIGURE Page

FIGURE Page

FIGURE Page

FIGURE Page

FIGURE Page

FIGURE Page

FIGURE Page

CHAPTER I

INTRODUCTION

A. Motivation

Today colloidal dispersions form an integral part of several industries namely, pharmaceutical, chemical, oil, paint, inks, ceramics, etc. [1–6] Colloids are composed of micron and submicron particles that undergo Brownian motion within a suspending medium. [7] The overall bulk properties of colloidal suspensions depend upon the dispersion stability which in turn is impacted by the balances of forces which act on the ensemble of particles. Consequently, by understanding and predicting the forces which act on particle ensembles, the design and tailoring of colloidal product quality may be optimized.

The interaction potential among the particles in a dispersion can be due to electrostatic forces (due to charges on the particle in equilibrium with a medium); Van der Waals dispersion forces; steric forces which can arise from polymer chains on the particle; and excluded volume interactions due to hard core particles. The dispersions can be destabilized by means of external agitation or the addition of agents that alter their particle interaction by changing the balance of electrostatic forces, polymeric(steric) forces, or by a combination of both. The combination of forces results in correlated positions that form structure patterns or exhibit crystal states such as FCC or BCC lattice configurations over short length scales. Due to the positional correlations among the particles in the medium, the macro or bulk dispersion properties such as rheology, structure, osmotic pressure, etc. are influenced.

At high volume fractions the spatial correlations among particles result in a

---

The journal model is *IEEE Transactions on Automatic Control.*

microstructure. An electromagnetic wave such as light passing through this dispersion is scattered several times and may be absorbed by the particles during its transit through the dispersion. Analysis of the dispersion structure becomes possible by understanding how structure influences the scattering and absorption of propagating light.[[8], [9]]

A goal of this research is to understand how electromagnetic wave scattering measurements in dense colloidal dispersions can be used to monitor changes in electrostatic potential, which arise from the simple addition of salt. Specifically we focus upon the visible wavelengths of the electromagnetic spectrum.

Herein, we seek to measure multiply scattered light from dense monodisperse and bidisperse dispersions and then use forward models of electrostatic interaction to predict time dependent measurements of light propagation from the diffusion approximation to the radiative transport equation. Our studies first start with monodisperse dispersions and then progress to bidisperse dispersions with two different sizes of particles in a medium. This is important for the study of polydisperse mixtures of particles, since interactions depend upon size and charge polydispersity, and polydispersity impacts the structure and light scattering data.

Time-dependent light propagation measurements made in the frequency domain, termed frequency domain photon migration or FDPM were employed. In FDPM, sinusoidally modulated light is launched into the dense dispersion and the multiple scattering results in amplitude attenuation and phase delay of emitted light relative to the incident light.

The goals of this research proposal are to:

1. Determine the particle size distribution of a colloidal dispersion at high concentration from multiwavelength FDPM measurements;

2. Understand the effect of changing ionic strength on the scattering properties of monodisperse dispersions at high concentrations; and to

3. Investigate the effect of changing electrostatic interactions on the scattering properties in bidisperse dispersions at high concentrations.

The specific aims of this research proposal are:

1. To conduct multiwavelength FDPM measurements of:

   (a) Dense dispersions at high ionic strengths (to minimize electrostatics) in order to show predictiveness with a model of hard sphere interactions; and

   (b) Dense, charged bidisperse dispersions of varying ionic strengths in order to explore electrostatics and to show predictiveness using a model of electrostatic interaction.

2. To develop models for monodisperse and bidisperse mixtures of particles with changing electrostatic interactions (as a function of solution ionic strength) in order to investigate:

   (a) Analytical and numerical theories that predict changing structure for altered ionic strength; and

   (b) The sensitivity of the predictions from models for changing electrostatic interactions and changing particle size.

3. To compare model-predicted data with those obtained from FDPM measurements.

4. To investigate the sensitivity of FDPM measurements of structure owing to changing particle size and electrostatics.

B. Organization of the dissertation

The flowchart in Figure(1) provides the sequence of chapters and the topics presented. The theory of light scattering and the influence of structure on bulk properties of the dispersion will be introduced in the background of Chapter II.

Ensemble measurements are described in Chapter III which describes the techniques that are useful for analyzing and understanding bulk colloidal dispersions.

The specific models employed to describe experimental FDPM data will be introduced in Chapter IV, along with a summary of available analytical and numerical theories for describing electrostatics.

Chapter V discusses the experimental FDPM technique and the methods and materials used for this research proposal.

The validation of our measurement approach is shown by successfully determining particle size from FDPM experimental measurements as presented in Chapter VI. The inversion algorithms employed for particle size recovery from FDPM are presented along with a review of the various particle sizing techniques and algorithms used for inversion of the experimental measurements.

Chapter VII presents the multiwavelength FDPM measurements for study of changing electrostatic interactions in a monodisperse dispersion as a function of ionic strength of the dispersion. Model comparisons are provided along with the experimental measurements.

Bidisperse dispersions with changing electrostatic interactions are discussed in Chapter VIII. Models, experimental data, and comparison of models are provided for four different wavelengths, are presented.

Finally Chapter IX summarizes the research proposal and significant conclusions are presented.

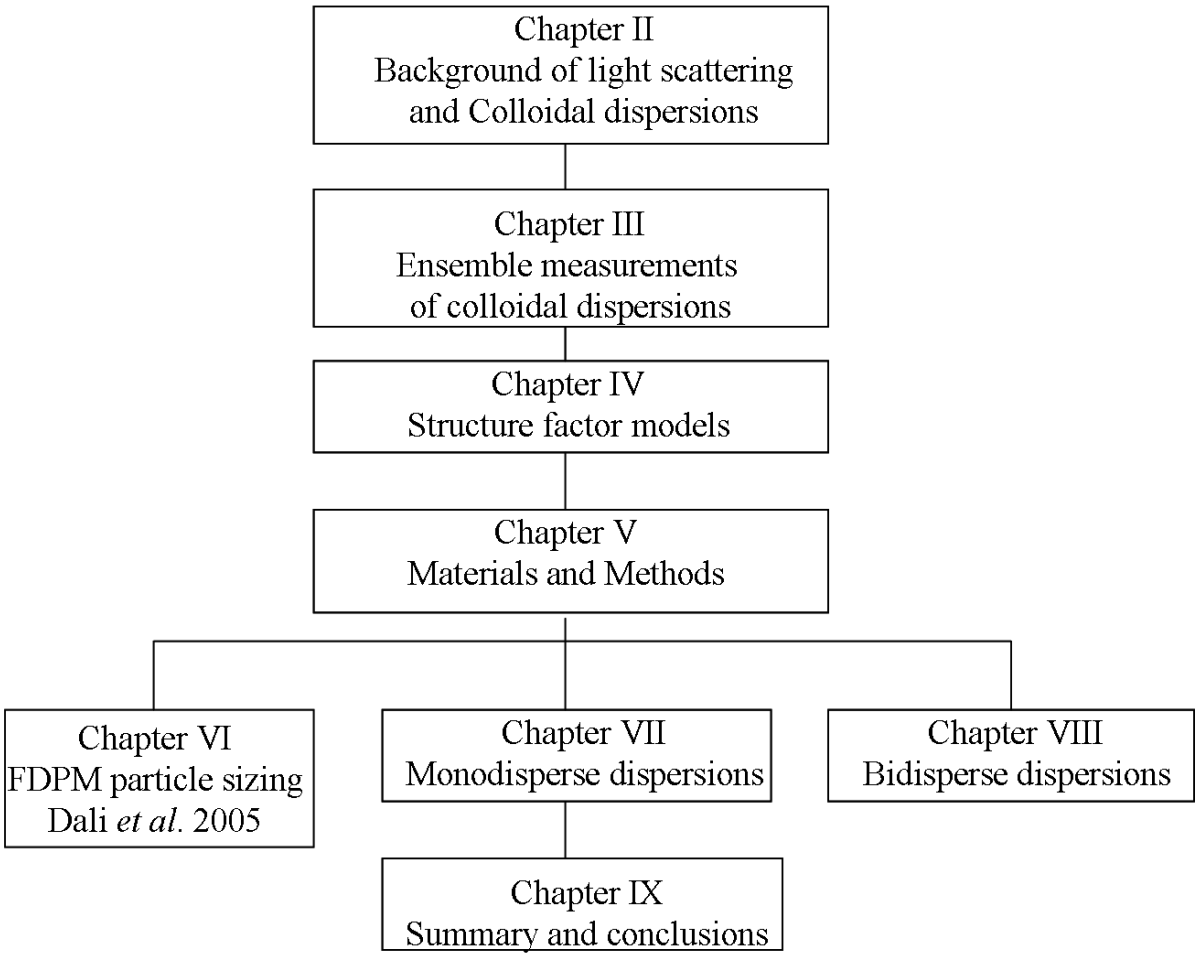

Fig. 1.: Flow diagram for the chapters and the topics discussed in this dissertation.

CHAPTER II

BACKGROUND

A. Light scattering by a particle

Electromagnetic radiation incident upon an electronic charge, causes excitation of the electronic charge and subsequent relaxation causing reradiation of some part of the absorbed energy. The reradiated energy is called the scattered field and the rest of the energy manifests itself in thermal energy, which results from absorbed electromagnetic radiation. Figure (2) shows the incident E_{or}, E_{ol} and scattered E_r, E_l electric fields from a particle. The angle between incident and scattered fields is defined as θ. The incident electric field is represented as a vector sum of E_{or} and E_{ol}, in the XY plane where r and l refer to perpendicular and parallel to the scattering plane respectively. The azimuthal angle of scattering is defined as $\phi^{'}$.

For the most general case involving a single particle, the scattering formulation relating incident and scattered fields can be written as a function of four scattering amplitude functions S_1, S_2, S_3 and S_4, all functions of θ and $\phi^{'}$. [10]

$$\begin{pmatrix} E_l \\ E_r \end{pmatrix} = \begin{pmatrix} S_2 & S_3 \\ S_4 & S_1 \end{pmatrix} \cdot \frac{e^{-ikr+ikz}}{ikr} \begin{pmatrix} E_{ol} \\ E_{or} \end{pmatrix} \tag{2.1}$$

For spherical particles, $S_3 = 0$ and $S_4 = 0$ and S_1 and S_2 are complex amplitude functions for any scattering direction, θ. The incident wave vector Q_0 is scattered by an angle θ and the scattering wave vector, Q, can be represented with magnitude $\mid Q \mid = \frac{4\pi m sin(\theta/2)}{\lambda}$, where m is the refractive index of the surrounding medium. Figure (3) illustrates the concept of scattering of incident wave vector by an angle θ and the effective change, defined as the scattering wave vector.

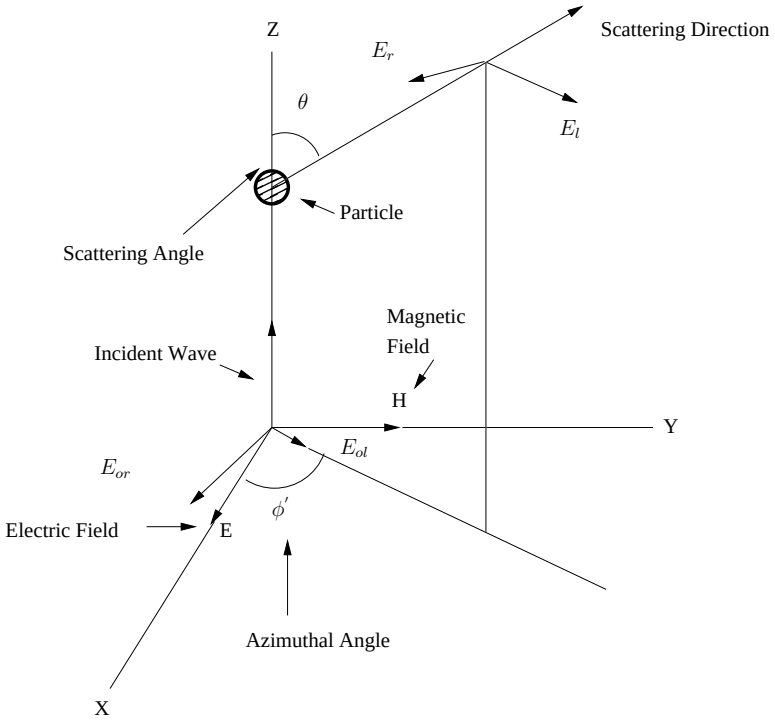

Fig. 2.: Incident and scattered electromagnetic waves from a particle.

The total energy scattered in all directions is defined as the energy of the incident wave falling on the area C_{sca}, and is defined for the case of elastic scattering as

$$C_{sca} = \frac{1}{k^2} \int F(\theta, \phi^{'}) d\omega \tag{2.2}$$

where $d\omega = \sin(\theta) d\theta d\phi^{'}$ is the element of the solid angle and the integral is taken over all directions. F is the form factor of the particle and $k = \frac{2\pi m}{\lambda}$ is the wave number. The energy absorbed is similarly defined to be the energy incident on the area C_{abs}, and the total energy removed from the original direction is defined to be the energy

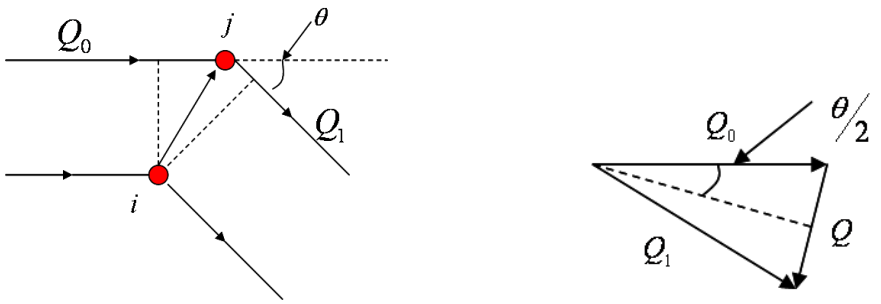

(a) scattering (b) scattering

Fig. 3.: Change in the scattering wave vector from Q_0 to Q_1, Q is the change referred to as the scattering wave vector.

incident on the area C_{ext}. Since energy is conserved,

$$C_{ext} = C_{sca} + C_{abs}. \tag{2.3}$$

The quantities C_{ext}, C_{sca}, and C_{abs} are called the extinction, scattering, and absorption cross sections of the particle. Each have the dimension of area. Efficiency factors for extinction, scattering, and absorption, are obtained by dividing the scattering areas with the cross sectional areas of the particle. For a spherical particle with cross sectional area of $G = \pi(\sigma/2)^2$, where σ is the particle diameter, the efficiency factors Q_{ext}, Q_{scat}, and Q_{abs} are defined as:

$$Q_{ext} = C_{ext}/G \tag{2.4}$$

$$Q_{sca} = C_{sca}/G \tag{2.5}$$

$$Q_{abs} = C_{abs}/G \tag{2.6}$$

1. Rayleigh scattering

When the size of the particle is small compared to the wavelength of light used, the scattering is referred to as Rayleigh scattering. Under conditions of Rayleigh scattering, the scattering matrix can be written as

$$\begin{pmatrix} S_2 & S_3 \\ S_4 & S_1 \end{pmatrix} = ik^3\alpha \begin{pmatrix} \cos(\theta) & 0 \\ 0 & 1 \end{pmatrix} \tag{2.7}$$

where the scattering angle is θ; the polarizability, α is a scalar; and $k = \frac{2\pi}{\lambda}$ is the wave number.

For incident natural light of intensity I_o, with no preferred polarization, the scattered intensity I, can be described by

$$I = \frac{(1 + \cos^2(\theta))k^4 \mid \alpha \mid^2}{2r^2} I_o \tag{2.8}$$

where r is the distance at which the scattered intensity is measured away from the particle.

For Rayleigh scattering, the refractive index should be small such that the electric field penetrates into the particle fast and polarizes the particle in a short period of time, i.e. the electric field of the incident light displaces the charges away from their positions. Rayleigh scattering is valid when $\mid n_p \mid \cdot\sigma \ll \lambda/(2\pi)$, where n_p is the particle refractive index, and σ is the diameter of the particle.

For the case of a sphere, the scattering efficiency is

$$Q_{scat} = \frac{8}{3}x^4 \mid \frac{m^2 - 1}{m^2 + 2} \mid^2 \tag{2.9}$$

where x is the size parameter and is defined as $k\sigma/2$.

2. Rayleigh Gans scattering

In Rayleigh Gans scattering, it is assumed that

1. The particle refractive index, n_p, relative to the surrounding medium is close to 1: $\mid n_p - 1 \mid \ll 1$, and

2. The phase shift of the scattered wave from the incident wave is small: $2k(\sigma/2) \mid m - 1 \mid \ll 1$.

The physical understanding of Rayleigh Gans scattering is that a particle is comprised of small elements of volume dV, each of which act as a Rayleigh scatterers. The scattering fields from each volume element interfere in the far field, and the complex amplitudes add up according to the phase δ from each volume element with respect to a common origin. The scattering matrix for each element is of the form:

$$\begin{pmatrix} S_1(\theta) \\ S_2(\theta) \end{pmatrix} = \frac{ik^3(n_p - 1)}{2\pi} e^{i\delta} dV \begin{pmatrix} 1 \\ \cos(\theta) \end{pmatrix} \tag{2.10}$$

The volume elements scatter very weakly, and the applied field to each volume element does not differ in phase or amplitude from the incident wave. Also the weakly scattered wave from each volume element exits the particle without being modified or distorted by the presence of other volume elements. The summation of all the phases for the volume elements can be integrated and calculated as

$$R(\theta, \phi') = \frac{1}{V} \int e^{i\delta} dV \tag{2.11}$$

and the scattering matrix for the entire particle is given as

$$\begin{pmatrix} S_1(\theta) \\ S_2(\theta) \end{pmatrix} = \frac{ik^3(n_p - 1)}{2\pi} V R(\theta, \phi') \begin{pmatrix} 1 \\ \cos(\theta) \end{pmatrix} \tag{2.12}$$

For the case of a spherical particle in X-ray scattering, the function $R(\theta, \phi^{'})$ is calculated to be

$$R(\theta, \phi^{'}) = \frac{3}{u^3}(\sin u - u \cos u) \tag{2.13}$$

where $u = 2k(\sigma/2)\sin(\theta/2)$.

3. Mie theory

For spheres of arbitrary size and refractive index, Mie theory is used to calculate the amplitude functions S_1 and S_2; scattering area, C_{scat}; and the scattering efficiency, Q_{scat} and the absorption efficiency Q_{abs}. Mie theory provides a solution to the Maxwell's equations for a spherical geometry and is the most complete theory of scattering for spherical particles.

The amplitude scattering functions are calculated as a summation series and can be written as:

$$S_1(\theta) = \sum_{n=1}^{\infty} \frac{2n+1}{n(n+1)}(a_n \pi_n(\cos(\theta)) + b_n \tau_n(\cos(\theta))) \tag{2.14}$$

$$S_2(\theta) = \sum_{n=1}^{\infty} \frac{2n+1}{n(n+1)}(b_n \pi_n(\cos(\theta)) + a_n \tau_n(\cos(\theta))) \tag{2.15}$$

The intensity of light scattered in an arbitrary direction is denoted as $F(\theta, \phi^{'})$ and also called form factor for incident linearly polarized light. It can be written as

$$F(\theta, \phi^{'}) = i_2(\theta)\cos^2\phi^{'} + i_1(\theta)\sin^2\phi^{'} \tag{2.16}$$

where $i_1 =\mid S_1(\theta) \mid^2$ and $i_2 =\mid S_2(\theta) \mid^2$. The scattering efficiency can be calculated from the above quantities and is written as:

$$Q_{sca} = \frac{C_{sca}}{\pi(\sigma/2)^2} = \frac{1}{x^2}\int_0^{\pi}(i_1(\theta) + i_2(\theta))\sin(\theta)d\theta \tag{2.17}$$

where $x = k\sigma/2$ is the dimensionless size parameter. The efficiency, Q_{sca}, also describes the case of arbitrary polarization of the incident wave (i.e. elliptic polarization).

The part of the forward momentum of the incident wave, which is carried by the scattered wave is proportional to $\cos(\theta)$, and can be calculated as

$$\overline{\cos(\theta)}C_{sca} = \frac{1}{k^2}\int F(\theta,\phi')\cos(\theta)d\omega. \tag{2.18}$$

The average of $\cos(\theta)$, also represented above as $\overline{\cos(\theta)}$, is called the anisotropy factor g. For small particles where the scattering of light is isotropic, (i.e. the size is smaller than wavelength), $g = 0$. Whereas larger particles (i.e. size is comparable to wavelength) are forward scattering and the anisotropic scattering function g is close to 1.

4. Collection of particles

The scattering efficiency of a suspension is a function of the particle concentration. When the concentration of particles in a medium is low, light may be scattered once before exiting the solution. This corresponds to a single scattering event. As the concentration of particles is increased, the light may be scattered more than once inside the medium. Such scattering events are called multiple scattering events and will be described in detail in Chapter III. Dilute dispersions of particles can also be multiple scattering, if the path length the photon travels is long enough to be scattered by the particles more than once. Figure 4 illustrates the difference between the two scattering phenomenon of single and multiple scattering, respectively.

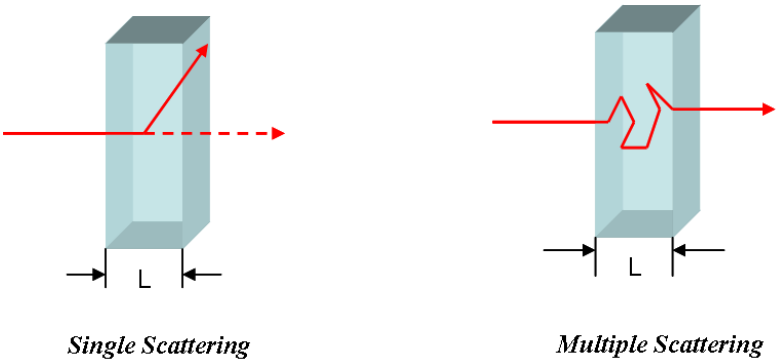

(a) single scattering (b) multiple scattering

Fig. 4.: Scattering of light from a dilute and dense dispersion of particles.

When the concentration of the particles is high, particles order themselves in such a way that the radiation scattered from each of the particles interferes with the field scattered from its nearest neighbors. This form of scattering is called dependent scattering and is incorporated in the expressions of intensity, by considering the correlations of the particles in the reciprocal space, by means of a structure factor expression S(Q). Dependent scattering occurs when the distance between the particles is less than the wavelength of light used. Figure (5) illustrates the concept of dependent scattering.

Dilute dispersions that have the intra-particle distances which are larger than the wavelength of light do not cause dependent scattering. Consequently the scattered fields arising from different particles do not interfere in either near or far fields and scattering power is proportional to the volume fraction of the particles. Increasing the particle concentrations beyond a specific limit leads to dependent scattering and

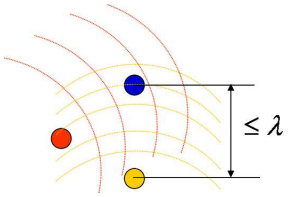

Fig. 5.: Dependent scattering occurs when the distance between the particles in the dispersion is less than or equal to the wavelength of light.

can be studied using the concept of Interference Approximation (IA). According to this approximation, [11]:

1. The incident field on a particle is not impacted by its neighbors;
2. Particle scattering is not impacted by its neighbors in the near field, i.e. particles scatter independently; and
3. The scattered fields interfere in the far field.

The interference approximation implies that the absorption efficiency of the particles is unaltered by volume fraction even under conditions of dependent scattering. Recently using FDPM measurements to separate absorption and scattering properties in dense colloid suspensions, by Huang, *et al.* [11] demonstrated the validity of the interference approximation.

Particle correlations can be determined from light scattering measurements by means of the structure factor. In broad terms, the structure factor provides information about the arrangement of the particles in the reciprocal space or Q space. At small Q, S(Q) provides information about the long range order in the dispersion and

at large Q, S(Q) provides information about the local ordering of the particles. S(Q) is derived from the positional correlations of the particles and, in liquid state theory, can be represented as the Fourier transform of the radial distribution function, g(r):

$$S(Q,R) = 1 + 4\pi\rho \int_0^R dr r^2 [\frac{\sin(Qr)}{Qr}][g(r) - 1] \tag{2.19}$$

where R is the distance at which the pair distribution function g(r) approaches or becomes unity, and r is the radial distance measured from the center of a particle.

Structure factors can be determined using Monte Carlo simulations of particle positioning or from the Ornstein Zernike integral equation solved using appropriate closure expressions, such as Percus Yevick, Hypernetted chain closure (HNC), and Rogers Young (RY). Analytical solutions of the Ornstein Zernike Equations can be obtained using the MSA (Mean Spherical Approximation) closure. The detailed technique for obtaining the structure factors is described in Chapter IV.

Structure factors can be experimentally determined from small angle X-ray or neutron scattering measurements [12]. While we employ multiply scattered light, the ability to directly obtain S(Q) is compromised since we measure light of all Q. Consequently, as shown below, our measurements reflect a weighted averaged structure factor. This work seeks to demonstrate that FDPM measurement of multiply scattered light can nevertheless detect changes in structure that can be predicted from first principle models of electrostatic interactions.

B. Factors which govern the structure factor

1. Potential energy

The interaction potential between colloidal particles determines their position correlations in space. The potential energy between two particles is determined by the

particle size, charge, and the medium within which they interact. Some of the common potential models are described below.

Hard sphere: Hard Sphere interactions occur due to volume exclusion effects among the particles or in other words, a random orientation of particles is limited by the fact that two particles cannot occupy the same volume. Particles far away from each other do not experience any forces of repulsion or attraction, but at contact, they experience an infinite potential energy, which restricts volume overlap. Their interaction assumes the particles act as non-deformable hard spheres. Figure(6) depicts the intraparticle potential U_{HS} that arises from volume exclusion or hard sphere type of interactions.

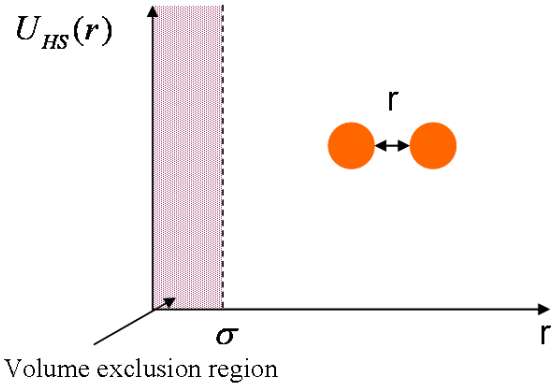

Fig. 6.: Hard sphere potential model.

Yukawa: The Yukawa or soft sphere type of interactions occurs among charged

particles in a dispersion and arises due to the electric double layer surrounding each particle. The potential energy reduces with distance by a factor of $\frac{exp(-r)}{r}$. Closely positioned the particles repel each other due to double layer repulsion. Figure(7) depicts the potential form for Yukawa potential model, $U_{HSY}(r)$

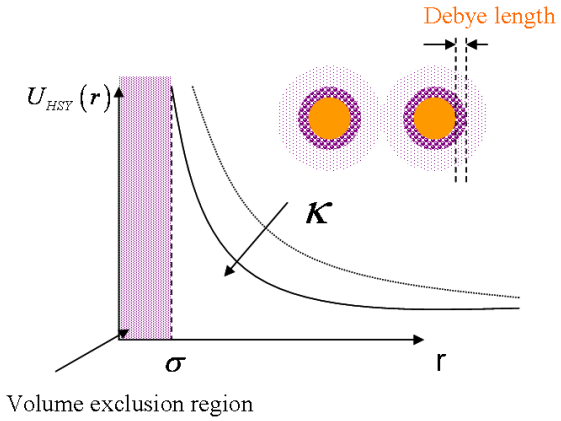

Fig. 7.: Yukawa potential.

where κ is the Debye Huckel parameter and is defined as $\kappa = \sqrt{\frac{\sum_i n_i z_i^2 e^2}{\epsilon_o \epsilon k_B T}}$ and depends upon the ionic strength of the medium or the concentration of smaller ions. Here n_i are the number of ions; z_i is the charge on individual ions; e is the electronic charge; ϵ_o is the dielectric permittivity of vacuum; and ϵ is the relative permittivity of the dielectric medium; k_B is the Boltzmann constant; and T is the temperature.

The inverse of the Debye Huckel parameter is the screening length of the ions in the dispersion.

DLVO: The Derjaguin Landau Verwey Overbeeks (DLVO) potential represents the sum of the repulsive and the attractive potential energies among particles. The attractive energy or the Van der Waals dispersion forces are long ranged, which leads to a primary minimum in the potential energy curve followed by a potential barrier and a secondary minimum when the particles are far apart. Figure(8) describes the summation of the two energy terms, and depicts the primary and secondary minima.

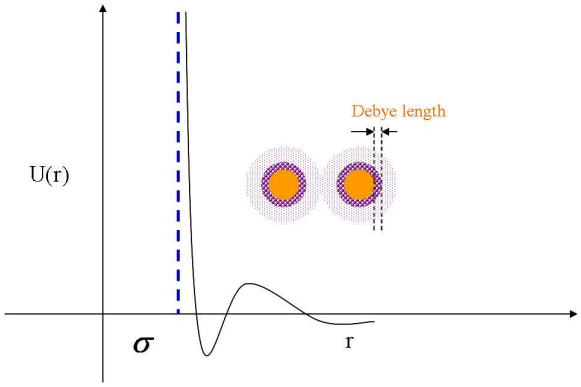

Fig. 8.: DLVO potential.

2. Depletion interactions

When colloid particles are immersed in a solution of macromolecules, such that the distance between two particles in the dispersion is less than the diameter of the macromolecules in solutions, an osmotic pressure is created due to the lack of macromolecules between the spherical particles. This pressure difference due to excess macromolecules in the bulk, gives rise to an attraction among the colloid particles, which is called a depletion interaction. [13, 14]

The range of attraction is dependent upon the size of the macromolecules and the strength of the attractive force is dependent upon the concentration of the macromolecules in the bulk. Asakura *et al.* [15] have developed a model to predict this pressure difference due to depletion of macromolecules between spherical particles.

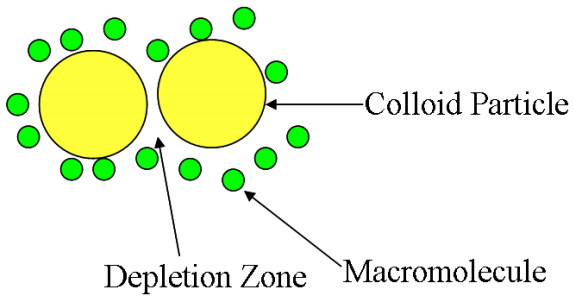

Fig. 9.: Depletion interactions.

Figure 9 illustrates the concept of depletion interactions. The depletion zone has no macromolecules and hence an osmotic pressure difference is created due to an excess amount of macromolecules in the bulk solution.

C. Influence of structure on bulk properties

The microstructure of the particles affects the bulk properties of colloidal dispersions. For example, rheology is altered for systems interacting with different potential energies among the particles. [16–19] The rheological behavior of these dispersions is viscoelastic, with the elastic component becoming increasingly important as the interaction is increased [20,21]. An excellent review on the impact of interaction potential on rheological properties is provided by Quemada *et al.* [22]

Similarly, the osmotic compressibility which is the resistance of the dispersion to compression, increases when the potential among the particles becomes increasingly repulsive. Osmotic pressure measurements [23] can be performed which are a function of the volume fraction and the number density of the particles in the dispersion. The osmotic pressure can be directly related to the thermodynamic and statistical mechanical properties of the dispersion. Osmotic pressure measurements are made when a colloidal dispersion is held in equilibrium with a salt reservoir with the help of a membrane and the osmotic pressure difference is measured. Osmotic pressure measurements have been found to be a useful technique in determining the effective charge on the colloid particles in a dispersion.

D. Particle characterization techniques using discrete measurements

Experimental techniques involved with determining individual particle properties can be categorized as discrete measurement techniques, while bulk property measurements

can be investigated by ensemble based techniques. Single particle characterization broadly involves determining the size, shape, charge, and refractive index of the particle. Particle size plays an important role in the product's quality, while charge can be important for determining the stability of a particle in a dispersion. Refractive index plays a crucial role in the optical properties of the dispersion, as absorption and scattering properties of the particle change with refractive index. Optical properties are important for the final product quality for cosmetic, paint, and pigment industries.

Particle size can be determined directly by directly probing individual particles with techniques such as dynamic light scattering. Particle charge can be determined by Zeta potential measurements in an electrolyte medium, by electrophoresis techniques or from conductometric titration measurements. Zeta potential is defined as the potential at the shearing plane of the ions in equilibrium with the particle surface. Electrophoresis refers to the motion of suspended particles in an applied electric field and the particle velocity is found to be proportional to the applied electric field strength. While the measurement techniques for characterization of a particle in a dispersion are explained in Chapter V, in this dissertation, we seek to perform ensemble measurements in dense suspensions where particle interactions can predominate.

E. Summary

This chapter reviews the basic concepts of light scattering from a single particle, and the validity of available theories to explain the scattering of light from a single particle. The scattering of light from a collection of particles is also described along with the concepts of single scattering and multiple scattering of light. The concept of structure is introduced which depends upon the potential of interaction between

the particles and how structure affects the bulk properties of dispersions.

In the following chapter, the description of ensemble based techniques available to make scattering based measurements on bulk dispersions are described.

CHAPTER III

THEORY OF ENSEMBLE MEASUREMENTS

Particles in a colloidal dispersion are in constant Brownian motion and as a result the structure, and hence properties of the dispersion, change dynamically with time. The experimental techniques described in this chapter are ensemble techniques, which measure time averaged dispersion properties. Static ensemble techniques represent properties averaged over long times while dynamic techniques probe the fluctuations of properties over short times that arise from Brownian motion.

The chapter begins with the introduction of two widely used scattering techniques, Small Angle Neutron Scattering (SANS) and Small Angle X-ray Scattering (SAXS), followed by dynamic light scattering in dilute dispersions and photon diffusion techniques to analyze multiple scattering in dense dispersions.

A. Static neutron scattering

Neutron scattering occurs due to the interaction of nuclei and neutrons obtained from a neutron source, a nuclear reactor. The bombarding neutron energy is determined by their de Broglie wavelength

$$\lambda = h/m_n v \tag{3.1}$$

where h is the planck's constant; m_n is the mass of the neutron; and v is its velocity. The wavelength of the neutrons is in the angstrom range which provides a means to interrogate angstrom length scales of the dispersions. The energy of the neutron is controlled by a moderator and neutrons at room temperature are called thermal neutrons. Those at lesser energy are called cold neutrons.

Since neutron scattering represents the combination of both the form and struc-

ture factors, i.e. $I(Q) \propto F(Q)S(Q)$, it [24,25] is used as an investigative tool to study structure factors as the form factors (introduced in Chapter II) of the particles is typically close to unity at small scattering angles. Consequently (SANS) is capable of obtaining the structure factors of dispersions, as well as the partial structure factors from mixtures, since $F(Q) \rightarrow 1$ as $Q \rightarrow 0$.

The drawback of using neutrons is the high cost associated with the measurement. A nuclear reactor is needed as a source for the neutrons used to study colloidal scattering.

B. X-Ray scattering: static

X-ray scattering is used to investigate the size, shape, and internal structure of colloidal particles. [26], [27] Colloidal dispersions can be investigated using SAXS to determine particle form factor and the structure factor. [28, 29] X-rays, as with electromagnetic radiation, interact with the electrons in the particles, and excite them to a higher energy level. The electrons return to their ground state, and reradiate the energy, resulting in x-ray scattering. X-ray scattering is similar to neutron scattering by providing a greater range of Q values that can be explored by light scattering. Different Q values are investigated by changing the angle of scattering θ as well as the small wavelength of radiation, λ. As in the case for neutron scattering, the source for X-ray scattering is expensive and cannot be used to make small scale instruments with wide applicability. An alternate is to use economical laser light sources for the study of laser light scattering in colloidal dispersions.

C. Dynamic light scattering

The basic principle underlying Dynamic Light Scattering (DLS) [[30], [31]] is of measuring the intensity fluctuations of a speckle spot of light through a sample, using a photomultiplier tube and an autocorrelator. Figure 10 shows the intensity fluctuations measured from the dynamic light scattering apparatus and the autocorrelation function measured thereof. The characteristic decay time of the autocorrelation function is related to the dynamics of the medium through the length scale set by the inverse of the wave vector Q^{-1}. Since only a single scattering event is valid to fix the length scale and hence the wave vector, multiple scattering is not allowed. Only very dilute solutions ($\phi < 0.1\%$) of particles can be analyzed using this technique, although fiber optic light scattering techniques are being investigated and can analyze higher volume fractions.

In DLS, the fluctuations in the intensity of light scattered are characterized by the temporal autocorrelation function, $g_2(t)$.

$$g_2(t) \equiv \frac{1}{\beta}\left(\frac{< I(t)I(0) >}{< I >^2} - 1\right) = \left(\frac{< E^*(t)E(0) >}{<\mid E^2 \mid>}\right)^2 \equiv \mid g_1(t) \mid^2 \qquad (3.2)$$

where β is a constant determined by the collection optics of the experiment; $I(t)$ is the intensity of light measured at an instant of time; $E(t)$ is the electric field amplitude measured corresponding to the intensity of light detected; and $E^*(t)$ is the complex conjugate of the electric field measured above. The second equality is called the Siegert relation.

The first order autocorrelation function is related to the diffusion coefficient,D_p, of the particles by the relation

$$g_1(t) = exp(-Q^2 D_p t) \qquad (3.3)$$

where $Q = \frac{4\pi m}{\lambda}\sin(\theta/2)$ is the wave vector and m is the refractive index of the solvent medium. The auto correlation function decays with a time constant, τ, and the characteristic decay time τ is related to the Stokes Einstein diffusion coefficient D_p of the particles by

$$\tau = 1/D_p Q^2 \tag{3.4}$$

The particle diffusion coefficient for a spherical particle of diameter σ is given by the Stokes Einstein relation

$$D_p = \frac{k_B T}{6\pi\eta\sigma} \tag{3.5}$$

where k_B is the boltzmann constant; T is the temperature; and η is the viscosity of the solvent.

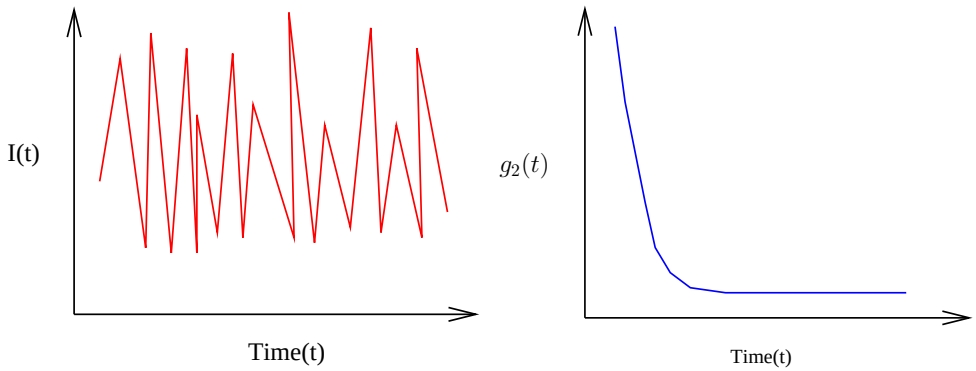

(a) Intensity fluctuations (b) Decay of autocorrelation function with time

Fig. 10.: Measurements from a dynamic light scattering apparatus.

The wave vector, Q can be altered by changing the wavelength of light or by changing the angle of detection for the detector.

D. Photon diffusion techniques

This section enlists the experimental techniques that are based upon the diffusion of light through a dense optical multiple scattering medium. A brief review is first provided about photon diffusion through dense, multiple scattering media.

Theory of multiple scattering: The propagation of light through a multiply scattering medium, such as a colloidal dispersion, atmospheric media, fog, biological media, etc. can be described in two ways. The first method involves solving the complete Maxwell's equations for the waves travelling in a medium. This method can be called the analytic theory, and can solve for complete diffraction and interference effects in the dispersions.

The second method involves the concepts of radiative transfer or Boltzmann transport theory of light. The concepts of radiative transfer can be learnt from the analogous theory of neutron transport, where at every position in space conservation of neutrons is studied. [32]

The density of photons $U(r,t)$ and the photon current density $J(r,t)$ satisfy the diffusion approximation to the Boltzmann transport equation. [33]

$$\frac{\partial U(r,t)}{\partial t} + v\mu_a U(r,t) + \nabla \cdot J(r,t) = q_o(r,t) \tag{3.6}$$

$$\nabla U(r,t) + \frac{3\partial J(r,t)}{v^2 \partial t} + \frac{J(r,t)}{vD} = 0 \tag{3.7}$$

where v is the speed of light in the transporting medium, and D is the optical diffusion coefficient,

$$D = 3[\mu_a + \mu_s(1-g)]^{-1} \tag{3.8}$$

Here μ_a is the linear absorption coefficient or the inverse of the mean free path for photon absorption which has units of inverse distance. The parameter μ_s is the linear scattering coefficient, or the inverse of the mean free path for photon scattering, with units of inverse distance. The term g is the mean of the cosine of the scattering angle; and $q_o(r,t)$ is the photon source.

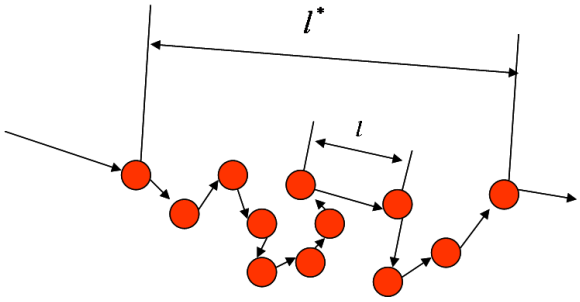

Fig. 11.: Mean free path lengths for scattering and isotropic scattering of photons.

Figure 11 describes the mean free path length of scattering for a photon of light, l ($\mu_s = 1/l$) and the isotropic mean free path of scattering of photon l^* ($\mu_s^{'} = 1/l^*$) respectively. The isotropic mean free path is the distance a photon has to travel through the scattering medium after which the direction of the photon becomes completely randomized. The isotropic scattering coefficient can be calculated from the scattering coefficient as $\mu_s^{'} = (1-g)\mu_s$. For very small particles, the scattering is isotropic, and $g = 0$, whereas larger particles have a highly forward scattering pattern

and $g \approx 1$.

Diffraction and interference effects are included in the description of scattering and absorption of a single particle, even though transport theory itself does not include diffraction effects. In transport theory, the addition of specific fields is valid, but no consideration is given to the behavior of fields. [34]

For a sinusoidally intensity-modulated point source of light, the photon source is

$$q_o(r,t) = \delta(r)S\{1 + Aexp[-i(\omega t + \epsilon)]\} \tag{3.9}$$

Here $\delta(r)$ is the Dirac delta function located at the origin; S is the fluence of the source(photons per second); A is the modulation of the source; ω is the angular modulation frequency of the source; and ϵ is the arbitrary phase. Assuming the form for $U(r,t)$ and $J(r,t)$ as below,

$$U(r,t) = [U(r)]_{dc} + [U(r)]_{ac}exp[-i(\omega t + \epsilon)] \tag{3.10}$$

$$J(r,t) = [J(r)]_{dc} + [J(r)]_{ac}exp[-i(\omega t + \epsilon)] \tag{3.11}$$

and substituting into the diffusion equation (3.6) and (3.7), the steady state diffusion equation can be obtained as

$$\nabla^2[U(r)]_{dc} - (\mu_a/D)[U(r)]_{dc} = -(S/vD)\delta(r), \tag{3.12}$$

and the frequency dependent diffusion equation can be obtained as

$$\nabla^2[U(r)]_{ac} - \left(\frac{v\mu_a - i\omega}{vD}\right)[U(r)]_{ac} = -\frac{SA}{vD}\delta(r), \tag{3.13}$$

For an infinite medium, the above equations (3.12) and (3.13) can be solved to give

$$U(r,t) = \frac{S}{4\pi vDr} exp\left[-r\left(\frac{\mu_a}{D}\right)^{\frac{1}{2}}\right] + \frac{SA}{4\pi vDr}$$
$$\times exp(-r\left(\frac{v^2\mu_a^2+\omega^2}{v^2D^2}\right)^{1/4}\cos\left[\frac{1}{2}\tan^{-1}\left(\frac{\omega}{v\mu_a}\right)\right])$$
$$\times exp(ir\left(\frac{v^2\mu_a^2+\omega^2}{v^2D^2}\right)^{1/4}\sin\left[\frac{1}{2}\tan^{-1}\left(\frac{\omega}{v\mu_a}\right)\right] - i(\omega t+\epsilon)) \quad (3.14)$$

The above equation (3.14) is the Fourier transform equivalent of

$$\rho(r,t) = \frac{1}{(4\pi vDt)^{3/2}} exp\left(-\frac{r^2}{4vDt} - \mu_a vt\right) \quad (3.15)$$

which has been solved for the case of a pulse of light by Patterson *et al.* [35] The fluence rate from the solutions to the diffusion equation can be accurately calculated if $\mu_a \ll (1-g)\mu_s$, i.e. the absorption coefficient of the medium is much smaller than the isotropic scattering coefficient of the medium; and if the detection point is far from the source and the boundaries.

The solution from the intensity modulated source $U(r,t)$, for the source immersed in a strongly scattering infinite medium constitutes a scalar field that is propagating at constant speed in a spherical wave and attenuates as $exp(-\alpha r)/r$ as it propagates. The photon density generated by a sinusoidally intensity-modulated source at any given frequency propagates with a single phase velocity. The wavelength of the photon density wave is calculated to be

$$\lambda = 2\pi(2vD/\omega)^{1/2} \quad (3.16)$$

and its wave front advances at a constant speed of

$$V = (2vD\omega)^{1/2} \quad (3.17)$$

The wavelength given by (3.16) and the velocity given by (3.17) are for the photon

density wave and not of the electromagnetic wave which is multiply scattered in a strongly scattering medium.

Figure 12 illustrates the concept of photon density waves in a highly scattering media. The point source of light from the input optical fiber acts as a isotropic point source of light after 10 isotropic scattering lengths travelled in the medium. [34, 36]

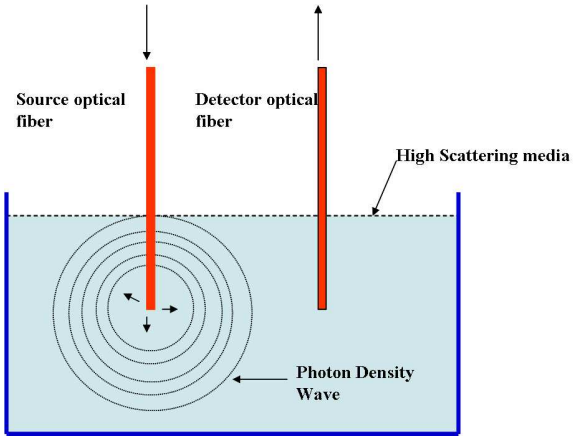

Fig. 12.: Photon density waves in a highly scattering medium.

Colloidal dispersions with microstructures as illustrated in Figure 13, can be studied using the above described procedure of photon transport in the dispersion. The length scale for the structure should be less than the isotropic mean free path, for the structure factor $S(Q)$ to be included in the expressions for the isotropic scattering

coefficient predictions, as described later in Chapter IV.

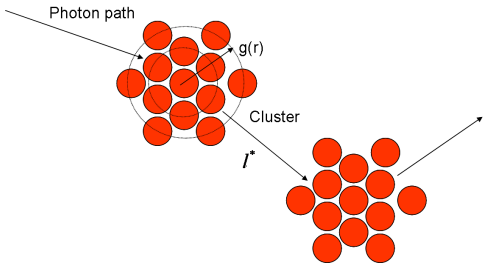

Fig. 13.: A cluster of particles which scatters light.

1. Diffusing wave spectroscopy: dynamic

Diffusing Wave Spectroscopy(DWS) [37] is similar in its approach to dynamic light scattering in which the intensity fluctuations are measured from a single speckle spot. The autocorrelation function decay time provides information about the dynamics of the system under investigation. In contrast to DLS, DWS is used for multiple scattering of light in dense opaque dispersions.

The technique is based upon the diffusion theory of light which is typically valid for most experimental systems. The scattering of light should never be too strong for localization of light, which is also referred to as "weak Anderson localization," and is caused by the constructive interference of two waves traversing in the opposite

directions. [38]

The equations for the autocorrelation function of DWS, have a probability attached for the several paths that a photon traverses through the opaque dense dispersion. Each scattering event is represented by an average over the whole ensemble and a probabilistic weight is attached to the path. The summation of all such paths gives the total correlation function.

The autocorrelation function, for the multiple scattering case without interactions among the particles, can be written as

$$g_1(t) = \int_0^\infty P(s) e^{-(2t/\tau)s/l^*} ds \tag{3.18}$$

where P(s) is the probability attached with each path; $\tau = (k_o^2 D)^{-1}$; D is the diffusion coefficient of the particle; s is the path length; and l^* is the isotropic mean free path. The characteristic decay time for a path of length s is $\tau l^*/(2s)$, which is the time it takes the total path length to change by $\approx \lambda$.

When particles are interacting and have correlations among them, the autocorrelation can be modified and the structure factor as well as a term for hydrodynamic interactions can be included to represent the correlations among the particles. The autocorrelation function can be written as

$$g_1(t) = \int_0^\infty P(s) exp\left(-2k_o^2 D_o t \frac{[H(Q)]}{[S(Q)]} \frac{s}{l^*}\right) ds \tag{3.19}$$

where H(Q) is the hydrodynamic coefficient dependent upon the wave vector. *The advantages of Diffusing Wave Spectroscopy are:*

1. DWS can be used for multiple scattering dispersions and can obtain information about the dynamics of highly concentrated opaque samples; and

2. It can discern between long path lengths and short path lengths, by the time

taken for the decay of the autocorrelation function, thus providing information about the length scales of particle motion.

The applications of DWS are:

1. Particle sizing can be done in both backscattering and transmission geometries, but only for monodisperse dispersions;
2. Particle motion can be studied on short length and time scales; and
3. Hydrodynamic interactions can be studied in transmission geometry.

Qiu *et al.* [39] have studied the hydrodynamic interactions in hard sphere particles with DWS and have found a linear relation of the ratio of effective diffusion coefficient and self diffusion coefficient with the volume fraction of the dispersion of particles.

The disadvantages of DWS are:

1. A probability has to be attached to each path under consideration, which may be unknown;
2. The scattering and absorption coefficients cannot be determined independently of each other and maybe unknown; and
3. Particle sizing is limited only to monodisperse dispersions, and polydispersity cannot be accounted for.

2. Diffuse transmission spectroscopy: static

In contrast to DWS, the measurements from the technique diffuse transmission spectroscopy [40] are static measurements. The photon diffusion is studied in the transmission geometry, and the solution to the diffusion equation is obtained in the transmission geometry.

The isotropic mean free path can be obtained for the transmission geometry, by use of the transmission coefficient,

$$T = \left(\frac{l^*}{L}\right) \frac{\frac{2}{3}\left(\frac{1+R}{1-R}\right) + \alpha}{1 + \frac{4}{3}\left(\frac{1+R}{1-R}\right)\frac{l^*}{L}} \tag{3.20}$$

where α is a parameter of the diffuse model of photon transport which is roughly unity, and R is the diffuse reflection coefficient from the dispersion-glass-air boundary which contains the sample.

3. Time domain: static

Time resolved measurements involve the use of a single pulse of light obtained from a laser, which has a pulse width of pico to femto seconds. The pulse propagates through the dense dispersion and the photons scatter and absorb, resulting in a broadened and attenuated pulse arising at the detection end of the sample under study.

Figure 14 illustrates the propagation of a pulse of light in a dense medium of scatterers and the resulting waveform which is dispersed from the original wave pulse. The spreading is due to different time of flights through the medium of scatterers.

The governing equation for the propagation of light through a multiple scattering medium in the diffusion approximation can be written as equation (3.6). [41]

Patterson *et al.* [35] have used the time domain technique to obtain the optical properties of a human calf muscle using an in vivo technique. A incident pulse from a laser on one end of the muscle and the arriving pulse which was detected at the other end. The optical properties were obtained by fitting the detected pulse profile to the solution of the time resolved diffusion equation. Similarly Saulnier *et al.* [42] and Garg *et al.* [41] have obtained the optical properties of scattering and absorption of polystyrene lattices at high volume fractions, using time resolved transmission

technique. They used 10psec pulses from a synchronously pumped dye laser delivered into the sample using an optical fiber. The deviation from Mie theory of light scattering at higher volume fractions due to hindered scattering was demonstrated and the effect of microstructure on the isotropic mean free path was analyzed. Wolf *et al.* [[43], [44]] also studied the properties of dispersions in the back scattering geometry.

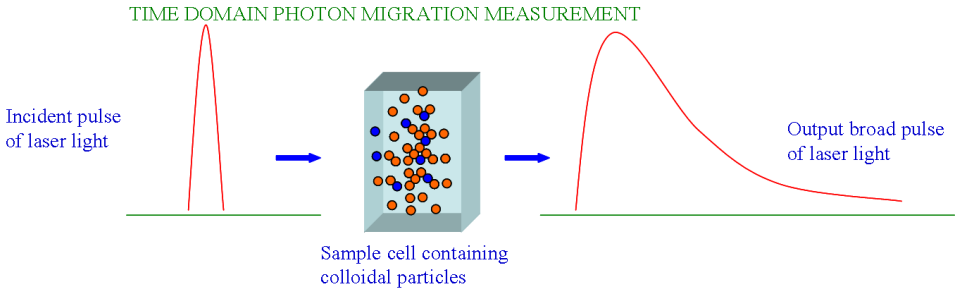

Fig. 14.: Time domain photon migration.

4. Frequency domain photon migration: static

Figure 15 embodies the principles of FDPM measurement as conducted in this work. Intensity modulated light (typically modulated at 30-100's MHz) is launched into a multiply scattering medium via a fiber optic. As the light propagates through the medium, it is phase shifted and amplitude attenuated with respect to the incident wave, due to the optical properties of the medium. The phase and amplitude of the

propagated wave are measured at known distances away from the point of incident illumination. The measurement approaches and instrumentation setup are provided in Chapter V.

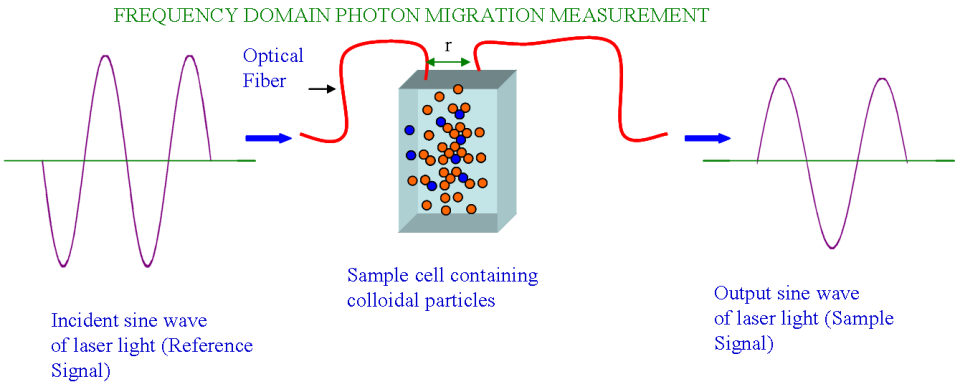

Fig. 15.: Principle of FDPM measurement for characterization of dense colloidal dispersions.

The propagation of the photon density wave can be modeled using the diffusion approximation to the radiative transfer equation, which is valid when the photon trajectory becomes completely randomized.

Herein, the analytical solution to Eqn 3.13 for the case of a sinusoidally intensity-modulated point of illumination in an infinite medium is used to predict $\Phi(r,\omega) = I_{AC}\exp(-iPS)$, where I_{AC} is the amplitude of the photon density wave; and PS is the phase lag that occurs between the incident and detected wave that has propagated

within the medium. The time average photon density at the detector is the DC component of the waveform.

Figure 16 depicts the two different waveforms of incident and sample photon density waves, with their respective *AC* and *DC* values. The waves are phase shifted with respect to each other, and the attenuations and phase shift values can be obtained from analysis of the data.

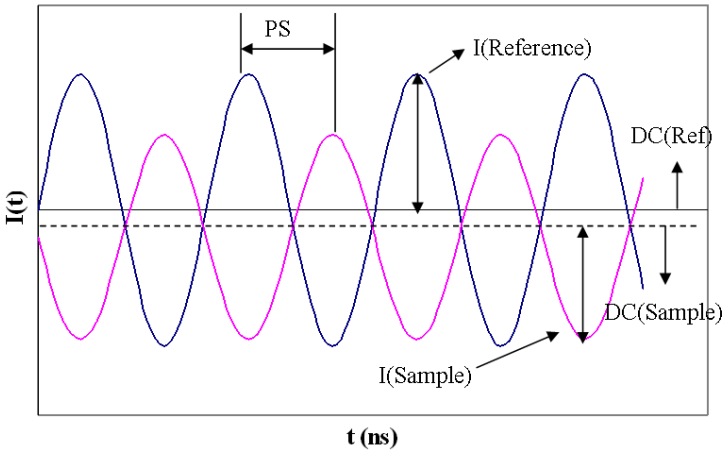

Fig. 16.: Data analysis in FDPM as reference (incident light) and sample signals are compared.

From FDPM measurements of AC, DC, and PS as a function of distance away

from the point of illumination, the optical properties of isotropic scattering and absorption coefficient, (μ_s' and μ_a), can be accurately fit to the solution of Eqn 3.13. [45], [46], [47], [48], [49] The measurements of AC, DC and PS taken at two different distances r_o and r helps make predictions of relative quantities which can be written as follows

$$DC_{rel} \equiv \frac{DC(r)}{DC(r_o)} = \frac{r_o}{r} exp[-(r-r_o)(\frac{\mu_a}{D})^{\frac{1}{2}}] \tag{3.21}$$

$$AC_{rel} \equiv \frac{AC(r)}{AC(r_o)} = \frac{r_o}{r} exp[-(r-r_o)(\frac{v^2\mu_a^2+\omega^2}{v^2D^2})^{\frac{1}{4}} cos[\frac{1}{2}\tan^{-1}(\frac{\omega}{v\mu_a})]] \tag{3.22}$$

$$PS_{rel} \equiv PS(r) - PS(r_o) = (r-r_o)(\frac{v^2\mu_a^2+\omega^2}{v^2D^2})^{\frac{1}{4}} sin[\frac{1}{2}\tan^{-1}(\frac{\omega}{v\mu_a})] \tag{3.23}$$

The relative modulation of the photon density wave is given as;

$$Mod_{rel} \equiv \frac{AC_{rel}}{DC_{rel}} \tag{3.24}$$

The above equations can be modified to expressions which are proportional to the distance between the source and detector fibers r and r_o respectively.

$$\ln(\frac{r}{r_o} DC_{rel}) = -(r-r_o)[3\mu_a(\mu_a+\mu_s')]^{\frac{1}{2}} \tag{3.25}$$

$$\ln(\frac{r}{r_o} AC_{rel}) = -(r-r_o)\sqrt{[\frac{3\mu_a(\mu_a+\mu_s')}{2}]}[\sqrt{1+(\frac{\omega}{v\mu_a})^2}+1]^{\frac{1}{2}} \tag{3.26}$$

$$\ln(Mod_{rel}) = -(r-r_o)\sqrt{[\frac{3\mu_a(\mu_a+\mu_s')}{2}]}[\sqrt{2}-((\sqrt{1+(\frac{\omega}{v\mu_a})^2}+1)^{\frac{1}{2}})] \tag{3.27}$$

$$\ln(PS_{rel}) = (r-r_o)\sqrt{[\frac{3\mu_a(\mu_a+\mu_s')}{2}]}[\sqrt{1+(\frac{\omega}{v\mu_a})^2}-1]^{\frac{1}{2}} \tag{3.28}$$

The experimental data of DC, AC and PS at two different distances can be regressed using the above equations which are linear with respect to the distance among the fibers. From the slopes of the experimental data which correspond to the analytical expressions prepared above, and by non linear numerical fitting, the

isotropic scattering and the absorption coefficients can be obtained independently of each other, which is not possible from time-independent photon diffusion techniques. FDPM also provides a way to measure the optical properties of the dispersion without the need of calibration of the instrument.

E. Acoustic scattering methods: static

Acoustic scattering methods involve the use of sound waves in a colloidal dispersion to determine its properties. The sound waves attenuate in the dispersion and the attenuation as a function of frequency, as well as the speed of sound are determined. [[50], [51]]

Electroacoustic spectroscopy method involves the coupling of electrodynamic phenomena and the sound wave pressure field.[[52], [53]] The method involves measuring the colloid vibration potential (CVP) or electrosonic amplitude (ESA).

Acoustic scattering methods are useful for concentrated colloidal dispersions where the particle size distribution and the volume fraction of the dispersion have to be determined. However several thermodynamic properties of the materials need to be known for making successful measurements. The optical properties of the dispersion for paint or pigment industry, cannot be found using acoustic techniques.

The various loss mechanisms for acoustic waves passing through a colloidal dispersion are viscous, thermal, acoustic scattering, intrinsic, structure and electrokinetic losses. Usually, the first four loss mechanisms are more important than the others. Viscous effects are observed in high density contrast systems, whereas thermal effects are observed in low density contrast systems.

F. Summary

This chapter reviews the experimental techniques available to make ensemble measurements of colloidal dispersions. Neutron and X-ray scattering techniques are useful techniques to study the structure of the dispersions and how the particles arrange themselves. The sources for these techniques are expensive and hence cannot be used to make real time measurements. Light scattering techniques offer an easier alternative and measurements can be made offline, wherein a small amount of sample is removed from the main process and analyzed after dilution.

Photon diffusion based techniques can be used to investigate dense colloidal dispersions and multiple scattering of light can be studied in dense colloidal dispersions enabling the determination of dispersion properties through multiple scattering data. Photon diffusion based techniques offer the possibility of successful determination of dispersion properties without dilution and in real time.

The next chapter discusses the concepts of structure factor determination from available methods, which are used to model the scattering data from the ensemble based techniques, using microstructure information of particles in the dispersions.

CHAPTER IV

MODELS OF STRUCTURE FACTORS

A. Introduction

This chapter describes the fundamentals for obtaining the structure factor models from analytical models and numerical computations as well as Monte Carlo simulations of monodisperse and bidisperse dispersions. The first section gives a brief review of direct integration methods to compute structure factors. Analytical models of the available structure factors are summarized and explained in the second section. These include the Percus-Yevick (PY) closure for hard spheres and the MSA closure for charged particles. The chapter is subsequently divided into two parts addressing monodisperse and bidisperse dispersions. Within each major part, sections on numerical computations using the Hypernetted Chain closure (HNC) and PY closure models for the Ornstein Zernike (OZ) equation are described. Monte Carlo simulations using scalar and vector methods, to obtain the structure factors are also described.

Figure (17) illustrates the various techniques used to obtain the static structure factors from theory and simulations. As illustrated in the flow diagram, the structure factors can be obtained from the solution of the coupled OZ equations using appropriate closure expressions, or by Monte Carlo simulations. The solution of the OZ equation is possible both analytically as well as numerically. Analytical solutions are however possible only for certain combination of potential models and closure expressions, such as Hard Sphere potential (HS) and (PY) closure model or Yukawa potential model and Mean Spherical Approximation (MSA). Numerical solutions of the OZ equations can be carried out for any suitable available potential model and either HNC or PY closures. The only limitation lies with the convergence issues of

numerical techniques.

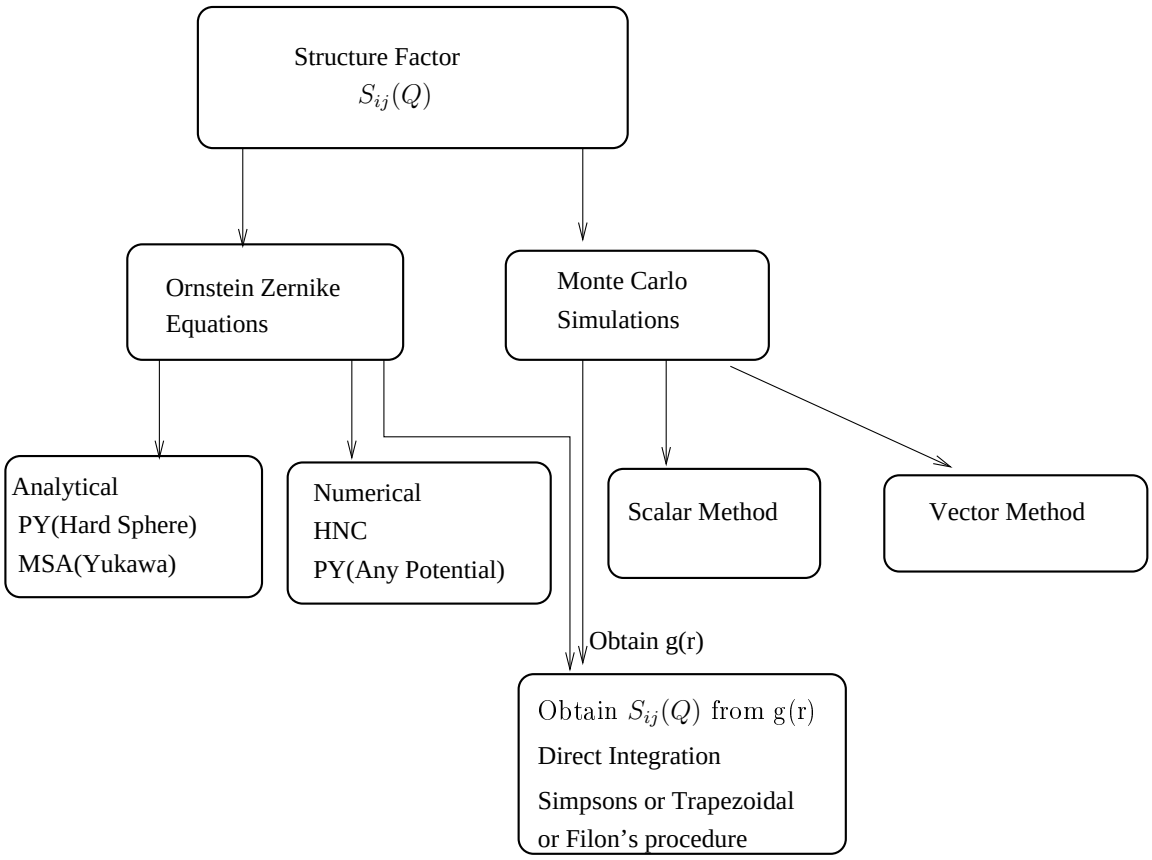

Fig. 17.: Flow diagram of different methods for obtaining structure factor.

An approach is to obtain the radial distribution function g(r) of the particles from Monte Carlo simulations or from the solution of the OZ equations, for a par-

ticular potential model and to use direct integration methods to compute structure factors. Direct integration method however fails to produce accurate results in the low Q region and cannot be used to explain experimental data. The method will be explained as the first section of this chapter.

The alternative route which is the most general and versatile way of obtaining structure factors is from Monte Carlo simulations. Two methods of scalar and vector methods are presented which can be used to obtain the structure factor directly from the positions of the particles in the simulation box with an arbitrary potential model. Any particle size or distribution can also be considered. The only drawback is the time involved in the computations of the structure factors from Monte Carlo techniques.

The basic idea behind developing the methods in this chapter is to create a general framework for structure factor calculations, for any potential model and size distribution of particles, which can subsequently be used for analyzing experimental data from many available experimental techniques, such as x-ray, neutron or light scattering.

1. Introduction to OZ equations and closure expressions: monodisperse

A brief introduction is first provided about OZ equations and the terminology used throughout the chapter. Monodisperse dispersions are first described, followed by the bidisperse case for polydisperse samples.

The underlying concept behind the OZ equation is to model the interaction between two particles mediated by the presence of a third particle. The OZ equation is written in terms of the direct correlation function, $c(r)$, and the total correlation function, $h(r)$,

$$h(r) - c(r) = n \int dr' c(\mid r - r' \mid) h(r') \tag{4.1}$$

where n is the particle number density. Here $h(r) = g(r) - 1$ where $g(r)$ is the radial distribution function, or the probability of finding a particle at a certain distance away from another particle. Conceptually the direct correlation function implies the direct interaction between two particles or molecules and the total correlation function between two particles is the complete interaction between two particles or molecules. Figure (18) provides a diagrammatic representation of the interactions between particles mediated by surrounding particles.

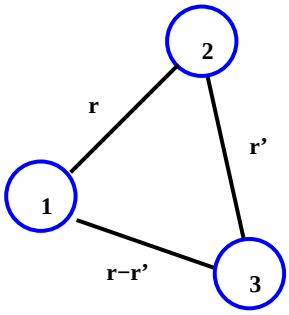

Fig. 18.: Particle interaction between particles 1 and 2 mediated by particle 3.

Hence in the above expression the total correlation function $h(r)$ is written as a sum of the direct correlation function $c(r)$ and the number density times the integral of the product of the direct correlation function with a third particle at distance $r^{'}$ and the total correlation function with the third particle at distance $r^{'}$.

When discretized over the radial distance between particles, eqn 4.1 leads to a coupled set of equations between two unknown functions. In order to be solved, a closure expression is needed. The closure expression relates the direct correlation function with the total correlation function and describes the mean potential of interaction between the particles or molecules. For example, the HNC closure is written as

$$c(r) = exp(-\beta\phi(r) + \gamma(r)) - \gamma(r) - 1 \tag{4.2}$$

where $\phi(r)$ is the mean potential of interaction described in chapter II and $\gamma(r) = h(r) - c(r)$.

The structure factor is defined to be

$$S(Q) = 1 + \rho h(Q) \tag{4.3}$$

or

$$S(Q) = \frac{1}{1 - \rho c(Q)} \tag{4.4}$$

where $h(Q)$ and $c(Q)$ are the Fourier transforms of the total and the direct correlation functions. For the remainder of the chapter, Fourier variable k is used instead of Q.

2. Introduction to MC and structure factor: monodisperse

For the Monte Carlo vector simulation, the expression for structure factor is given by

$$S = \frac{1}{N}\langle\sum_{i=1}^{N}\sum_{j=1}^{N} e^{(iQ.(r_i - r_j))}\rangle \tag{4.5}$$

which reduces to the expression provided in Eqn. (4.3), where N is the total number of particles; r_i and r_j are the particle positions. The difference with the OZ equation solution lies in the method of approach, as the vector method uses the particle

positions in the simulation box directly.

Eqn. (4.3) also reduces to the form given below

$$S(Q,R) = 1 + 4\pi\rho \int_0^R dr r^2 \left[\frac{\sin(Qr)}{Qr}\right][g(r) - 1] \tag{4.6}$$

which forms the basis for the Monte Carlo scalar method and the direct integration method which are described below.

3. Introduction to OZ and closure expressions: polydisperse

Similarly for a mixture of particles of different size, the OZ equations can be written as

$$h_{pq}(r) - c_{pq}(r) = \sum_{n=1}^{m} \rho_n \int c_{pn}(\mid s \mid) h_{nq}(\mid r - s \mid) ds \tag{4.7}$$

where p and q represent particles of two different types, and m is the total number of particles in the mixture. The above set of equations are solved for a particular closure model and a potential model of interaction. The technique is described later in the chapter.

From $h_{pq}(r)$ the definition of the partial structure factor is

$$S_{ij}(Q) = 1 + \rho_{ij} h_{ij}(Q) \tag{4.8}$$

For the binary mixture case, the structure factors are written as S_{11}, S_{22} and S_{12}.

4. Introduction to MC and structure factors: polydisperse case

For the vector method of Monte Carlo simulations the expression for the structure factor for polydisperse suspensions is written as:

$$S_{ij} = \frac{1}{\sqrt{N_i N_j}} \langle \sum_{i=1}^{N_i} \sum_{j=1}^{N_j} e^{iQ.(r_i - r_j)} \rangle \tag{4.9}$$

where N_i and N_j are the number of particles of type i and j; Q is the scattering wave vector; r_i and r_j are the positions of the particles in the simulation box. The above expression reduces to the form of Eqn. (4.8).

These equations form the basis of calculations for the remainder of the chapter.

B. Direct integration method for Fourier transformation of the radial distribution from Monte Carlo simulation and OZ solution methods

The direct Fourier transformation of the radial distribution function obtained from methods such as the MC simulation or solution of the OZ equation, is expressed as:

$$S(Q, R) = 1 + 4\pi\rho \int_0^R dr r^2 \left[\frac{\sin(Qr)}{Qr} \right] [g(r) - 1] \tag{4.10}$$

The above equation can be computed by direct integration procedures such as Simpson's rule or trapezoidal rule, or by using techniques such as Filon's Procedure. [54] However, large oscillations result in low Q regions and restrict direct Fourier transform of the radial distribution function for accurate determination of structure factors. The vector and scalar methods have proven to be more effective, and can be used to study polydisperse mixtures which are the cornerstone to understanding the properties of colloidal dispersions. Also the structure factor obtained from the solution of the OZ equations is from the Fourier transform of the direct correlation function, which gives most accurate structure factors in the low Q region. Hence the direct integration technique was not used in this research.

C. Analytical models of structure factor

The analytical models of the structure factors are obtained only for specific closure and potential models. An analytical result for the cases of monodisperse, bidisperse and polydisperse hard sphere potential can be obtained from the PY closure of the OZ equation. Also for the case of charged spheres, MSA is used to solve for the direct correlation function and the structure factor for Yukawa potential model.

The analytical models for the structure factors have been provided in the Appendix A and B of this dissertation.

D. Numerical methods for calculating the structure factor (Monodisperse case)

The goal of this work is to solve more general predictions of structure factor from Monte Carlo simulations and from numerical solutions of the OZ equations with various closure models which are the most general methods to predict the partial structure factors. The solution of the OZ equations can be carried out by a combination of Newton Raphson and Picard iterations and is presented as Gillan's method [55]. Good agreement has been found for Monte Carlo simulations of the Yukawa potential and truncation of the potential, for HNC and PY Closure. The MSA closure model has an analytic solution and the solution provided by JN Herrera [56] is employed for the study. This analytic model is provided in Appendix B.

We study the structure factor models to obtain accurate structure factors for the analysis of the isotropic scattering data obtained from experiment.

1. Monte Carlo simulations

The approach in the MC simulations uses the constant NVT ensemble method described by Allen and Tildesley [54]. The term NVT represents a constant number of particles N, at constant volume V, and at constant temperature T of the system. The algorithm for Monte Carlo simulations is described on the following page. In this approach the potential of interaction, and the errors in the calculation due to its truncation are incorporated as corrections to the energy terms. Using truncation of potential for charged systems or for long ranged forces can lead to erroneous MC simulation results. Rosenfeld [57] has described an ewald summation technique to handle long ranged forces in Monte Carlo simulations. The use of the ewald technique can eliminate the problems occurring due to truncation of potential for long ranged interactions. A recent publication by Giacometti *et al.* [58] discussed the use of the ewald method for understanding interactions in binary Yukawa mixtures of globular proteins. However in our study, the number of particles in the system is kept large to eliminate the errors due to truncation of potential, and the ewald method is not used in the Monte Carlo simulations.

The structure factors obtained from Monte Carlo simulations are accurate in the low Q region and do not suffer from errors due to truncation of potential.

The constant NVT Monte Carlo technique is described in the flow diagram of Figure(19). The procedure is described as follows:

1. Constant NVT (N is the number of particles; V is the volume of the region occupied by the particles; T is the temperature) or canonical ensemble method is used to simulate the particles.

2. The particles are initially arranged on a regular lattice such as FCC or BCC .

3. In one cycle of the MC technique all the particles are given a random displacement of variable length, which is a multiple of the particle diameter times a random factor between 0 and 1.

4. The random displacement of one particle is accepted if the energy of the ensemble is less than the ensemble in its previous configuration or if $exp(-\beta(\delta v))$ is greater than a random number. Here $\beta = \frac{1}{k_B T}$, where k_B is the Boltzmann constant and T is the temperature; and δv is the change in the energy associated with a change in the configuration of the particles. This sampling is called Boltzmann sampling.

5. Periodically throughout the MC simulations, the particle positions are used to calculate the radial distribution function and the structure factor of the dispersion.

6. The above steps are repeated for a fixed number of cycles. Here in one cycle all the particles are moved by one step in a random direction and the new positions are either accepted or rejected according to the energy criterion described in step 4.

The Monte Carlo methods for determining monodisperse structure factors using the scalar and vector methods is described in subsections a & b which are to follow.

The variables used in the flowchart are described in the table I as follows:

Table I.: Variables defined in the Monte Carlo simulation flowchart

Variable	Description
vold	Energy in the old configuration
vnew	Energy in the new configuration
deltv	Change in energy associated with change in configuration
rxinew	New position of the particle
rxiold	Old position of the particle
rand	Random number generated by the algorithm
len	Length of the simulation box
drmax	Maximum allowable displacement per particle

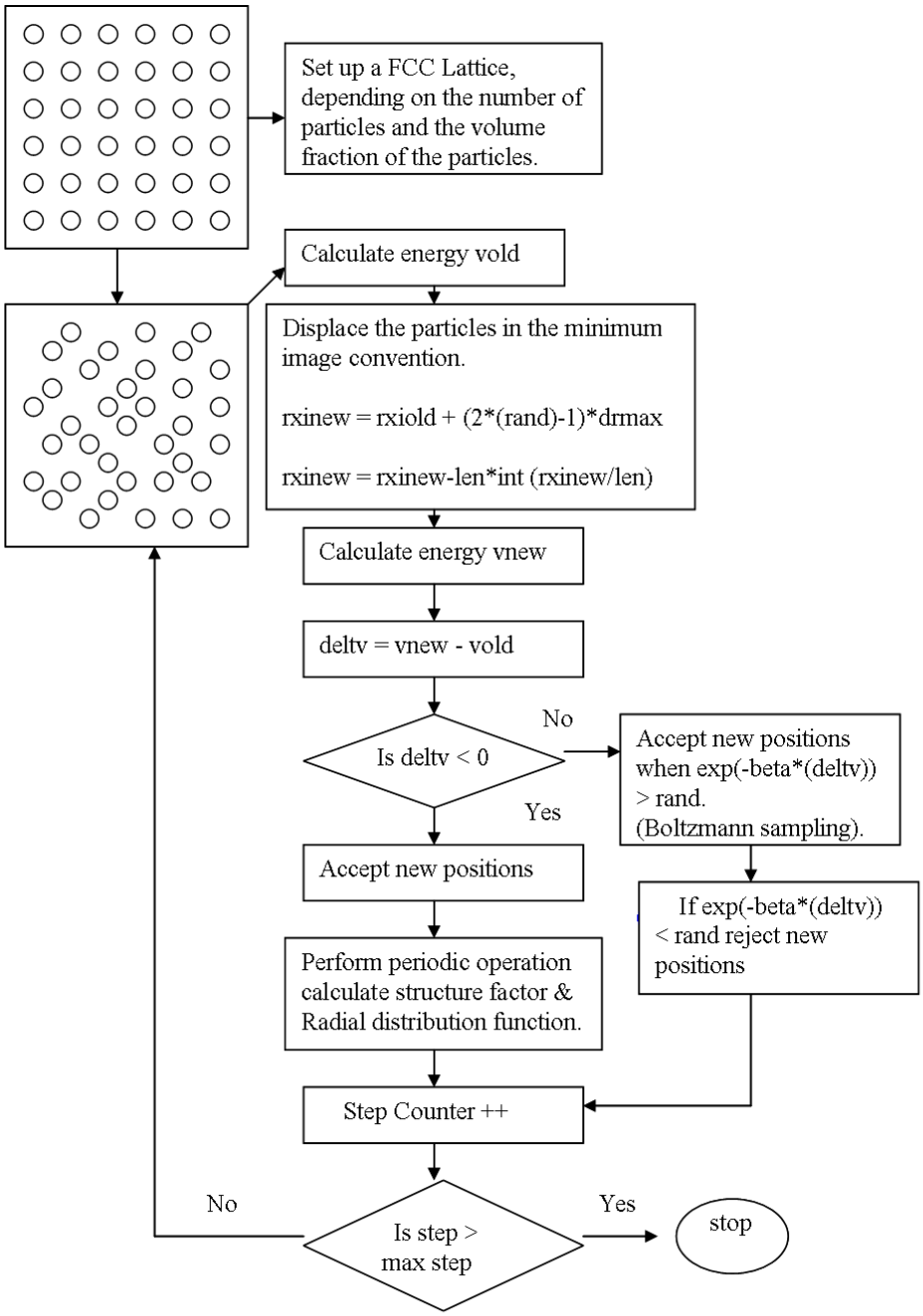

Fig. 19.: Steps in a constant NVT Monte Carlo simulation procedure.

a. Scalar method of evaluating structure factors from MC simulations

The scalar method developed by Egelstaff *et al.* [59–61] provides a good description of the structure factor at higher wave vector values, but requires a correction at low wave vector values. Since isotropic scattering coefficients are obtained by integrating the wave vector values from 0 to Q_{max}, values of the structure factor in the low Q region need to be accurate.

The formulation for the scalar method for monodisperse dispersions is written as:

$$S_N(Q,R) = 1 + 4\pi\rho \int_0^R dr r^2 \left[\frac{sin(Qr)}{Qr}\right] [g_N(r) - 1] \tag{4.11}$$

where S_N and g_N are the structure factor and radial distribution function within the finite size simulation box for N particles; R is the cut off or half the length of the simulation box; ρ is the density of particles in the dispersion. S_N can be rewritten as

$$S_N(Q,R) =< N(Q,R) > -\bar{N}(Q,R) \tag{4.12}$$

where the terms $< N(Q,R) >$ and $\bar{N}(Q,R)$ are defined as

$$< N(Q,R) > \equiv 1 + 4\pi\rho \int_0^R dr r^2 \left[\frac{sin(Qr)}{Qr}\right] [g_N(r)] \tag{4.13}$$

and,

$$\begin{aligned} \bar{N}(Q,R) &= 4\pi\rho \int_0^R dr r^2 \left[\frac{sin(Qr)}{Qr}\right] \\ &= \frac{4}{3}\pi\rho R^3 u(QR) \end{aligned} \tag{4.14}$$

The term $< N(Q,R) >$ is computed from the quantity

$$
\begin{aligned}
< N(Q,R) > &= X_k(Q) \\
X_k(Q) &= \frac{1}{N}\sum_{i=1}^{N}\sum_{j=1}^{N}\left[\frac{sin(Qr_{ij})}{r_{ij}}\right]\triangle_{ijk}(R) \\
&= \frac{2}{N}\sum_{i=1}^{N-1}\sum_{j=i+1}^{N}\left[\frac{sin(Qr_{ij})}{r_{ij}}\right]\triangle_{ijk}(R) + 1 \qquad (4.15)
\end{aligned}
$$

where

$\triangle_{ijk}(R) = 1$ if $r_{ij} \leq R$

$\triangle_{ijk}(R) = 0$ if $r_{ij} > R$

Here $X_k(Q)$ is a statistical quantity that is evaluated for k configurational spaces; r_{ij} is the distance between the particles i and j in the simulation box; and N is the number of particles in the simulation box.

The second term is evaluated by the use of the function $u(QR) \equiv \frac{3}{x^3}(sinx - xcosx) = \frac{3}{x}j_1(x)$, in which $j_1(x)$ is the spherical Bessel function.

To show results for the simplest case of hard spheres, the structure factors obtained from simulations for a hard sphere potential, for monodisperse and bidisperse cases, were compared with analytical models from Ashcroft *et al.* [62] and Hunter [63], showing favorable comparisons.

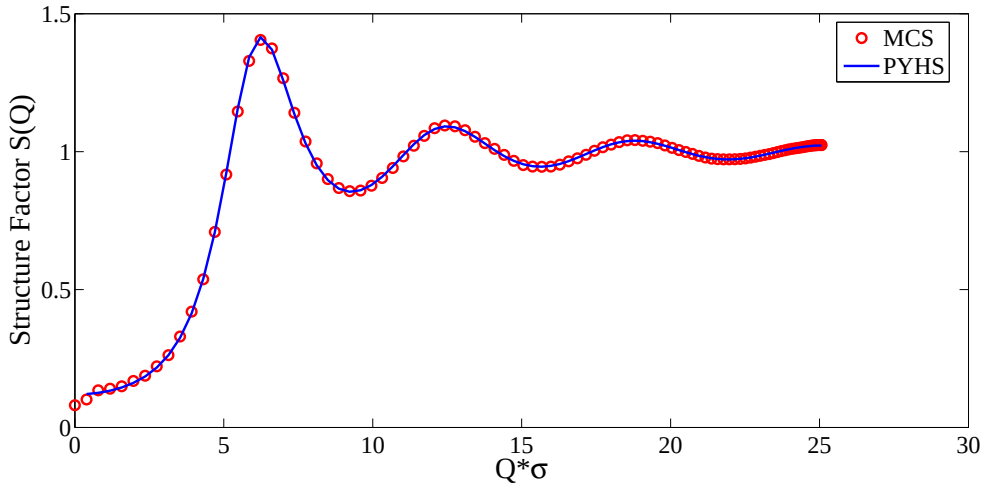

Fig. 20.: Structure factors S(Q), predicted from MC scalar method (symbols) and hard sphere PY model (line) versus the product of $Q\sigma$ for monodisperse spheres at volume fraction of $\phi = 0.27$ (points), for 1372 particles.

Figure 20 shows the comparison of the *monodisperse* structure factor obtained from Monte Carlo simulations using the scalar method and the Percus Yevick hard sphere structure factor model. Good agreement is found with the analytical model and the structure factor is stable in the low Q region.

The Monte Carlo simulation method for the scalar case is described as below:

1. MC simulations are run for 150,000-200,000 steps of particle rearrangement and the configuration space is sampled after every 100-200 steps for ensemble averaging across 150-200 configurations. Simulation times on a P4 2.8 GHz takes $\geq$ 12 hrs, and depends upon the number of particles in the simulation box and the number of particle arrangements.

2. The scalar method provides a straightforward way of calculation by sampling the quantities described above along with the calculations of the radial distribution function, to obtain structure factors. The advantage of the MC scalar method is that S(Q) values at any Q can be determined by changing the magnitude of Q as $NQ(\frac{4\pi m}{\lambda}\sin(\theta/2))$, where NQ can be a fraction or any integer value. This method also results in less statistical fluctuations of S(Q) as a function of Q. However, accuracy depends upon the size of the simulation box and hence the number of particles. The S(Q) peak predictions can be made appropriately only when the number of particles in the simulation box is large, or equivalently when the radial distribution function approaches a value of 1.

b. Vector method of evaluating structure factors from Monte Carlo simulations

The vector method was developed by Frenkel *et al.* [64] and has the advantage that direct Fourier transformation of the particle positions leads to fewer oscillations in the low Q region of the wave vector. The vector method consists of Fourier transforming the particle positions along 13 directions (three along P[100], six along P[110], and four along P[111], where P represents permutations). Figures (21) and (22) depict the reciprocal lattice and the thirteen wave vector directions.

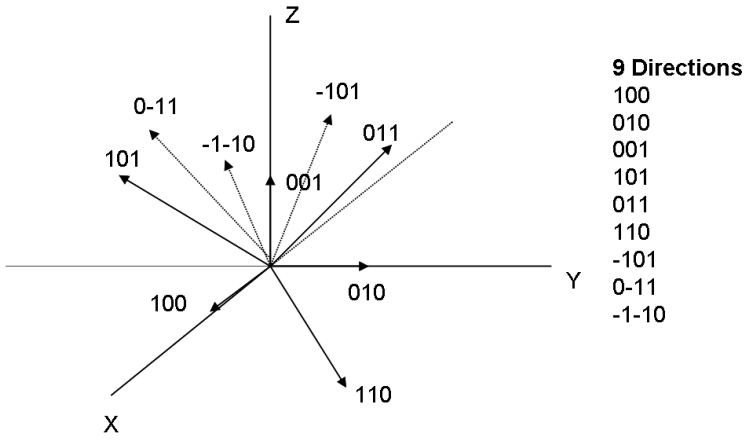

Fig. 21.: Wave vector directions for the reciprocal space evaluation of the structure factors. The numbers correspond to the directions h,k,l of the reciprocal lattice space.

The structure factor for the monodisperse case has the following form

$$S = \frac{1}{N}\langle \sum_{i=1}^{N}\sum_{j=1}^{N} e^{(iQ.(r_i - r_j))} \rangle \tag{4.16}$$

where the angular brackets denote averaging for a number of configuration space points collected during the simulation. Here Q is the wave vector and r_i, r_j are the vector positions of the particles during the simulation. The magnitude of the wave vector depends upon the length of the simulation box and can be computed as,

$\mid Q \mid = \frac{2\pi p\sqrt{h^2+k^2+l^2}}{L}$ p = 1,2,3...;L = Length of simulation box

where h,k,l are the indices of the reciprocal lattice vectors and are described in Figures (21) and (22).

Figure 23 shows the comparison of the *monodisperse* structure factor obtained

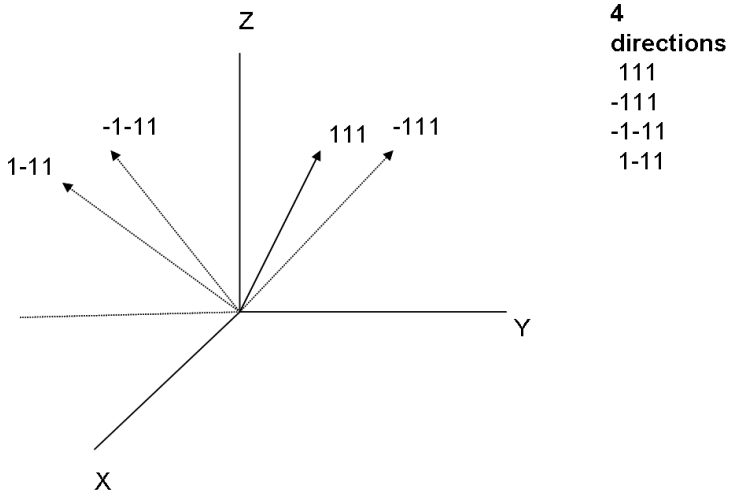

Fig. 22.: Wave vector directions for the reciprocal space evaluation of the structure factors. The numbers correspond to the directions h,k,l of the reciprocal lattice space.

from Monte Carlo simulations using the vector method and the Percus Yevick hard sphere structure factor model. Good agreement is found with the analytical model and the structure factor is stable in the low Q region.

The vector method of Monte Carlo simulation is described as following:

1. MC simulations are run for 150,000-200,000 steps of particle rearrangement and the configuration space is sampled after every 100-200 steps for ensemble averaging across 150-200 configurations. Simulation times on a P4 2.8 GHz takes $\geq$ 12 hrs, and depends upon the number of particles in the simulation box and the number of particle arrangements.

2. In our studies the number of particles was chosen to be large, i.e. values of 864, 1372, and 2048. This helps in obtaining as low a Q value as possible.

The equation for the magnitude of the wave vector Q has the length of the simulation box, which in turn depends upon the number of particles used in the simulation, via the equation $L = \sigma(\frac{N\pi}{6\phi})^{1/3}$ for monodisperse systems and via $L = \frac{\pi}{6\phi}(n_1\sigma_1^3 + n_2\sigma_2^3)^{1/3}$ for bidisperse systems of particles. Since the data for Q = 0 cannot be obtained, the curves of S(Q) vs. Q can then be extrapolated to Q = 0.

3. The usefulness of this approach is that even with a few number of particles (e.g. 108), the peak height predictions are accurate for hard spheres and the low Q region is effectively sampled. The number of S(Q) predictions from the vector method is limited to only those points at Q values that are multiples of $2\pi\frac{\sqrt{h^2+k^2+l^2}}{L}$. Consequently fewer number of S(Q) predictions are made using the vector MC method. Nonetheless this approach is the most stable and takes the same time to evaluate the structure factors as the scalar method described in the previous section.

4. This technique can suffer from statistical variations, which can be reduced by running the simulations for larger number of particle configurations and rearrangements.

To summarize, the scalar method provides a greater number of wave vector points than the vector method, and good over all agreement. In the low Q region the vector method is shown to have less oscillations than the scalar method. Consequently the vector method is used to predict the data of isotropic scattering coefficients from experimental FDPM measurements.

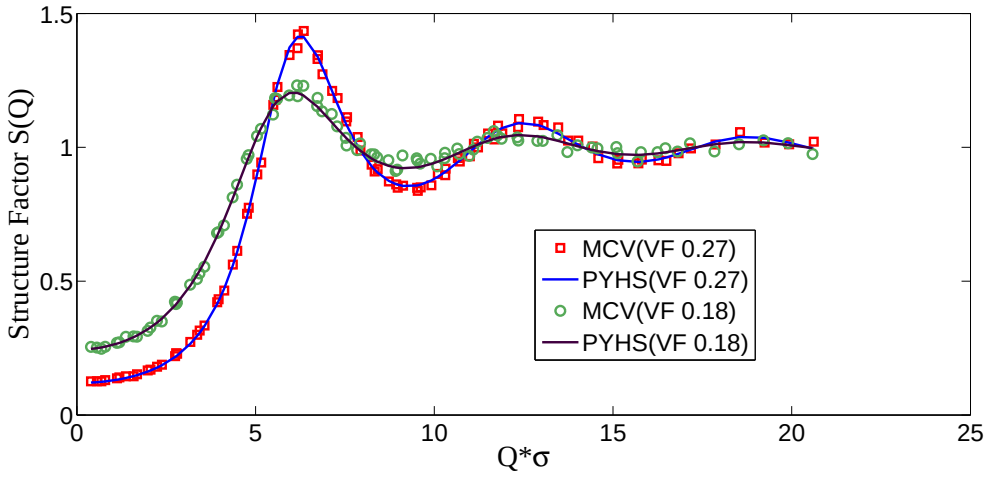

Fig. 23.: Structure factors S(Q) versus $Q\sigma$, predicted from MC vector method (symbols) and hard sphere PY model (lines) versus the product of $Q\sigma$ for monodisperse spheres at volume fractions of $\phi = 0.18$(circles) and $\phi = 0.27$ (squares).

2. Structure Factor evaluation from Ornstein Zernike Equation

The Ornstein Zernike equation is written in terms of the direct correlation function $c(r)$ and the total correlation function $h(r)$,

$$h(r) - c(r) = n \int dr' c(\mid r - r' \mid) h(r') \tag{4.17}$$

where n is the particle number density. The above equation is solved along with

closure expressions of (PY) and (HNC) which are written as

$$c(r) = (1 + \gamma(r))(exp(-\beta\phi(r)) - 1) \qquad Percus \quad Yevick \tag{4.18}$$

$$c(r) = exp(-\beta\phi(r) + \gamma(r)) - \gamma(r) - 1 \qquad Hypernetted \quad Chain \tag{4.19}$$

where, $\gamma(r) = h(r) - c(r)$; $\phi(r)$ is the interaction potential

The procedure used to solve the above OZ equation for various closure expressions is that of Gillan [55].

1. The space is discretized into a finite mesh along the radial direction and the initial estimate for the function $\gamma(r)$ is used to generate the direct correlation function $c(r)$ from the closure expressions. The three dimensional Fourier transform of $c(r)$ is then taken [65] and inserted into the OZ equation, to obtain the Fourier transform of $\gamma(r)$.

$$\tilde{\gamma}(k) = \frac{n\tilde{c}(k)^2}{1 - n\tilde{c}(k)} \tag{4.20}$$

The output can be transformed back to obtain the value of $\gamma^{'}(r)$. The initial estimate of γ_i is decomposed into coarse and fine parts. This is achieved by means of a choice of basis functions to represent the coarse part. In this work, roof functions have been employed to represent the coarse part of the initial guess for $\gamma(r)$. The decomposition of γ in the discrete form is done in the following manner

$$\gamma_i = \sum_{\alpha} a_\alpha P_\alpha^i + \triangle\gamma_i \tag{4.21}$$

where

$$\sum_i P_\alpha^i \triangle\gamma_i = 0 \forall \alpha \tag{4.22}$$

2. The discrete equations must be solved so that after a Newton Raphson cycle, the estimate obtained is $\gamma^{'}$

$$\gamma_i^{'} = \sum_\alpha a_\alpha^{'} P_\alpha^i + \triangle\gamma_i^{'} \tag{4.23}$$

If $\gamma^{'}$ is the exact solution, then

$$d_\alpha \equiv a_\alpha - a_\alpha^{'} \tag{4.24}$$

and

$$\triangle\gamma_i^{'} = \triangle\gamma_i \tag{4.25}$$

For an arbitrary $\triangle\gamma_i$ the last equation may not be satisfied and instead, the set of a_α must be sought which satisfies the difference in the values. This set of values can be found using a Newton Raphson (NR) scheme. From the old estimate of a_α a new estimate $\bar{a}_\alpha$ is obtained

$$\bar{a}_\alpha = a_\alpha - \sum_\beta (J^{-1})_{\alpha\beta} d_\beta \tag{4.26}$$

where d_β are the differences defined by equation 4.24, and the Jacobian matrix is

$$J_{\alpha\beta} = \frac{\partial d_\alpha}{\partial a_\beta} \tag{4.27}$$

3. A closure expression like the Percus Yevick equation in the discrete form can be written as

$$c_i = (1 + \gamma_i)(exp(-\beta\phi_i) - 1) \tag{4.28}$$

and in fourier space the above equation is transformed as

$$\tilde{c}_j = \frac{4\pi\delta r}{k_j} \sum_{i=1}^{N-1} r_i c_i sink_j r_i \tag{4.29}$$

$$\tilde{\gamma}_j = \frac{n\tilde{c}_j^2}{1 - n\tilde{c}_j} \tag{4.30}$$

$$\gamma_i^{'} = \frac{\delta k}{2\pi^2 r_i} \sum_{j=1}^{N/2-1} k_j sink_j r_i \tilde{\gamma}_j \tag{4.31}$$

where

$$r_i = i\delta r, k_j = \frac{2\pi j}{N\delta r} \tag{4.32}$$

For the HNC equation, (4.28) is replaced by

$$c_i = (1 + \gamma_i)(exp(-\beta\phi_i) - 1) \tag{4.33}$$

4. The Jacobian matrix $J_{\alpha\beta}$ is defined by equation(4.27). The definition of d_α provides the expression

$$J_{\alpha\beta} = \delta_{\alpha\beta} - \frac{\partial a_{\alpha}^{'}}{\partial a_{\beta}} \tag{4.34}$$

$$= \delta_{\alpha\beta} - \sum_{i} \frac{\partial a_{\alpha}^{'}}{\partial \gamma_i} . \frac{\partial \gamma_i}{\partial a_{\beta}} \tag{4.35}$$

$$= \delta_{\alpha\beta} - \sum_{ij} Q_{\alpha}^{i} \frac{\partial \gamma_i^{'}}{\partial \gamma_j} P_{\beta}^{j} \tag{4.36}$$

An expression for $\frac{\partial \gamma_i^{'}}{\partial \gamma_j}$ can be obtained using the relation

$$\frac{\partial \gamma_i^{'}}{\partial \gamma_j} = \sum_{m=0}^{\frac{N}{2}-1} \frac{\partial \gamma_i^{'}}{\partial \tilde{\gamma}_m} . \frac{\partial \tilde{\gamma}_m}{\partial \tilde{c}_m} . \frac{\partial \tilde{c}_m}{\partial c_j} . \frac{\partial c_j}{\partial \gamma_j} \tag{4.37}$$

By inserting expressions for the four factors in equation (4.37), the results for the PY case are

$$\frac{\partial \gamma_i^{'}}{\partial \gamma_j} = (\frac{\delta r r_j}{\pi r_i})(exp(-\beta\phi_j) - 1)(D_{i-j} - D_{i+j}) \tag{4.38}$$

for $i \neq 0$, where

$$D_l = \delta k \sum_{m=0}^{\frac{N}{2}-1} cosk_m r_l (\frac{2n\tilde{c}_m}{1 - n\tilde{c}_m} + (\frac{n\tilde{c}_m}{1 - n\tilde{c}_m})^2) \tag{4.39}$$

For the special case $i = 0$, the expression is

$$\frac{\partial \gamma_0^{'}}{\partial \gamma_j} = (\frac{2\delta r r_j}{\pi})(exp(-\beta\phi_j) - 1)E_j \tag{4.40}$$

where

$$E_j = \delta k \sum_{m=0}^{\frac{N}{2}-1} k_m sink_m r_j (\frac{2n\tilde{c}_m}{1 - n\tilde{c}_m} + (\frac{n\tilde{c}_m}{1 - n\tilde{c}_m})^2) \tag{4.41}$$

For the HNC case there is only a difference in the replacement of $exp(-\beta\phi_j)-1$ by $exp(-\beta\phi_j+\gamma j)$ in equations (4.38) and (4.40).

5. The direct correlation function values can be obtained from the closure expressions of (4.28) and (4.33), by solving for the unknown γ_i iteratively, while reducing the errors defined below

   - Coarse part refinement: Newton Raphson Cycle (Finding coefficients of the first term of Eqn. (4.21))

$$error1 = \sqrt{(\mathbf{a}_\alpha - \mathbf{a}'_\alpha)^2} \tag{4.42}$$

   - Fine part refinement: Picard Iteration Cycle to approximately $10e^{-8}$(Second term of Eqn. (4.21))

$$error2 = \sqrt{(\triangle\gamma_i - \triangle\gamma'_i)^2} \tag{4.43}$$

6. Subsequently, after obtaining the direct correlation function values at discrete points c_i, the structure factor can be determined from the Fourier transform of the direct correlation function, $\mathbf{c}(k)$, by the following expression

$$S(k) = \frac{1}{1-\rho c(k)} \tag{4.44}$$

The above method is illustrated in Figure (24) in the form of a flow diagram adapted from Gillan's work.

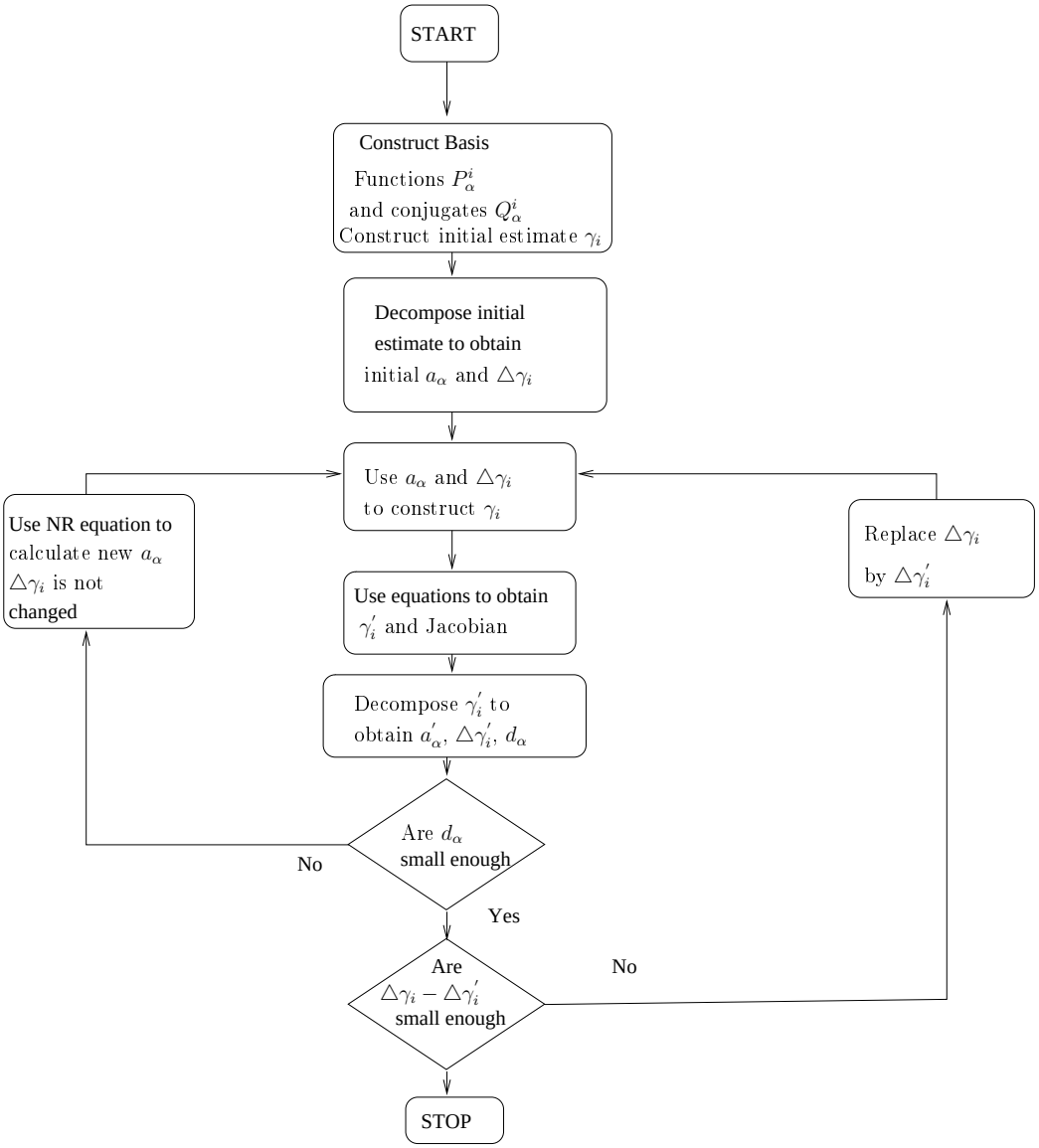

Fig. 24.: Flow diagram for the calculation of the direct correlation function from the OZ equation and closure models.

E. Numerical methods of calculating the structure factor (Bidisperse Case)

1. Monte Carlo simulations

a. Structure factor from Monte Carlo simulations: Scalar method

We have extended the definitions provided by Egelstaff *et al.* for a monodisperse system of particles to find the partial static structure factors for a bidisperse mixture. [59–61] For a bidisperse mixture the equations can be modified to write the expressions for structure factors as

$$X_k(Q, r_{ij}) = \frac{1}{\sqrt{N_i N_j}} \sum_{i=1}^{N_i} \sum_{j=1}^{N_j} \left[\frac{sin(Qr_{ij})}{Qr_{ij}} \right] \triangle_{ijk}(R) \tag{4.45}$$

$$S_{N_{ij}}(Q, R) = \bar{X}(Q, R) - \frac{4}{3}\pi\rho_{ij}R^3 u(QR) \tag{4.46}$$

where the density $\rho_{ij} = \frac{\sqrt{N_i * N_j}}{L^3}$. Here N_i and N_j are the number of particles of type i and j. In the second term $u(QR) \equiv \frac{3}{x^3}(sinx - xcosx) = \frac{3}{x} j_1(x)$, in which $j_1(x)$ is the spherical Bessel function. This method provides a good comparison for the partial structure factors over the entire Q range, except for low Q values where only the vector method is found to be stable. Also, the number of Q values that are available by the use of this method are not limited as in the case of the vector method, making it useful for a general comparison.

Figure (25) depicts the results obtained from Monte Carlo scalar method simulations and Percus Yevick hard sphere analytical results.

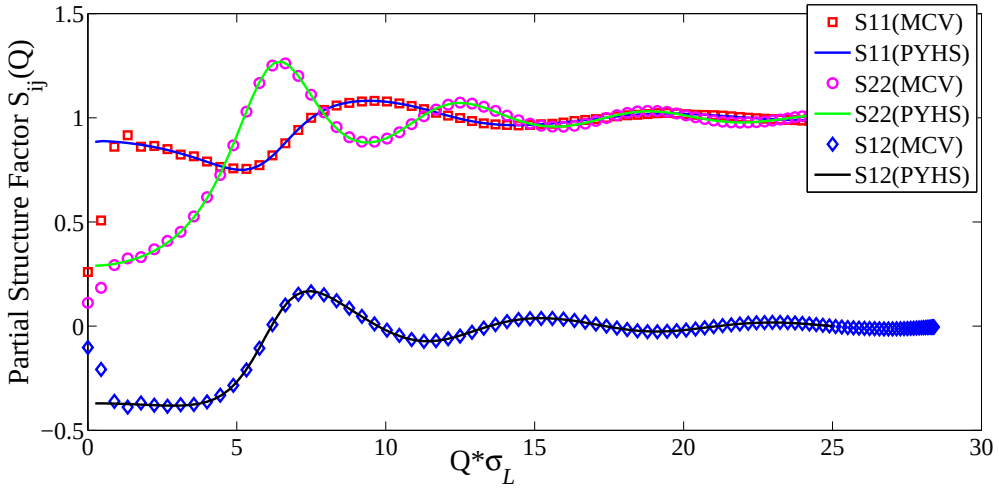

Fig. 25.: Bidisperse partial static structure factors for hard spheres. S_{11} represents contributions to interactions between small spheres,S_{22} represents contributions to interactions between large spheres and S_{12} represent interactions between small and large spheres. Points are Monte Carlo results (scalar method) and lines are hard sphere PY model. Here N is the total number of particles in the simulation box; $x_{num} = 0.437$ is the number ratio of the larger diameter particles; $\alpha = \frac{\sigma_s}{\sigma_l}$is the ratio of the smaller diameter particle to the larger diameter particles and $\phi = 0.27$ is the volume fraction of the particles in the simulation box. MCV refers to Monte Carlo Vector method and PYHS refers to Percus Yevick Hard sphere results.

b. Structure factor from Monte Carlo simulations: Vector method

The vector method was developed by Frenkel *et al.* [64]. The partial structure factors can be obtained by direct Fourier transformation of the particle positions within the simulation box. The partial structure factors are obtained by the following expressions

$$S_{ij} = \frac{1}{\sqrt{N_i N_j}} \langle \sum_{i=1}^{N_i} \sum_{j=1}^{N_j} e^{iQ.(r_i - r_j)} \rangle \tag{4.47}$$

where Q is the wave vector, N_i and N_j are the number of particles of type i,j and r_i, r_j are the vector positions of the i,j particles during the simulation. The magnitude of the wave vector depends upon the length of the simulation box and can be computed as,

$| Q | = \frac{2\pi p\sqrt{h^2+k^2+l^2}}{L}$ p = 1,2,3...;L = Length of simulation box

where h,k,l are the indices of the reciprocal lattice vectors and are described in the figure.

c. Comments on Binary structure factors from Monte Carlo simulations (Vector and Scalar methods)

In all the Monte Carlo simulations the potential is truncated to half the length of the simulation box. The particles do not penetrate each other, and we have not considered attractive potential energy terms when defining the potential.

We have obtained structure factors for the case of purely hard sphere mixtures and have found them to be in good agreement with those obtained from analytical solutions in the Percus-Yevick closure by Ashcroft *et al.* [62] After verification of the simulation programs for hard spheres with available analytical model for hard spheres, charged particles were placed in the simulation box interacting with each other via the binary Yukawa potential model. The ionic strength of the dispersion medium determined the Debye Huckel parameter κ and hence the screening length κ^{-1}. The Debye Huckel parameter is calculated as $\kappa = \sqrt{\frac{\sum_i n_i z_i^2 e^2}{\epsilon_o \epsilon k_B T}}$, where, n_i is the number of ions; z_i is the charge on the ions; e is the electronic charge; ϵ_o is the dielectric constant of vacuum; ϵ is the relative permittivity; k_B is the Boltzmann's constant; and T is the temperature. The simulations were carried out for the mixtures of particles, with different charges and ionic strengths of the surrounding medium was changed.

Figure (26) shows the comparison of Monte Carlo simulations of bidisperse structure factors for the hard sphere potential with the Percus Yevick hard sphere structure factor model. The method of simulations here is the *vector* method. Good agreement is found with the analytical results and stable solutions are found in the low Q region.

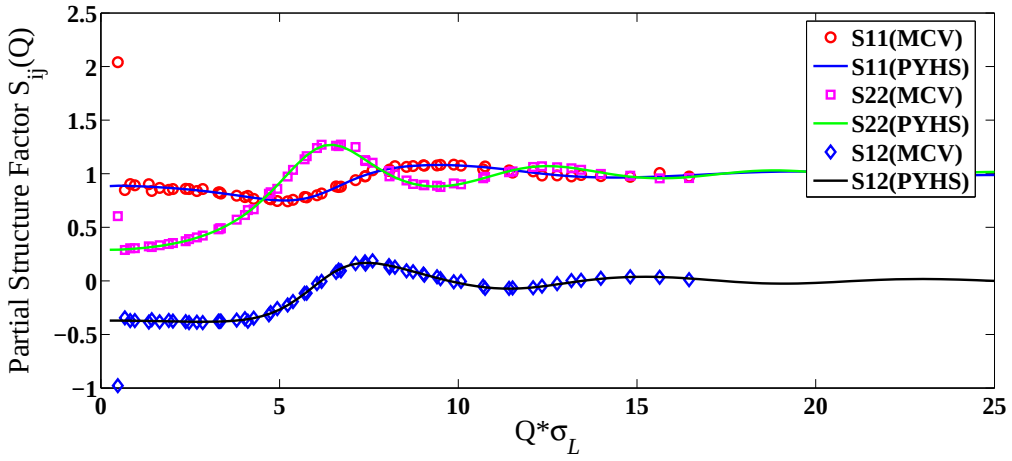

Fig. 26.: Bidisperse partial static structure factors for hard spheres. S_{11} represents contributions to interactions between small spheres, S_{22} represents contribution to interactions between large spheres and S_{12} represent interactions between small and large spheres. Points are Monte Carlo results (vector method) and lines are hard sphere Percus- Yevick model predictions. Here N is the total number of particles in the simulation box; $x_{num} = 0.437$ is the number ratio of the larger diameter particles; $\alpha = \frac{\sigma_s}{\sigma_l}$is the ratio of the smaller diameter particle to the larger diameter particles and $\phi = 0.27$ is the volume fraction of the particles in the simulation box. MCV refers to Monte Carlo Vector method and PYHS refers to Percus Yevick Hard sphere results.

2. Binary structure factors from the Ornstein Zernike Equation

The OZ equation for a mixture can be represented as [55, 66, 67]

$$h_{pq}(r) - c_{pq}(r) = \sum_{k=1}^{m} \rho_k \int c_{pk}(\mid s \mid) h_{kq}(\mid r - s \mid) ds \tag{4.48}$$

where m is the number of species in the mixture; ρ_k is the number density of the k^{th} species of the mixture.

The indirect correlation function can be written as a summation of the direct correlation function and the total correlation function

$$h_{pq}(r) = c_{pq}(r) + \gamma_{pq}(r) \tag{4.49}$$

The closure relationships can be written for a mixture as

1. Percus Yevick Closure

$$c_{pq} = (1 + \gamma_{pq}(r))(exp(-\beta u_{pq}(r)) - 1) \tag{4.50}$$

2. Hypernetted Chain Closure

$$c_{pq} = exp[-\beta u_{pq}(r) + \gamma_{pq}(r)] - \gamma_{pq}(r) - 1 \tag{4.51}$$

To solve the equations numerically the indirect correlation function $\gamma_{pq}(r)$ is divided as previously described for the monodisperse case, into two terms

$$\gamma_{pq}(r) = \gamma^{c}_{pq}(r) + \triangle\gamma_{pq}(r) \tag{4.52}$$

where $\triangle\gamma_{pq}(r)$ is the fine part solved by Picard iterations and $\gamma^{c}_{pq}(r)$ is the coarse part solved by the Newton Raphson method. The coarse part can be represented in

terms of orthogonal basis functions in the following form

$$\gamma_{pq}^{c}(r) = \sum_{\alpha} a_{pq}^{\alpha} P_{pq}^{\alpha}(r). \tag{4.53}$$

The orthogonal functions used in the above expansion are roof functions. The OZ equation (4.48) can be changed into a simple algebraic equation by Fourier transform. The Fourier transforms of $h_{pq}(r)$ and $c_{pq}(r)$ are given by $\tilde{h}_{pq}(r)$ and $\tilde{c}_{pq}(r)$ respectively. The OZ equations in the Fourier domain for a mixture are written as

$$\tilde{h}_{pq}(s) - \tilde{c}_{pq}(s) = \sum_{k=1}^{m} \rho_k \tilde{c}_{qk}(s) \tilde{h}_{kp}(s). \tag{4.54}$$

Using equation (4.50), the Fourier transform of the indirect correlation function can be written as

$$\tilde{\gamma}_{pq}(s) = \sum_{k=1}^{m} \rho_k \tilde{c}_{pk}(s)(\tilde{c}_{kq}(s) + \tilde{\gamma}_{kq}(s)). \tag{4.55}$$

For a binary mixture, solving the Fourier transformed equations leads to three explicit expressions for the indirect correlation functions, namely $\tilde{\gamma}_{11}(s)$, $\tilde{\gamma}_{12}(s)$, and $\tilde{\gamma}_{22}(s)$. Similar expressions can be obtained for ternary and higher order mixtures .

The Fourier transformed indirect correlation functions solved for in terms of the Fourier transformed direct correlation functions can be written as

$$\tilde{\gamma}_{12} = \frac{\rho_1 \tilde{c}_{11}\tilde{c}_{12} + \rho_2 \tilde{c}_{12}\tilde{c}_{22} + \rho_1\rho_2(\tilde{c}_{12}^3 - \tilde{c}_{11}\tilde{c}_{12}\tilde{c}_{22})}{(1-\rho_1\tilde{c}_{11})(1-\rho_2\tilde{c}_{22}) - \rho_1\rho_2\tilde{c}_{12}^2} \tag{4.56}$$

$$\tilde{\gamma}_{11} = \frac{\rho_1\tilde{c}_{11}^2 + \rho_2\tilde{c}_{12}^2 + \frac{\rho_2\tilde{c}_{12}(\rho_1\tilde{c}_{11}\tilde{c}_{12}+\rho_2\tilde{c}_{12}\tilde{c}_{22}+\rho_1\rho_2(\tilde{c}_{12}^3-\tilde{c}_{11}\tilde{c}_{12}\tilde{c}_{22}))}{(1-\rho_1\tilde{c}_{11})(1-\rho_2\tilde{c}_{22})-\rho_1\rho_2\tilde{c}_{12}^2}}{1-\rho_1\tilde{c}_{11}} \tag{4.57}$$

$$\tilde{\gamma}_{22} = \frac{\rho_1\tilde{c}_{12}^2 + \rho_2\tilde{c}_{22}^2 + \frac{\rho_1\tilde{c}_{12}(\rho_1\tilde{c}_{11}\tilde{c}_{12}+\rho_2\tilde{c}_{12}\tilde{c}_{22}+\rho_1\rho_2(\tilde{c}_{12}^3-\tilde{c}_{11}\tilde{c}_{12}\tilde{c}_{22}))}{(1-\rho_1\tilde{c}_{11})(1-\rho_2\tilde{c}_{22})-\rho_1\rho_2\tilde{c}_{12}^2}}{1-\rho_2\tilde{c}_{22}}. \tag{4.58}$$

a. Methodology of OZ Numerical Calculation: Bidisperse

The method described below is adapted from Lotfollahi *et al.* [66]

1. The indirect correlation functions are decomposed into fine and coarse parts using the set of orthogonal basis functions $P^{\alpha}_{pq}(r)$ and the conjugate basis functions $Q^{\alpha}_{pq}(r)$, as:

$$\gamma_{pq}(r) = \sum_{\alpha} a^{\alpha}_{pq} P^{\alpha}_{pq}(r) + \triangle\gamma_{pq}(r) \tag{4.59}$$

2. The radial distance r is divided into N division as $r_i = i\delta r$ where δr is the step size of the interval and the initial estimates of γ^i_{pq} are generated by the method of Lloyd [68]. The coefficients of the basis functions are, a^{α}_{pq}, and are calculated by the following equation:

$$a^{\alpha}_{pq} = \sum_{i} (Q^{\alpha}_{pq})_i \gamma^i_{pq} \tag{4.60}$$

where linear combinations of the $P^{\alpha}_{pq}(r)$ are $Q^{\alpha}_{pq}(r)$

$$Q^{\alpha}_{pq}(r) = \sum_{\beta} B^{\alpha\beta}_{pq} P^{\beta}_{pq}(r) \tag{4.61}$$

where $B^{\alpha\beta}_{pq}$ are the components of the inverse of the symmetric positive definite matrix $R^{\alpha\beta}_{pq}$ defined as

$$R^{\alpha\beta}_{pq} = P^{\alpha}_{pq}.P^{\beta}_{pq}. \tag{4.62}$$

3. The direct correlation functions, c^i_{pq} are calculated from the initial guess of γ^i_{pq} by substituting in the closure equations, and the Fourier transfom of c^i_{pq} can be obtained as

$$\tilde{c}^j_{pq} = \frac{4\pi\delta r}{k_j} \sum_{p=1}^{\frac{N}{2}-1} r_i sin k_j r_i c^i_{pq} \tag{4.63}$$

where $k_j = \frac{2\pi j}{N\delta r}$. The fourier transforms $\tilde{c}^j_{pq}$ are inserted in the expressions obtained for the Fourier transforms of γ^i_{pq} i.e. $\tilde{\gamma}^j_{pq}$. The iterations are carried out in a manner similar to the monodisperse case by solving for the new estimates of the coefficients a^α_{pq}, by using the Newton Raphson scheme and Picard iterations to find the fine part defined by $\triangle\gamma_{pq}(r)$. Jacobian calculations are similar to the monodisperse case and can be defined for both the PY and HNC closure expressions.

4. The new values of γ^i_{pq} are compared with previous values, by using the inverse Fourier transform of $\tilde{\gamma}^j_{pq}$ with the expansion:

$$\gamma^{i'}_{pq} = \frac{\delta k}{2\pi^2 r_i} \sum_{j=1}^{\frac{N}{2}-1} k_j sin k_j r_i \tilde{\gamma}^j_{pq}. \tag{4.64}$$

New expansion coefficients $a^{\alpha'}_{pq}$ are evaluated using the above values of $\gamma^{i'}_{pq}$.

5. The error, Error 1, compares two successive values of a^α_{pq} and $a^{\alpha'}_{pq}$ and can be calculated by the following equation:

$$Error1 = \sqrt{\sum_{p=1}^{m}\sum_{q=1}^{m}\sum_{\alpha} \mid a^\alpha_{pq} - a^{\alpha'}_{pq} \mid^2} \tag{4.65}$$

If the Error 1 is less than the errors limit ($\tilde{1}0^{-6}$), $\triangle\gamma'_{pq}$ is calculated by the equation (4.67), and the calculation is continued from step 6. Otherwise the new estimate of a^α_{pq} are calculated by the Newton Raphson method,

$$\bar{a}^\alpha_{pq} = a^\alpha_{pq} - \sum_{\beta} (J^{-1}_{pq})_{\alpha\beta} d^\beta_{pq} \tag{4.66}$$

where J_{pq} is the matrix Jacobian evaluated at the old estimate and the calculations are continued from step 3.

6. The error, Error 2, compares the values of $\triangle\gamma_{pq}^{i'}$ and $\triangle\gamma_{pq}^{i}$ obtained from two successive iteration calculations,

$$Error2 = \sqrt{\sum_{p=1}^{m}\sum_{q=1}^{m}\sum_{i} \triangle\gamma_{pq}^{i'} - \triangle\gamma_{pq}^{i}} \tag{4.67}$$

On completion of the iterations for obtaining a fixed value of error the structure factors are obtained from the fourier transforms of the direct correlation functions from the definitions of Ashcroft *et al.* The definitions for the partial structure factors are given by

$$S_{11}(k) = \left(\frac{1 - n_1 C_{11}(k) - n_1 n_2 C_{12}^2(k)}{1 - n_2 C_{22}(k)}\right)^{-1} \tag{4.68}$$

$$S_{22}(k) = \left(\frac{1 - n_2 C_{22}(k) - n_1 n_2 C_{12}^2(k)}{1 - n_1 C_{11}(k)}\right)^{-1} \tag{4.69}$$

$$S_{12}(k) = (n_1 n_2)^{\frac{1}{2}} C_{12}(k)([1 - n_1 C_{11}(k)] \times [1 - n_2 C_{22}(k)] - n_1 n_2 C_{12}^2(k))^{-1}. \tag{4.70}$$

F. Summary

This chapter summarizes the various techniques available to calculate the static structure factor from analytical methods, numerical computations and simulations. The analytical methods are most convenient to use, and sought for. But the lack of accurate analytical models for nonlinear closures, leads us to investigate numerical methods. The solution of the OZ equations and Monte Carlo simulations provide us with accurate structure factors which have less oscillations in the low Q region. These calculations have enabled us to obtain the structure factors for bidisperse mixtures which can be extended to obtain the solution for polydisperse mixtures of particles.

The next chapter presents the materials and methods used in this investigation, namely the samples are described, their characterization is done and the instruments used to make FDPM measurements are described.

CHAPTER V

METHODS AND MATERIALS

A. FDPM instrumentation

FDPM measurements were made at seven different wavelengths, 488, 514, 568, 650, 687, 785, and 828 nm using both external modulation of laser light and direct modulation of laser diodes, for particle size inversion. The measurements for understanding the electrostatic interactions in the monodisperse and bidisperse dispersions, were carried out at four wavelengths of 660, 685, 785 and 828nm. While the details of FDPM instrumentation and method have been presented elsewhere [45, 69], a brief description of both approaches is presented here.

Figure 27 is a schematic of the setup utilizing direct modulation of laser diodes to gather FDPM data at 650 through 828 nm. As shown, a laser diode (650 nm TOLD 9442M, Thorlabs, Newton, NJ; 660 nm Mitsubishi Electric Corp, Type 101J8-01; 687 nm HL 6738MG, Thorlabs, Newton, NJ; 785 nm DL7140-201) was modulated with a radio frequency (RF) signal (Marconi Instruments Signal Generator 2022A, Mountain View, CA) to produce an intensity-modulated light at modulation frequency, ω. The beam was split to produce reference and sample beams. The reference beam was sent directly to a photomultiplier tube (PMT, Model H6573, Hamamatsu, Japan) for assessment of incident modulated light. The sample beam was delivered to the polystyrene suspension via an optical fiber (1000m FT -1.0 -EMT, ThorLabs, Inc. Newton, NJ). Another fiber located at a distance r, from the source fiber was used to collect the diffused light and deliver it to the sample PMT. Both PMT's were gain modulated with another RF signal at a modulation frequency of $\omega + \Delta\omega$ generated from a second slave generator (Marconi Instruments Signal Generator 2022A), which

was phase locked with the master signal generator by a 10 MHz signal. The signals at the reference and sample PMT's were mixed with the RF from the slave generator to give output signals at frequency $\Delta\omega$. The signals were amplified by transimpedance amplifiers and then acquired using an internally authored Labview program, which retrieves the phase differences between the reference and sample beams, as well as their amplitudes.

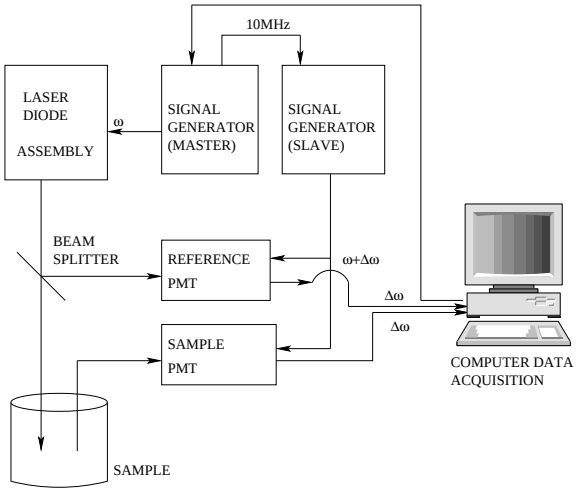

Fig. 27.: Frequency domain photon migration measurement using a laser diode set up. Here direct modulation of the laser diode is possible and the wavelengths obtained using this set up are 650,660,685,687,785 and 828nm.

To collect data at lower wavelengths (488, 514, and 568 nm), light from an Argon-

Krypton laser (Model 643R-AP-A01, Melles Griot, Barloworld Scientific, Carlsbad, CA) was modulated externally with an electro-optic modulator (Model 350-160, ConOptics, Danbury, CT) as shown in Figure 28. An additional amplifier (Model 3100LA, ENI, Rochester, NY) was also required to amplify the RF signal from the signal generator to the modulator. For both the apparatuses described above, data was collected as the distance, r between collected and incident light, varied from 3 to 15 mm at modulation frequencies ranging from 70 to 90 MHz. From values of DC and PS, values of $\mu_s^{'}$ and μ_a were obtained.

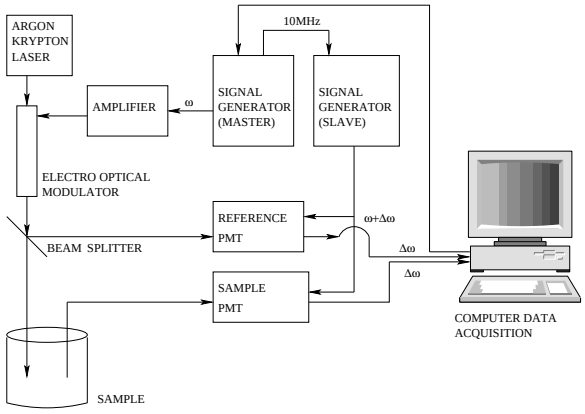

Fig. 28.: Frequency domain photon migration measurement using an argon krypton laser set up. Here external modulation of the laser light is required and the wavelengths obtained using this set up are 488,514 and 568nm.

B. Materials

Samples were prepared from two polystyrene solutions of 143 nm and 223 nm diameter particles, from DOW Chemical Company. The solutions were dialyzed to remove residual surfactants and salts arising from the manufacturing process and then characterized using dynamic light scattering (DLS, Zetasizer 3000, Malvern Instruments, U.K.) to obtain the mean particle size, spread of the distribution, and the polydispersity. Table II lists the results. The solids volume fractions of the dialyzed suspensions were determined by evaporation measurements conducted at 80^0 C. The density of polystyrene used in the calculations is $1.0549 gm/cm^3$.

Particle size inversion required the colloidal dispersions to mimick hard sphere like interactions among the particles. The salt content in the dispersions was kept high to disallow any repulsive forces arising from electrostatic interactions. From each dialyzed suspension of the two particle sizes, 100 ml volumes at particle volume fractions of 0.03, 0.10, 0.18, and 0.27 were prepared by dilution with deionized water and sodium chloride in order to achieve ionic strengths of 120 mM of NaCl.

Electrostatic interactions were made significant for another study of monodisperse and bidisperse dense dispersions. The dialyzed polystyrene was completely deionized using an ion exchange resin(Bio Rad AG 501-X8 Resin 20-50 mesh, Bio-Rad Laboratories, CA) which removed all traces of salt and surfactants. The dispersions showed a marked change in color (iridescence) after deionization exhibiting crystal like order among the dispersions. The completely dialyzed and deionized dispersions at high volume fraction were then diluted to the desired volume fraction with deionized water (obtained from Millipure). For a particular volume fraction a bulk sample was diluted to provide consistency among the samples. The ionic strength was varied by using a high ionic strength solution of sodium chloride (200mM). Drops of

the high ionic strength solution were added into polystyrene sample volumes (60 $\sim$ 70ml) to bring them up to the desired ionic strength, by using a 1ml syringe. The ionic strengths investigated were 0.5,1,2,3, and 4mM. The volume fractions of the dispersions investigated were 0.24,0.22, 0.18, and 0.15.

C. Dynamic light scattering measurements

The particle size of the dispersions was measured with the aid of dynamic light scattering measurements(Malvern Zetasizer 3000HSA) (Table II). A small amount of extremely dilute polystyrene solution ($\phi < 0.1\%$) with some amount of salt solution was put into a transparent cuvette and the measurement sequence was run for approximately ten runs. The polydispersity and the mean size was obtained from the average of the runs.

Table II.: Characterization results of polystyrene lattices using dynamic light scattering

Suspension	Mean(nm)	Spread(nm)	polydispersity(%)
Dow 755	223.6 $\pm$ 3.6	32.4 $\pm$ 15.2	14.5
Dow 788	143.6 $\pm$ 3.7	35.0 $\pm$ 7.2	24.4

D. Charge titration

The intrinsic particle charge of a colloidal particle can be determined by the techniques of conductometric and potentiometric titration methods.([70], [71], [72] & [73]) The latex sample was completely dialyzed against deionized water. The dialyzed latex was then cleaned [74] with an ion exchange resin, which replaced the cations with hydrogen ions and anions with hydroxyl ions. A known concentration of latex was then titrated against a known strength (10mM and 100mM in this study) of sodium hydroxide (NaOH). The conductivity of the latex was monitored using a titration controller (Fisher, Accumet Model 150).

The sodium ions from the alkali replace the hydrogen ions from the surface of the particles. Figure(29) illustrates the principle of removal of hydrogen ions from the surface of the particle and replacement with sodium ions.

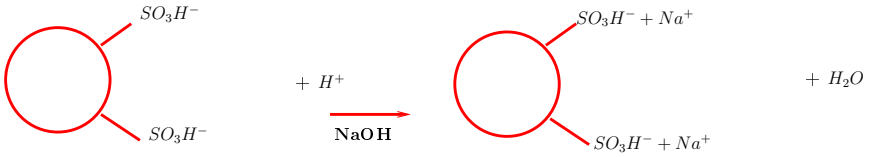

Fig. 29.: Titration of the latex dispersion with sodium hydroxide leads to a release of hydrogen ions in the dispersion.

The cations have a lesser mobility than hydrogen ions, which leads to a reduction of the conductivity of the dispersion when sodium hydroxide is added to it, as the hydrogen ions continually combine with the hydroxyl ions to form water. The buildup of sodium ions in the medium after the particles have combined with the sodium ions, leads to an increase in the conductivity of the dispersion. The point where the conductivity is a minimum is referred to as the equilibrium point. At this point the amount of titrant used is then used to calculate the number of ions displaced from the particles in the medium. The number of ions displaced is used to calculate the charge on the particles with Eqn. 5.1.

Figures 30 and 31 provide the conductometric titration measurements of conductivity versus the volume of sodium hydroxide added to the polystyrene latex dispersion for the lattices. The strengths of sodium hydroxide solutions used are 10mM and 100mM respectively. The charges on the particles and their charge densities are calculated using the titration data and are provided in Table III.

Table III.: Charge determination from conductometric titration measurements

Latex	Strength of NaOH	Z_p (e^-s)	Charge Density($\mu C/cm^2$)
788	10mM	1.324×10^5	32.5
	100mM	1.324×10^5	32.5
755	10mM	4.5319×10^4	4.5189
	100mM (1)	5.4382×10^4	5.423
	100mM (2)	5.4382×10^4	5.423

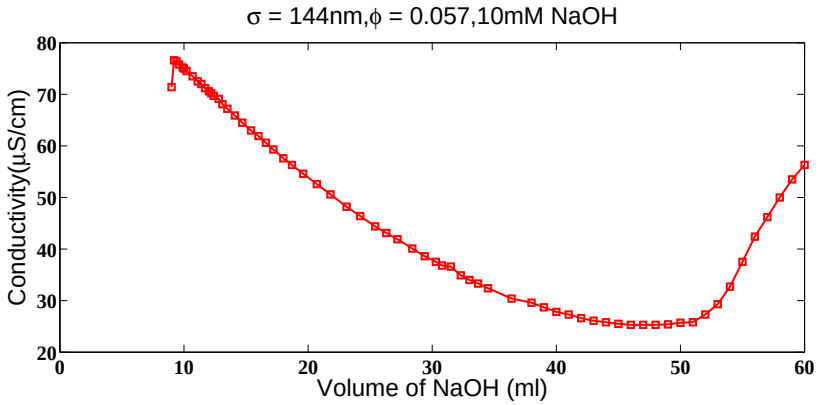

(a) 10mM NaOH

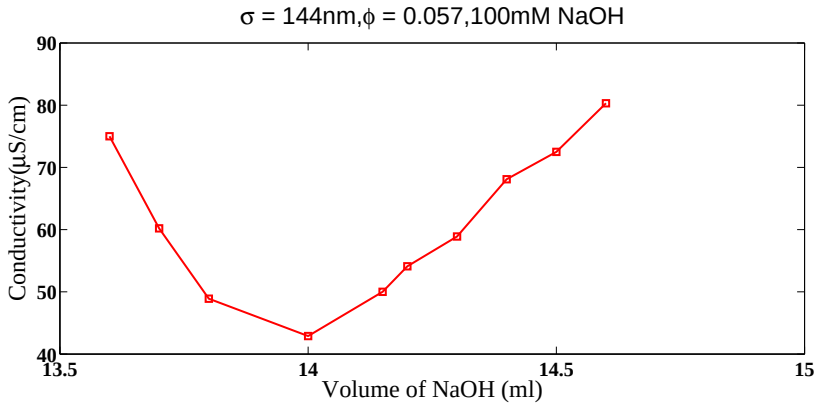

(b) 100mM NaOH

Fig. 30.: Conductometric titration measurements of Dow 788 with 10mM NaOH and 100mM NaOH solutions. The volume fraction $\phi = 0.057$ and diameter $\sigma = 144nm$. Square symbols are the points at which conductivity is measured and lines are connecting the square symbols.

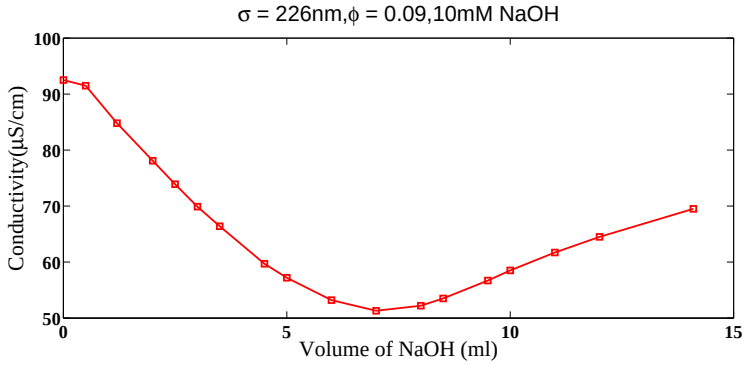

(a) 10mM NaOH

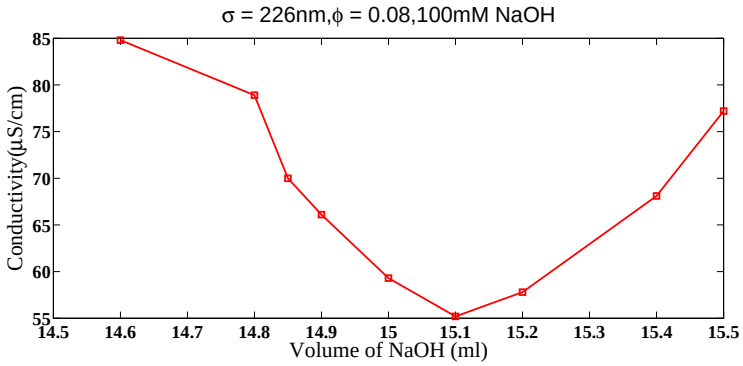

(b) 100mM NaOH

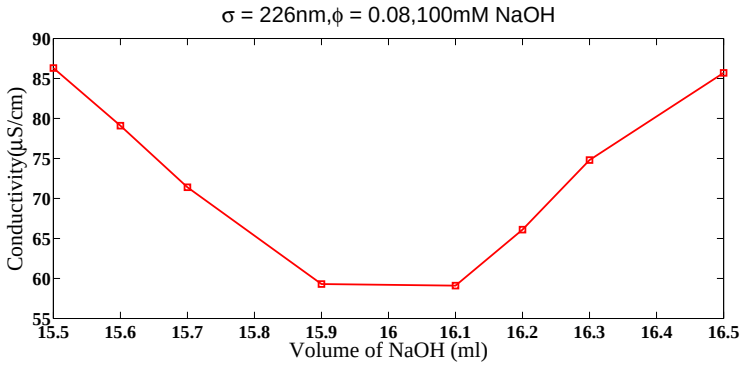

(c) 100mM NaOH

Fig. 31.: Conductometric titration measurements of Dow 755 with 10mM NaOH and 100mM NaOH solutions. The volume fraction $\phi = 0.08, 0.09$ and diameter $\sigma = 226nm$. Square symbols are the points at which conductivity is measured and lines are connecting the square symbols.

The charge on the particles can be calculated using the number of ions displaced by titration with sodium hydroxide. The charge on the particle is given by

$$Z_p = \frac{N_A V_{NaOH} C_{NaOH} \pi \sigma^3}{6 V \phi \times 10^{-6}} \tag{5.1}$$

where N_A is the avogadro's number; V_{NaOH} is the volume of base used; C_{NaOH} is the strength of the base used for the study; V is the volume of latex used in the study; ϕ is the volume fraction of the dispersion used for the titration.

The charge density is calculated as

$$\sigma_c = \frac{Z p e_o \times 10^{-4}}{\pi \sigma^2} C/cm^2 \tag{5.2}$$

The particle charge value is used to calculate the effective charge value on the particle using the method described in chapter VII.

E. Zeta potential measurements

The counter ions in the solution of the dispersion, i.e. the hydrogen ions, arrange themselves around the particle. A layer of ions is formed close to the surface of the particles, and is called the Stern layer. Beyond the Stern layer there is a cloud of counterions, which is called the diffuse layer. The plane at which the diffuse and Stern layers can be demarcated is called the shear plane. The potential difference between this shear plane and the bulk is called the zeta potential, and can be used to obtain a rough estimate of the charge on the particle. Figure(32) illustrates the concept of a charged particle surrounded by counterions, the formation of a stern layer and the difference in potentials of the surface of the particle and the bulk.

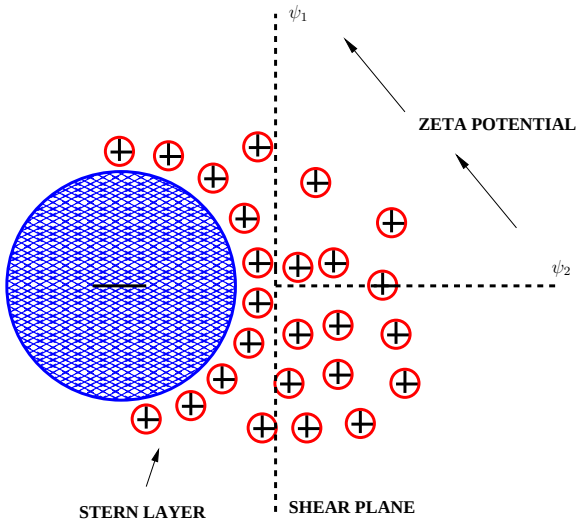

Fig. 32.: Negatively charged particle surrounded by positive counterions.

The zeta potential of the particles is obtained by putting a dilute solution of polystyrene particles at some ionic strength through an electrophoresis cell (Malvern Zetasizer 3000HSA), in which an electric field is applied to the dilute solution and the particles move under the influence of the electric field. The velocity of the particles is measured with laser doppler velocimetry, and is used to determine the zeta potential of the particle.

The electrophoretic mobility, U, is defined as the ratio of the velocity of the particle, v, to the externally applied electric field, E, by the relation $U = \frac{v}{E}$. The measured mobility can be related to the zeta potential, ζ, by the relation:

$$\zeta = \frac{\eta v F}{E \sigma \epsilon_0} \tag{5.3}$$

where η and ϵ_0 are the viscosity and electric permittivity of the solvent respectively. F

is a constant, of 1.5 which is valid for the Smoluchowski approximation, and when the thickness of the double layer is less than the diameter of the particle. This condition is met when $\kappa\sigma/2 > 1$, where $\kappa = \sqrt{\frac{\sum_i n_i z_i^2 e^2}{\epsilon_o \epsilon k_B T}}$ is the Debye Huckel parameter. The double layer thickness depends upon the ionic strength of the medium or the concentration of smaller ions only. In the D-H parameter n_i is the number of ions; z_i is the charge on individual ions; e is the electronic charge; ϵ_o is the dielectric permittivity of vacuum; ϵ is the relative permittivity of the dielectric medium; k_B is the Boltzmann constant; and T is the temperature. The Debye-Huckel approximation is used when the double layer is thick and the surface potential is less i.e. $\kappa\sigma/2 < 1$,

The zeta potential of the particles was measured from Malvern Instruments Zetasizer and the zeta potential values for the two particles are provided in Table IV.

Table IV.: Zeta potential measurements and charge calculation Z_p (eqn 5.1) of the two lattices used in the experiment

Latex	Zeta potential (mV)	Z_p (e^-s)
Dow 788(1mM NaCl)	74.5	4446
Dow 755(1mM NaCl)	58.0	2482

F. Summary

This chapter provides the materials and methods used to determine particle size distributions from multiply scattering colloids and to understand the behavior of colloids

with variation of electrostatic interactions within the medium. The particle size distributions were obtained from a commercial instrument for a very low concentration of the particles. The charges on the particle were determined from conductometric titration measurements and from zeta potential measurements. A brief overview of the instrumentation used to analyze dense colloidal dispersions is given, and the experimental technique frequency domain photon migration is presented. In the following chapter, the particle size distribution obtained from dense colloidal dispersions using multiwavelength frequency domain photon migration measurements is presented.

CHAPTER VI

INVERSION OF EXPERIMENTAL DATA TO OBTAIN PARTICLE SIZE*

A. Objective

Characterization of dense polydisperse suspensions of mean diameters 143 and 226 nm and volume fractions ranging from 0.03 to 0.27 was conducted using time-dependent measurement of multiply scattered light. Frequency-domain photon migration measurements of isotropic scattering coefficients at wavelengths between 488 and 828 nm were found to agree with those predicted from the Mie theory and the polydisperse hard sphere Percus-Yevick model. The wavelength dependent isotropic scattering data were then used to successfully recover the particle size distribution and volume fraction of the suspensions, by minimizing a nonlinear least squares problem. The mean particle size and volume fractions were recovered within an error range of 0 - 15.53% and 0 - 24% respectively, when compared with dynamic light scattering results and experimental volume fractions.

Keywords:

Frequency Domain Photon Migration, concentrated suspensions, polydisperse static structure factor, hard sphere Percus-Yevick approximation, particle sizing, multiple scattering, nonlinear least squares minimization, Genetic Algorithms.

B. Introduction

Characterization of dense colloidal suspensions via optical or acoustical ensemble scattering techniques may offer the opportunity for non-destructive and non-invasive process control and product quality measurement [75]. Yet the inverse problem associated with determining the particle size distribution,$f(x)$, and volume fraction, ϕ, is made difficult by the influence of non-random particle orientation, governed predominantly by volume exclusion effects as well as other forces, such as electrostatic, depletion, and Van der Waals forces [7]. The structure of dense suspensions impacts both the static and dynamic scattered fields, requiring one to account for ordering effects when solving the inverse problems for characterization of dense colloidal suspensions. Table V summarizes the static and dynamic optical ensemble techniques, their measurements as well as the integral equations which represent their respective inverse problems for characterizing dilute, and dense suspensions. Since acoustic ensemble approaches are being increasingly implemented for particle characterization in industry, they are also included in Table V.

Of the static light scattering measurements, turbidity and angular light scattering (ALS, also termed diffraction) measurements are restricted to dilute suspensions that do not multiply scatter light. Since the measurements consist of monitoring the amount of light scattered out of an optical path, L, dense suspensions which multiply scatter light back into the path represent invalid turbidity and ALS samples. While one can alleviate multiple scattering by decreasing the pathlength and/or index matching, wavelength-dependent turbidity or ALS measurements are typically not conducted for particle characterization in dense suspensions. Dynamic light scattering (DLS) is similar to turbidity in that it does not account for multiply scattered light, but instead reflects the collective Brownian motion of the particles that con-

Table V.: Ensemble methods for particle sizing

Measurement Method	**Measured Quantity**	***a priori* Information**	**Fredholm's Equation**	**References**
Turbidity(Static) (Dilute)	Intensity (I(λ)) at $\theta = 0^o$	n & m	$-\frac{1}{L}\ln\left[\frac{I(\lambda)}{I_0(\lambda)}\right] = \mu_s(\lambda) = = \int_0^\infty \frac{3Q_{scat}(x,n,\lambda)}{2x}\phi f(x)dx$	Garcia-Rubio *et al.* [76]
ALS(static) (Dilute)	Intensity I(λ) at several θ	n & m	$\ln\left[\frac{I(\lambda)}{I_0(\lambda)}\right] \propto q_{scat}(x,n,\lambda,\theta) = \int_{V_j}\int_{\Delta\theta_j}\int_{x_i}^{x_f} Nf(x)\frac{dq_{scat}(x,n,\lambda,\theta)}{d\theta}dxd\theta dV$	H.N.Frock [77, 78]
DLS (Dynamic) (Dilute)	Intensity Fluctuations I(t), to obtain $g^{(2)}(\tau)$	solvent viscosity	$g^{(2)}(\tau) = 1 + \beta \mid g^{(1)}(\tau) \mid^2$ $g^{(1)}(\tau) = \int_{x_{min}}^{x_{max}} f(x)\exp(-Q^2D\tau)dx$ (For Concentrated) $D(Q) = D_0\frac{H(Q)}{S(Q)}$	Berne & Pecora [30]
DWS (Dynamic) (Concentrated)	Intensity Fluctuations I(t), to obtain $g^{(2)}(\tau)$	Cell Geometry, P(s), n, m & (point or planar source)	$g^{(2)}(\tau) = 1 + \beta \mid g^{(1)}(\tau) \mid^2$ $g_1(\tau) \propto \int_0^\infty P(s)\exp[-2k_0^2D_0t\frac{[H(q)]}{[S(q)]}\frac{s}{l^*}]ds$	Horne & Davidson [79] ; F. Scheffold [37, 80]
DTS (Static) (Concentrated)	Transmitted intensity $I(\lambda)$	n & m	$(1-g)\mu_s(\lambda) = \frac{3}{2}\phi\int_{x_{min}}^{x_{max}}\frac{Q_{scat}(x,n,\lambda)[1-g(x,n,\lambda)]}{x}f(x)S(q)dx$	Kaplan *et al.* [7]
FDPM (Static) (Concentrated)	AC, DC and PS of the Photon density wave	n & m	$\mu_s'(\lambda) = \int_0^\pi \frac{12\phi}{k^2}\int_0^\infty\frac{f(x_i)}{x_i^3}\int_0^\infty\frac{f(x_j)}{x_j^3}F_{i,j}(n,x_i,x_j,\lambda,\theta)$ $\times S_{i,j}(n,x_i,x_j,\lambda,\theta)\sin\theta(1-\cos\theta)dx_jdx_id\theta$	Sun *et al.* [81]
AS (Static) (Concentrated)	Attenuation coefficient, α & ultrasonic velocity	Viscosity, specific heat capacity, thermal expansivity thermal conductivity	$\alpha(\omega) = \int_0^\infty \alpha(\omega,x)f(x)dx$	McClements, D.J. [82] & Alba *et al.* [83] & Alexander *et al.* [84]

n Refractive index of the particle
m Refractive index of the medium
H(q) Hydrodynamic Function
S(q) Static Structure Factor

tribute to the decay of the autocorrelation function. From the ensemble measurement of particle diffusion coefficient, characterization of particle size and volume fraction may be obtained from the solution of the inverse problem. Index matching, the use of fiber optics [85, 86], and the use of conventional optical methods to eliminate the predominant multiply scattered signal [87, 88] may enable DLS characterization of dense suspensions. Yet again DLS measurements are generally employed for dilute suspensions. Efforts to eliminate the predominant multiply scattered light for measurement of the small component of singly scattered light are done at the expense of signal to noise ratio (SNR) for both DLS and ALS measurements.

In contrast, diffuse transmission (DTS) and diffuse wave spectroscopy (DWS) entail respective static and dynamic measurements of multiply scattered light and therefore are predisposed to dense colloidal suspensions. Diffuse transmission measurement consists of determining the isotropic scattering coefficient as a function of wavelength and then inverting for suspension characterization [40]. Diffuse wave spectroscopy [37] measures the fluctuation of multiply scattered light arising from the collective Brownian motion of the particles in colloids and depends upon *a priori* information of the optical properties for prediction of the distribution of pathlengths traveled by photons in order to determine the ensemble particle diffusion coefficient, and from the inverse solution, size information.

Wavelength dependent, time-resolved diffuse transmission and reflectance measurements are the subject of this contribution and can be accomplished in either time- or frequency-domains [81, 89, 90]. In simple terms, time-dependent techniques measure the distribution of photon times-of-flight in order to determine the absorption and isotropic scattering coefficients of multiply scattering, dense suspensions with accuracy and precision [91]. While time-resolved diffuse measurements have temporal resolution of photon transport on the order of pico- to nano- seconds, dynamic mea-

surements assess particle motion on the order of microseconds to milliseconds. Few dynamic time-resolved measurements have been attempted [92] and to date, there have been no static measurements of wavelength-dependent isotropic scattering for characterization of dense colloidal suspensions. Prior work in our research group has focused upon conducting measurements of isotropic scattering at one wavelength as a function of known volume fraction in order to extract size and interaction parameters. However, for industrial relevancy, multi-wavelength measurements are needed for non-destructive and non-invasive measurement.

In the following we extend frequency domain photon migration (FDPM) for multi-wavelength measurements of isotropic scattering in order to demonstrate recovery of particle size and volume fraction using a polydisperse hard sphere exclusion model and global and local search routines for nonlinear optimization. Below, the FDPM approach is first briefly outlined, followed by the Materials and Methods section which describes the samples, multi-wavelength FDPM measurements and optimization algorithms employed.

C. Theory and background

Inverse problems are a large class of problems in which the parameters of a model describing the observed experimental data are determined. Inverse problem theory is applied in several fields such as geophysics [93–96], inverse radiative transport theory [97], particle sizing by spectral methods [78], [98] etc.

The theory for the recovery of particle size distribution entails a forward problem describing the modelling of the experimental data with suitable structure factor models, and followed by an inversion of the experimental data to recover the particle size distribution using an assumed gaussian form for the distribution. Previously, fre-

quency domain photon migration methods have been used to obtain the particle size distribution from the monodisperse, bidisperse [99] and polydisperse [81] dispersions by Sun *et al.*, Jiang *et al.* and Balgi *et al.* [100], [101], [102]

A most general way of inverting the particle size distribution using basis functions to represent the particle size distribution $f(x)$, with attached weights to the basis functions, was developed by Sun *et al.* [89] In this algorithm the forward problem was created as a linear problem from which the particle size distribution and the volume fraction were obtained by using Tikhonov regularization techniques and the regularization parameter was obtained by the L-Curve method. His work also provides a review of several such methods using tikhonov regularization to obtain the particle size distribution.

Although the previous techniques have been able to recover the particle size distribution accurately, the most general approach is of recovery of the particle size distribution with a polydisperse static structure factor model, which Sun *et al.* have used, but with known volume fractions of the dispersions, and a local minimization algorithm. Here we provide a detailed analysis using a Percus Yevick hard sphere polydisperse static structure factor model and recover the mean size and the standard deviation of the assumed gaussian distribution of particle size, by using genetic algorithms [103], [104] which help determine a global optimum of the minimization problem. Also, the experimental data used in this study is multiwavelength data, which spans the structure factor. The volume fraction is kept unknown and is determined along with the other parameter from the inversion algorithms.

1. FDPM theory

The theory for FDPM has been described earlier in chapter V as materials and methods. In this study seven wavelengths are used, 488, 514, 568,(Argon krypton gas laser)

650, 687, 785, and 828(diode lasers)nm respectively. The experimental procedure is illustrated in the Figure 33.

2. Forward problem

The elastic wavelength-dependent isotropic scattering coefficient, μ_s', of a concentrated colloidal suspension is dependent upon individual particle scattering efficiencies as well as their correlated position as indicated by the following integral equation:

$$\mu_s'(\lambda) = \int_0^{\pi} \frac{12\phi}{k^2} \int_0^{\infty} \frac{f(x_i)}{x_i^3} \int_0^{\infty} \frac{f(x_j)}{x_j^3} F_{i,j}(q, x_i, x_j) S_{i,j}(q, x_i, x_j, \phi) \sin\theta(1-\cos\theta) dx_j dx_i d\theta \quad (6.1)$$

where $F_{i,j}$ is the binary form factor evaluated by the Mie scattering as [9]:

$$F_{ij}(q, x_i, x_j) = Re(f_{1,i} f_{1,j}^* + f_{2,i} f_{2,j}^*) \quad (6.2)$$

where $f_{1,i}$ and $f_{2,i}$ are the scattering amplitudes in two orthogonal polarization states arising from a particle with size x_i; and the terms $f_{1,j}^*$ and $f_{2,j}^*$ are the complex conjugates of $f_{1,i}$ and $f_{2,i}$ respectively, from particle with size x_j. The term q is the scattering vector and is given as $2k \sin\frac{\theta}{2}$, where k is the wavenumber of the medium $[\frac{2\pi m}{\lambda}]$; m is the refractive index of the surrounding medium; λ is the wavelength of the incident radiation; θ is the scattering angle; ρ is the total number density of the particles; x_i, x_j are the particle diameters; and $f(x_i)$ and $f(x_j)$ are the volume based particle size distributions which are assumed to have a known form for the inverse problem.

The term $S_{ij}(q, x_i, x_j, \phi)$ is the polydisperse partial static structure factor [105] that accounts for hard-sphere particle interactions within the concentrated suspension of volume fraction, ϕ.

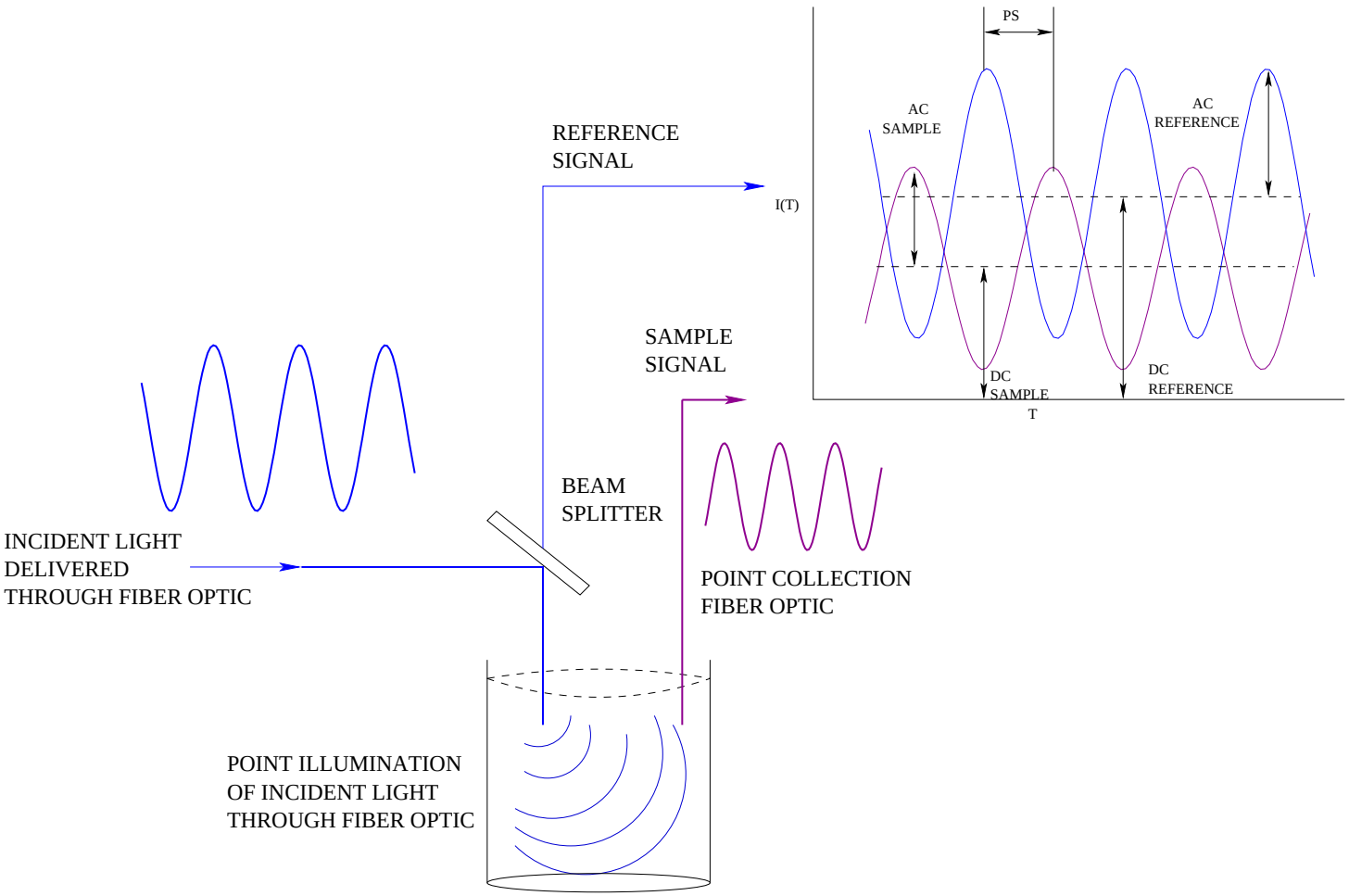

Fig. 33.: Principle of Frequency Domain Photon Migration and data acquisition.

3. Inverse problem

The inverse problem consists of minimizing either a nonlinear absolute or a relative least squares difference between experimentally measured isotropic scattering functions and that predicted by Eqn 6.1, in order to retrieve the particle size distribution parameters and the volume fraction, ϕ, of the suspension. In this work, we assume particle size distributions to be Gaussian,

$$f(x) = \frac{1}{\sqrt{2\pi}\overline{\sigma}} \exp\left(-\frac{(x-\bar{X})^2}{2\overline{\sigma}^2}\right) \tag{6.3}$$

with $\bar{X}$ as the mean particle diameter and $\overline{\sigma}$ the spread of the distribution.

Alternatively, we also assume a particle distribution of a more general form as predicted by the Johnson's SB function [106], which is given as

$$f_{SB}(x) = \frac{\sigma_J}{\sqrt{2\pi}}[t'(1-t')]^{-1} \exp\left(-0.5\left[\mu_J + \sigma_J \ln\left(\frac{t'}{1-t'}\right)\right]^2\right) \tag{6.4}$$

where $t' = \dfrac{x - x_{min}}{x_{max} - x_{min}}$ and $0 \leq t \leq 1$. The terms x_{max} and x_{min} represent the limits of particle diameter. Here μ_J and σ_J are the parameters describing the distribution, and are the required unknowns.

D. Materials and methods

1. Materials used

Samples were prepared from two polystyrene solutions of 143 nm and 223 nm particle size, from DOW Chemical Company, as described in Chapter V. The solutions were dialyzed to remove residual surfactants and salts arising from the manufacturing process and then characterized using dynamic light scattering (DLS, Zetasizer 3000, Malvern Instruments, U.K.) to obtain the mean particle size, spread of the distribution, and the polydispersity. The solids volume fractions of the dialyzed sus-

pensions were determined by evaporation measurements conducted at 80^0 C. From each dialyzed suspension of the two particle sizes, 100 ml volumes at particle volume fractions of 0.03, 0.10, 0.18, and 0.27 were prepared by dilution with deionized water and sodium chloride in order to achieve ionic strengths of 120 mM of NaCl.

2. Optimization procedure

The particle size distributions and volume fraction of the dense colloidal suspensions, were determined by minimizing the absolute and relative squared differences between experimentally measured isotropic scattering coefficients, $\mu_s^{'e}(\lambda)$, at each wavelength and $\mu_s^{'c}(\lambda)$ or that predicted by Eqn. 6.1 . The three objective functions $\chi_1^2 = \sum_{\lambda_i}(\mu_s^{'c} - \mu_s^{'e})^2$, $\chi_2^2 = \sum_{\lambda_i}\left(\frac{\mu_s^{'c} - \mu_s^{'e}}{\mu_s^{'e}}\right)^2$, and $\chi_3^2 = \sum_{\lambda_i}\left(\frac{\mu_s^{'c} - \mu_s^{'e}}{\mu_s^{'c}}\right)^2$ were minimized using genetic algorithms and MatLab local search subroutines. Since genetic algorithms render close values to the global optimum, they were used to obtain initial guesses for local search MatLab algorithms.

Genetic algortithms are a class of evolutionary algorithms, which search the entire space of feasible solutions, within some given bounds using a random search technique. The genetic algorithm software coded by Houck, Joines, and Kay [107, 108] was used and implemented in MatLab. The algorithm offers both binary and floating-point representations of the parameter space. Operators for floating point representation has been described by Michalewicz [108]. The local search algorithms used were *Fmincon* and *Lsqnonlin*. *Fmincon* uses sequential quadratic programming (SQP), and solves a Quadratic Programming (QP) sub problem at each iteration. *Lsqnonlin* uses a subspace trust region method based on the interior- reflective trust region method with bounds placed on the estimates. Bounds considered for the Gaussian distribution are $\bar{X}$ [50-1000] nm, σ [5-50] nm and ϕ [1-40]%. The local search convergence criteria required no greater than (10^{-12}) absolute change in the estimates

on the scattering prediction before the final iteration. The inverse problem was solved for two cases in which (i) ϕ was assumed known and the distribution parameters ($\bar{X}$,σ) were estimated, and (ii) all three parameters were considered unknown i.e. ($\bar{X}$, σ, and ϕ).

E. Results and discussion

The interactions between the charged particles have been modeled as effective hard spheres. This is true for the suspending fluid containing 120 mM sodium chloride, which screened repulsive electrostatic forces. As can be observed from the Figure 34, the hard-sphere Percus-Yevick (HSPY) structure factor model for a polydisperse system of particles accounts for interparticle interactions and is able to describe the experimental data well. This validates the use of the HSPY model for concentrated suspensions.

Tables VI and VII list the final results for minimization assuming a gaussian distribution, using relative least squares (χ_2^2 & χ_3^2). Least squares functions of χ_1^2 did not perform well as errors are squared and outliers overly influenced the results. The minimization procedure is significantly affected by the initial guess value of the mean particle size. Consequently, we find the genetic algortihms provided an efficient means to provide the first initial guess value for all subsequent local searches.

The parameters of the distribution $f(x)$ obtained from relative least squares functions predict the mean values closely when compared to that obtained from DLS measurements of diluted suspensions. As shown in Figure 35 the relative error for recovery of mean particle size $\bar{X}$ was between 0 and 15.53% for $\bar{X}$ = 143.6 nm and 1.83 and 11.90% for $\bar{X}$ = 223.6 nm. The results for a more general SB distribution (which can take into account any skewness in the form of the particle size distribution)

Table VI.: Minimization results for DOW 788 for assumed Gaussian distribution, $\bar{X} = 143.6$ nm & $\sigma = 35.0 \pm 7.2$ nm

Function Minimized	Volume Fraction	Local Algorithm			
		3 Unknowns			
		$\bar{X}$	σ	ϕ	residual
$\chi_2^2 = \sum_{\lambda_i} \left(\frac{\mu_s'^c - \mu_s'^e}{\mu_s'^e} \right)^2$	0.030	121.30	5.50	0.043	0.007681
	0.100	144.42	6.04	0.096	0.003749
	0.180	142.96	7.87	0.191	0.012318
	0.270	156.16	6.26	0.314	0.031741
$\chi_3^2 = \sum_{\lambda_i} \left(\frac{\mu_s'^c - \mu_s'^e}{\mu_s'^c} \right)^2$	0.030	121.03	9.61	0.042	0.007752
	0.100	140.20	11.51	0.096	0.003740
	0.180	143.65	10.10	0.178	0.011790
	0.270	148.20	13.93	0.346	0.031545

Table VII.: Minimization results for DOW 755 for assumed Gaussian distribution, $\bar{X} = 223.6nm$ & $\sigma = 32.4 \pm 15.2nm$

Function Minimized	Volume Fraction	Local Algorithm			
		3 Unknowns			
		$\bar{X}$	σ	ϕ	residual
$\chi_2^2 = \sum_{\lambda_i} \left(\frac{\mu_s'^c - \mu_s'^e}{\mu_s'^e} \right)^2$	0.030	197.00	23.70	0.298	0.003827
	0.100	204.00	24.20	0.960	0.007870
	0.180	206.95	20.34	0.176	0.010433
	0.270	219.37	10.58	0.245	0.001981
$\chi_3^2 = \sum_{\lambda_i} \left(\frac{\mu_s'^c - \mu_s'^e}{\mu_s'^c} \right)^2$	0.030	196.88	24.30	0.299	0.003829
	0.100	203.84	25.17	0.963	0.007831
	0.180	206.84	21.89	0.176	0.010353
	0.270	219.50	10.35	0.246	0.002017

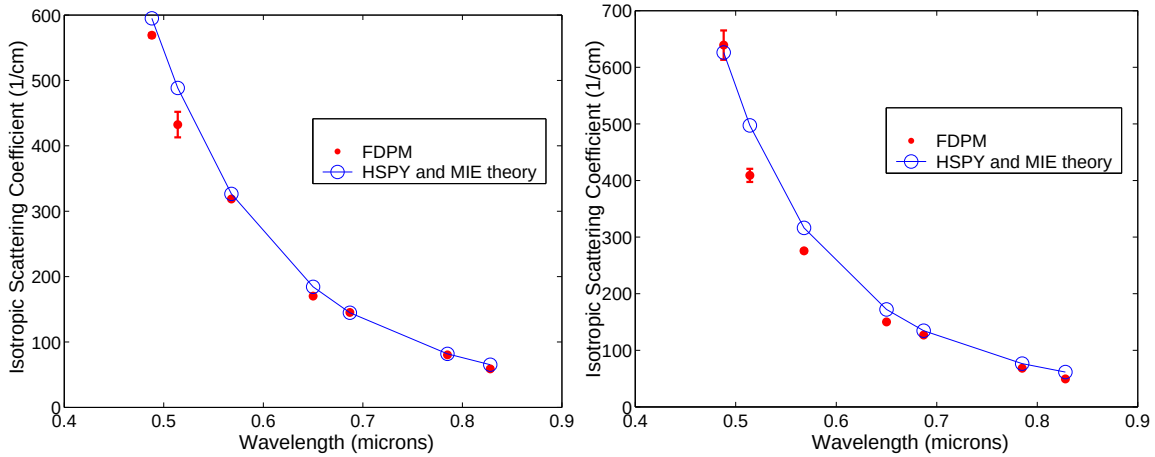

(a) $\bar{X} = 143.6$ nm, $\sigma = 35.0 \pm 7.2$ nm & $\phi = 18\%$

(b) $\bar{X} = 143.6$ nm, $\sigma = 35.0 \pm 7.2$ nm & $\phi = 27\%$

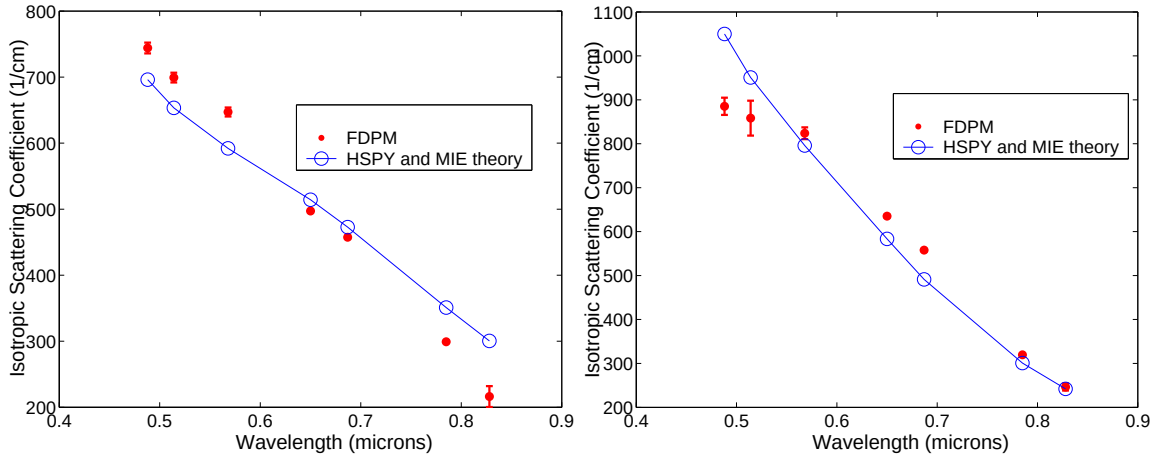

(c) $\bar{X} = 223.6$ nm, $\sigma = 32.4 \pm 15.2$ nm & $\phi = 18\%$

(d) $\bar{X} = 223.6$ nm, $\sigma = 32.4 \pm 15.2$ nm & $\phi = 27\%$

Fig. 34.: FDPM (solid points) and model prediction (open symbols connected by line) for an assumed Gaussian distribution. Error bars represent the standard error propagated from the measurements. Model prediction used Mie-theory with Hard Sphere Percus Yevick approximation to predict structure.

show the same trend for inversion of the data, as shown in figure(36). In addition, the mean particle size predictions are more accurate for the higher volume fraction samples ($\phi > 0.03$).

Volume fraction predictions are found to be in good agreement with experimental volume fractions. The relative error for recovery of particle volume fraction was between 0.96 and 24% for $\bar{X} = 143.6$ nm and 0 and 9.03% for $\bar{X} = 223.6$ nm. When the volume fraction was assumed known, the inversion of data recovered the mean particle sizes that were accurate.

These observations validate the use of the structure factor model for concentrated suspensions. It is notable that the mean of the particle size can be determined along with the volume fractions.

F. Summary

Particle sizing in a dense colloidal suspension using FDPM with multiple wavelengths is possible by accounting for interaction forces among different sizes of particles. This has been achieved by using a most general model for polydisperse interacting systems and finding a global minimum of the optimization problem by first using genetic algorithms and then using local search algorithms to recover $f(x)$ and ϕ. FDPM has proved to be a powerful tool providing multiple wavelength data using a discrete set of laser diodes and gas lasers, for the inversion problem. Since FDPM has the ability to make independent measurements of the scattering and the absorption coefficients in dense multiply scattering systems, common instruments working at several wavelengths provided by laser diode arrays could be used to determine the particle sizes at industrially relevant concentrations. This work was supported in part by the National Science Foundation CTS - 0213280.

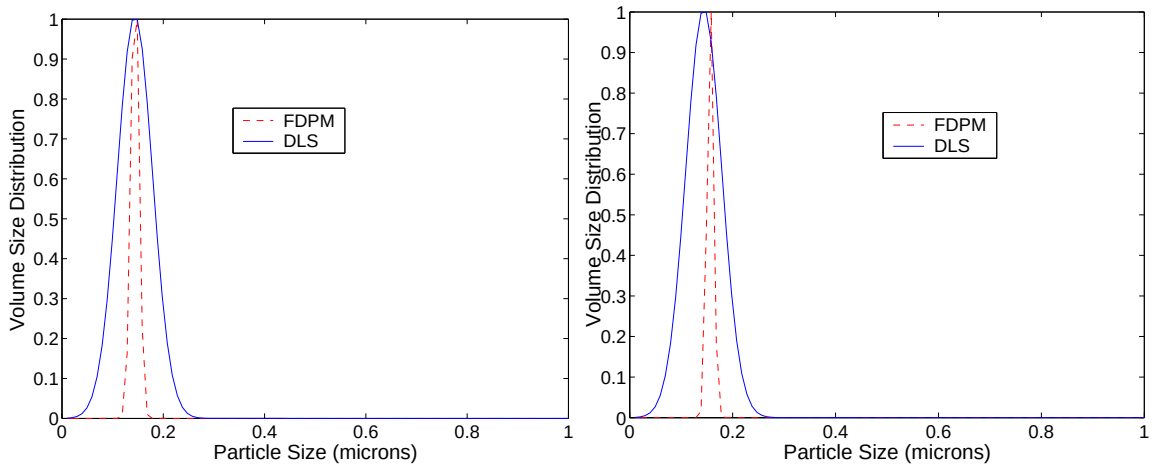

(a) $\bar{X} = 143.6$ nm, $\sigma = 35.0 \pm 7.2$ nm & ϕ =18%

(b) $\bar{X} = 143.6$ nm, $\sigma = 35.0 \pm 7.2$ nm & ϕ =27%

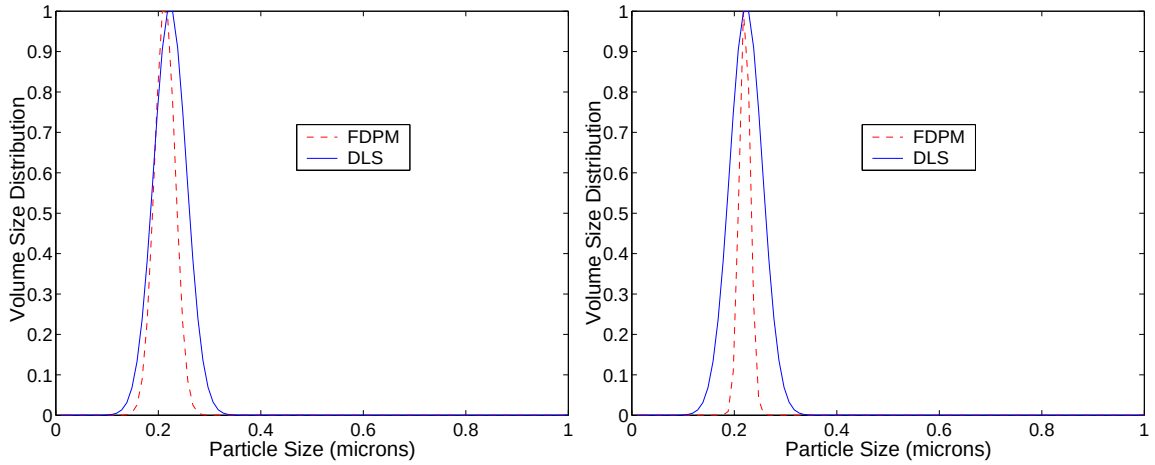

(c) $\bar{X} = 223.6$ nm, $\sigma = 32.4 \pm 15.2$ nm & ϕ= 18%

(d) $\bar{X} = 223.6$ nm, $\sigma = 32.4 \pm 15.2$ nm & ϕ= 27%

Fig. 35.: Comparison between experiment (dashed) and actual particle size distribution(solid) assuming a Gaussian distribution.

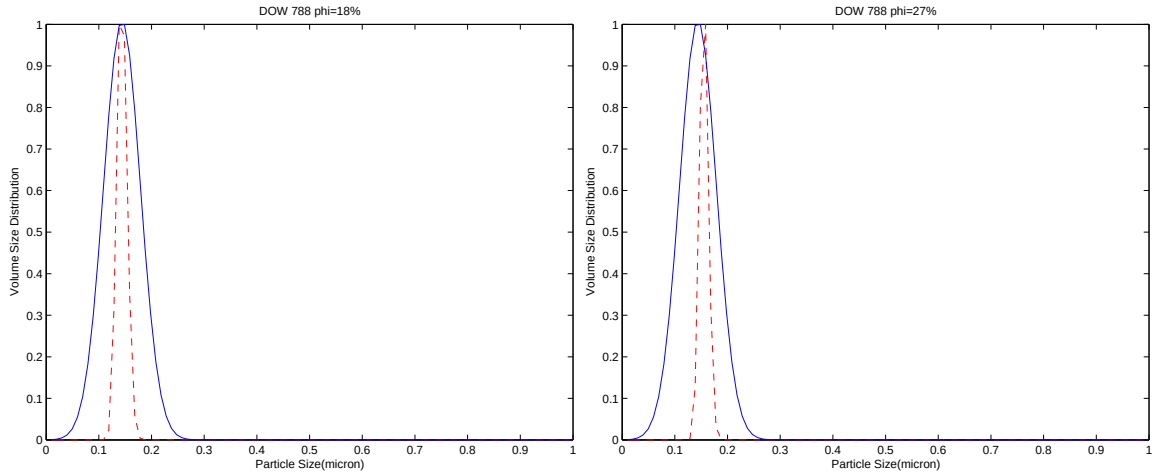

(a) $\bar{X} = 143.6$ nm, $\sigma = 35.0 \pm 7.2$ nm & ϕ =18%

(b) $\bar{X} = 143.6$ nm, $\sigma = 35.0 \pm 7.2$ nm & ϕ =27%

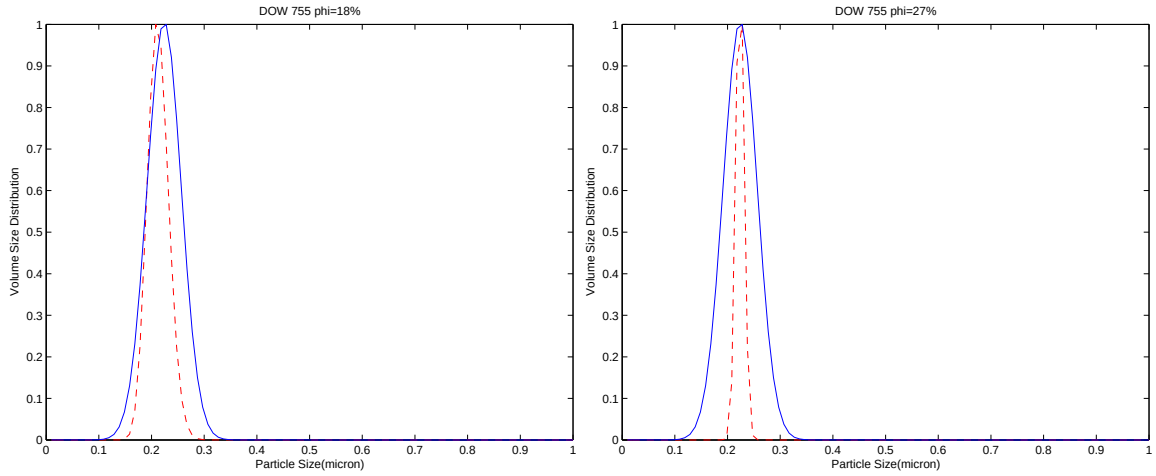

(c) $\bar{X} = 223.6$ nm, $\sigma = 32.4 \pm 15.2$ nm & ϕ= 18%

(d) $\bar{X} = 223.6$ nm, $\sigma = 32.4 \pm 15.2$ nm & ϕ= 27%

Fig. 36.: Comparison between Experimental(dashed) and actual particle size distribution(solid) assuming a Johnson SB distribution.

CHAPTER VII

MONODISPERSE CHARGED DISPERSIONS

A. Introduction

There are several scattering techniques, such as dynamic light, turbidity, x-ray and neutron scattering, that can provide analysis of dilute colloidal dispersions but when the concentration of the colloidal particles increases, multiple scattering of light occurs and the information obtained from single scattering on a particle is "smeared" by several single scattering events from closely correlated particles. The ionic strength of the medium determines how the interactions among the particles are tuned and how they arrange with respect to each other in a dense dispersion. Colloidal particles carry a native charge and their interactions are mediated by the presence of a dielectric liquid medium. Huang *et al.* [90, 109–111] conducted FDPM measurements to understand electrostatic interactions in dense polystyrene dispersions. The dispersion ionic strength values investigated in their work were 1,5,25,60 and 120mM NaCl eqv. In their studies, the isotropic scattering coefficients of polystyrene lattices were shown to be sensititve to changing ionic strengths of the suspending fluid. The work was limited due to negligible change in the isotropic scattering coefficient at lower ionic strengths(i.e. 0.5mM - 5mM NaCl). Also in that work, comparisons were provided to those predicted with the MSA closure of the OZ equation. The current work extends the previous work, by demonstrating sensitive changes to the isotropic scattering coefficient due to small changes in ionic strength values. Experimental results are also compared with structure factor models obtained using the HNC and the PY closures described in Chapter IV.

B. Theory and background

Colloidal dispersions in aqueous or non aqueous media can be imparted with electrostatic stability by making the particles charged, or by means of steric stability when polymer chains are added to the surface of the particle. Charged particles interact with each other by means of long ranged repulsive forces and Van der Waals attractive forces. The balance between these two forces leads to regimes of stability of the dispersion. [112, 113] The study of charged particles arises due to the increasing need to study (i) the stability and phase behavior of charged particles, and (ii)how the interaction forces affect the bulk properties of the dispersions. In most experimental measurements of colloidal dispersions, polymer colloids have been the basis of study due to the ease of preparing monodisperse charged particles, among which polystyrene and poly methyl methacrylate (PMMA) is most widely used. Silica particles represent another class of particles employed in studies found in the literature.

Cebula *et al.* [114] presented experimental results of neutron scattering on concentrated polystyrene colloidal dispersions with charged particles. They changed the interactions among the particles by changing the electrolyte content in the medium whereby the highest concentration of particles investigated was $\phi = 0.14$. The maximum electrolyte content used in their study was 5mM salt concentration. The structure factors for the monodisperse dispersions were obtained by carrying out experiments at two different volume fractions such that $S(Q) = 1$ for one of the dispersions. The structure factor for the higher concentration dispersion was then obtained as a ratio of intensities multiplied with the reciprocal ratio of volume fractions. Discrepancies were found in the structure factors obtained from measurements and those predicted from OZ solution with PY closure and Hard sphere potential.

Pusey *et al.* [115,116] described a study of phase behaviour involving hard spheres

whereas Auer *et al.* [117] studied the crystallization of weakly charged colloids by means of Monte Carlo simulations. They found a reduction in the nucleation barrier when the strength of repulsion increased and an increase in nucleation rate. Azhar *et al.* [118] described phase diagrams of Yukawa fluids by means of extensive Monte Carlo simulations. Robbins *et al.* [119] studied the phase diagrams of Yukawa colloids, with extensive molecular dynamics simulations. They evaluated the order-disorder phase transitions and compared the FCC-BCC transitions with experiments. Sirota *et al.* [120] used a small angle x-ray scattering study to understand the phase diagrams of charged colloidal particles up to volume fractions of 0.30. Dhont *et al.* [121] studied the crystallization of silica colloidal particles with time-resolved static light scattering techniques. Palberg [122] provides an excellent review on crystallization kinetics of colloidal particles studied with small angle light scattering and Bragg microscopy.

Ohtsuki *et al.* [123], [124] studied the dynamical rigidity and viscosity of polystyrene latexes using a torsional quartz crystal method. The dynamical rigidity was found to decrease and the viscosity to increase at the order- disorder transition in the colloidal latex with the addition of salt to the ordered dispersion.

Brunner *et al.* [125] studied the charge stabilized polystyrene colloid particle pair interactions in two dimensions by video microscopy, and found that multibody interactions become important as the density of particles increased. The pair interaction potential was found to be dependent upon the density of particles in the volume observed with video microscopy.

Hartl *et al.* [126, 127] studied the structure factor of charged colloidal dispersions using static laser light scattering and approximated their expressions for the structure factors by using an effective charge calculated using the Poisson Boltzmann Cell model, for finding the renormalized charge.

Confocal microscopy is also used to study colloidal dispersions [128–134], by fluo-

rescent labeling of the colloidal particles and studying the three dimensional positions of the colloidal particles. Royall *et al.* [129] obtained coexisting regions of high density and low density colloidal crystals, and void formation using the technique.

In the following sections, the potential models for interaction are provided, followed by models of (discussion of effective charge) colloidal charge renormalization and the theory for predicting the isotropic scattering coefficient from Mie Scattering theory. The structure factors are obtained from MC simulations and solution of the OZ equations, and are then used to predict the experimental data.

1. Potential models for interaction

The charge on the colloidal particles makes them mutually repulsive except for distances close enough for attractive energies to predominate. The interplay of repulsive and attractive forces determines the stability of the colloidal dispersion. The potential energy is determined for various potential models of repulsive and attractive forms.

a. Repulsive forces

1. Yukawa potential

The Yukawa potential is defined to be a hardcore part at the surface of the particle, where the particles encounter an infinitely repulsive potential when the particles contact each other. Beyond its surface, a softcore part of the particle is encountered and the potential falls off exponentially with distance away from the surface of the particle.

$$\begin{aligned} \beta u(r) &= \infty \quad if \quad r < \sigma \\ &= \pi \epsilon_o \epsilon \sigma^2 \psi_o^2 \frac{e^{-\kappa(r-\sigma)}}{r} \quad if \quad r > \sigma \end{aligned} \tag{7.1}$$

where $\kappa = \sqrt{\frac{\sum_i n_i z_i^2 e^2}{\epsilon_o \epsilon k_B T}}$ is the Debye Huckel parameter and depends upon the ionic strength of the medium or the concentration of small ions.

b. Attractive forces

The Van der Waals energy is calculated by the following expression

$$V_A = -\frac{A}{12}\left(\frac{1}{x^2+2x} + \frac{1}{x^2+2x+1} + 2ln\left(\frac{x^2+2x}{x^2+2x+1}\right)\right) \tag{7.2}$$

where $x = \frac{h}{2a}$; h is the distance between the surfaces of the particles; a is the radius of the particles; and A is the composite Hamaker constant for the particles in the medium as given by

$$A = (\sqrt{A_{11}} - \sqrt{A_{22}})^2 \tag{7.3}$$

with A_{11} is the Hamaker constant of the particles and A_{22} that of the medium. [7,135] A combination of the Van der Waals and Yukawa potential is the most general way the potential among the particles can be treated. In this study only repulsive forces of Yukawa type are considered, assuming negligible attractive forces among the particles.

2. Renormalized charge and colloidal stability

Colloidal particles in a dispersion are surrounded by counterions which are in equilibrium with the particle surface and ions from the added electrolyte. The interactions among the particles are therefore due to an effective charge of the particles in the medium and not due to the native particle charge which could be high. Alexander *et al.* [136] introduced the concept of effective charge of the colloidal particles in a Wigner Seitz cell. The potential at the surface of the cell obtained from Poisson Boltzmann theory along with the density of counterions surrounding the particles, is made equal to the potential obtained from Debye-Huckel theory with an effective

charge value. The effective charge for a particle is found to saturate upon increasing the native charge on the particle. Belloni *et al.* [137] also addressed the concept of effective charge and provided a methodology for finding the effective charges for spheres and cylinders. While Alexander's approach is for a canonical ensemble, a semi grand canonical approach is presented by Trizac *et al.* [138], [139], which is used in this work to determine the effective charges of the particles.

The non-dimensional Poisson Boltzmann cell equation is solved for a particular volume fraction of the particles and concentration of salt in the medium. The potential at the surface of the Wigner Seitz cell is fixed and the charge on the particle is determined after solving for the potential profile in the Wigner Seitz cell. The charge obtained through the analytical expression in Trizac's work is used to then predict the effective charge at the cell boundary for the charge value of the particle obtained from titration measurements and zeta potential measurements.

The Poisson Boltzmann cell equation that must be solved is given as

$$\nabla^2\psi(r) = \kappa^2 \sinh\psi(r) \quad a < r < R \tag{7.4}$$

where the boundary conditions are

$$\overrightarrow{n} \cdot \nabla\psi(r) = Z_p\lambda_B/a^2 \qquad r = a$$

$$\overrightarrow{n} \cdot \nabla\psi(r) = 0 \qquad r = R$$

λ_B is the Bjerrum length; a is the radius of the particle; R is the radius of the Wigner Seitz cell; Z_p is the charge on the particle; and $\psi(r)$ is the potential in the Wigner Seitz (WS) cell.

The potential at the cell boundary ψ_R is evaluated from the above calculation and the inverse screening length from the microion density at the WS boundary is

given as

$$\kappa_{PB}^2 = \kappa^2 \cosh \psi_R. \tag{7.5}$$

The analytical expression for the effective charge is given as

$$Z_{eff} = \frac{\gamma_0}{\kappa_{PB}\lambda_B}\{(\kappa_{PB}^2 aR - 1)\sinh[\kappa_{PB}(R-a)] + \kappa_{PB}(R-a)\cosh[\kappa_{PB}(R-a)]\} \tag{7.6}$$

where $\gamma_0 = \tanh \psi_R$. The value of the Z_{eff} obtained from the above expression is then used to obtain the structure factors from MC and OZ methods.

3. Isotropic scattering coefficient for the monodisperse case

The isotropic scattering coefficient $\mu_s^{'}$ measured from experiment can be modelled by means of the scattering cross section C_{sca} of the particle obtained from Mie scattering theory coupled with the structure factor $S(Q)$, which takes into account the particle interactions and provides the arrangement of the particles in reciprocal space. The frequency of the reciprocal space is of the order of the magnitude of the wave vector $Q = \frac{4\pi m sin(\frac{\theta}{2})}{\lambda}$. The governing equation in the case of a monodisperse dispersion of particles is

$$\mu_s^{'} = \frac{12\phi}{(\frac{2\pi m}{\lambda})^2}\int_0^{\pi} \frac{F(n,\theta,\lambda,\sigma)}{\sigma^3} S(Q) sin\theta(1 - cos\theta)d\theta \tag{7.7}$$

Here $F(n,\theta,\lambda,\sigma)$ is the Mie scattering theory form factor and $S(Q)$ is the static structure factor for monodisperse particles. This structure factor has been obtained for charged particles using a Yukawa potential model from Monte Carlo simulations and numerical solutions from OZ equations for the HNC and PY closures, as described in Chapter IV. An analytical model for the structure factor using the MSA closure developed by Herrera *et al.* [56] was also used.

The refractive index of the particles varies with the wavelength. The variation of the refractive index for the particles with respect to wavelength for polystyrene has been provided by Nikolov *et al.* [140] The experimental data obtained from Nikolov's work are fit to a Sellmeier's formula and has the form [140]:

$$n_\lambda^2 - 1 = \frac{B_1\lambda^2}{\lambda^2 - C_1} + \frac{B_2\lambda^2}{\lambda^2 - C_2} + \frac{B_3\lambda^2}{\lambda^2 - C_3} \tag{7.8}$$

The coefficients were found by non linear fitting to the experimental data and are provided below for polystyrene in table VIII.

Table VIII.: Sellmeier's coefficients for polystyrene

B_1	B_2	B_3	C_1	C_2	C_3
1.5308	-0.2078	0.2596	0.0195	-0.1710	-1.7881

The refractive index predicted by Eqn. 7.8 is used to model the isotropic scattering data at different wavelengths instead of using a constant value of 1.59 for polystyrene. Our observations indicated high sensitivity of the isotropic scattering data to the refractive index when the concentration of particles was high.

C. Results and discussion

The structure factors from various theories are compared in this study. At high charge values and low ionic strengths, the repulsive interactions are strong. The solution to the OZ equation using the MSA closure fails in these cases when compared with the Monte Carlo simulations with truncated potential. Figures (37,38,39 and 40) provide structure factor comparisons between the numerical solution of HNC and HSY potential model, along with Monte Carlo results of vector and scalar methods, for arbitrary effective charge values of the particles in the dispersions. In the figures provided, the structure factor is plotted versus the non dimensional wave vector($Q\sigma$), for a particular particle size (σ), volume fraction (ϕ), concentration of salt (C_s) and effective charge on the particle, Z_{eff}. For all the results, OZ solutions using the HNC and the PY closure forms show good comparisons with the Vector Monte Carlo simulations.

The results for OZ solution using the MSA closure model and PYHS model are also plotted. In general, the numerical solutions are in good agreement with the MC simulation results and expectedly differ for the PYHS solution, simultaneously validating the simulations and the numerical methods. In the subsequent sections the predictions of isotropic scattering coefficients are henceforth provided only for HNC closure and HSY potential model. As the electrolyte content in the dispersions was increased to 4mM, the numerical results from the HNC and PY calculations were found to converge to the PYHS static structure model. The results for the structure factors in the low Q region are found to be stable and no oscillations are found in this region. The structure factor peaks are found to be much more pronounced for dispersions with the lower particle diameter as compared to that with the larger diameter particle.

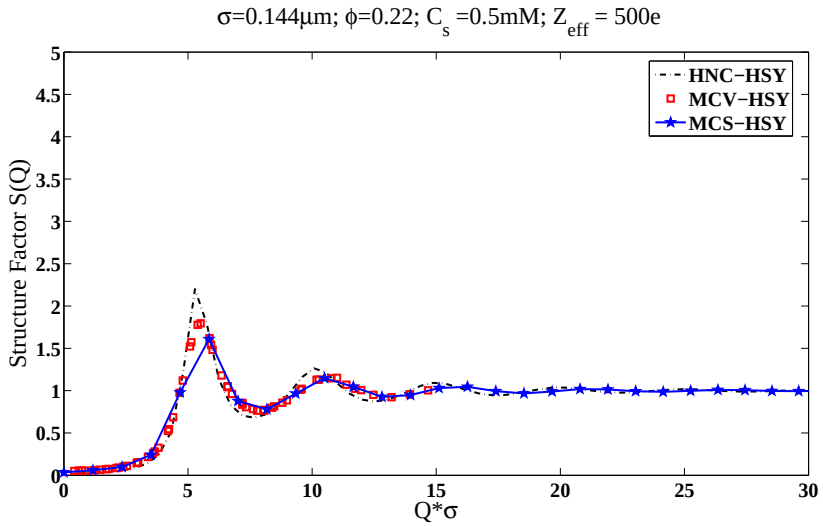

(a)

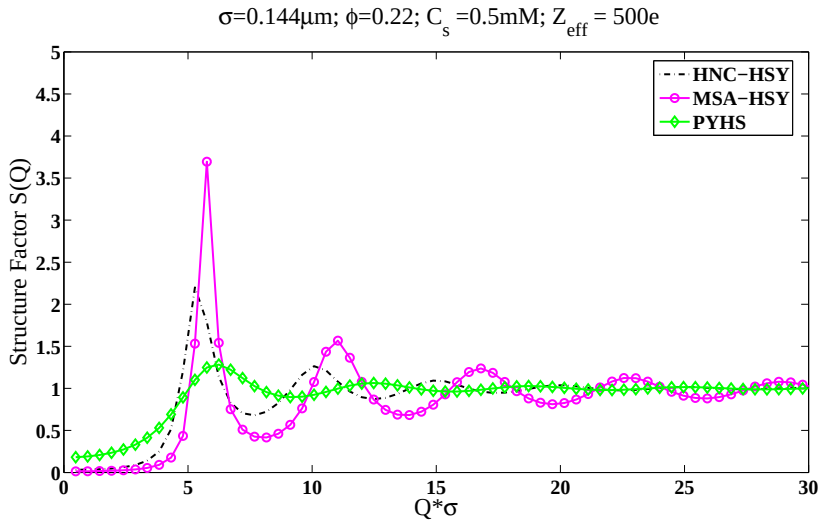

(b)

Fig. 37.: Structure factor versus non dimensional wave vector for monodisperse dispersions; (a) Comparsions for the MC-vector(squares) and MC-scalar methods(star connected with solid lines) with the numerical solutions of Hypernetted Chain Closure(HNC)(dash dot lines). (b)Comparison of the analytical solution using the Mean Spherical Approximation (MSA)(circle connected with lines), the analytical solution of the OZ equation for PYHS (diamond connected with lines) and the numerical solutions of Hypernetted Chain Closure(HNC)(dash dot lines) . The particle size simulated was $\sigma = 0.144\mu m$, ionic strength $C_s = 0.5mM$, $\phi = 0.22$ and $Z_{eff} = 500$.

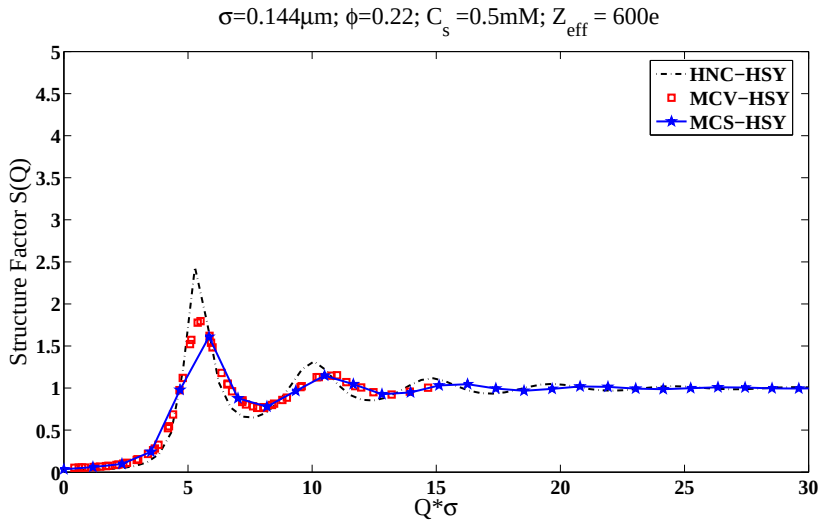

(a)

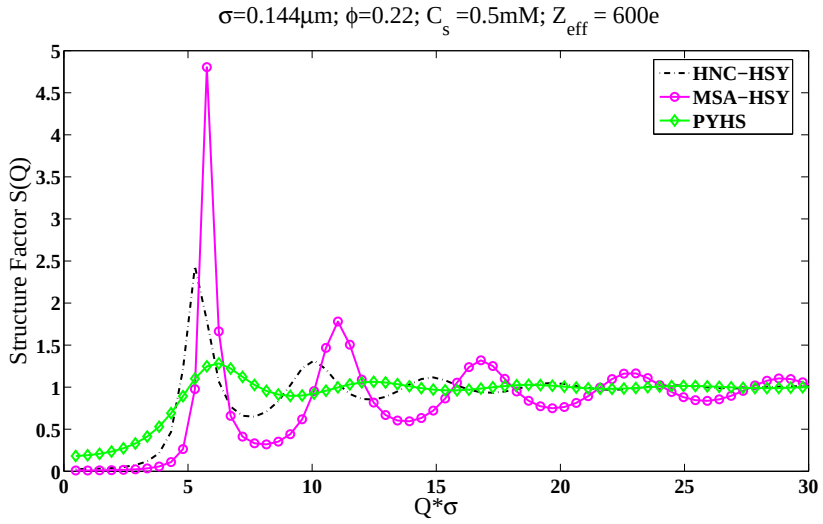

(b)

Fig. 38.: Structure factor versus non dimensional wave vector for monodisperse dispersions; (a) Comparsions for the MC-vector(squares) and MC-scalar methods(star connected with solid lines) with the numerical solutions of Hypernetted Chain Closure(HNC)(dash dot lines). (b)Comparison of the analytical solution using the Mean Spherical Approximation (MSA)(circle connected with lines), the analytical solution of the OZ equation for PYHS (diamond connected with lines) and the numerical solutions of Hypernetted Chain Closure(HNC)(dash dot lines) . The particle size simulated was $\sigma = 0.144\mu m$, ionic strength $C_s = 0.5mM$, $\phi = 0.22$ and $Z_{eff} = 600$.

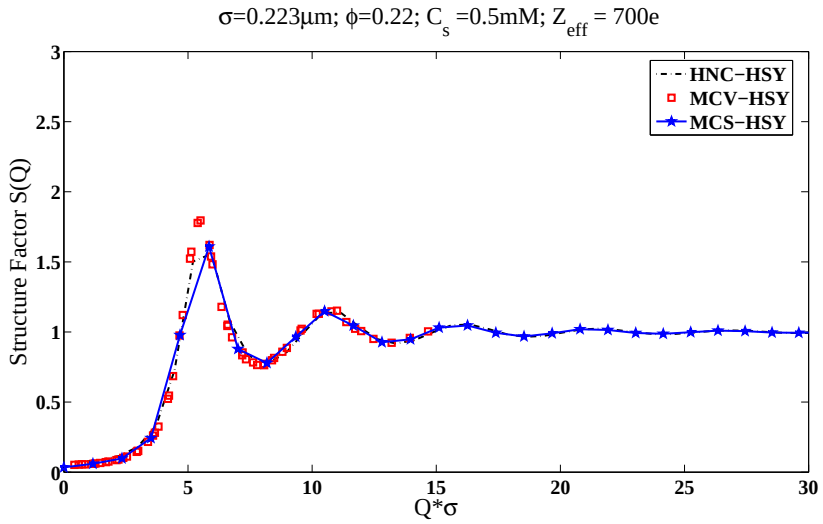

(a)

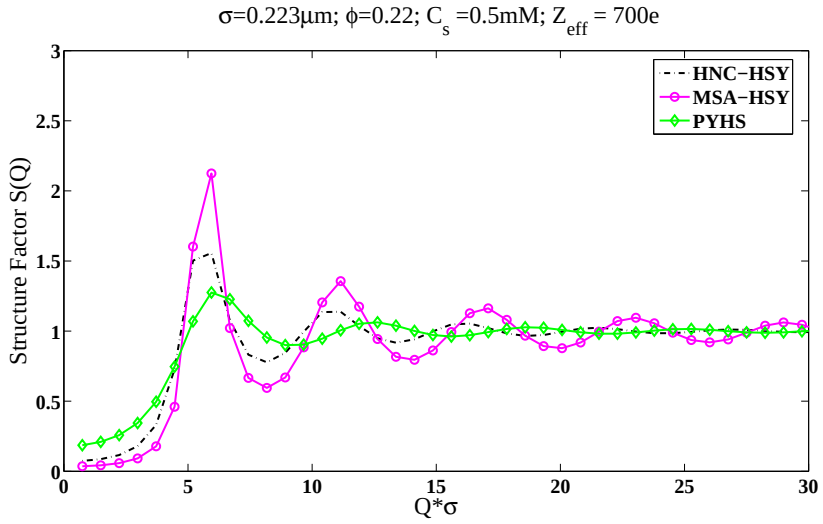

(b)

Fig. 39.: Structure factor versus non dimensional wave vector for monodisperse dispersions; (a) Comparsions for the MC-vector(squares) and MC-scalar methods(star connected with solid lines) with the numerical solutions of Hypernetted Chain Closure(HNC)(dash dot lines). (b)Comparison of the analytical solution using the Mean Spherical Approximation (MSA)(circle connected with lines), the analytical solution of the OZ equation for PYHS (diamond connected with lines) and the numerical solutions of Hypernetted Chain Closure(HNC)(dash dot lines) . The particle size simulated was $\sigma = 0.223\mu m$, ionic strength $C_s = 0.5mM$, $\phi = 0.22$ and $Z_{eff} = 700$.

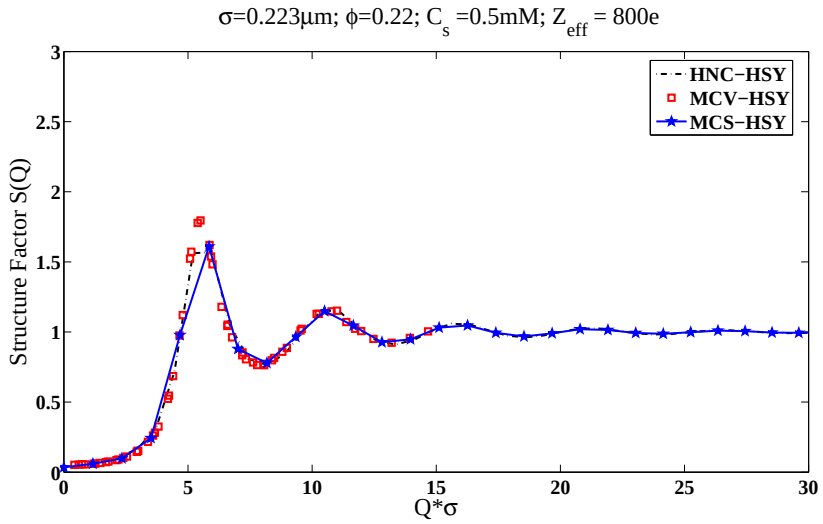

(a)

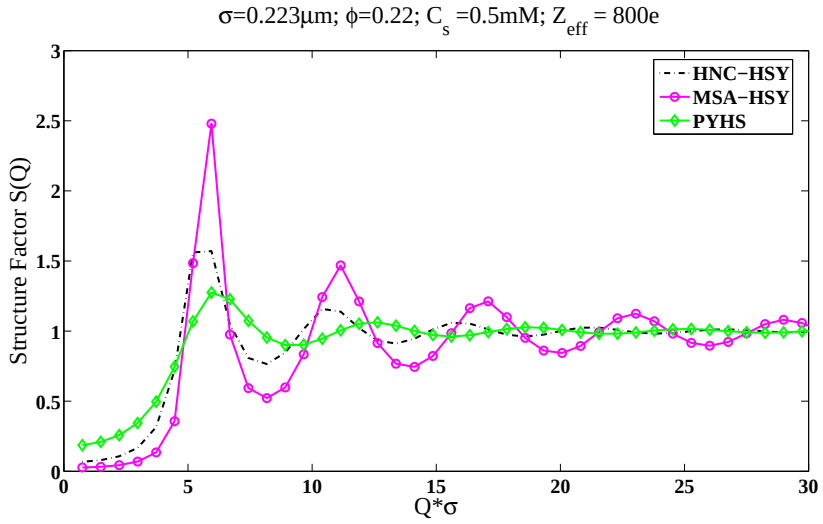

(b)

Fig. 40.: Structure factor versus non dimensional wave vector for monodisperse dispersions; (a) Comparsions for the MC-vector(squares) and MC-scalar methods(star connected with solid lines) with the numerical solutions of Hypernetted Chain Closure(HNC)(dash dot lines). (b)Comparison of the analytical solution using the Mean Spherical Approximation (MSA)(circle connected with lines), the analytical solution of the OZ equation for PYHS (diamond connected with lines) and the numerical solutions of Hypernetted Chain Closure(HNC)(dash dot lines) . The particle size simulated was $\sigma = 0.223\mu m$, ionic strength $C_s = 0.5mM$, $\phi = 0.22$ and $Z_{eff} = 800$.

Window of structure factor under investigation

The modelling of the isotropic scattering coefficient data requires the range of values of $S(Q)$ for the corresponding values of $Q\sigma$ that are being used to study the structure factors. The window of investigation is shown in the Figure 41. Reference is made to the window of investigation, for understanding the isotropic scattering coefficient data obtained from experimental data, later in this Chapter and in Chapter VIII.

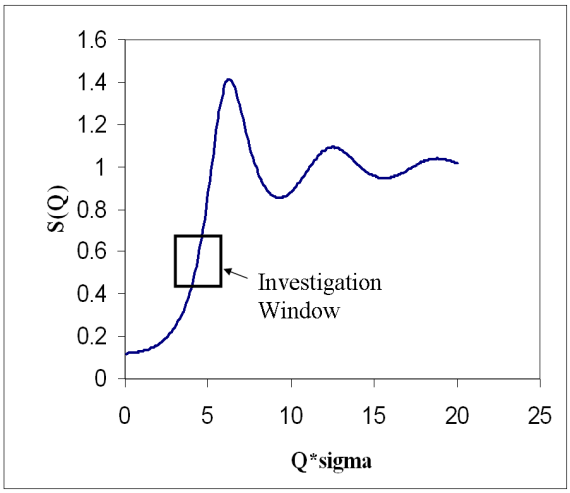

Fig. 41.: Window of investigation of structure factor for isotropic scattering coefficient modelling.

Isotropic Scattering Coefficient versus Ionic Strength

Figure 42 provides experimental data for four different wavelengths used to measure isotropic scattering coefficient as a function of ionic strength and at volume fractions of $\phi = 0.22$, 0.18, and 0.15 for 144nm diameter colloidal particles. The isotropic scattering coefficient is plotted versus the ionic strength and the data points are plotted as points connected by lines and the error bars are provided. The error bars are calculated from three FDPM experimental measurements at each ionic strength and volume fraction values. The experimental data are collected at four different diode wavelengths of 660, 685, 785 and 828 nm and dispersion ionic strengths of 0.5mM, 1mM, 2mM, 3mM and 4mM. Observations of the experimental data show that as the volume fraction of the dispersions is increased, the scattering is hindered and the isotropic scattering coefficient decreases, due to the increase in correlations among the particles. This result implies a higher amount of ordering among the particles of the dispersion, due to the strong repulsive forces which predominate at high volume fractions. When the ionic strength in the dispersions is increased, the dispersions become less structured, the hindrance to scattering is reduced, and the isotropic scattering coefficient increases. This result also implies that the dispersions become less structured and more randomized with the addition of electrolyte to the dispersion.

The range of non dimensional wave vectors ($Q\sigma$) accessed have the maximum value of 3.6465 corresponding to the wavelength of 660nm. Hence the peak of the structure factor is not accessed by the measurements.

From these results it is evident that changing ionic strength alters the microstructure of the particles. The salt ions replace the counterions from the particle on the surface of the particle and hence change the interactions from a strongly repulsive to more hard sphere like interactions. The particles become more random and the structure of the medium disappears resulting in an increase in scattering. These phenomena are more evident at higher volume fractions than at the lower volume fractions. In the following, the isotropic scattering data from each volume fraction is compared with predictions of the structure factors from HNC closure model and the Hard Sphere Yukawa (HSY) potential model.

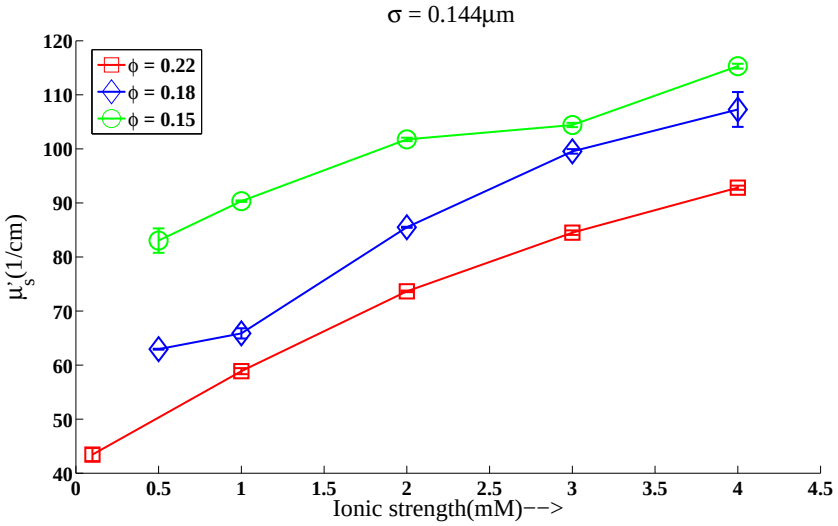

(a) $\lambda = 660nm$

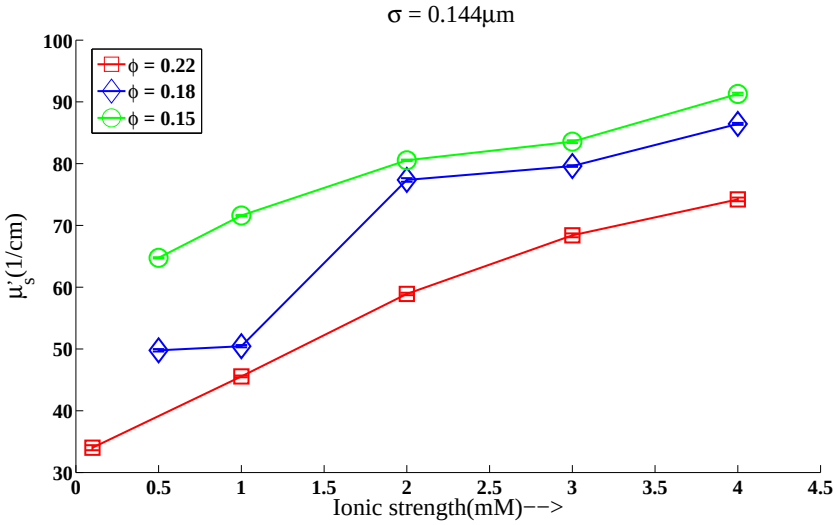

(b) $\lambda = 685nm$

Fig. 42.: Isotropic scattering coefficient measurements versus ionic strength of polystyrene latex, $\sigma = 144nm$, at volume fractions of $\phi = 0.22, 0.18$ and 0.15 and ionic strengths of 0.5,1,2,3 and 4mM at (a) $\lambda = 660$, (b) $\lambda = 685$, (c) $\lambda = 785$, and (d) $\lambda = 828$nm.

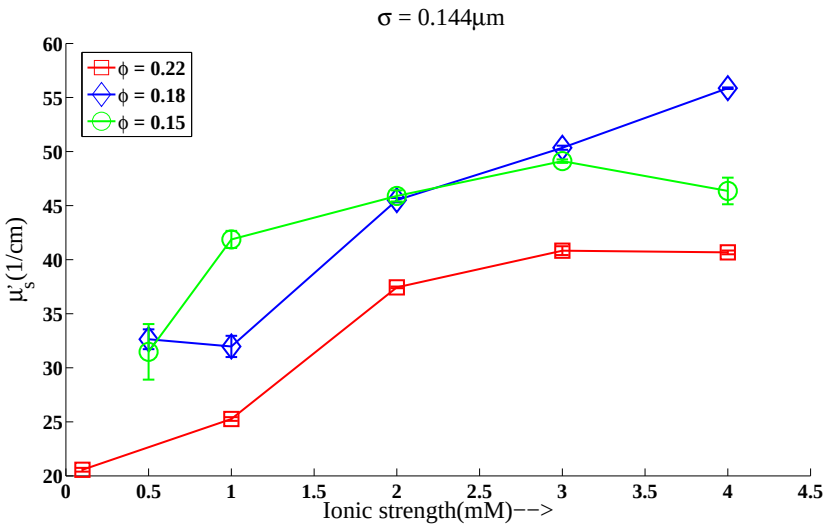

(c) $\lambda = 785nm$

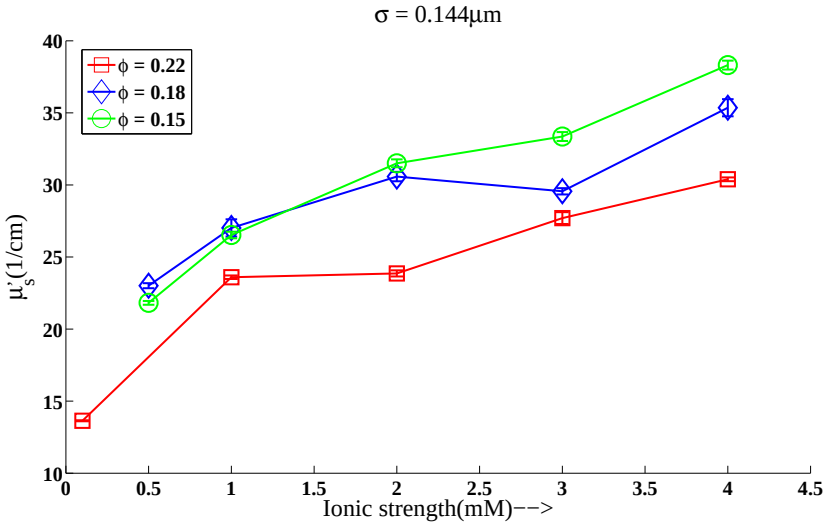

(d) $\lambda = 828nm$

Fig. 42.: Continued.

Model Predictions of isotropic scattering versus ionic strength

Figure (43) provides forward model comparisons of the isotropic scattering data with those obtained from FDPM measurements for a volume fraction of $\phi = 0.22$. The isotropic scattering coefficients are plotted versus the ionic strength of the dispersion. The red open square connected by lines are experimental data, whereas the points connected by lines are predictions from the models as a function of Z_{eff}. The exact hard sphere result for the same volume fraction and particle size is also plotted as cross connected by lines. The charge values used in the models are effective charge values, which are estimates of effective charge obtained using the technique of charge renormalization described in Chapter V. The effective charge values used are estimates obtained from an expected range of effective charge values on the particles.

The forward model comparisons are provided for a maximum effective charge value of 800 electrons, for which the OZ equations converge. An estimate for the effective charge on the particles was found to increase with ionic strength in the dispersion. This may explain why experimental data deviate with increasing ionic strength from the model prediction into a region of greater effective charge on the particle. This result is consistent with the analysis by Huang *et al.* [90], as well as by the theoretical effective charge calculation by renormalization, whereby the effective charge on the particles increase with increasing ionic strength of the medium. The effective charge on the particles increases upon increasing the ionic strength of the dispersion, for a particular volume fraction under consideration.

The increase in the isotropic scattering coefficient with ionic strength is found to have similar trends as the model predictions, and the structure factors increase (in the low Q range) from the highly repulsive case to the hard sphere case.

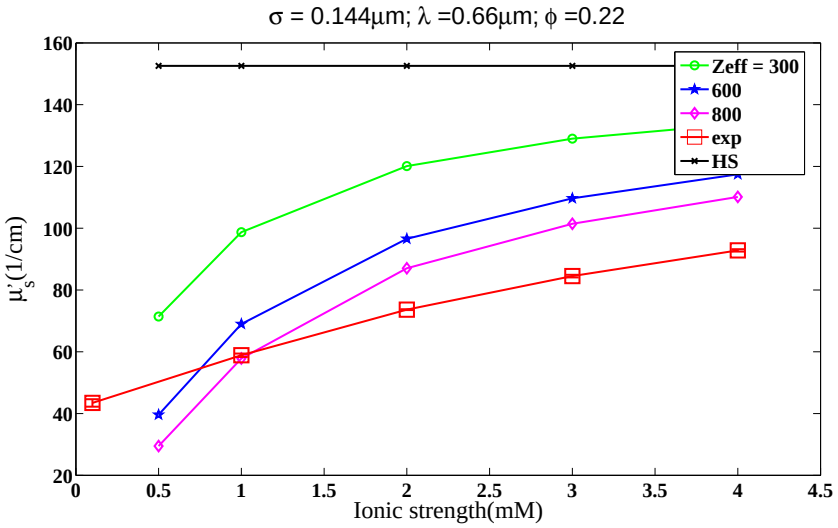

(a) $\lambda = 660nm$

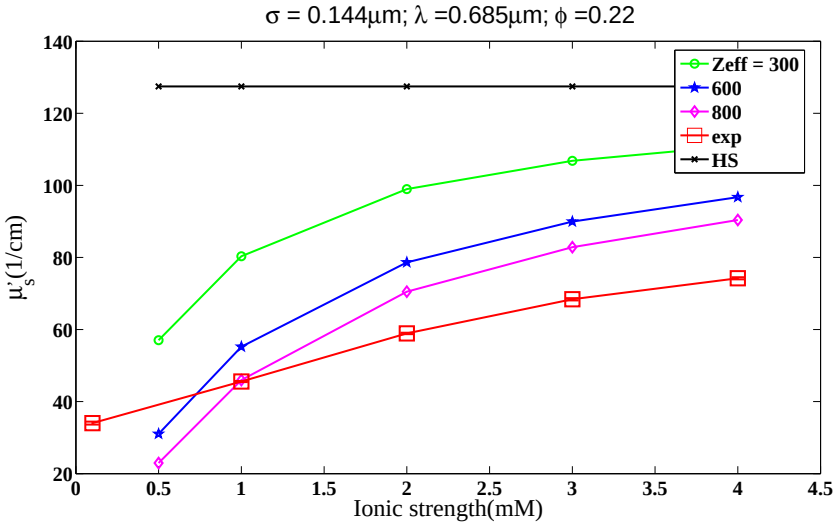

(b) $\lambda = 685nm$

Fig. 43.: Isotropic scattering coefficient measurements versus ionic strength of polystyrene latex. Open squares connected with solid lines are experimental measurements and points connected with solid lines are numerical solution of the OZ equation with Yukawa potential and HNC closure for $\sigma = 144nm$, at volume fraction of $\phi = 0.22$ and ionic strengths of 0.5,1,2,3 and 4mM at (a) $\lambda = 660$, (b) $\lambda = 685$, (c) $\lambda = 785$, and (d) $\lambda = 828$nm. The term HS refers to PYHS results and "exp" implies experimental results, and the effective charges used are $Z_{eff} = 300, 600$ and 800.

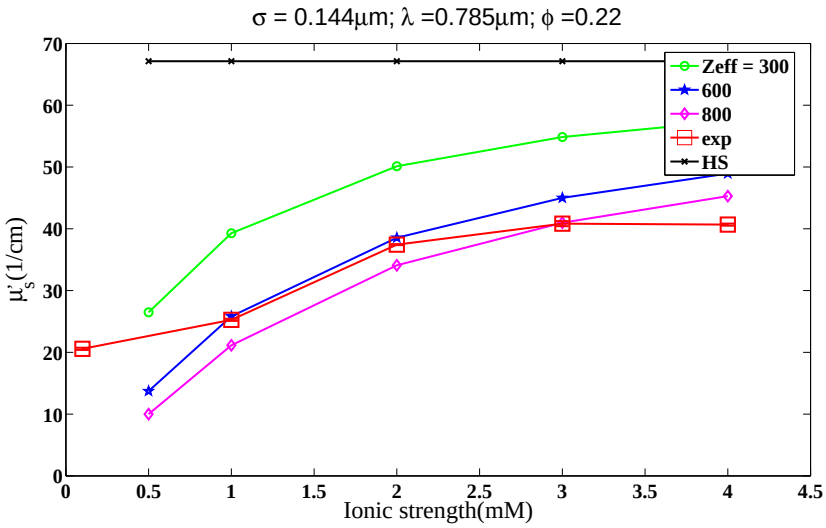

(c) $\lambda = 785nm$

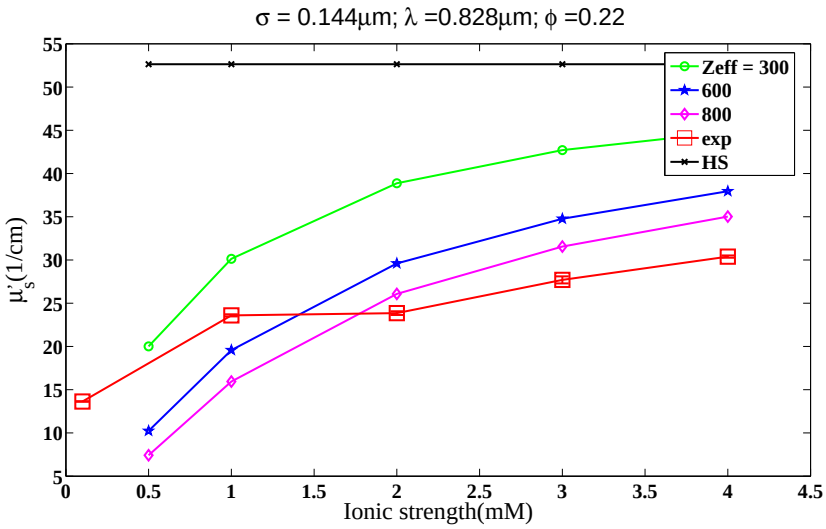

(d) $\lambda = 828nm$

Fig. 43.: Continued.

Figure (44) provides the forward model comparisons of the isotropic scattering data with those obtained from experimental measurement for volume fraction of $\phi = 0.18$. The isotropic scattering coefficient data are plotted versus the ionic strength of the dispersion for (a) $\lambda = 660$, (b) $\lambda = 685$, (c) $\lambda = 785$ and (d) $\lambda = 828$ nm. The open red squares connected by lines are experimental data, whereas the points connected by solid lines are predictions from the models. The exact PYHS result for the same volume fraction and particle size is also plotted as black cross connected by lines. The charge values used in the models are effective charge values, which are estimates of effective charge obtained using the technique of charge renormalization described in Chapter V. The effective charge values used are estimates obtained from an expected range of effective charge values on the particles. The effective charge values used are $Z_{eff} = 500, 1000$, and 1500.

The experimental data have similar trends as the model predictions and are found to increase with increasing ionic strength, hence reducing structure and bringing randomness to the dispersion.

When the wavelength is increased, the model predicted data are much closer to the experimental data implying the importance of refractive index of the particles at the lower wavelengths and alternatively the incorrect prediction of structure by the forward model data at the lower wavelengths. Also comparison of the experimental data with PYHS model predictions implies that the experimental data differ with that predicted by hard sphere potential. The data may be better predicted by the Yukawa potential or the soft core potential.

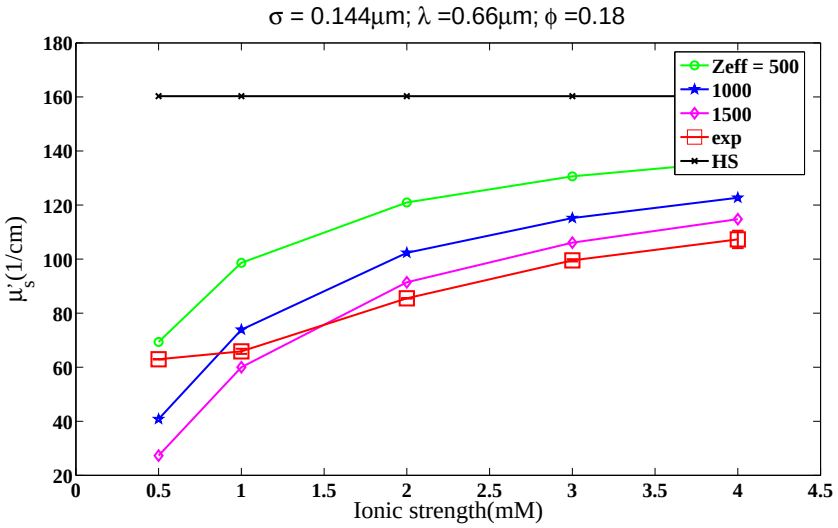

(a) $\lambda = 660nm$

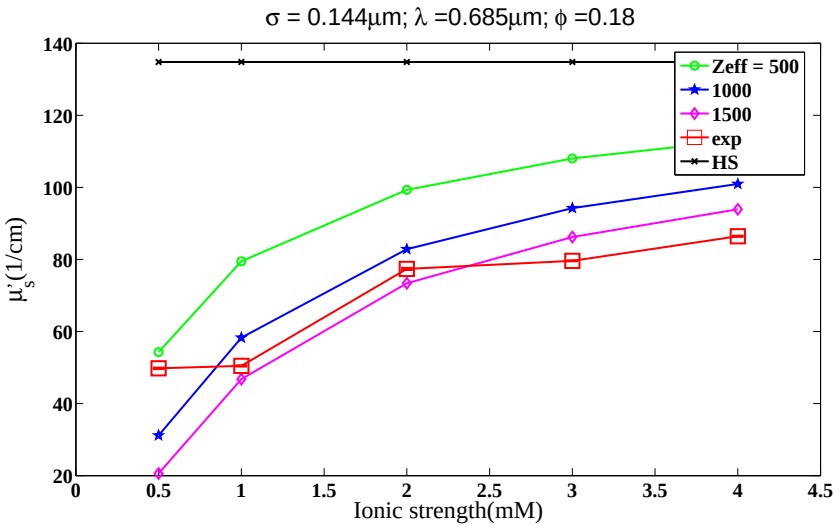

(b) $\lambda = 685nm$

Fig. 44.: Isotropic scattering coefficient measurements versus ionic strength of polystyrene latex. Open squares connected with solid lines are experimental measurements and points connected with solid lines are numerical solution of the OZ equation with Yukawa potential and HNC closure for $\sigma = 144nm$, at volume fraction of $\phi = 0.18$ and ionic strengths of 0.5,1,2,3 and 4mM at (a) $\lambda = 660$, (b) $\lambda = 685$, (c) $\lambda = 785$, and (d) $\lambda = 828$nm. The term HS refers to PYHS results and "exp" implies experimental results, and the effective charges used are $Z_{eff} = 500, 1000$ and 1500.

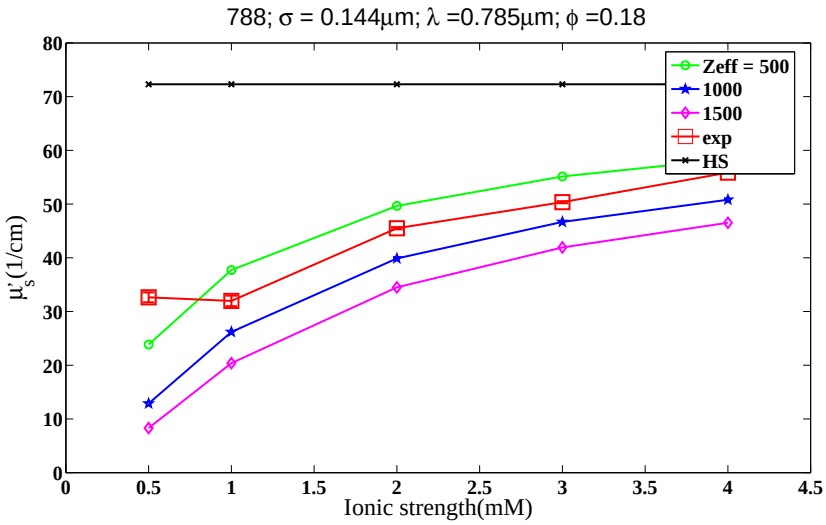

(c) $\lambda = 785nm$

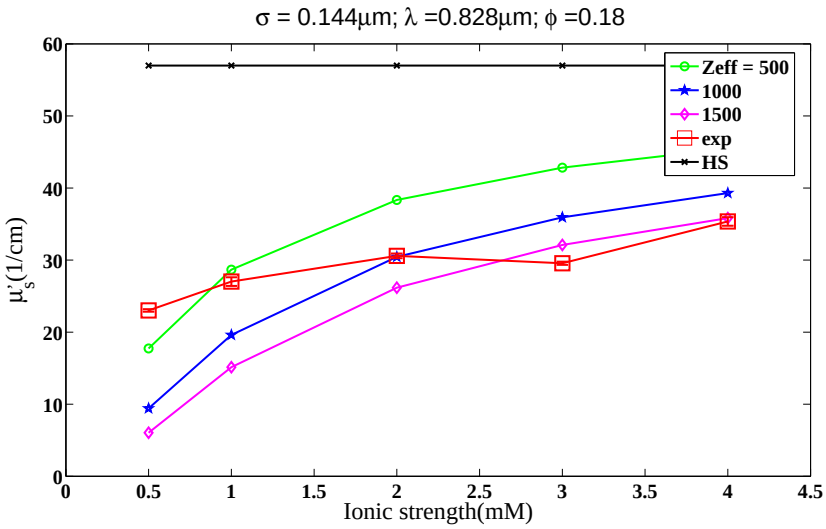

(d) $\lambda = 828nm$

Fig. 44.: Continued.

Figure (45) provides forward model comparisons of the isotropic scattering data with those obtained from experimental measurement for volume fraction of $\phi = 0.15$. The isotropic scattering coefficient data are plotted versus the ionic strength of the dispersion. The red open squares connected with lines are experimental data, whereas the points with lines are predictions from the models. The exact hard sphere result for the same volume fraction and particle size is also plotted as black cross connected by lines against the results for changing ionic strength. The charge values used in the models are effective charge values, which are estimates of effective charge obtained using the technique of charge renormalization described in Chapter V. The effective charge values used are estimates obtained from an expected range of effective charge values on the particles. The effective charge values used are $Z_{eff} = 500, 1000$, and 1500.

The experimental data are found to have similar trends with the model predictions and are found to increase with increasing ionic strength.

As in the past figure the model predicted data are much closer to the experimental data at higher wavelengths implying the importance of refractive index of the particles at the lower wavelengths and alternatively the incorrect prediction of structure by the forward model data at the lower wavelengths. Also comparison of the experimental data with PYHS model predictions implies that the experimental data differ with that predicted by hard sphere potential. The data may be better predicted by the Yukawa potential or the soft core potential.

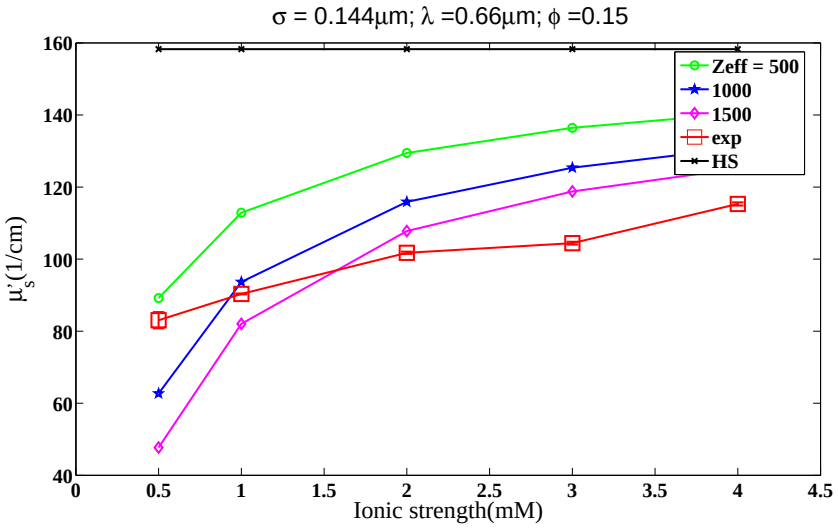

(a) $\lambda = 660nm$

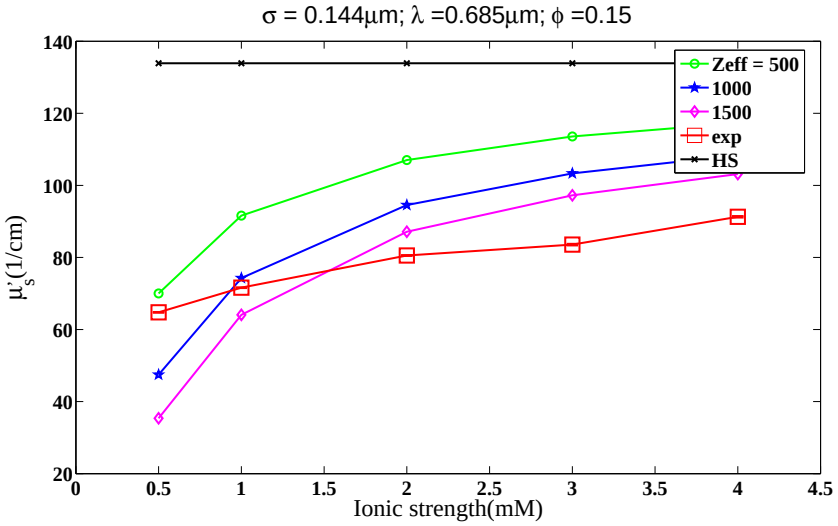

(b) $\lambda = 685nm$

Fig. 45.: Isotropic scattering coefficient measurements versus ionic strength of polystyrene latex. Open squares connected with solid lines are experimental measurements and points connected with solid lines are numerical solution of the OZ equation with Yukawa potential and HNC closure for $\sigma = 144nm$, at volume fraction of $\phi = 0.15$ and ionic strengths of 0.5,1,2,3 and 4mM at (a) $\lambda = 660$, (b) $\lambda = 685$, (c) $\lambda = 785$, and (d) $\lambda = 828$nm. The term HS refers to PYHS results and "exp" implies experimental results, and the effective charges used are $Z_{eff} = 500, 1000$ and 1500.

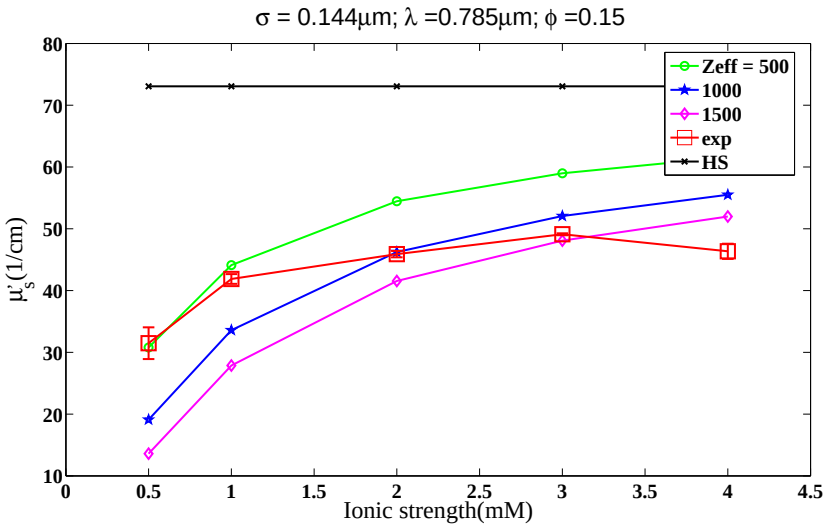

(c) $\lambda = 785nm$

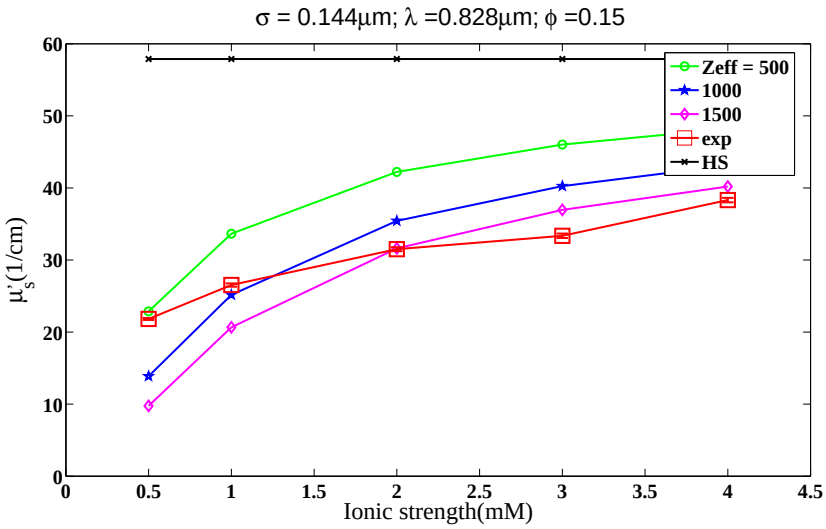

(d) $\lambda = 828nm$

Fig. 45.: Continued.

Figure (46) depicts the experimental data of isotropic scattering coefficient as a function of volume fraction for varying wavelengths and ionic strength of the dispersions. Results for the analytical solution of the PYHS case is presented alongside the experimental data. As the ionic strength increases the isotropic scattering coefficients are found to increase consistently towards the PYHS predictions for the different volume fractions.

The experimental data for different volume fractions provide insight into how the isotropic scattering coefficient differs for the cases of dispersions having low ionic strength to the cases of dispersions having higher ionic strength values. The latter mimic hard sphere like interactions and hence are closer to the PYHS model predictions. The experimental data at the lower wavelengths provide a much greater difference with predictions when compared to those at higher wavelengths.

Figure (47) depicts the experimental data of isotropic scattering coefficient as a function of wavelength. The isotropic scattering coefficients are found to increase as the wavelength of light is decreased. The change in isotropic scattering coefficient also increases with higher ionic strength values in the dispersion at all wavelengths.

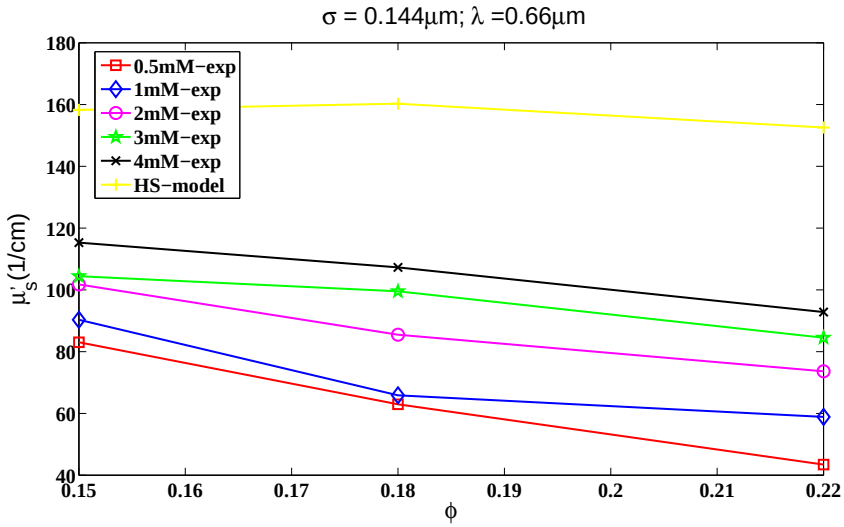

(a) $\lambda = 660nm$

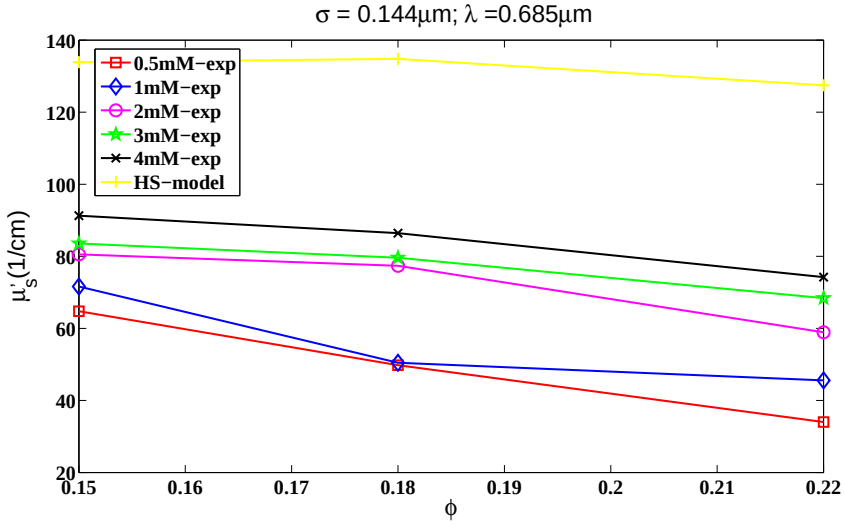

(b) $\lambda = 685nm$

Fig. 46.: Isotropic scattering coefficient measurements versus volume fraction of 144nm diameter polystyrene latex at ionic strengths of 0.5,1,2,3 and 4mM at (a) $\lambda = 660$, (b) $\lambda = 685$, (c) $\lambda = 785$, and (d) $\lambda = 828$nm. The term "HS" refers to the PYHS analytical solution.

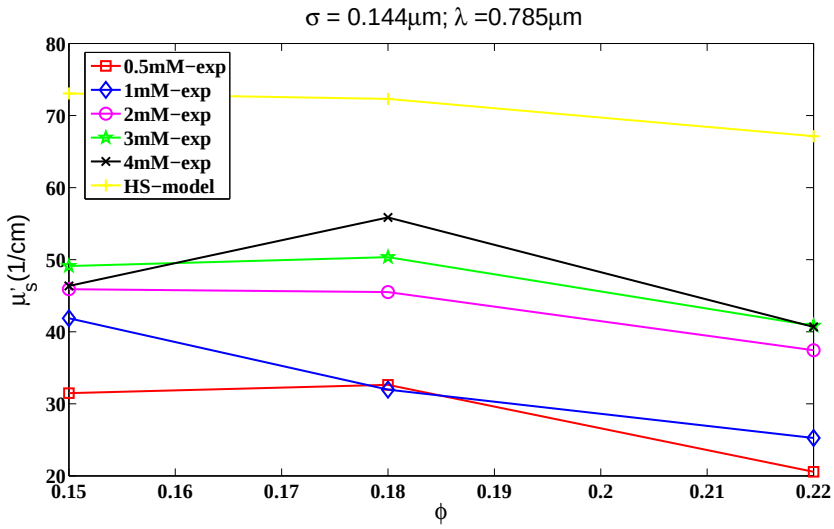

(c) $\lambda = 785nm$

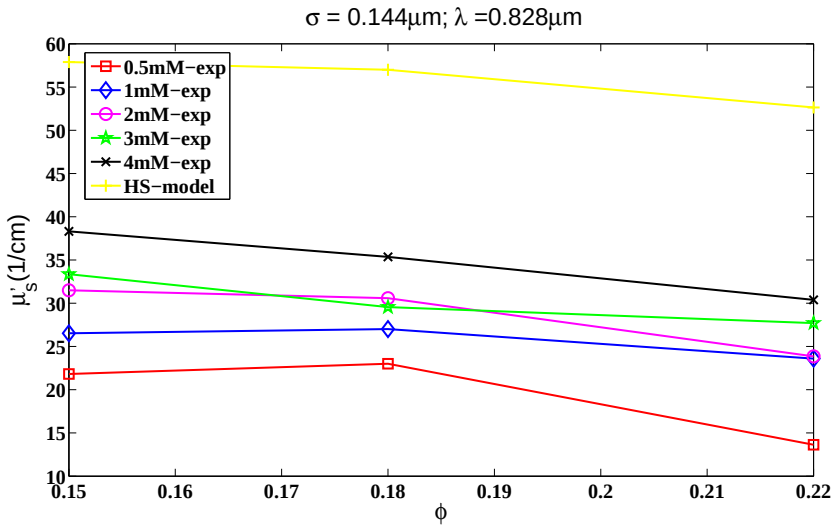

(d) $\lambda = 828nm$

Fig. 46.: Continued.

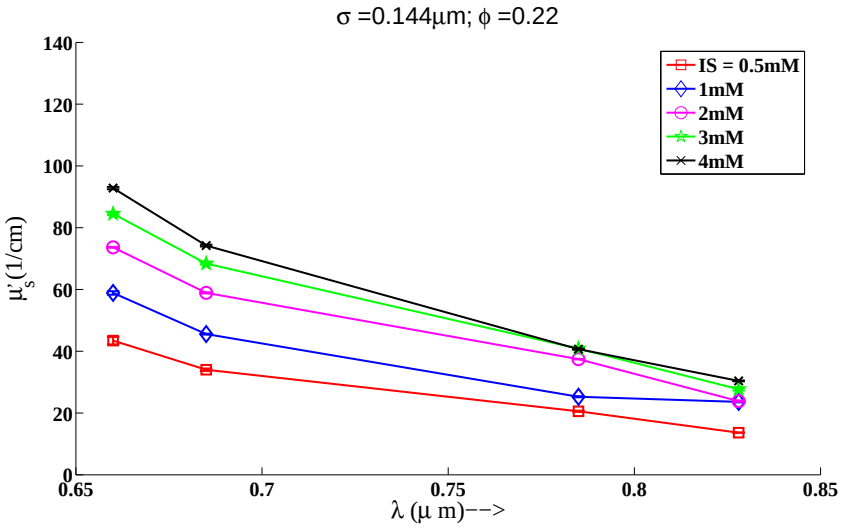

(a) $\phi = 0.22$

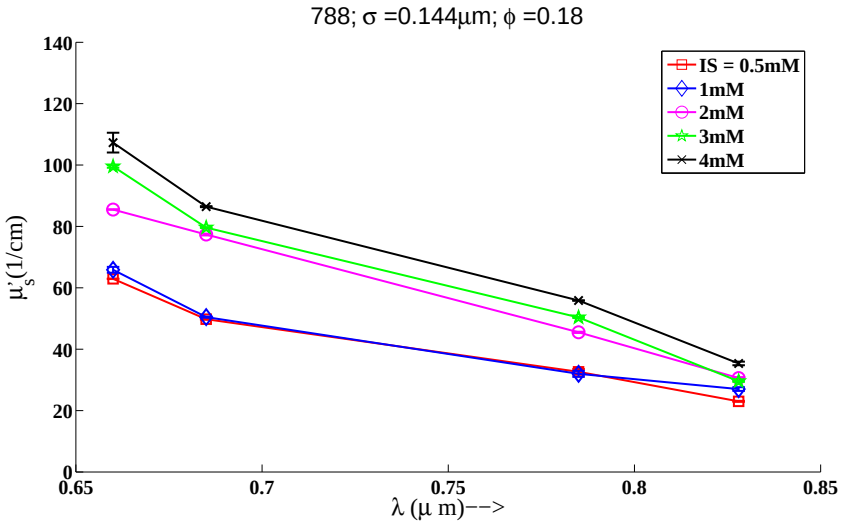

(b) $\phi = 0.18$

Fig. 47.: Isotropic scattering coefficient measurement versus wavelength of polystyrene latex, of diameter $\sigma = 144$nm, for ionic strengths of 0.5,1,2,3 and 4mM at (a)$\phi = 0.22$, (b)$\phi = 0.18$ (c) $\phi = 0.15$.

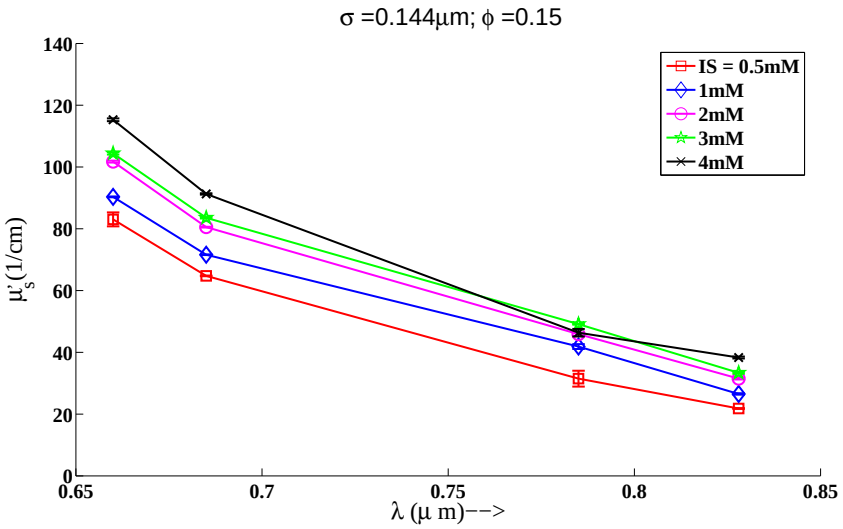

(c) $\phi = 0.15$

Fig. 47.: Continued.

Figure (48) plots the isotropic scattering coefficient versus the ionic strength for four different wavelengths of 660, 685, 785 and 828 nm. The particle diameter is 223nm. The volume fractions considered are $\phi = 0.22$ (red squares), $\phi = 0.18$ (blue diamonds) and $\phi = 0.15$ (green circles).

The dispersion ionic strength was varied and the values of ionic strength considered were 0.5mM, 1mM, 2mM, 3mM and 4mM. The preparation of the dispersions is described in Chapter V.

From the experimental data, we can observe that at the lower wavelengths of 660 and 685nm the isotropic scattering data decreases with increasing ionic strength of the dispersions. There is an onset of change in the trends as the wavelengths shift to 785 and 828nm.

Moreover as introduced earlier, the isotropic scattering coefficients for the larger volume fraction are higher than those observed at the lower volume fractions. This implies a reversal of trends in the observed isotropic scattering coefficients due to hindered scattering. This observation provides an insight into the window of the structure factor being investigated to model the isotropic scattering coefficient data, and implies that the first peak of the structure factor and beyond is being investigated.

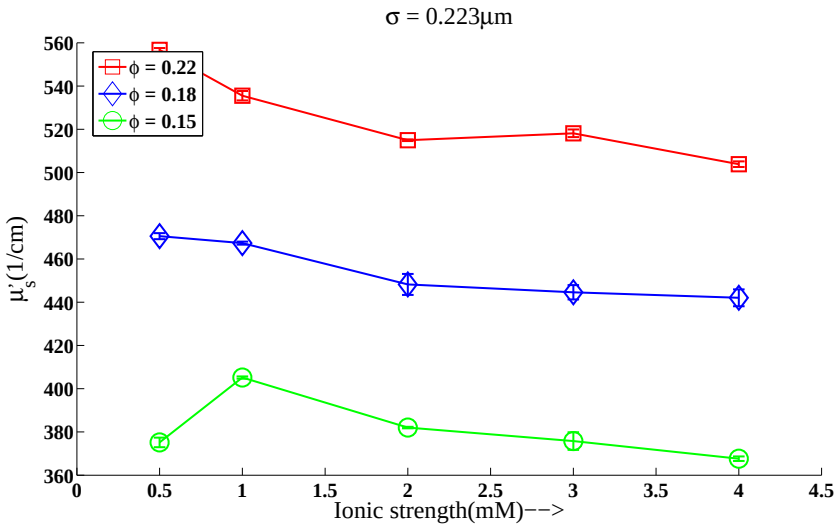

(a) $\lambda = 660nm$

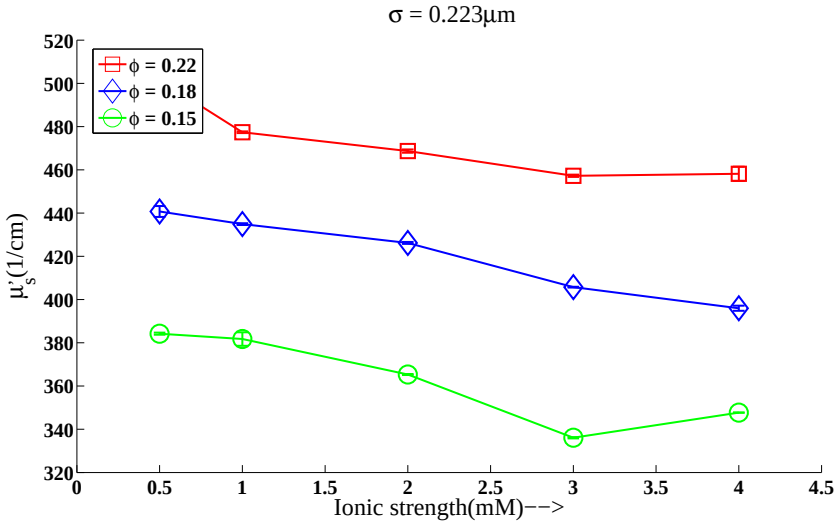

(b) $\lambda = 685nm$

Fig. 48.: Isotropic scattering coefficient measurements versus ionic strength of polystyrene latex for $\sigma = 223nm$, at volume fractions of $\phi = 0.22, 0.18$, and 0.15 and ionic strengths of 0.5,1,2,3 and 4mM at (a)$\lambda = 660$, (b)$\lambda = 685$, (c)$\lambda = 785$ and (d)$\lambda = 828$nm.

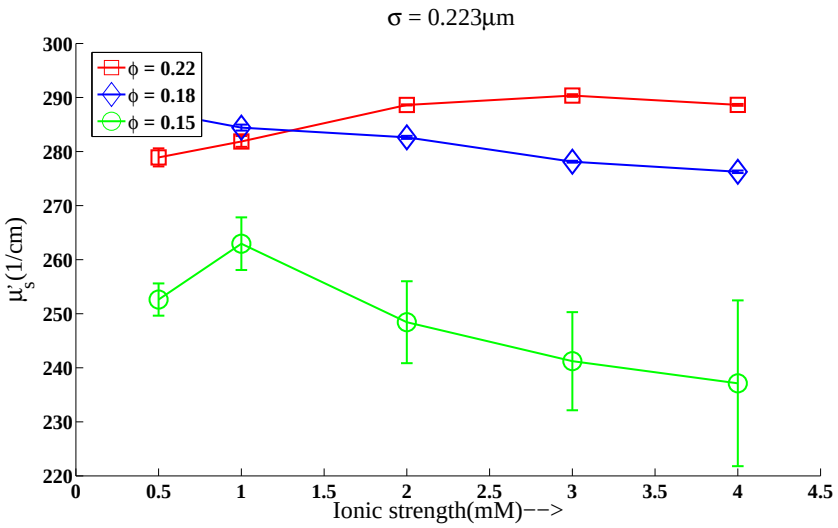

(c) $\lambda = 785nm$

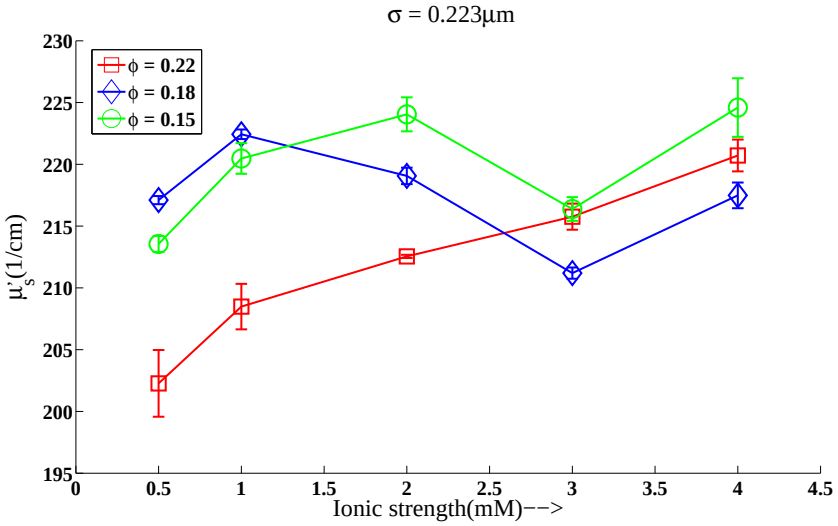

(d) $\lambda = 828nm$

Fig. 48.: Continued.

Figure (49) plots the isotropic scattering coefficient versus the ionic strength of the dispersion for volume fraction of $\phi = 0.22$. The red squares connected with lines are experimental data, whereas the points connected with solid lines are predictions from the models. The exact hard sphere result for the same volume fraction and particle size is also plotted as black cross connected by lines. The charge values used in the models are effective charge values, which are estimates of effective charge obtained using the technique of charge renormalization described in Chapter V. The effective charge values used are estimates obtained from an expected range of effective charge values on the particles. The effective charge values used are $Z_{eff} = 500, 1000,$ and 1500.

From the experimental results we can make an observation that the isotropic scattering coefficient decreases with increasing ionic strength for the lower wavelengths of 660nm and 685nm. At these wavelengths, the $Q\sigma$ values of the dimensionless wave vectors explored corresponds to 5.7230 and 5.5142, which are values around the peak region of the structure factors for this investigation. The reversal of trends occurs at higher wavelengths and the isotropic scattering coefficient increases with ionic strength. The offsets that occur between the predicted model data and the experimental data may be attributed to the incorrect values of refractive indices at these wavelengths, as they are not determined experimentally for the dispersions used. Also the larger particles tend to show a larger discrepancy with the model predicted data whilst the higher volume fractions tend to enhance this effect. Another reason for the discrepancy may be due to incorrect prediction of the structure from models as compared to the experimental investigation, or overprediction of changes in structure at the lower wavelengths.

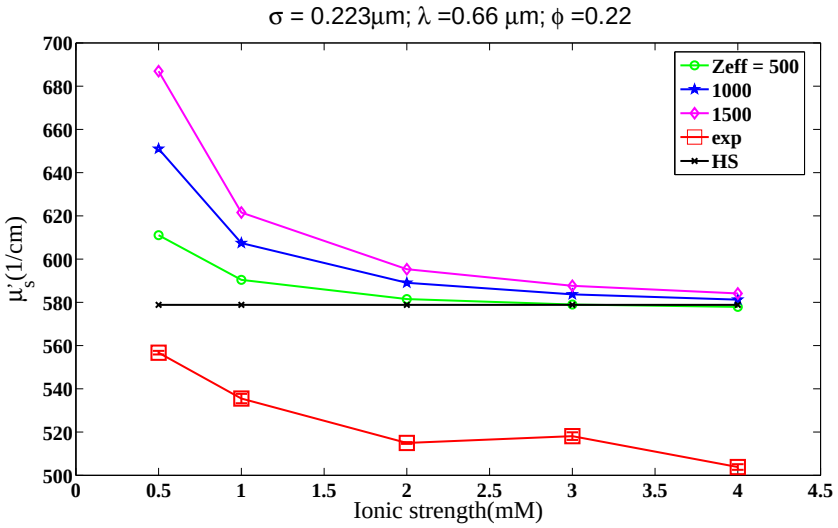

(a) $\lambda = 660nm$

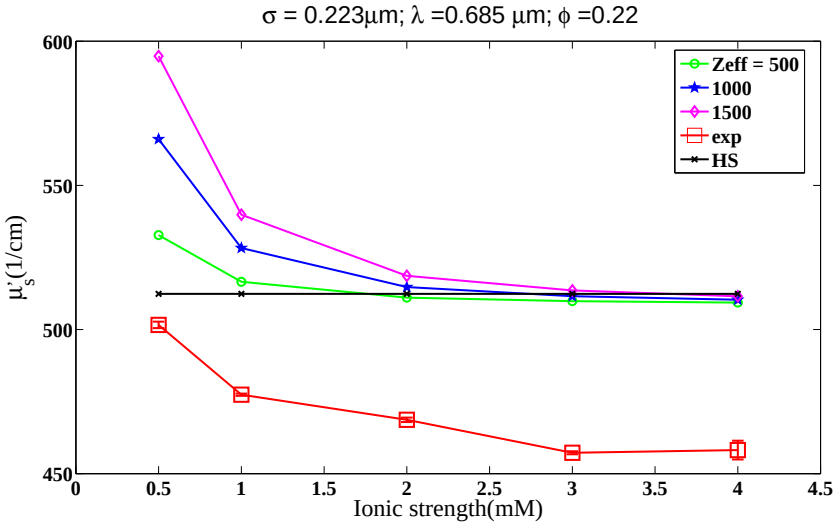

(b) $\lambda = 685nm$

Fig. 49.: Isotropic scattering coefficient measurements versus ionic strength of polystyrene latex. Open squares connected with solid lines are experimental measurements and points connected with solid lines are numerical solution of the OZ equation with Yukawa potential and HNC closure for $\sigma = 223nm$, at volume fraction of $\phi = 0.22$ and ionic strengths of 0.5,1,2,3 and 4mM at (a) $\lambda = 660$, (b) $\lambda = 685$, (c) $\lambda = 785$, and (d) $\lambda = 828$nm. The term HS refers to PYHS results and "exp" implies experimental results, and the effective charges used are $Z_{eff} = 500, 1000$ and 1500.

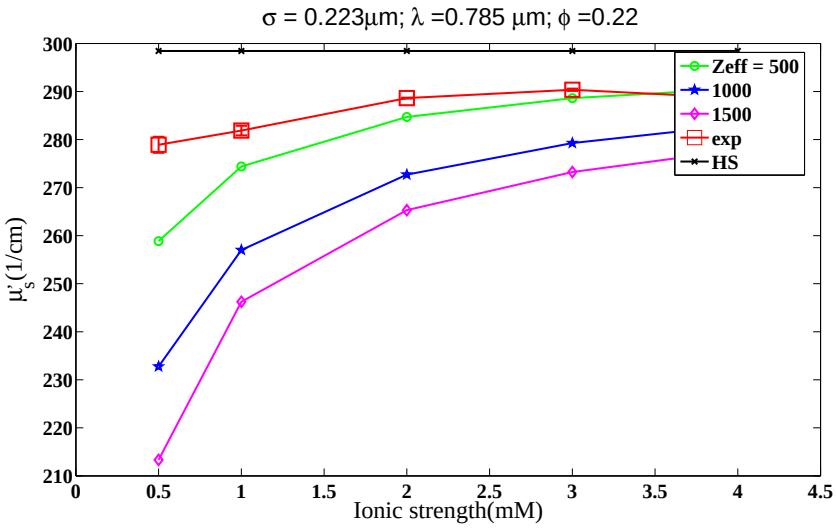

(c) $\lambda = 785nm$

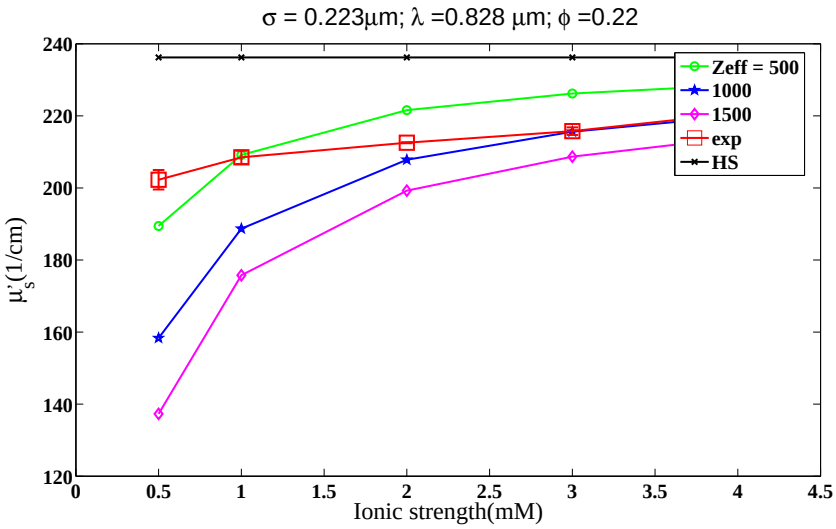

(d) $\lambda = 828nm$

Fig. 49.: Continued.

Comments on Refractive index:

Figure (50) plots the isotropic scattering coefficient versus the ionic strength of the dispersion for volume fraction of $\phi = 0.22$ and for refractive indices of 1.57, 1.58 and 1.59. The red squares connected by lines are experimental data, whereas the points connected by solid lines are predictions from the models. The exact hard sphere result for the same volume fraction and particle size is also plotted as black cross connected by line. The charge values used in the models are effective charge values, which are estimates of effective charge obtained using the technique of charge renormalization described in Chapter V. The effective charge values used are estimates obtained from an expected range of effective charge values on the particles. The effective charge values used are $Z_{eff} = 500, 1000$, and 1500.

As can be observed from Figures 50 (a), (b) and (c) the isotropic scattering coefficient is sensitive to the refractive index of the particles. The greater the volume fraction of the particles, the higher the impact of refractive index, as there are a greater number of particles within the dispersion medium. Also this effect is more prominent for a larger diameter particle, implying that the larger particle has a greater cross section area which the photons encounter and hence the refractive index plays a much more important role in determining the scattering of the photons.

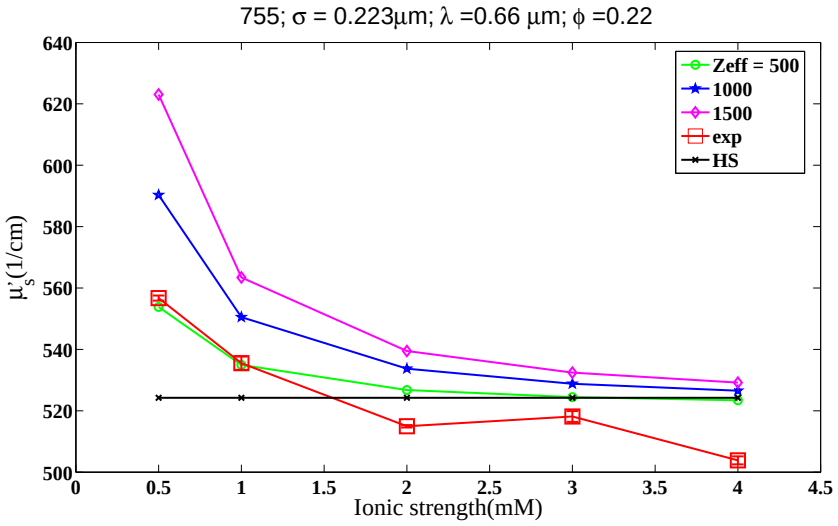

(a) $\lambda = 660nm$; $n_p = 1.57$

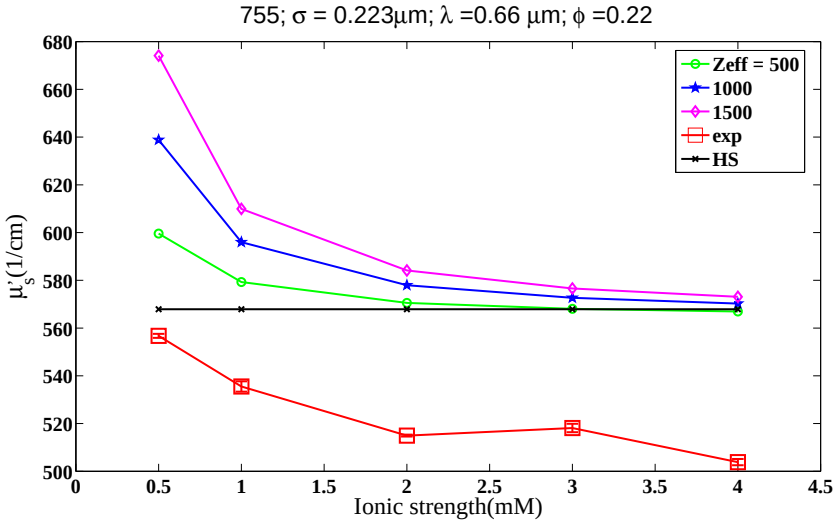

(b) $\lambda = 660nm$; $n_p = 1.58$

Fig. 50.: Isotropic scattering coefficient measurements versus ionic strength of polystyrene latex. Open squares connected with solid lines are experimental measurements and points connected with solid lines are numerical solution of the OZ equation with Yukawa potential and HNC closure for $\sigma = 223nm$, at volume fraction of $\phi = 0.22$ and ionic strengths of 0.5,1,2,3 and 4mM at (a) $\lambda = 660$; $n_p = 1.57$, (b) $\lambda = 660$; $n_p = 1.58$, (c) $\lambda = 660$;$n_p = 1.59$. The term HS refers to PYHS results and "exp" implies experimental results, and the effective charges used are $Z_{eff} = 500, 1000$ and 1500.

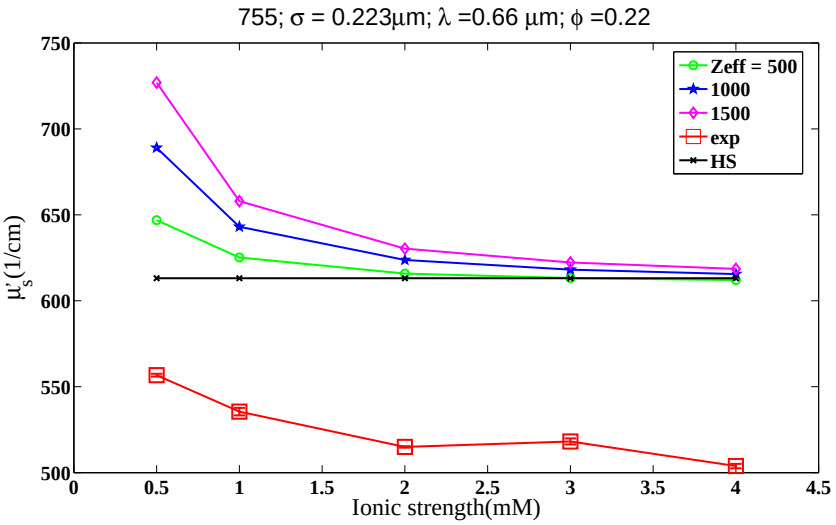

(c) $\lambda = 660nm$; $n_p = 1.59$

Fig. 50.: Continued.

Figure (51) plots the isotropic scattering data versus the ionic strength for varying volume fractions and ionic strengths at a volume fraction of $\phi = 0.18$. The red squares connected by lines are experimental data, whereas the points connected by solid lines are predictions from the models. The exact hard sphere result for the same volume fraction and particle size is also plotted as black cross connected by line against the results for changing ionic strength. The charge values used in the models are effective charge values, which are estimates of effective charge($Z_{eff} = 500, 1000$, and 1500) obtained using the technique of charge renormalization described in Chapter V.

While the isotropic scattering coefficient decreases with the ionic strength in the dispersion for the lower wavelengths, and are in conformity with the model predictions, the higher wavelength measurements do not follow the trend predicted by the solution of OZ equations with HNC closure and HSY potential model predictions. Data at the wavelength 785 nm shows a decreasing trend of isotropic scattering with increasing ionic strength. At wavelength of 828 nm the data shows a transition in trends of isotropic scattering coefficient versus ionic strength, from increasing to decreasing (no definitive trend), and cannot be accounted by model predictions. The possible reasons may be a changing effective charge for the ionic strengths investigated. Another reason could be the investigation of the structure factor peak by the higher wavelengths, which leads to a transition in the isotropic scattering coefficient data.

At the lower wavelengths of 660 and 685 nm, the offsets in the scattering coefficient predictions attributed to incorrect determination of the refractive indices for these wavelengths and incorrect structure predictions by the forward models. At the higher wavelengths, the experimental data decrease in comparison to what was obtained from model predictions. This implies that the structures are retained or the 785 nm wavelength can provide wave vector points close to the first peak of S(Q).

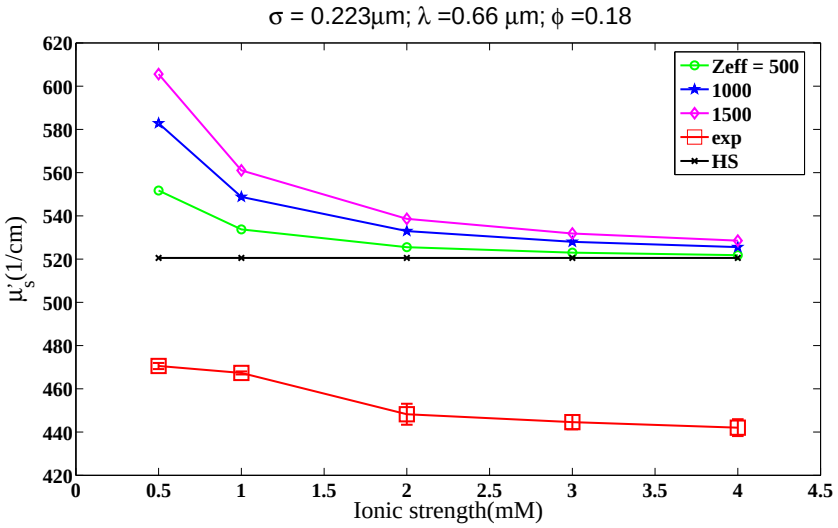

(a) $\lambda = 660nm$

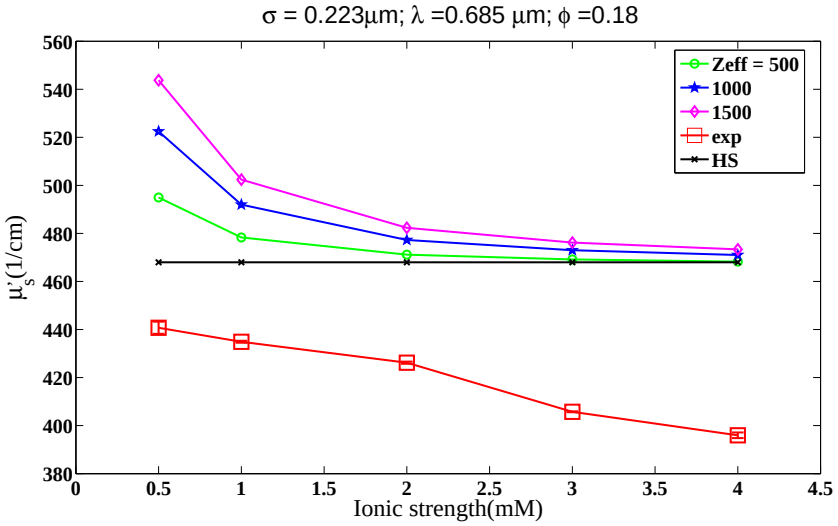

(b) $\lambda = 685nm$

Fig. 51.: Isotropic scattering coefficient measurements versus ionic strength of polystyrene latex. Open squares connected with solid lines are experimental measurements and points connected with solid lines are numerical solution of the OZ equation with Yukawa potential and HNC closure for $\sigma = 223nm$, at volume fraction of $\phi = 0.18$ and ionic strengths of 0.5,1,2,3 and 4mM at (a) $\lambda = 660$, (b) $\lambda = 685$, (c) $\lambda = 785$, and (d) $\lambda = 828$nm. The term HS refers to PYHS results and "exp" implies experimental results, and the effective charges used are $Z_{eff} = 500, 1000$ and 1500.

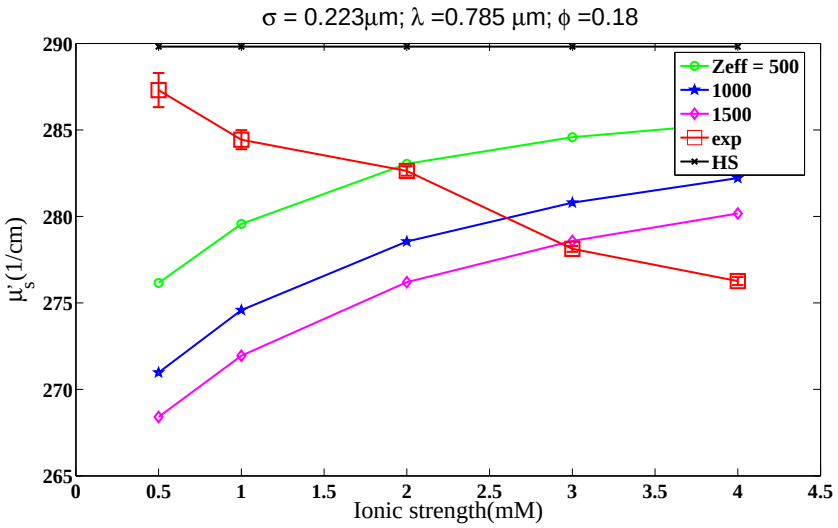

(c) $\lambda = 785nm$

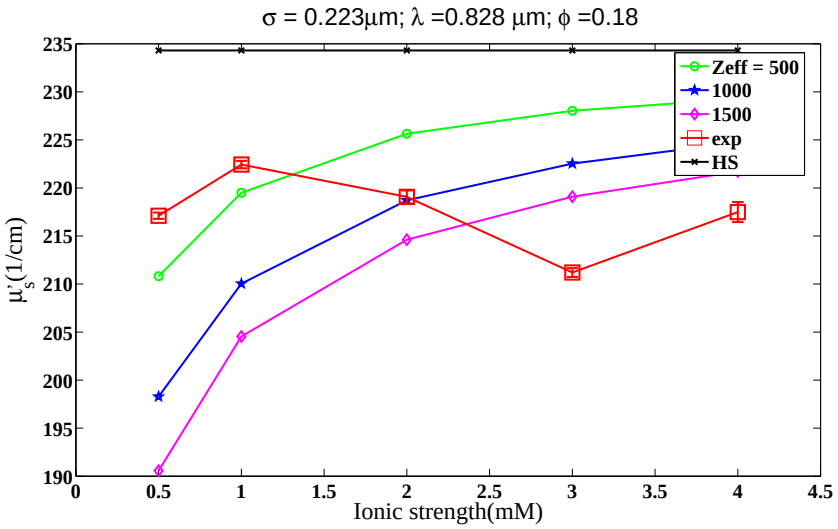

(d) $\lambda = 828nm$

Fig. 51.: Continued.

Figure (52) plots the isotropic scattering data versus the ionic strength for varying volume fractions and ionic strengths at a volume fraction of $\phi = 0.15$. The red squares connected with lines are experimental data, whereas the with points connected with solid lines are predictions from the models. The exact hard sphere result for the same volume fraction and particle size is also plotted as black cross connected with line versus the results for changing ionic strength. The charge values used in the models are effective charge values, which are estimates of effective charge obtained using the technique of charge renormalization described in Chapter V. The effective charge values used are estimates obtained from an expected range of effective charge values on the particles. The effective charge values used are $Z_{eff} = 500, 1000$, and 1500.

The arguments for these figures hold the same as for volume fraction $\phi = 0.18$. An observation can be made regarding the close similarity shared by the experimental data for wavelength 828nm for volume fractions of $\phi = 0.18$ and $\phi = 0.15$. Both the curves first increase until the ionic strength of 2mM is reached and then decrease at 3mM. While the change in the isotropic scattering coefficient is not large in either case for the increasing and decreasing trends, the possibility of structural changes cannot be ruled out at these volume fractions. An alternative approach would be to consider another larger sized particle with a higher particle charge value.

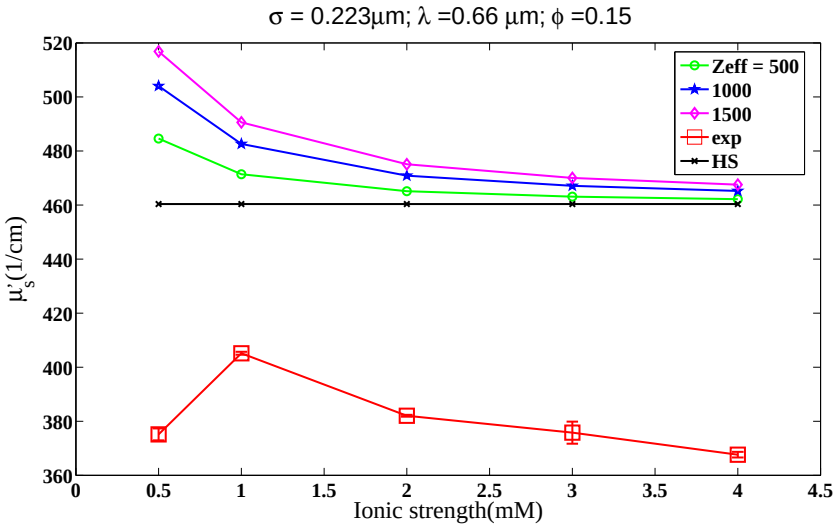

(a) $\lambda = 660nm$

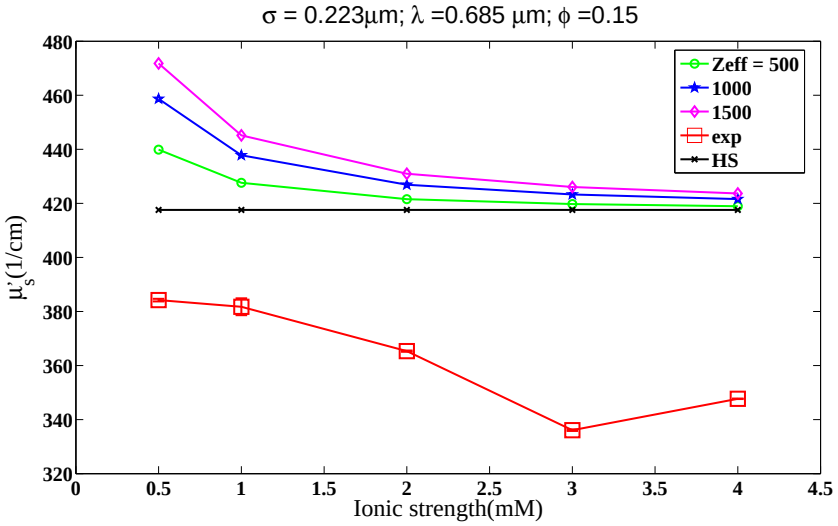

(b) $\lambda = 685nm$

Fig. 52.: Isotropic scattering coefficient measurements versus ionic strength of polystyrene latex. Open squares connected with solid lines are experimental measurements and points connected with solid lines are numerical solution of the OZ equation with Yukawa potential and HNC closure for $\sigma = 223nm$, at volume fraction of $\phi = 0.15$ and ionic strengths of 0.5,1,2,3 and 4mM at (a) $\lambda = 660$, (b) $\lambda = 685$, (c) $\lambda = 785$, and (d) $\lambda = 828$nm. The term HS refers to PYHS results and "exp" implies experimental results, and the effective charges used are $Z_{eff} = 500, 1000$ and 1500.

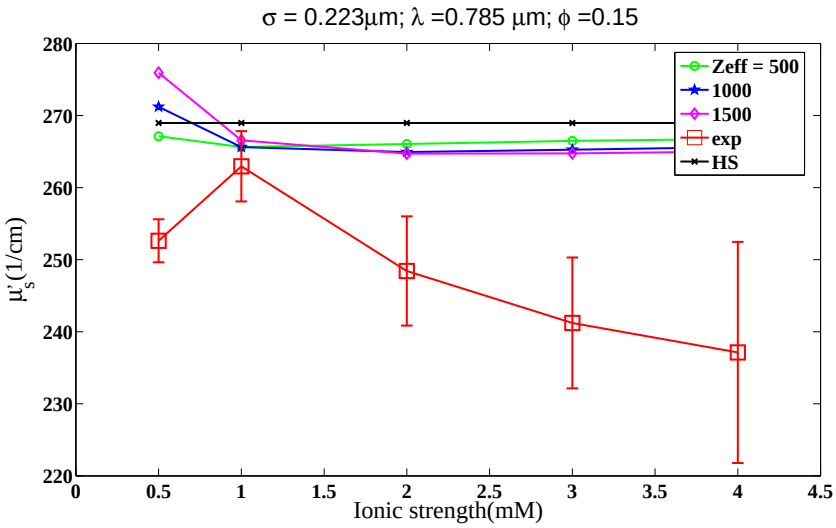

(c) $\lambda = 785nm$

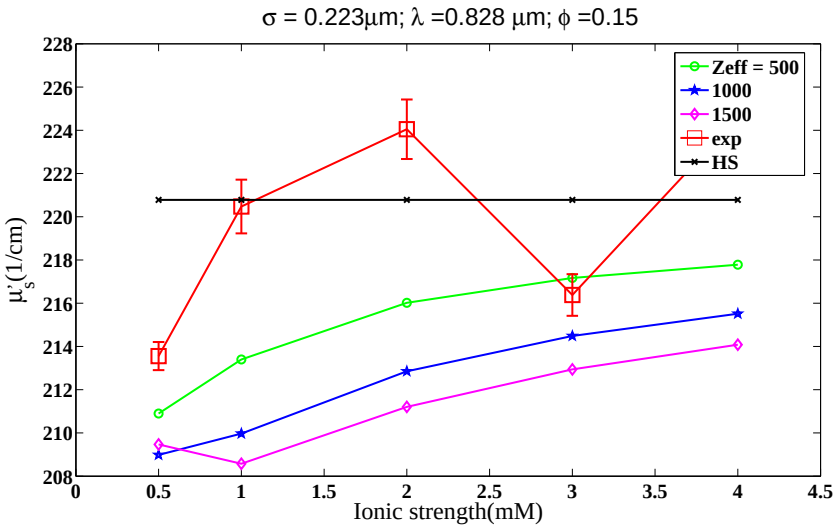

(d) $\lambda = 828nm$

Fig. 52.: Continued.

Figure (53) depicts the experimental data for changing isotropic scattering coefficient versus volume fraction. Results for PYHS predictions are presented alongside the experimental data.

Here the isotropic scattering coefficient values are reverse for the highest ionic strength in comparison to the hard sphere results, and leads us to understanding that the peak of the structure factor is shifting as the ionic strength is changed. This implies that the dispersions have not reached a hard sphere like state at the highest ionic strength of 4mM and transitions can be observed for the wavelength of 828nm.

Figure (54) depicts the experimental data of isotropic scattering coefficient for 223nm diameter latex as a function of wavelength at ionic strengths varying between 0.5-4mM. For the highest volume fraction $\phi = 0.22$ at the lower wavelengths of 660 and 685nm the isotropic scattering coefficient for the lowest ionic strength are higher than the isotropic scattering values for higher ionic strengths. As the wavelength is increased there is a reversal of dependency of the isotropic scattering coefficient upon ionic strength, and the isotropic scattering coefficients for the higher ionic strengths lie higher than the isotropic scattering coefficients at lower ionic strength. The reversal can be observed for $\phi = 0.22$ at $\lambda = 0.75\mu m$; for $\phi = 0.18$ at $\lambda = 0.8\mu m$ and for $\phi = 0.15$ at $\lambda > 0.8\mu m$.

The isotropic scattering coefficient data decreases with increasing wavelength as the ratio of particle size to the wavelength employed for investigation decreases, and hence the scattering changes from predominantly forward scattering to isotropic scattering.

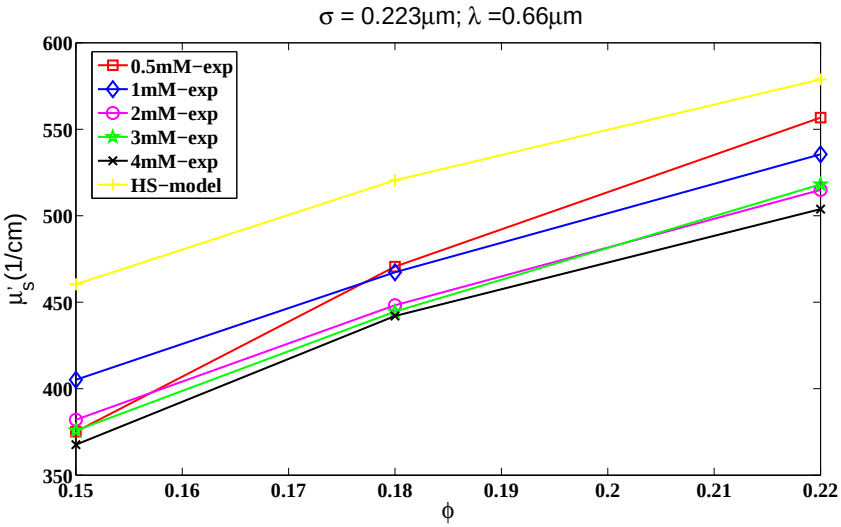

(a) $\lambda = 660nm$

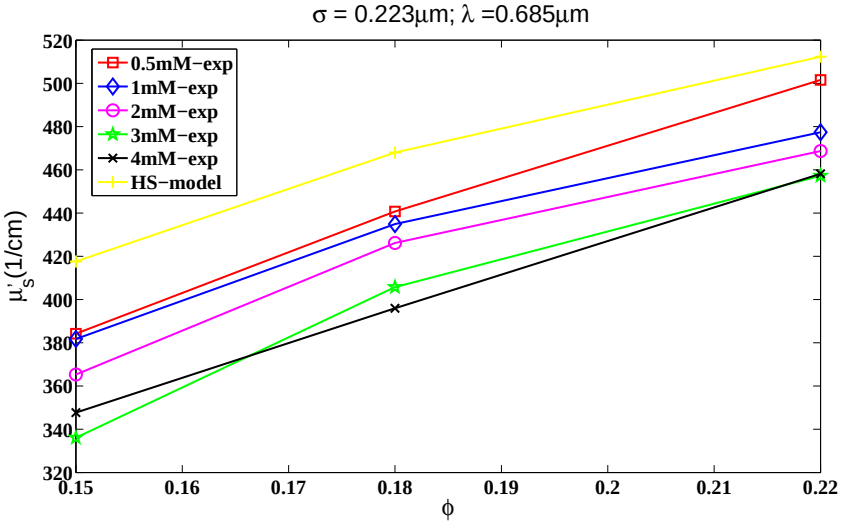

(b) $\lambda = 685nm$

Fig. 53.: Isotropic scattering coefficient measurements versus volume fraction of 223nm diameter polystyrene latex at ionic strengths of 0.5,1,2,3 and 4mM at (a) $\lambda = 660$, (b) $\lambda = 685$, (c) $\lambda = 785$, and (d) $\lambda = 828$nm. The term "HS" refers to the PYHS analytical solution.

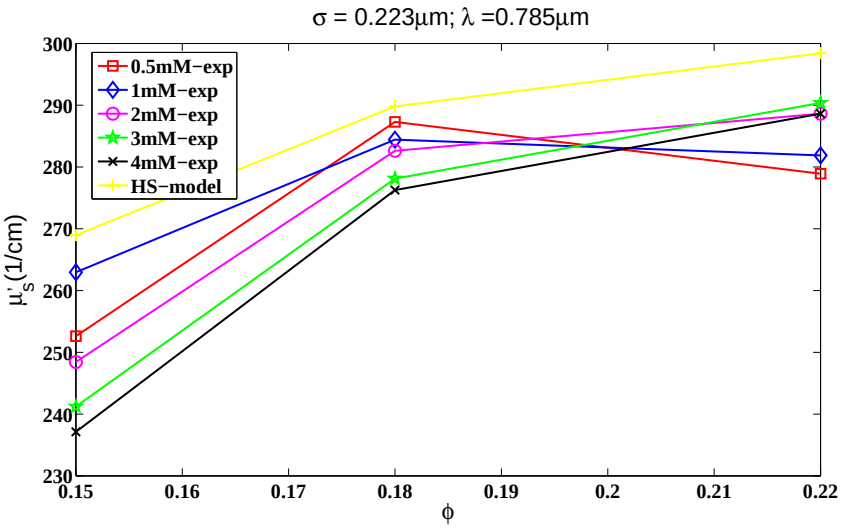

(c) $\lambda = 785nm$

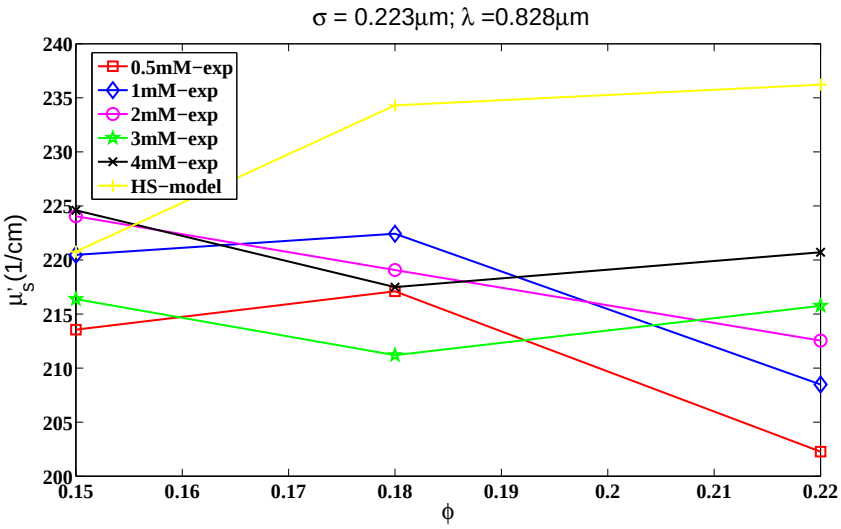

(d) $\lambda = 828nm$

Fig. 53.: Continued.

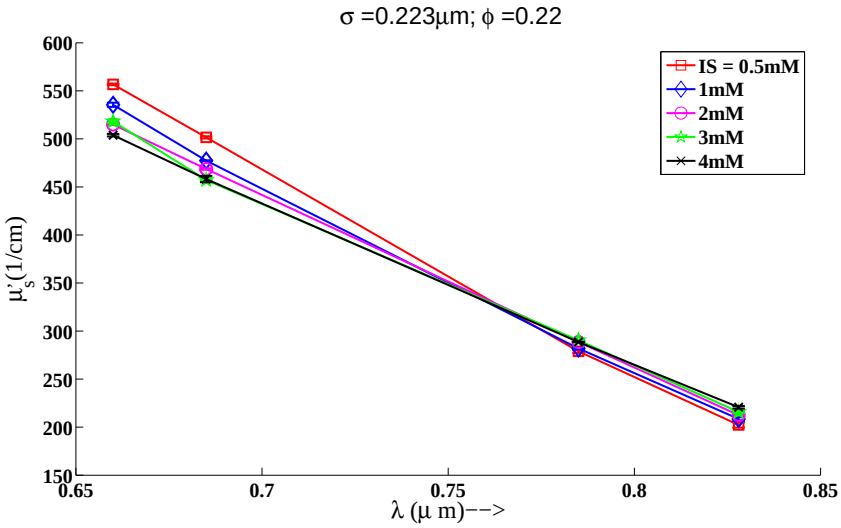

(a) $\phi = 0.22$

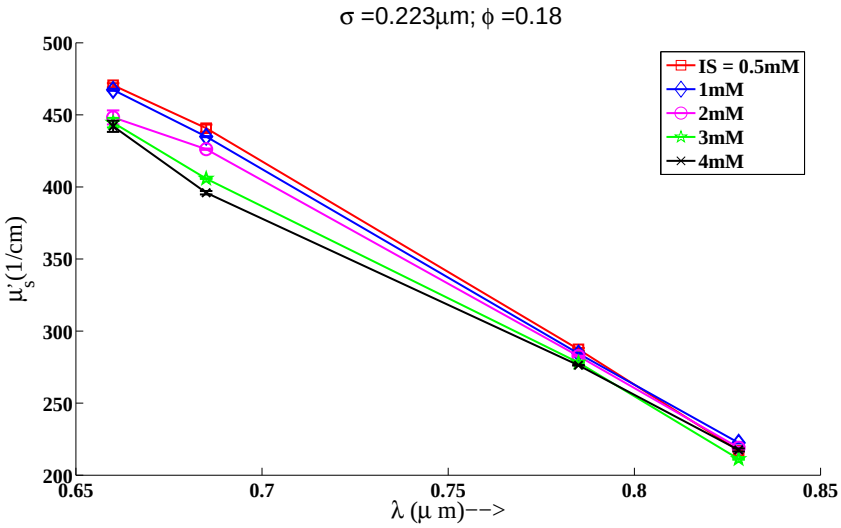

(b) $\phi = 0.18$

Fig. 54.: Isotropic scattering coefficient measurements versus wavelength of polystyrene latex, of diameter $\sigma = 223$nm, for ionic strengths of 0.5,1,2,3 and 4mM at (a)$\phi = 0.22$, (b)$\phi = 0.18$ and (c) $\phi = 0.15$.

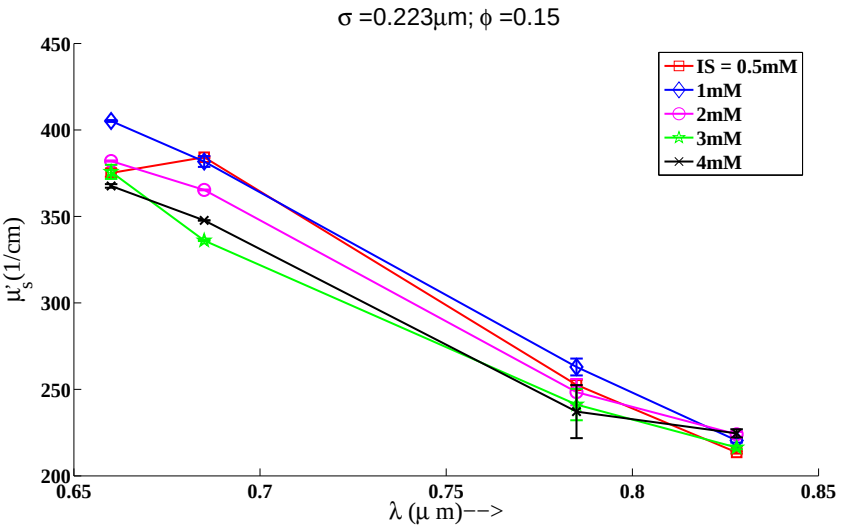

(c) $\phi = 0.15$

Fig. 54.: Continued.

D. Summary

The isotropic scattering coefficients obtained from FDPM measurements show sensitive changes to the change in ionic strength in the dispersions. The dependency of isotropic scattering coefficient upon ionic strengths are consistent with the model predictions for the smaller diameter particle and with the larger particle at the highest volume fraction. The reasons for offsets between the isotropic scattering coefficients measured and predicted may be those of incorrect determination of refractive indices at the lower wavelengths and incorrect predictions of structure by the forward models.

From the experimental data it is possible to obtain an estimate of the effective charge of the particles in the dispersions, and the results can be used as an aid to develop inversion techniques to determine charge and size values of the particles from highly concentrated dispersions. Data inversion methods have not been explained in this chapter, but the basic underlying models have been provided in detail which can form the basis for development of inversion techniques to obtain effective charge values and size values from experimental data.

CHAPTER VIII

BIDISPERSE CHARGED DISPERSIONS

A. Introduction

Colloidal particles exhibit variation in size, charge, and shape. Since the properties of dispersions depend upon polydispersity in size, charge, and shape, determining the influence of polydispersity on properties is important to enable rationale design of colloidal products. As a step towards understanding the relationship between polydispersity and bulk properties, models for static multiple light scattering have been developed using numerical methods and Monte Carlo simulations. Bidisperse colloidal mixtures have been studied in the past using various scattering techniques such as X-Ray and neutron scattering. With SAXS and SANS, it is possible to obtain the partial structure factors for a mixture of particles. The experiments of SAXS and SANS have led to particle configurations based upon the number ratio of two different sizes of particles in the dispersions, which can help understand the phase behavior and stability of the colloidal dispersions. Herein, we expand scattering experiments of bidisperse dispersions to visible light using techniques of FDPM.

B. Theory and background

The study of binary mixtures is of great importance in understanding the phase behavior of dispersions. Gilchrist *et al.* [141] have recently studied the phase behavior of mixtures of silica microspheres and polystyrene nanoparticles by the use of confocal laser scanning microscopy. The ratio of the number of smaller particles to the larger particles determines the phase behavior of the mixtures, and a fluid gel fluid transition was observed upon increasing the number ratio of smaller particles to larger particles.

The interactions are comprised of repulsion between particles of the same kind and attraction between particles of different materials. The attractive force between the particles leads to nanoparticle links being formed between the microspheres causing gelation with increasing number concentration. Finally, decorating the surface of the microspheres completely with nanoparticles gives rise to a strongly repulsive system of microparticles, which restores fluidity to the system.

Ottewill *et al.* [142] have studied binary mixtures of polystyrene particles with small angle neutron scattering measurements and determined the partial structure factors (a) at low concentrations of the particles to avoid multiple scattering and (b) at low ionic strengths in order to create predominant repulsive forces. In Ottewill's experimental study, the larger particles were found to retain their structure while the smaller particles formed clusters around the larger particles, providing possible clues for explaining phase separations in mixtures. Comparisons were drawn between single interacting components with Rescaled Mean Spherical Approximation(RMSA) theory.

Lutterbach *et al.* [143], [144] performed SAXS and SANS on a mixture of polystyrene (PS) particles and perflourinated (PFA) particles. The volume fraction was kept at 9% and the partial structure factors obtained from experiment were compared with OZ solution from HNC closure using a Newton-Raphson-Zeraph algorithm. The comparisons were made first for mixtures and provide good understanding of the structure of the dispersions. The PS particles in the mixture scattered relatively less in comparison to the PFA particles and the partial structure factors for the PFA particles could be obtained easily from SAXS measurements. The effective charges on the colloidal particles were then determined from the HNC models of the structure factors by fitting those obtained from experiment. The effective charges were also determined independently from the Poisson Boltzmann cell theory described earlier in chapter

VII. The determination of the effective charges from experimental measurement was considered as accurate and used for all calculations. The PFA partial structure factors were obtained from SAXS and the partial structure factors for the PS particles were obtained from SANS measurements for effective charge calculations.

Kaplan *et al.* [145] used diffusing wave spectroscopy measurements in dense binary suspensions of polystyrene and have probed the hydrodynamic coupling between unlike spheres. The partial static structure factors were determined for asymmetric hard sphere mixtures using PY theory and compared with experimental results. For the case of dynamic studies, hydrodynamic interactions led to a decrease in the effective diffusion coefficient, and the hydrodynamic coupling between dissimilar particles was found to be necessary to explain the effective diffusion coefficient data. The predictions for the isotropic mean free path of scattering using the PYHS analytical solution, were found to be in good agreement with the experimental data.

The partial static structure factor models used to describe charged dispersions are those obtained from the numerical solution of the OZ equations using HNC, Rogers Young (RY) or PY closure models. Analytical solutions are found for mixtures using the MSA closure to the OZ equations. The analytical solutions for mixtures were first developed by Blum and Hoye [146] in a continuation of their work on multiple Yukawa terms as closures. [147], [148] The solutions for mixtures were then extended by Ginoza [149], [150], [151], [152] such that the closure expressions could be factorized. The most recent analytical model has been made available by Vazquez *et al.* [153]. Ginoza's solution has been used to make comparisons for partial structure factors with MC results and SANS measurements by Ottewill, and by Petris *et al.* [154]. Arrieta *et al.* [155] have obtained a numerical solution of the OZ equation for the binary Yukawa potential using the MSA closure. Hoheisel *et al.* [113] presented comparisons with MC simulations of binary MSA analytical solutions and found good

comparison with the predictions from simulations.

Krause *et al.* [156] studied binary mixtures of polystyrene particles using static light scattering methods and compared the structure factors obtained from measurement, with the results from Integral Equation theories. They found that among the RMSA, HNC and RY closure models, the RY model was found to be most satisfactory to match experimental data. The structure factors obtained from measurement are however averaged structure factors over the concentration of the particles and the correlations among the particles under study.

In another study Klein *et al.* [157] obtained the structure factors from molecular dynamics simulations and compared them with those from the predictions using RY and HNC closure models. They used Zerah's [158] conjugate gradient approach to solve the set of equations for multicomponent mixtures of particles.

Bidisperse mixtures are a special case where polydispersity [159–161] is exhibited in the form of size, charge, shape, and interaction. The effects of size [162–167] and charge polydispersity on structure have been studied by Aguanno *et al.* [168] They solved the polydisperse OZ equation for the RY, HNC, and PY closure models, using the procedure given by Ng. [169] Beurten *et al.* [170] developed a small-angle scattering intensity expression for polydisperse colloids. Wagner *et al.* [171] measured small angle neutron scattering and angular static light scattering on charge-screened colloids with varying electrostatic interactions caused by the addition of salt to the medium. They compared with the polydisperse structure factor for charged colloids obtained by solving numerically the OZ equation with the RY Closure and with the bidisperse Yukawa potential. In their studies they encountered problems with the convergence when the number of components was greater than 5 and for high volume fractions. Wagner *et al.* [171] fit the structure factor obtained from measurement with the numerical results from the solution of the OZ equation using the charge on

the particles and salt in the medium as adjustable parameters. Rheological measurements on the samples were also conducted, and multiple relaxation times in their measurements have shown that a mixture of liquid and glassy phases could exist in their concentrated samples of the dispersions.

Herein we present FDPM measurement of bidisperse charged colloidal dispersions as a function of ionic strength.

The scalar and vector MC methods are used to predict the structure factors for a bidisperse mixture as described in chapter IV. MC simulations provide particle configurations based upon input of size, charge, number density, ionic strength, and the ratio of small to large particles. In the scalar method, the number of particles are counted within a circular distance around a central particle and averaged over several particle configurations, whereas in the vector method, particle positions are Fourier transformed to directly obtain the partial structure factors.

The numerical solution of the OZ equations also provides an alternative route to derive the partial structure factors and in this study, HNC closures were used to obtain the numerical solution of the OZ equations using the binary Yukawa potential model. The methods are described in chapter IV.

The OZ MSA closure solutions provided by Ginoza, failed to converge for the volume fractions and ionic strengths used in this study. Henceforth only the Monte Carlo simulation results and numerical solutions for the OZ solution with HNC closure expressions will be used for predicting the isotropic scattering data obtained from measurement.

C. Potential model of interaction

The potential model of interaction in a mixture of two different sized particles of diameter σ_i, σ_j with charge values z_i and z_j can be written in the form of a binary Yukawa potential model

$$\begin{aligned} u_{ij}(r) &= \infty \quad if \quad r < \sigma_{ij} \\ u_{ij}(r) &= \frac{z_i z_j}{4\pi\epsilon_o\epsilon} \frac{e^{\kappa\frac{\sigma_i}{2}}}{(1+\kappa\frac{\sigma_i}{2})} \frac{e^{\kappa\frac{\sigma_j}{2}}}{(1+\kappa\frac{\sigma_j}{2})} \frac{e^{-\kappa r}}{r} \quad if \quad r \geq \sigma_{ij}. \end{aligned} \tag{8.1}$$

The potential energy determines how particles arrange themselves with respect to each other. Consequently the partial structure factors will be dependent upon the arrangement of these particles. The pairwise additivity condition $\sigma_{ij} = \frac{\sigma_i+\sigma_j}{2}$ is applied in using this potential form.

D. Isotropic scattering coefficient and binary static structure factors

The isotropic scattering coefficient for a binary mixture of particles can be written as

$$\mu_s^{'}(\lambda) = \frac{\pi}{(\frac{2\pi m}{\lambda})^2} \int_0^\pi (FS) sin\theta (1 - cos\theta) d\theta \tag{8.2}$$

where

$$FS = \rho_s F_s S_{ss} + \rho_l F_l S_{ll} + 2\sqrt{\rho_s \rho_l} F_{ls} S_{ls}.$$

Here F_l and F_s are the form factors for the large and small particles obtained from Mie scattering theory as $\mid f_i \mid^2$, where f_i is the scattering amplitude; F_{ls} is the form factor for the two different types of particles and is given as $Re(f_{1l} * f_{1s}^* + f_{2l} * f_{2s}^*)$ where the starred quantities are the complex conjugates of the Mie scattering amplitudes; S_{ll}, S_{ss}, and S_{ls} are the partial structure factors for the mixture of like and un-like particles and ρ_l, ρ_s are the number densities of large and small particles. [145]

The next section discusses the data obtained from measurements and compar-

isons with model predictions for four different wavelengths of 660, 685, 785 and 828nm. MC simulations are presented and the results from OZ equations with HNC closure and hard sphere Yukawa potential are used to make model comparisons with FDPM measurements.

E. Results and discussion

The numerical solution of the OZ equations agrees well with the Monte Carlo simulation results with truncation of potential at half the length of the simulation box. The bidisperse partial structure factors obtained from Monte Carlo simulations and the solution of the OZ equations match, and are used to predict the isotropic scattering coefficients using the forward models.

Figures 55, 56, and 57 plot the experimental data of isotropic scattering coefficient versus the ionic strength of the dispersion. Three different volume fractions were considered at four different wavelengths of 660, 685, 785 and 828nm. In Figure 55 the symbols A3B1 represent three parts of sample A and one part of sample B, where sample A is the smaller 144nm diameter particle and sample B is the higher 223nm diameter particle.

Similarly in Figure 56 the symbol AB represents equal parts of sample A and sample B, where sample A is the smaller 144nm diameter particle and sample B is the larger 223nm diameter particle. In Figure 57 the symbol A1B3 represents one part of sample A and 3 parts of sample B where A is the smaller 144nm diameter particle and sample B is the larger 223nm diameter diameter particle.

Figure 55 contains the experimental data for the A3B1 samples and clearly shows increasing isotropic scattering coefficient as the ionic strength increases. The results are consistent with loss of structure associated with the smaller and the larger particles

as repulsive forces diminish. The trends are clearly visible at the 785 and 828nm wavelengths as the lowest region of the structure factors is explored leading to correct interpretation of the data. At the wavelengths $660nm$ and $685nm$ the structure factor peaks are explored for the two particle sizes in this experiment, and hence the interpretations are convoluted due to increasing and decreasing trends for the two particle sizes.

The experimental data for the samples with equal number of large and small particles are provided in Figure 56. The experimental data are found to have a transition from decreasing isotropic scattering coefficient as ionic strength increased at wavelengths of 660 and 685nm, to increasing isotropic scattering coefficient as ionic strength increased at higher wavelengths of 785 and 828nm. This reversal of trend with wavelength maybe due to (i) an increasing number of larger sized particles; and (ii) the interrogation of the structure factor peak and beyond at low wavelengths for the larger sized particles.

The experimental data for the samples A1B3 are provided in Figure 57. The experimental data of scattering versus ionic strength are nonlinear in their trends and have no resemblance to the earlier experimental data of A3B1 and AB mixtures. The trends marginally change from a trend of decreasing isotropic scattering with increasing ionic strength to a trend of increasing isotropic scattering coefficient with increasing ionic strength as the wavelength is increased. The most important observation that can be made about this experimental data is the fact that at the two lower wavelengths of 660 and 685nm the trends in the data are similar providing verity to the experiment and suggesting the correctness of the experimental data, as the wavelengths used are nearly close and the error bars on the data points are not large. There is a continuous change in the trends as the wavelength of light used is changed and the change in the experimental data provides evidence of changing structure.

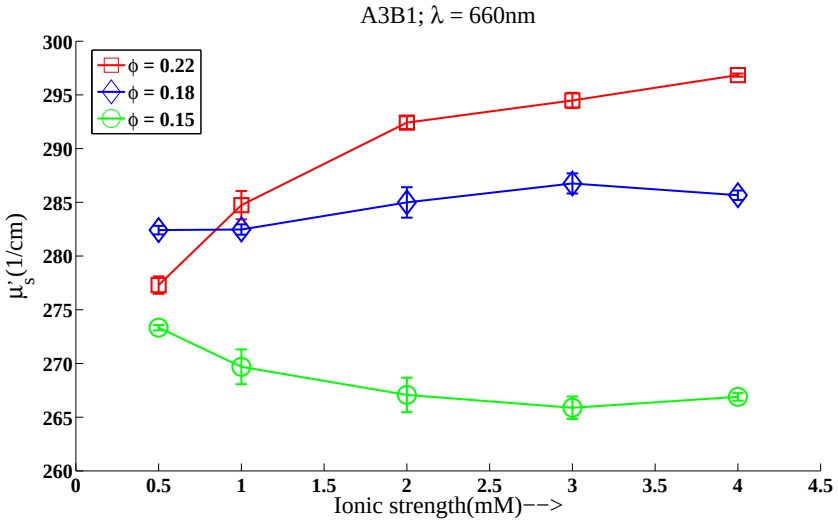

(a) $\lambda = 660$nm

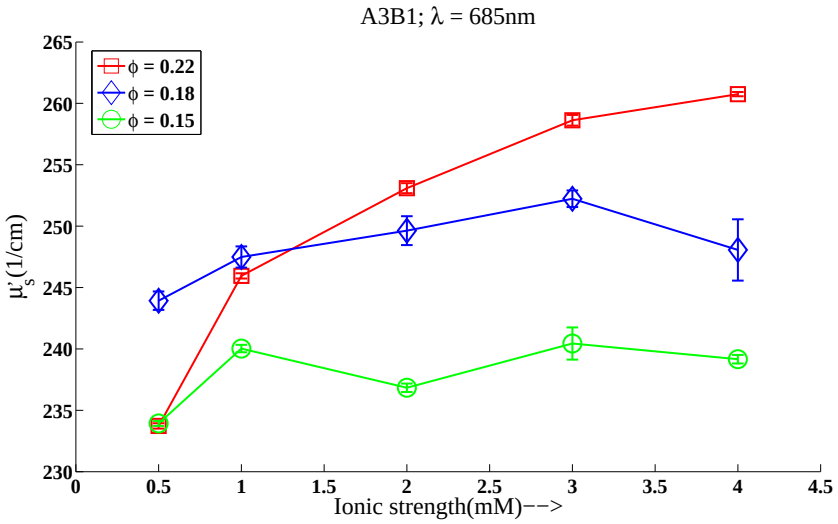

(b) $\lambda = 685$nm

Fig. 55.: Isotropic scattering coefficient measurements versus ionic strength of a mixture of polystyrene lattices, $\sigma_1 = 144nm$ and $\sigma_2 = 223nm$, at volume fractions of $\phi = 0.22, 0.18$ and 0.15 and ionic strengths of 0.5,1,2,3 and 4mM at (a)$\lambda = 660$,(b)$\lambda = 685$, (c)$\lambda = 785$ and (d)$\lambda = 828$nm. The mixture has a number density of smaller particles which is thrice that of the larger particles, i.e. $n_1 = 3n_2$.

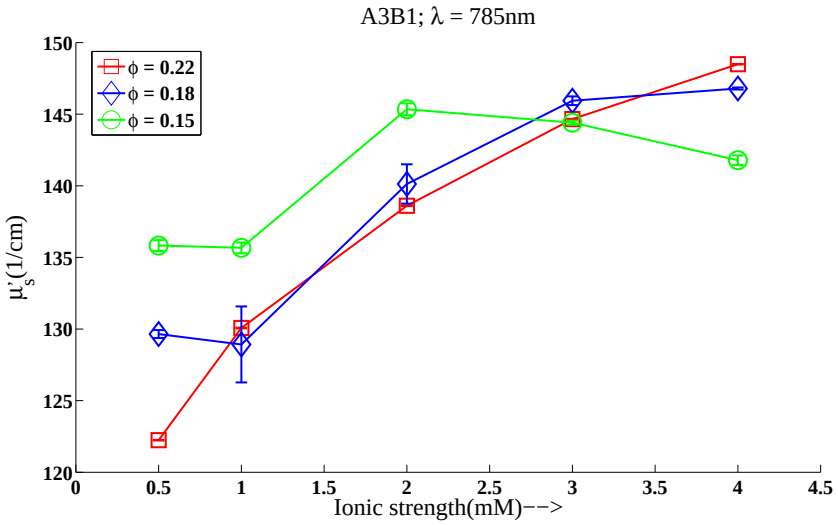

(c) $\lambda = 785$nm

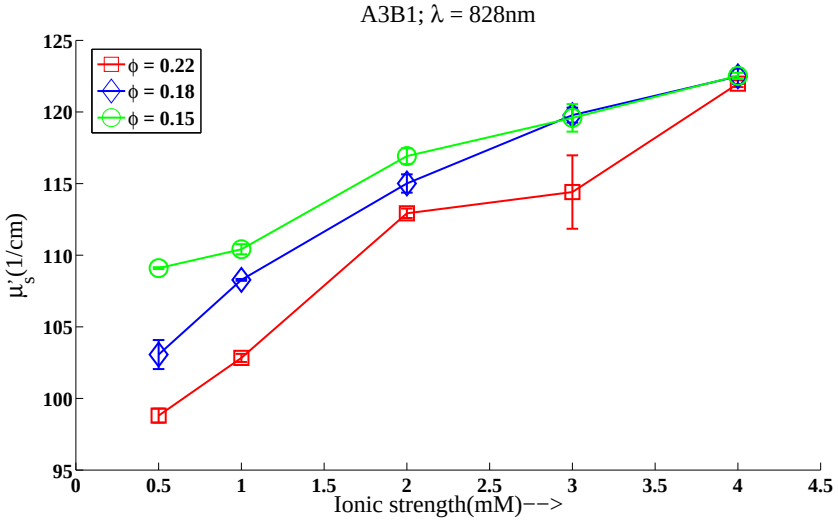

(d) $\lambda = 828$nm

Fig. 55.: Continued.

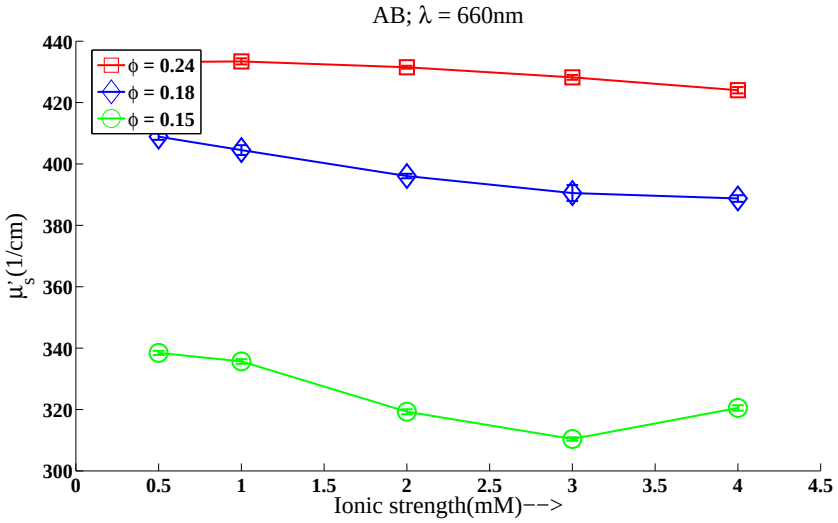

(a) $\lambda = 660$nm

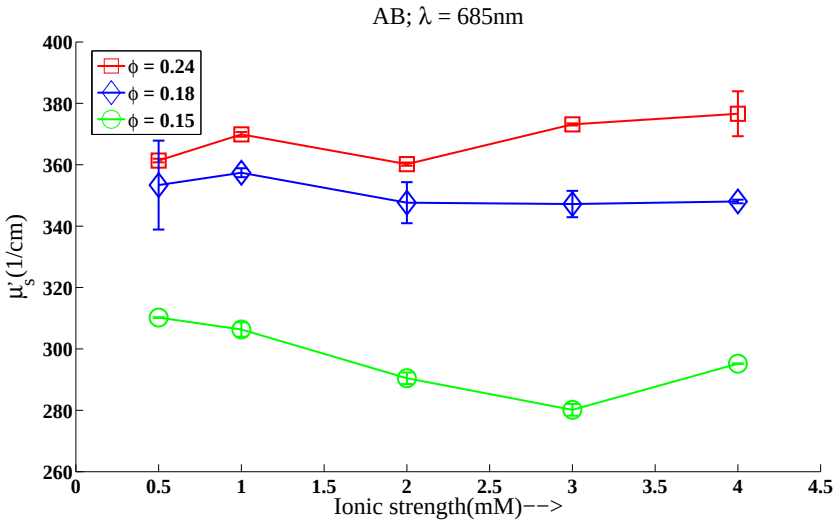

(b) $\lambda = 685$nm

Fig. 56.: Isotropic scattering coefficient measurements versus ionic strength of a mixture of polystyrene lattices, $\sigma_1 = 144nm$ and $\sigma_2 = 223nm$, at volume fractions of $\phi = 0.24, 0.19$ and 0.15 and ionic strengths of 0.5,1,2,3 and 4mM at (a)$\lambda = 660$,(b)$\lambda = 685$, (c)$\lambda = 785$ and (d)$\lambda = 828$nm. The mixture has a number density of smaller particles which is equal to that of the larger particles, i.e. $n_1 = n_2$.

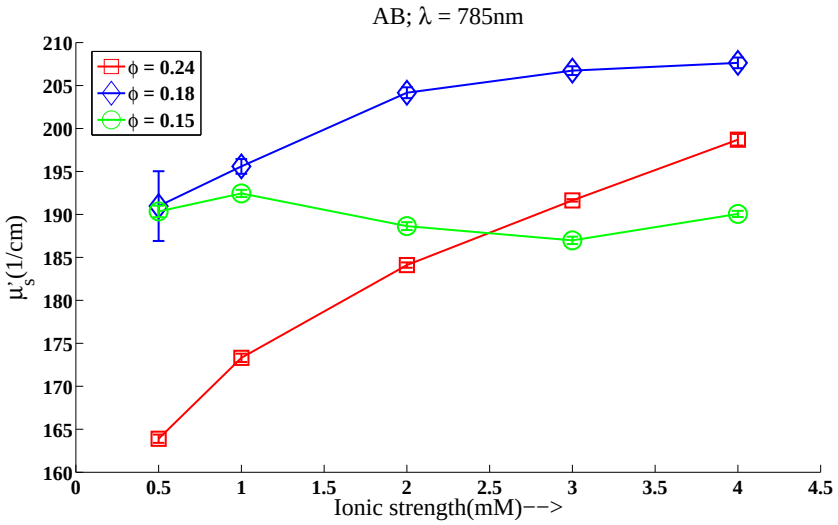

(c) $\lambda = 785$nm

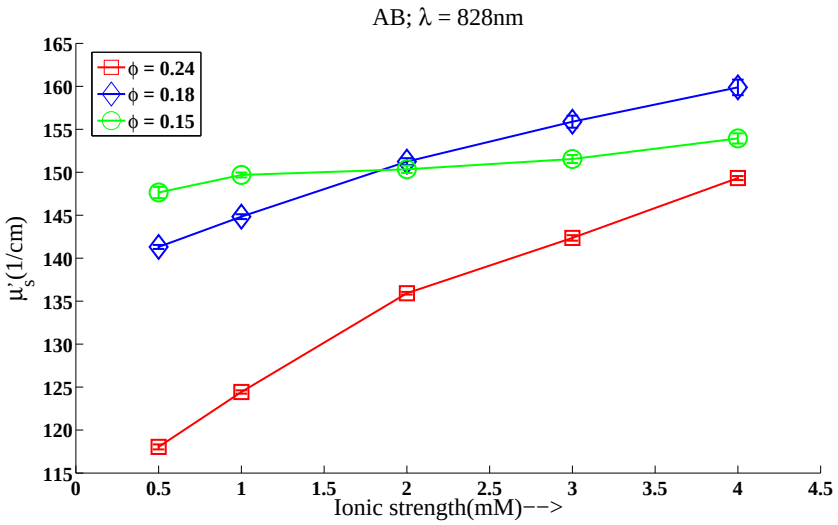

(d) $\lambda = 828$nm

Fig. 56.: Continued.

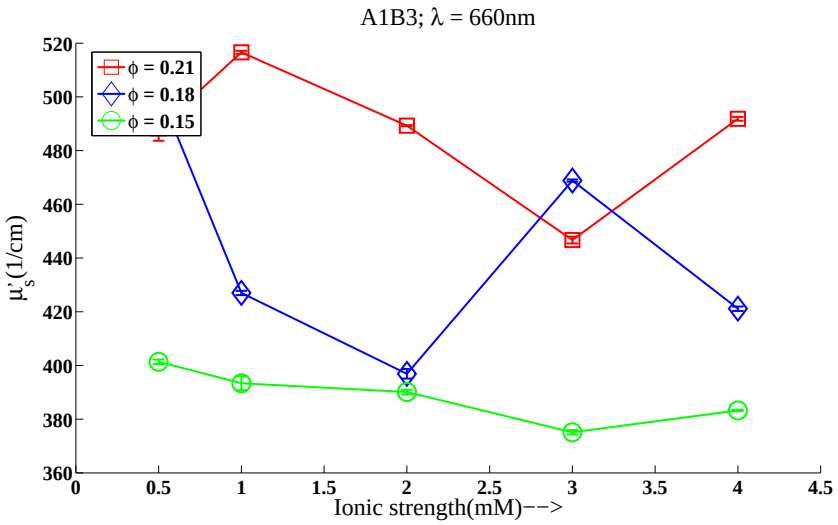

(a) $\lambda = 660$nm

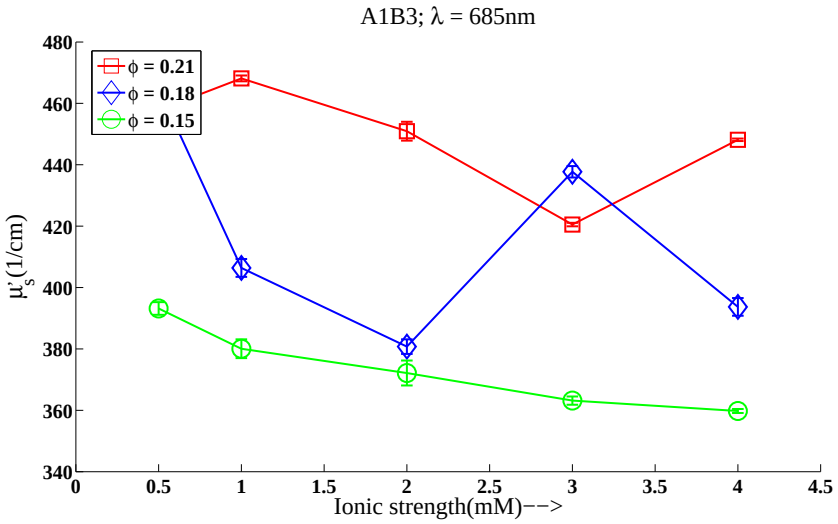

(b) $\lambda = 685$nm

Fig. 57.: Isotropic scattering coefficient measurements versus ionic strength of a mixture of polystyrene lattices, $\sigma_1 = 144nm$ and $\sigma_2 = 223nm$, at volume fractions of $\phi = 0.21, 0.18$ and 0.15 and ionic strengths of 0.5,1,2,3 and 4mM at (a)$\lambda = 660$,(b)$\lambda = 685$, (c)$\lambda = 785$ and (d)$\lambda = 828$nm. The mixture has a number density of smaller particles which is one third that of the larger particles, i.e. $3n_1 = n_2$.

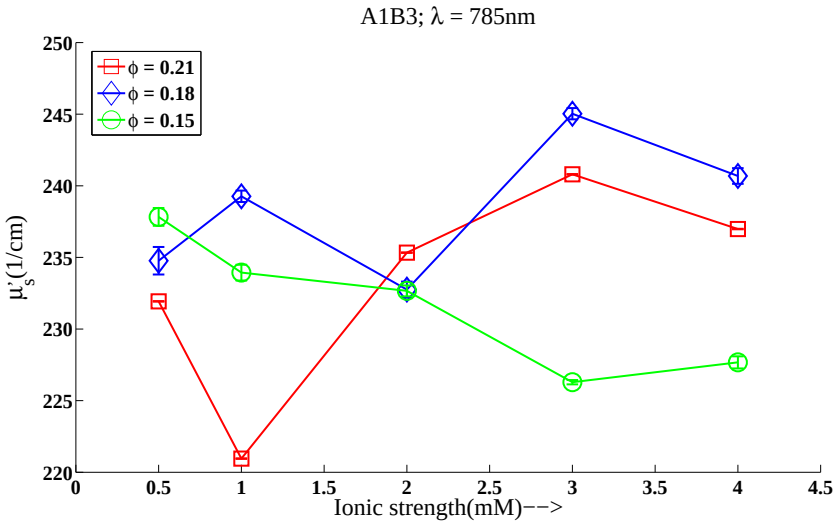

(c) $\lambda = 785$nm

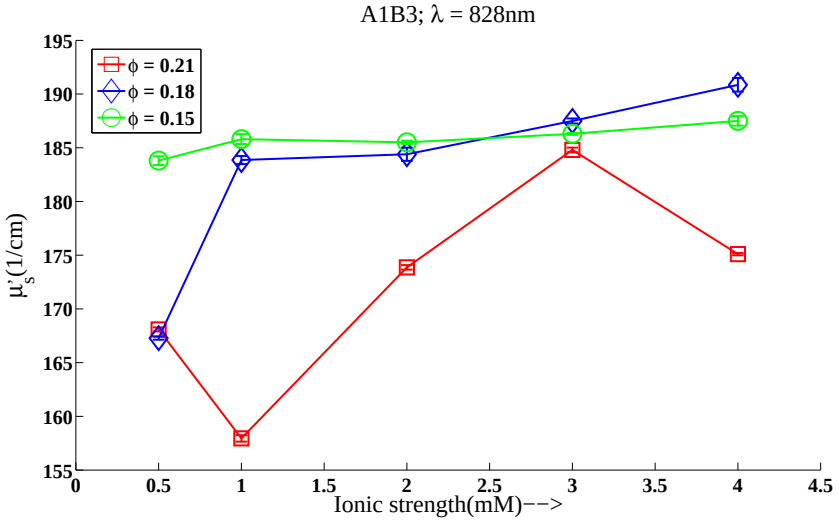

(d) $\lambda = 828$nm

Fig. 57.: Continued.

Figures 58, 59, and 60 provide the partial structure factors obtained from Monte Carlo simulations versus the non dimensional wave vector points, for 0.5mM NaCl equivalents, the lowest ionic strength investigated. The charge values on the particles were varied from 500 to 1500 and the volume fractions were taken to be highest value of $\phi = 0.22$. As shown in Figures 58 (a), 59 (a) and 60 (a) the structure factors obtained from both vector and scalar methods are comparable to each other.

Figures 58 (b), 59 (b) and 60 (b) provide comparisons of the analytical PYHS model for the same number ratio 0.25, along with structure factors obtained from Monte Carlo simulations of charged particles. The plots shows clear difference between the analytical structure factors for hard spheres and the structure factors obtained from Monte Carlo simulations for charged particles. From Figure 58 (b), the comparisons with analytical theory clearly show the smaller particles (S_{11}) shift from their positions much more strongly that the larger particles (S_{22}), upon being charged. The peak heights differ from the hard sphere structure factors, but the position of the peaks for the larger particles do not shift, indicating a lack of sensitivity in comparison to small particles.

The structure factors for the highest charge values were found to deviate from the expected pattern at the low $Q\sigma$ values, due possibly to polydispersity, strong repulsion among the particles, and the simulation method failing at the lower Q values. Investigation of the isotropic scattering coefficients using the structure factor result is performed by excluding the first few points in the low Q region and extrapolating the curve to the $Q = 0$ value.

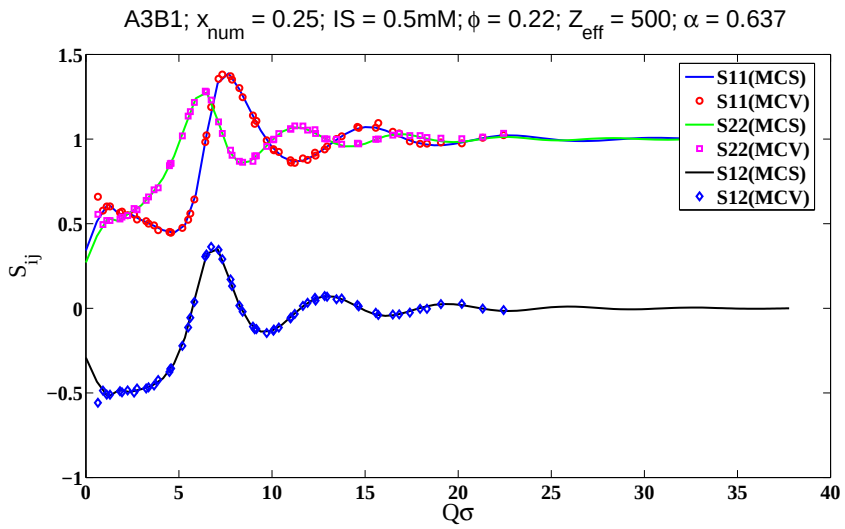

(a)

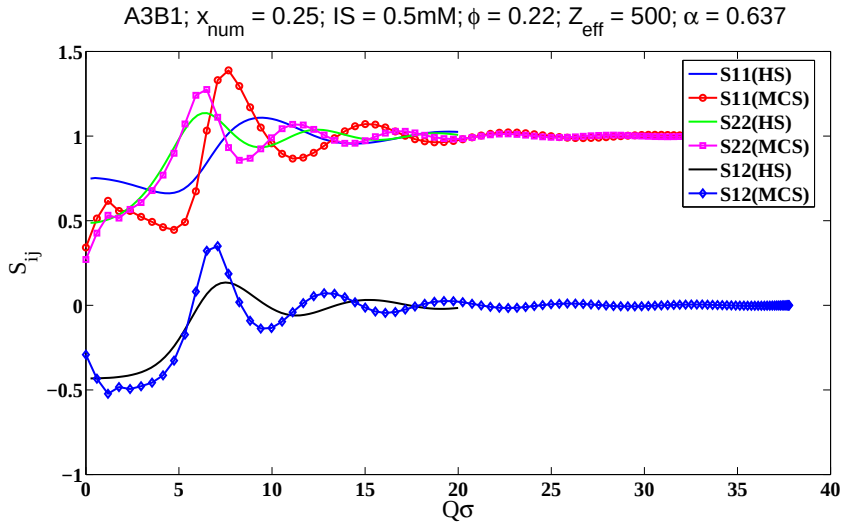

(b)

Fig. 58.: Partial structure factors versus non dimensional wave vector points of a binary mixture for $x_{num} = 0.25; \alpha = 0.637; \phi = 0.22; Z_{eff} = 500$. (a) Monte Carlo simulations - Vector and Scalar method comparisons (b) Monte Carlo simulations - Scalar method and PYHS theory comparison; MCS is the Monte Carlo Scalar method; MCV is the Monte Carlo Vector method; and HS is the analytical PYHS solution.

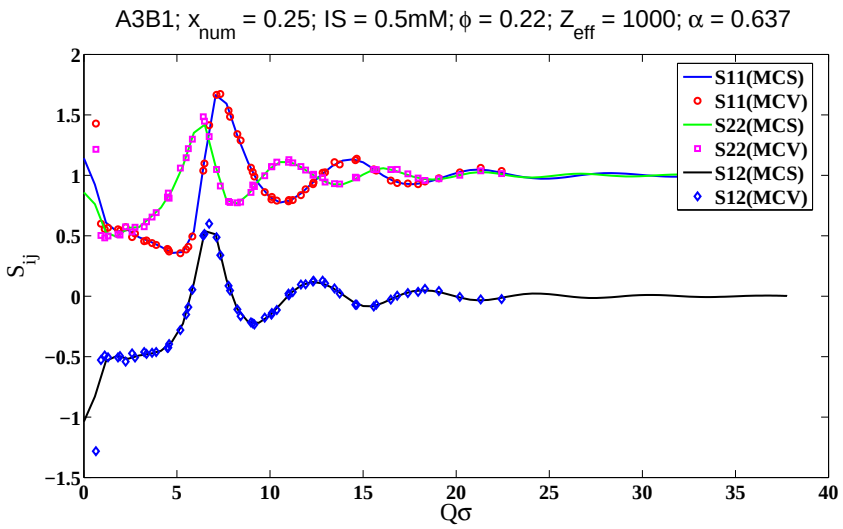

(a)

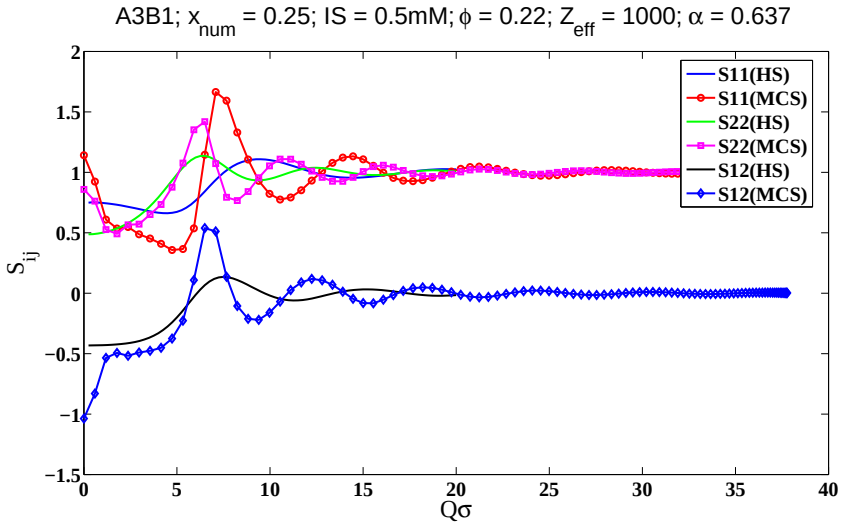

(b)

Fig. 59.: Partial structure factors versus non dimensional wave vector points of a binary mixture for $x_{num} = 0.25; \alpha = 0.637; \phi = 0.22; Z_{eff} = 1000$. (a) Monte Carlo simulations - Vector and Scalar method comparisons (b) Monte Carlo simulations - Scalar method and PYHS theory comparison; MCS is the Monte Carlo Scalar method; MCV is the Monte Carlo Vector method; and HS is the analytical PYHS solution.

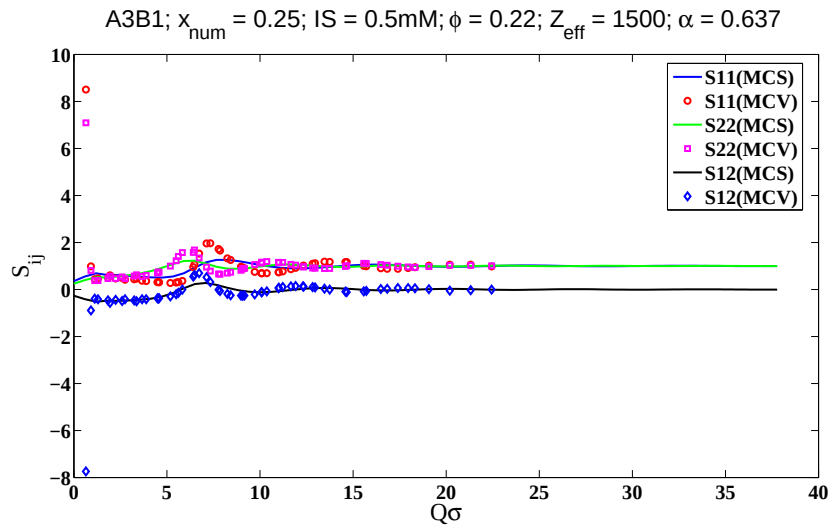

(a)

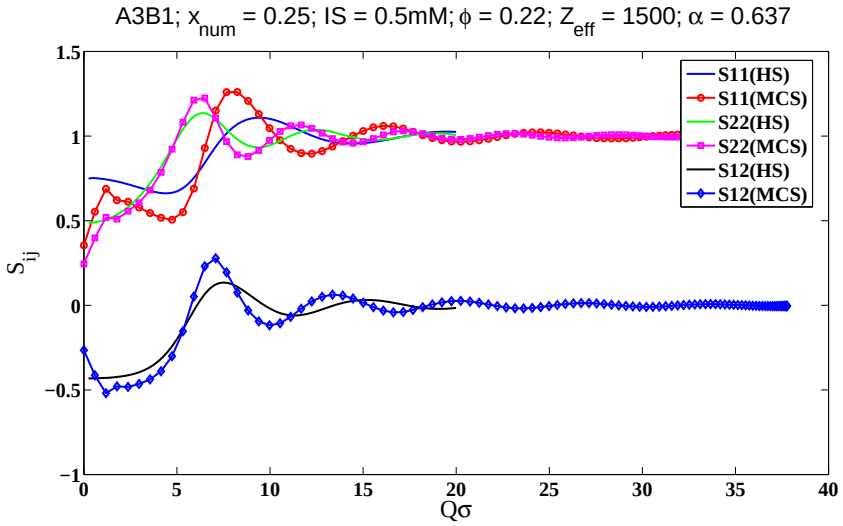

(b)

Fig. 60.: Partial structure factors versus non dimensional wave vector points of a binary mixture for $x_{num} = 0.25; \alpha = 0.637; \phi = 0.22; Z_{eff} = 1500$. (a) Monte Carlo simulations - Vector and Scalar method comparisons (b) Monte Carlo simulations - Scalar method and PYHS theory comparison; MCS is the Monte Carlo Scalar method; MCV is the Monte Carlo Vector method; and HS is the analytical PYHS solution.

Figures 61 and 62 provide the partial structure factors obtained from Monte Carlo simulations versus the non dimensional wave vector points, for the lowest ionic strength investigated by experiment of 0.5mM and the ratio of particles of 0.5. The charge values on the particles were varied from 500 to 1000 and the volume fractions are the highest value of $\phi = 0.24$ investigated in the experiment.

As shown in Figures 61 (a) and 62 (a) the structure factors obtained from both vector and scalar methods are comparable to each other. Figures 61 (b) and 62 (b) provide comparisons of the analytical PYHS model for the same number ratio 0.5, along with structure factors obtained from Monte Carlo simulations for charged particles. The plots shows clear difference between the analytical structure factors for hard spheres and the structure factors obtained from Monte Carlo simulations for charged particles.

As observed earlier the structure factors for the highest charge values are found to deviate from the expected pattern at the low $Q\sigma$ values, due to polydispersity, strong repulsion among the particles and the simulation method failing at the lower Q values. Further investigation of the isotropic scattering coefficients using these structure factor results, is performed by excluding the first few points in the low Q region and extrapolating the curve to the $Q = 0$ value.

Comparisons of the structure factors obtained from simulations with the PYHS model in Figures 61 (b) and 62 (b) results in prominent shifting of the peaks for the smaller sized particles, whereas the larger sized particles retain their peak positions, but increase in peak height is found for the larger sized particles.

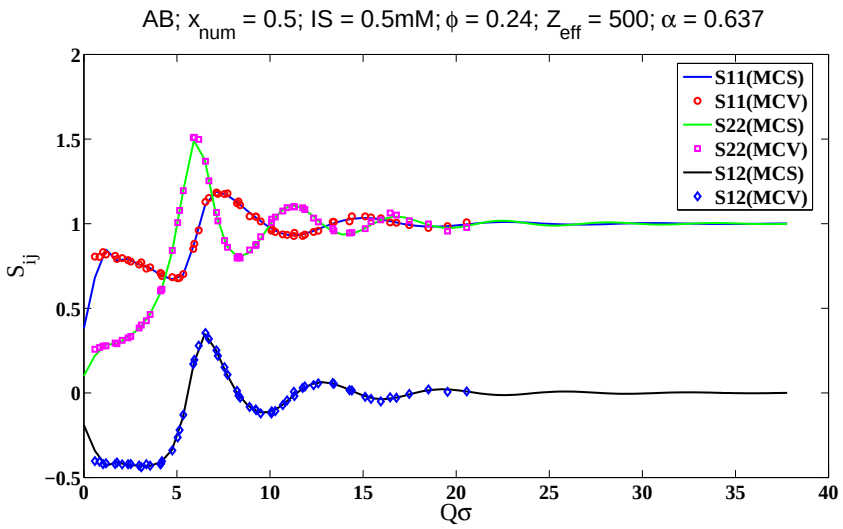

(a)

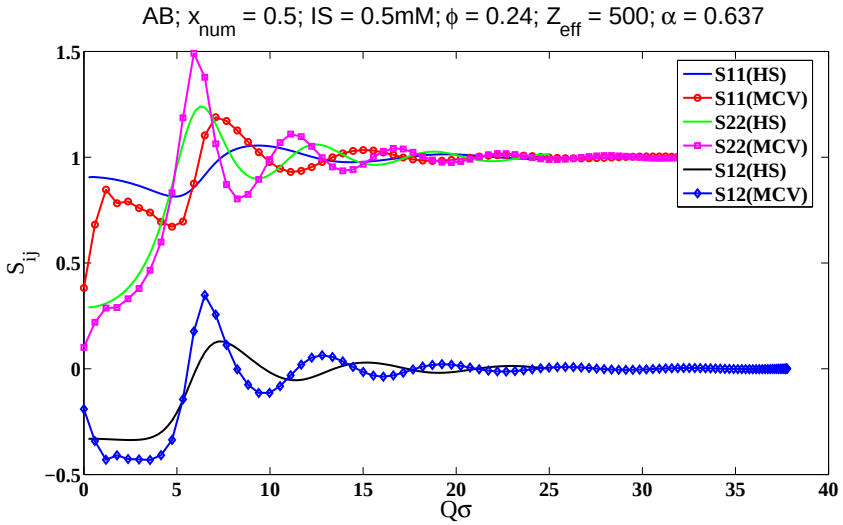

(b)

Fig. 61.: Partial structure factors versus non dimensional wave vector points of a binary mixture for $x_{num} = 0.5; \alpha = 0.637; \phi = 0.24; Z_{eff} = 500$. (a) Monte Carlo simulations - Vector and Scalar method comparisons (b) Monte Carlo simulations - Scalar method and PYHS theory comparison; MCS is the Monte Carlo Scalar method; MCV is the Monte Carlo Vector method; and HS is the analytical PYHS solution.

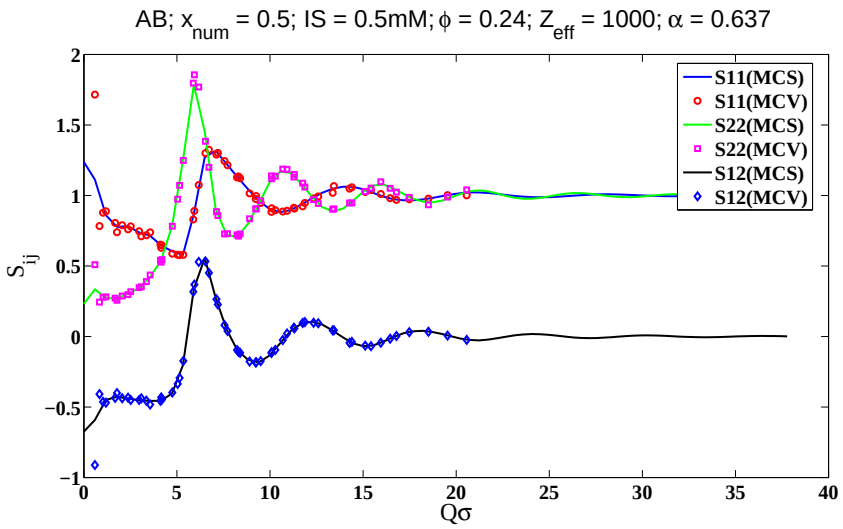

(a)

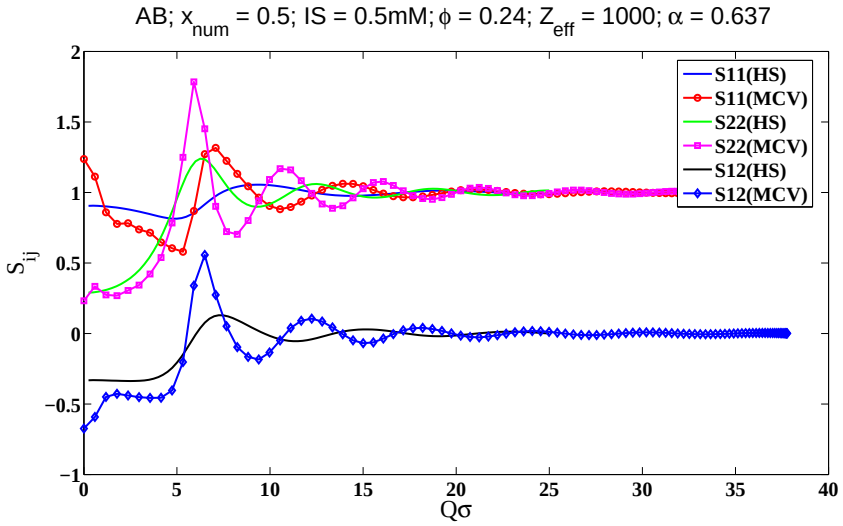

(b)

Fig. 62.: Partial structure factors versus non dimensional wave vector points of a binary mixture for $x_{num} = 0.5; \alpha = 0.637; \phi = 0.24; Z_{eff} = 1000$. (a) Monte Carlo simulations - Vector and Scalar method comparisons (b) Monte Carlo simulations - Scalar method and PYHS theory comparison; MCS is the Monte Carlo Scalar method; MCV is the Monte Carlo Vector method; and HS is the analytical PYHS solution.

Figures 63, 64 and 65 provide the partial structure factors obtained from Monte Carlo simulations versus the non dimensional wave vector points, for the lowest ionic strength investigated by experiment of 0.5mM and particle number ratio of 0.75. The charge values on the particles were varied from 500 to 1500 and the volume fractions are the highest value of $\phi = 0.22$ investigated in the experiment. As shown in Figures 63 (a), 64 (a) and 65(a) the structure factors obtained from both vector and scalar methods are comparable to each other.

Figures 63 (b), 64 (b) and 65(b) provide comparisons of the analytical PYHS model for the same number ratio 0.75, along with structure factors obtained from Monte Carlo simulations of charged particles. The plots shows clear difference between the analytical structure factors for hard spheres and the structure factors obtained from Monte Carlo simulations for charged particles.

Figure 66 provides comparison of Monte Carlo simulations from scalar method and the solution of the OZ equations using the hard sphere Yukawa potential model with HNC closure models. The OZ equations have only converged for the number ratio of 0.75 (A1B3), for a volume fraction of 0.22 and upto a charge value of 800. The results of comparison are provided for this number ratio only.

The comparison obtained for two charge values of 500 and 800 at the volume fraction of $\phi = 0.22$, show that the MC simulations and the solution of the OZ equations agree well and that either of the solutions can be used for prediction of the isotropic scattering data obtained from experiment.

Henceforth, for the number ratios of 0.25 (A3B1) and 0.5 (AB), where OZ solution could not be achieved the MC simulation results was used to predict the isotropic scattering data. For the number ratio of 0.75 (A1B3), the OZ equation results was used to predict the experimental isotropic scattering data.

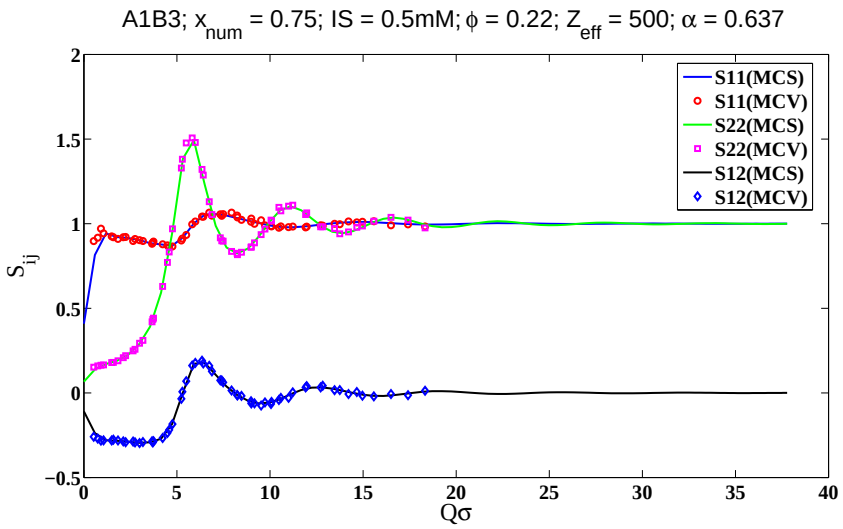

(a)

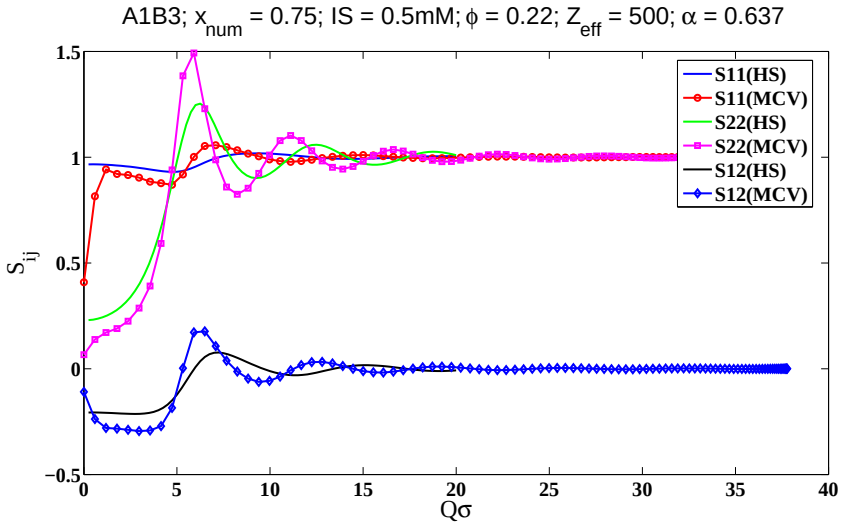

(b)

Fig. 63.: Partial structure factors versus non dimensional wave vector points of a binary mixture for $x_{num} = 0.75; \alpha = 0.637; \phi = 0.22; Z_{eff} = 500$. (a) Monte Carlo simulations - Vector and Scalar method comparisons (b) Monte Carlo simulations - Scalar method and PYHS theory comparison; MCS is the Monte Carlo Scalar method; MCV is the Monte Carlo Vector method; and HS is the analytical PYHS solution.

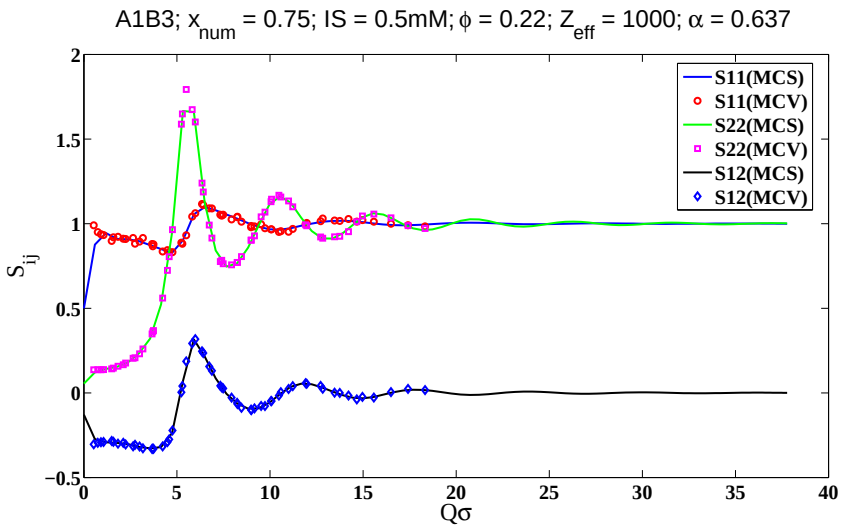

(a) Monte Carlo simulations- Vector and Scalar methods

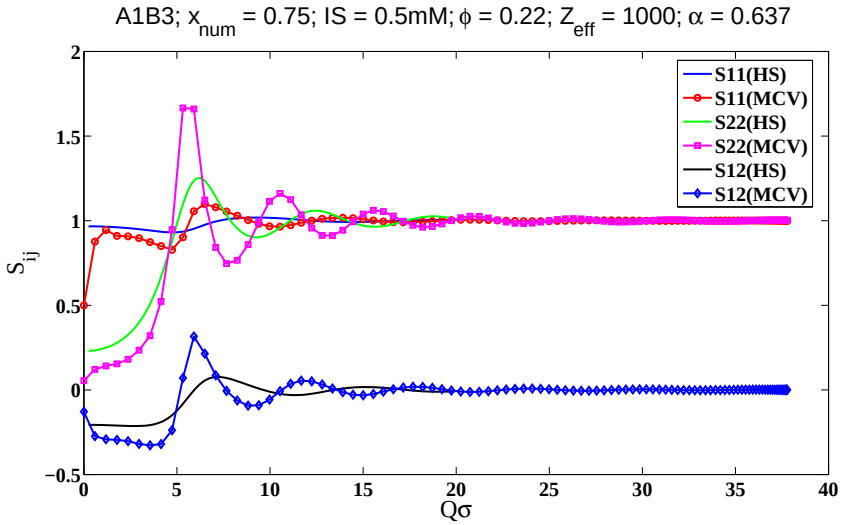

(b) Monte Carlo simulations -Scalar method and PYHS theory

Fig. 64.: Partial structure factors versus non dimensional wave vector points of a binary mixture for $x_{num} = 0.75; \alpha = 0.637; \phi = 0.22; Z_{eff} = 1000$. (a) Monte Carlo simulations - Vector and Scalar method comparisons (b) Monte Carlo simulations - Scalar method and PYHS theory comparison; MCS is the Monte Carlo Scalar method; MCV is the Monte Carlo Vector method; and HS is the analytical PYHS solution.

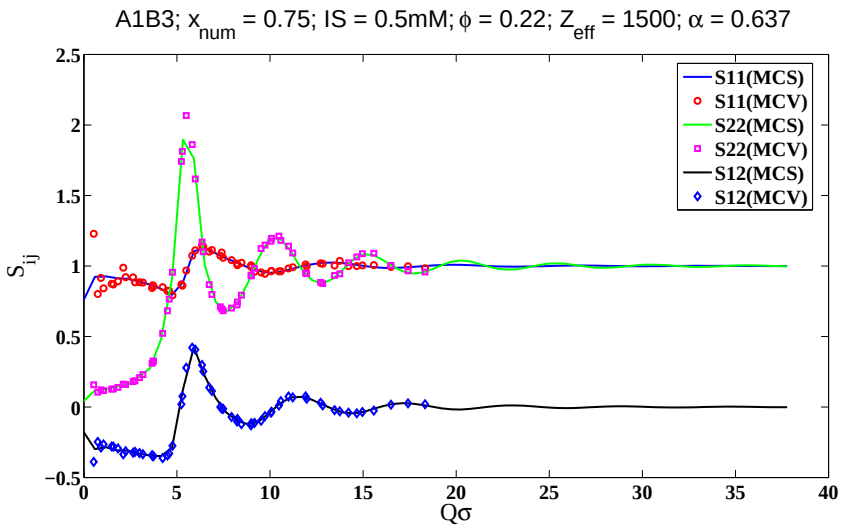

(a) Monte Carlo simulations- Vector and Scalar methods

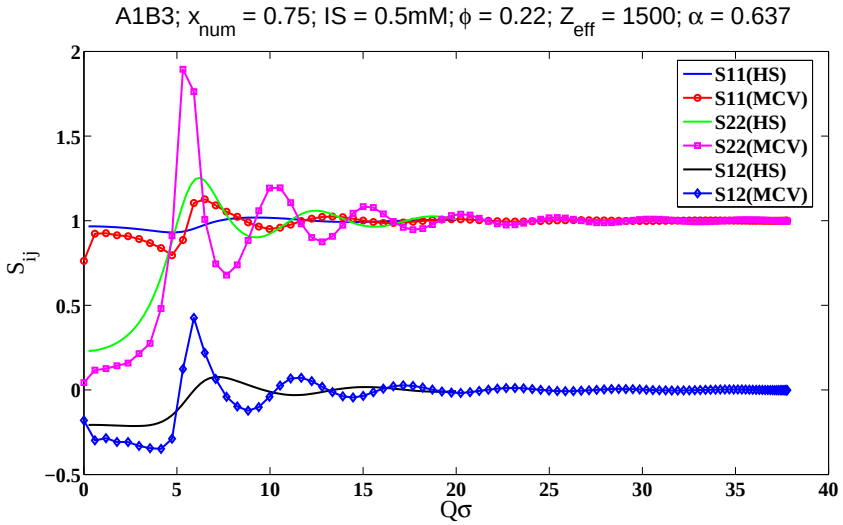

(b) Monte Carlo simulations -Scalar method and PYHS theory

Fig. 65.: Partial structure factors versus non dimensional wave vector points of a binary mixture for $x_{num} = 0.75; \alpha = 0.637; \phi = 0.22; Z_{eff} = 1500$. (a) Monte Carlo simulations - Vector and Scalar method comparisons (b) Monte Carlo simulations - Scalar method and PYHS theory comparison; MCS is the Monte Carlo Scalar method; MCV is the Monte Carlo Vector method; and HS is the analytical PYHS solution.

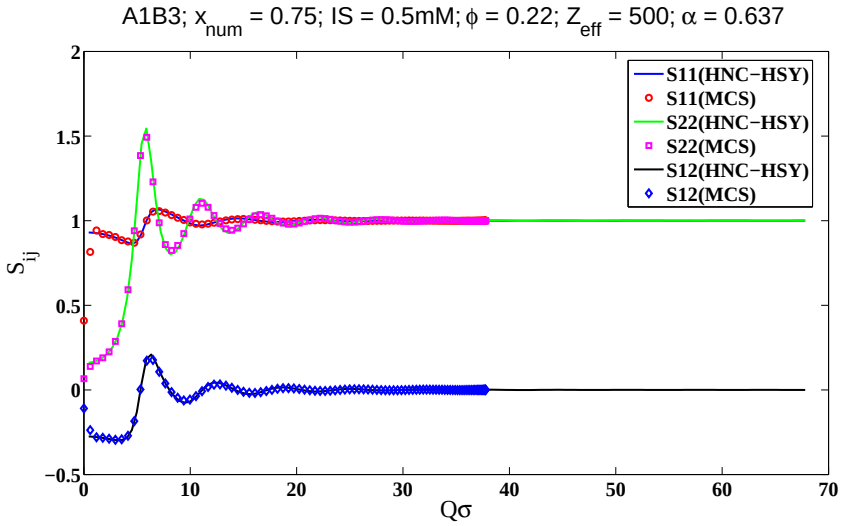

(a)

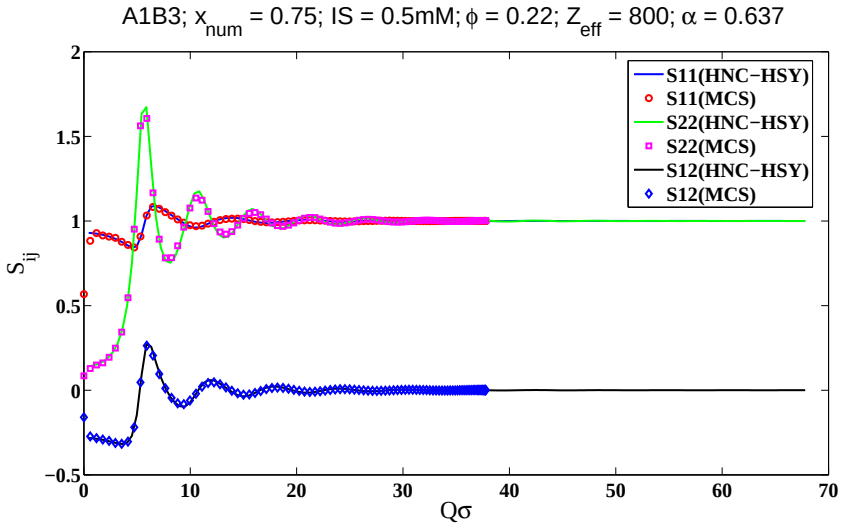

(b)

Fig. 66.: Partial structure factors versus non dimensional wave vector points of a binary mixture for $x_{num} = 0.75; \alpha = 0.637; \phi = 0.22$. (a) Monte Carlo simulations-Scalar method and HNC-HSY theory comparisons for $Z_{eff} = 500$ (b) Monte Carlo simulations -Scalar method and HNC-HSY theory comparisons for $Z_{eff} = 800$; MCS is the Monte Carlo Scalar method; HNC-HSY is the Hypernetted Chain Closure with the Hard Sphere Yukawa potential.

Figures 67, 68, 69, and 70 provide comparisons of the experimental isotropic scattering coefficient data versus the ionic strength for A3B1 samples at four wavelengths of 660, 685, 785 and 828nm, with models prepared from the results obtained from Monte Carlo simulations using similar parameters of effective charge, ionic strength, and volume fraction as considered in the experiment. The OZ equations have failed to converge for this number ratio, and hence the structure factors obtained from MC simulations were used to investigate the experimental results.

The structure factors obtained from simulations are extrapolated to $Q = 0$ and used to predict the experimental data, using the formulation of Eqn. (8.2). The model predictions used the variable refractive index described in Chapter VII to predict the isotropic scattering data. The Sellmeier coefficients used were the same as described in Chapter VII.

The isotropic scattering coefficient data do not match those predicted by MC simulation models with Yukawa potentials. The data are in the vicinity with those predicted by models and the trends of the data are similar. Since the effective charge on the particles increases with the ionic strength and this phenomenon is not captured in the models, the data predictions may not be expected to match.

At wavelengths of 660 and 685nm the discrepancy between model predicted data and the experimental data increases perhaps due to inaccurate refractive index values predicted for these wavelengths. We found that the isotropic scattering data is highly sensitive to the refractive index of the particles used in the experiment, as described in Chapter VII. At the wavelengths of 660 and 685nm the isotropic scattering coefficients differ from the model predictions, and the discrepancy increases as the number ratio of larger particles increases in the bidisperse mixtures. The observation of discrepancy at the wavelengths of 660 and 685nm is observed for all the monodisperse and bidisperse dispersions.

There is consistency in the observed differences at lower wavelengths. Further with increasing amount of larger size particles in the mixture the difference between prediction and measurement increases at lower wavelengths. This observation can be made from all figures where the experimental data are compared with the model predicted data.

In order to investigate whether volume fraction (ϕ) inaccuracies could result in differences between model predicted data and isotropic scattering data, figures are plotted for $\phi = 0.19$ (68) and $\phi = 0.22$ (67). The results for the two volume fractions do not differ much, and we can eliminate volume fraction as a variable to alter the isotropic scattering coefficient by orders of magnitude.

Also upon observing the lowest wavelengths of 660 and 685nm for all the available volume fractions of A3B1, we can see that there is an increasing difference between model predicted isotropic scattering coefficients and what we obtain from experiments. This implies that the particles are strongly structured even at lower volume fractions, whereas the predicted data are depicting a much more loosening of the structure of particles.

For the volume fraction of $\phi = 0.18$, Figure 69 plots the isotropic scattering coefficient versus the ionic strength at wavelengths of 660, 685, 785 and 828nm. The model predictions are those of MC simulations with HSY potential interactions and have similar trends as the experimentally determined isotropic scattering coefficient data. For the volume fraction of $\phi = 0.15$, Figure 70 plots the isotropic scattering coefficient versus the ionic strength at wavelengths of 660, 685, 785 and 828nm. The experimentally determined isotropic scattering coefficients do have a definitive trend at the wavelengths of 660 and 685nm. Only for wavelengths of 785 and 828nm do we observe that the isotropic scattering coefficient data increase with increasing ionic strength of the dispersion.

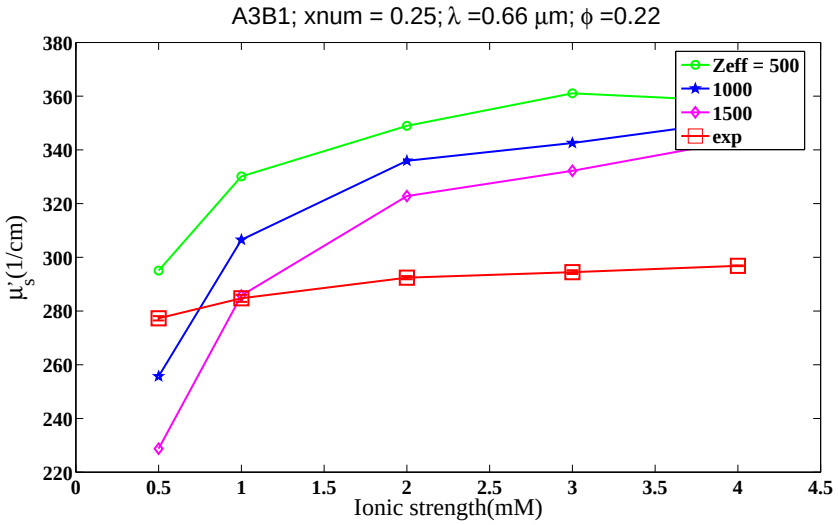

(a) $\lambda = 660$

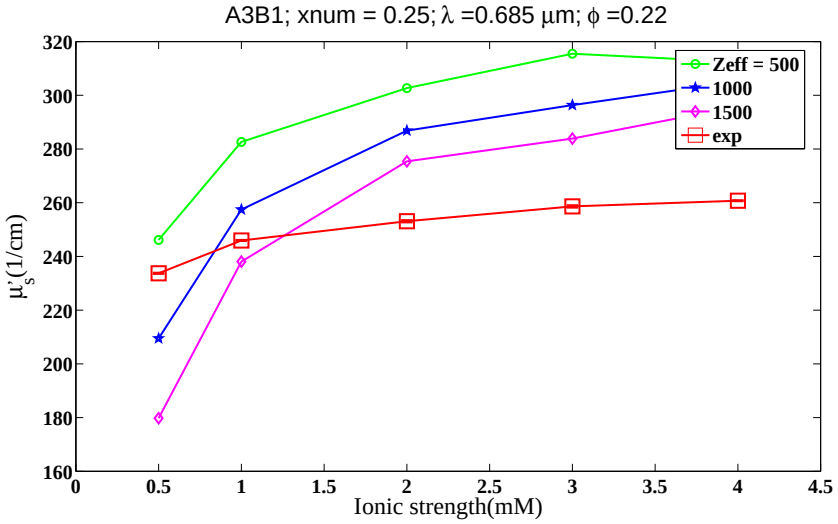

(b) $\lambda = 685$

Fig. 67.: Isotropic scattering coefficient measurements versus ionic strength of a bidisperse mixture of polystyrene latexes. Open squares connected with solid lines are experimental measurements and points connected with solid lines are numerical solution of the OZ equation with Yukawa potential and HNC closure. The particle sizes are $\sigma = 144nm$ and $\sigma = 223nm$, at a volume fraction of $\phi = 0.22$, $x_{num} = 0.25$ and ionic strengths of 0.5,1,2,3 and 4mM at (a)$\lambda = 660$,(b)$\lambda = 685$, (c)$\lambda = 785$ and (d)$\lambda = 828$nm.

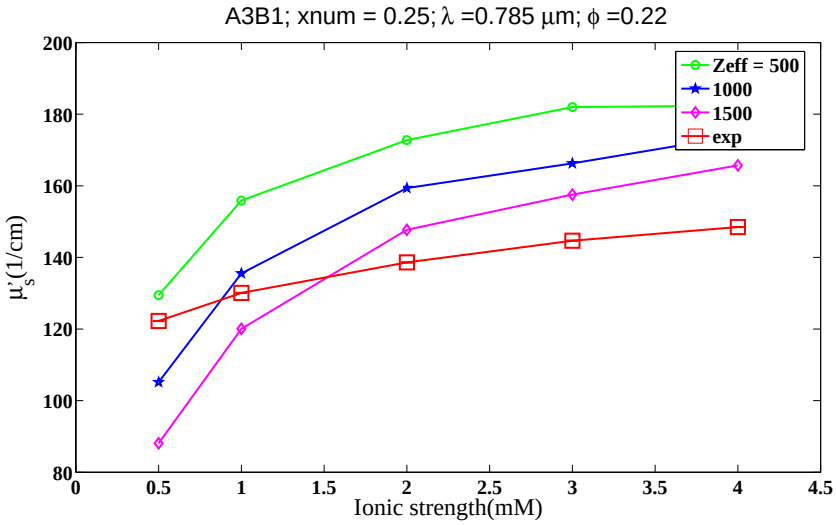

(c) $\lambda = 785$

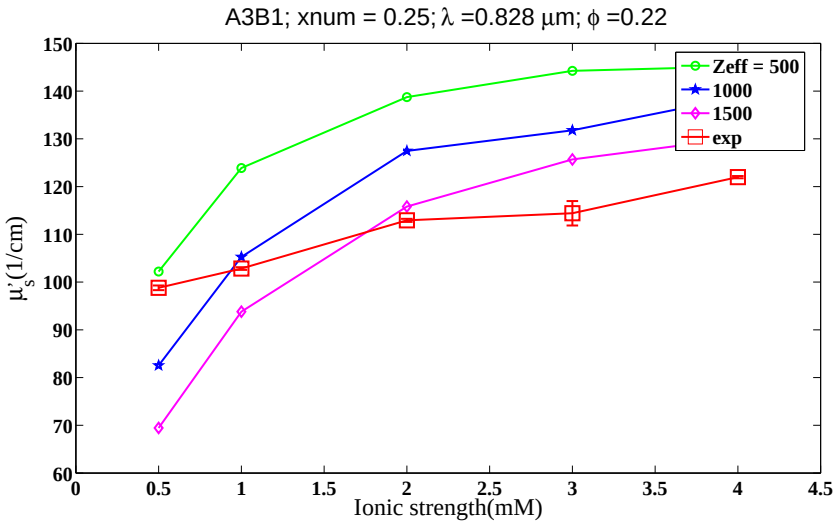

(d) $\lambda = 828$

Fig. 67.: Continued.

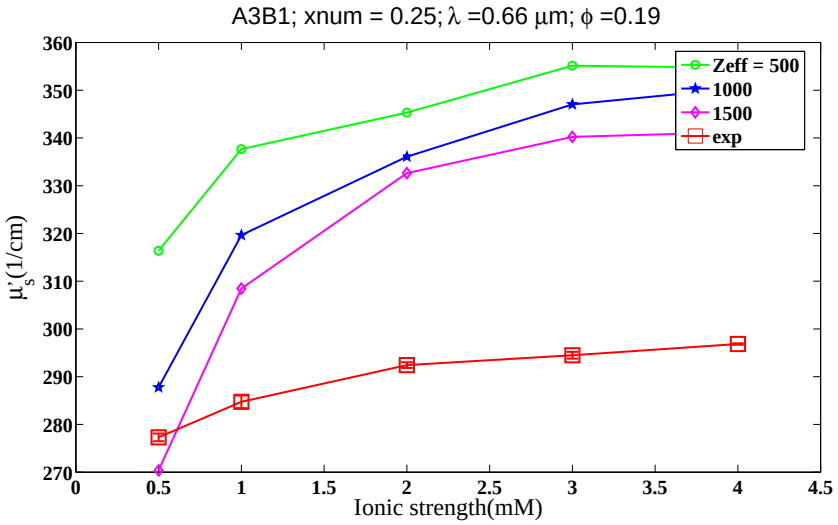

(a) $\lambda = 660$

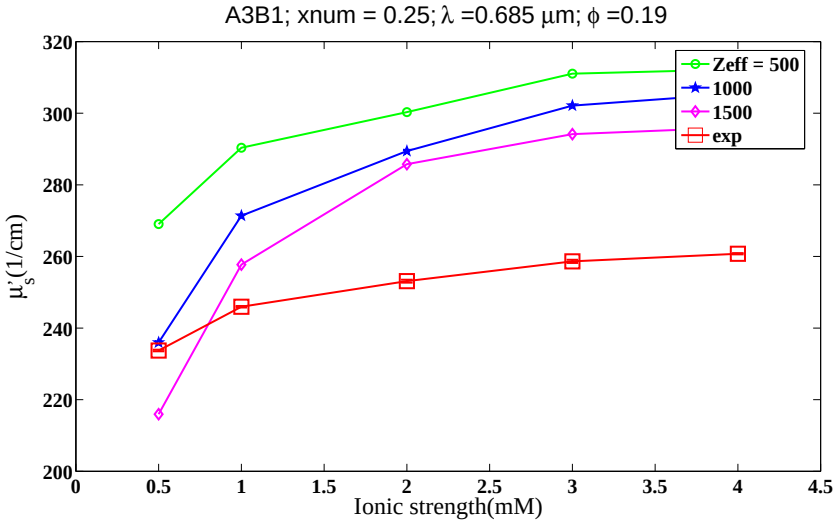

(b) $\lambda = 685$

Fig. 68.: Isotropic scattering coefficient measurements versus ionic strength of a bidisperse mixture of polystyrene latexes. Open squares connected with solid lines are experimental measurements and points connected with solid lines are numerical solution of the OZ equation with Yukawa potential and HNC closure. The particle sizes are $\sigma = 144nm$ and $\sigma = 223nm$, at a volume fraction of $\phi = 0.19$, $x_{num} = 0.25$ and ionic strengths of 0.5,1,2,3 and 4mM at (a)$\lambda = 660$,(b)$\lambda = 685$, (c)$\lambda = 785$ and (d)$\lambda = 828$nm.

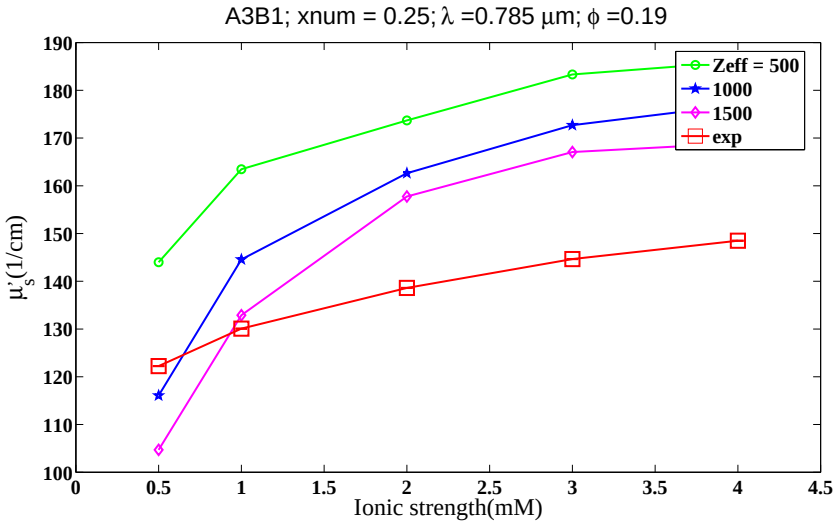

(c) $\lambda = 785$

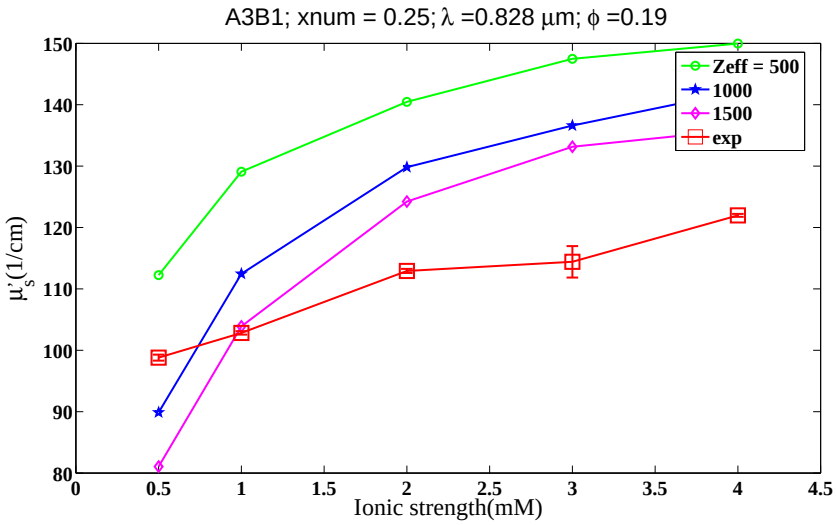

(d) $\lambda = 828$

Fig. 68.: Continued.

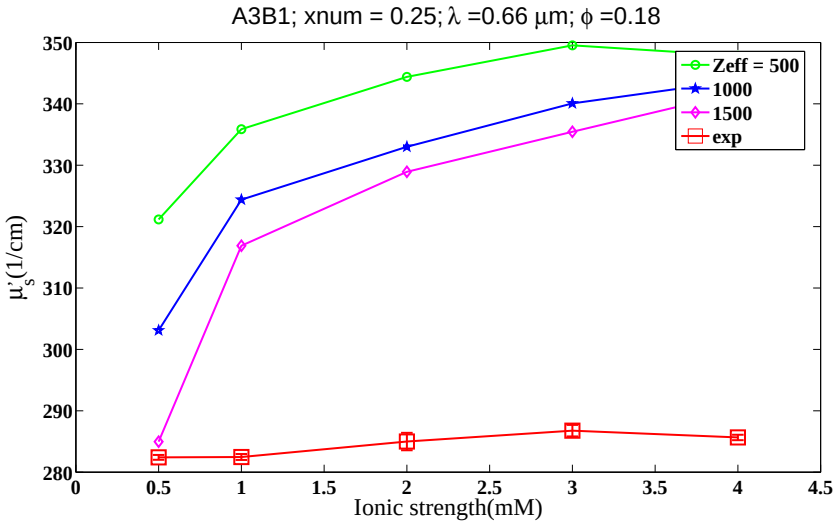

(a) $\lambda = 660$

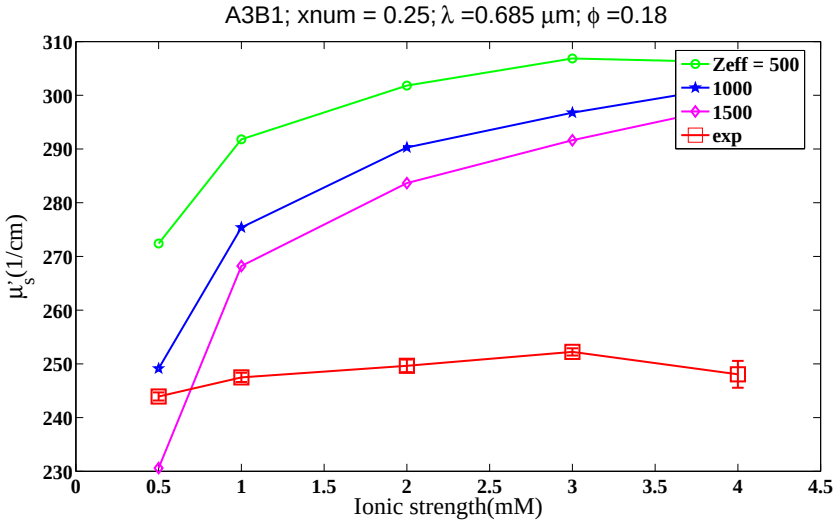

(b) $\lambda = 685$

Fig. 69.: Isotropic scattering coefficient measurements versus ionic strength of a bidisperse mixture of polystyrene latexes. Open squares connected with solid lines are experimental measurements and points connected with solid lines are numerical solution of the OZ equation with Yukawa potential and HNC closure. The particle sizes are $\sigma = 144nm$ and $\sigma = 223nm$, at a volume fraction of $\phi = 0.18$, $x_{num} = 0.25$ and ionic strengths of 0.5,1,2,3 and 4mM at (a)$\lambda = 660$,(b)$\lambda = 685$, (c)$\lambda = 785$ and (d)$\lambda = 828$nm.

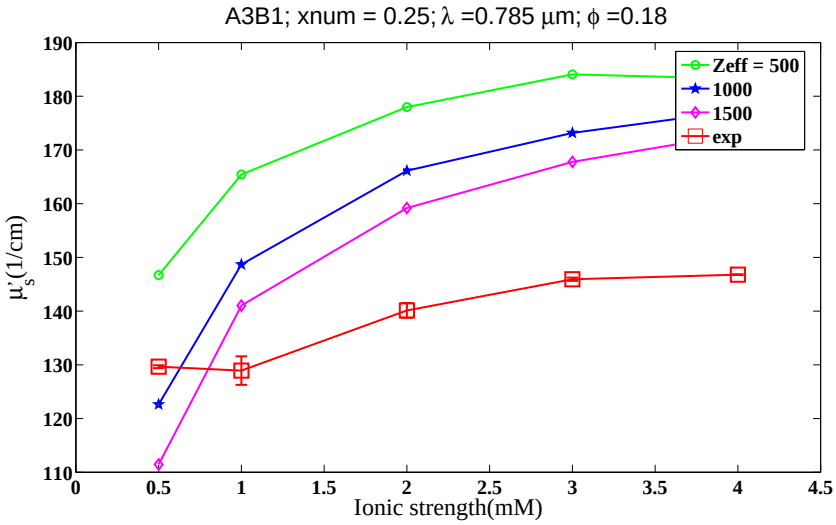

(c) $\lambda = 785$

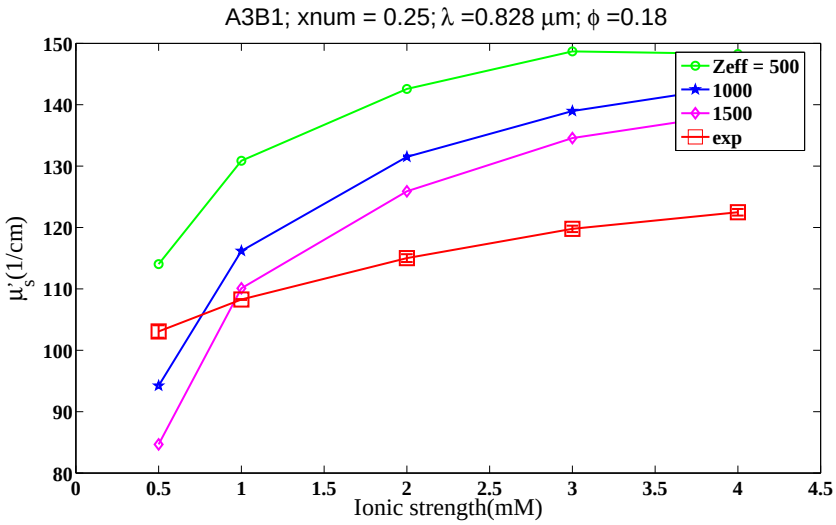

(d) $\lambda = 828$

Fig. 69.: Continued.

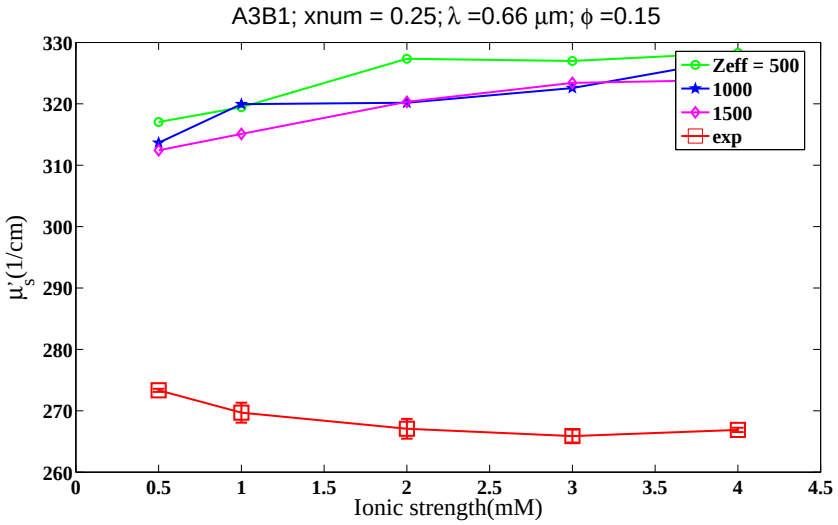

(a) $\lambda = 660$

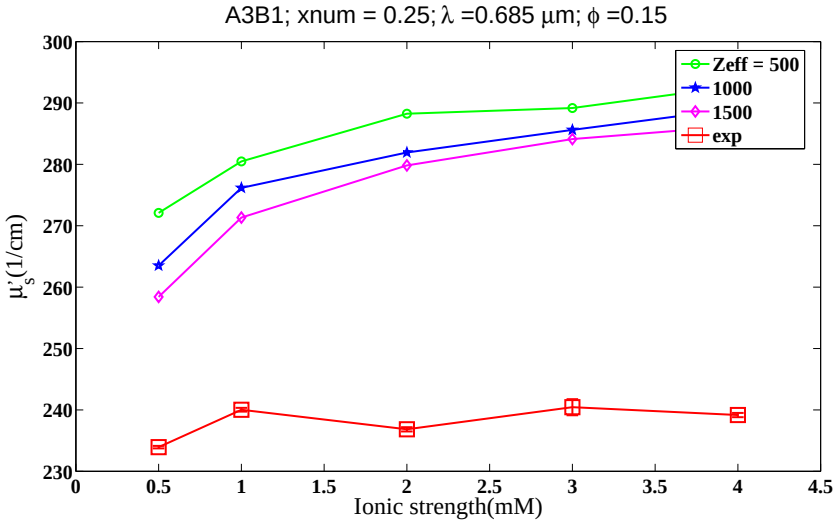

(b) $\lambda = 685$

Fig. 70.: Isotropic scattering coefficient measurements versus ionic strength of a bidisperse mixture of polystyrene latexes. Open squares connected with solid lines are experimental measurements and points connected with solid lines are numerical solution of the OZ equation with Yukawa potential and HNC closure. The particle sizes are $\sigma = 144nm$ and $\sigma = 223nm$, at a volume fraction of $\phi = 0.15$, $x_{num} = 0.25$ and ionic strengths of 0.5,1,2,3 and 4mM at (a)$\lambda = 660$,(b)$\lambda = 685$, (c)$\lambda = 785$ and (d)$\lambda = 828$nm.

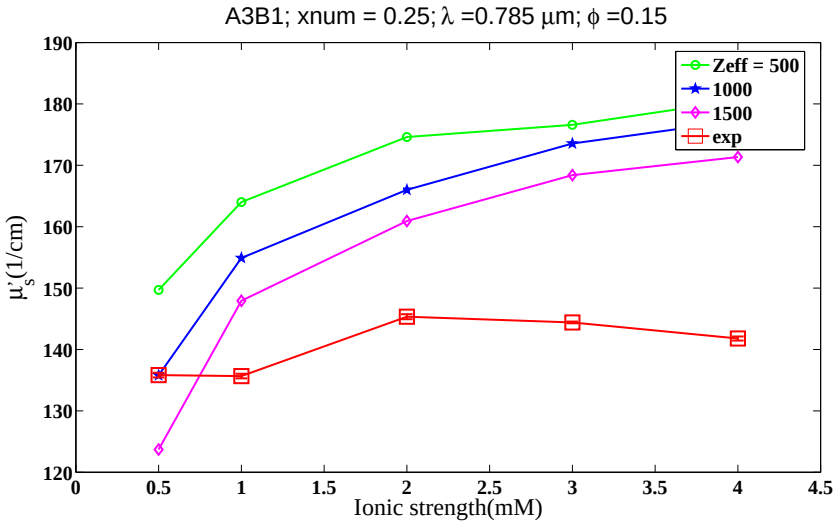

(c) $\lambda = 785$

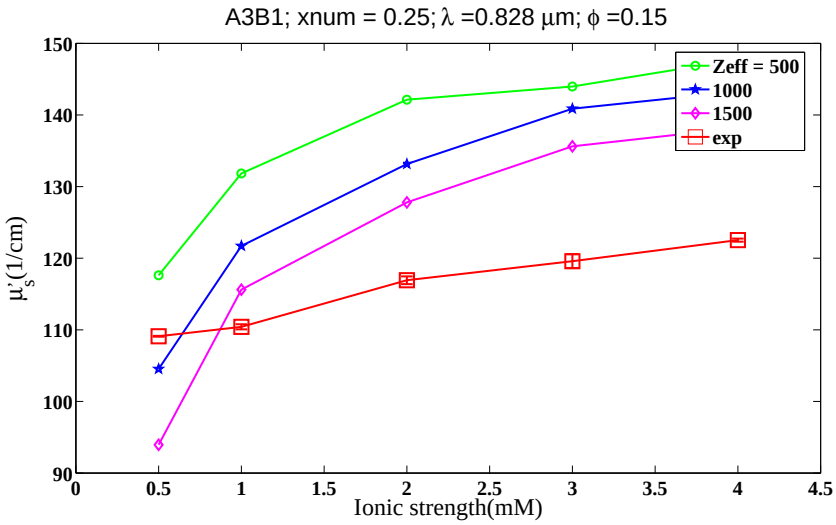

(d) $\lambda = 828$

Fig. 70.: Continued.

Figures 71, 72, and 73 provide the comparisons between isotropic scattering coefficient data and MC simulation model predictions for a number ratio of 0.5. The isotropic scattering coefficient is plotted versus the ionic strength of the dispersion. The refractive index is variable as described in Chapter VII and the Sellmeier coefficients used, are described in Chapter V.

As explained previously the comparisons between experimental data have similar trends (monotonously increasing or decreasing) with those provided by model predictions. There is a variation in trends or trend reversal of decreased isotropic scattering coefficients with increased ionic strength to increasing isotropic scattering coefficients with increased ionic strength, as the wavelength of light is increased. The observation is prominent in lower volume fractions of $\phi = 0.18$ and $\phi = 0.15$.

Also, the difference in the model predicted data and experimental data increases in the lower wavelengths at increasing concentration of larger size particles. This phenomenon is prominent in the lower volume fractions of number ratio 0.5, and the disparity is larger between model predicted and experimental data, when compared to the number ratio 0.25 (A3B1), where the larger sized particles are fewer in number.

The refractive index used for model predictions is again important for the isotropic scattering coefficient predictions and at the lower wavelengths the discrepancy can be accounted to inaccurate refractive indices.

Also if we observe the data obtained at lower wavelengths and varying volume fractions, then it is evident that the difference in model data and experimental data increases with decreasing volume fraction. This could imply that the model predictions are not correctly describing the structural changes effectively even though the trends are similar for the plots. Similar results were observed earlier for sample ratio 0.25, could imply that the particles are still strongly structured in the dispersion, whereas the model predicts lesser structure within the dispersion.

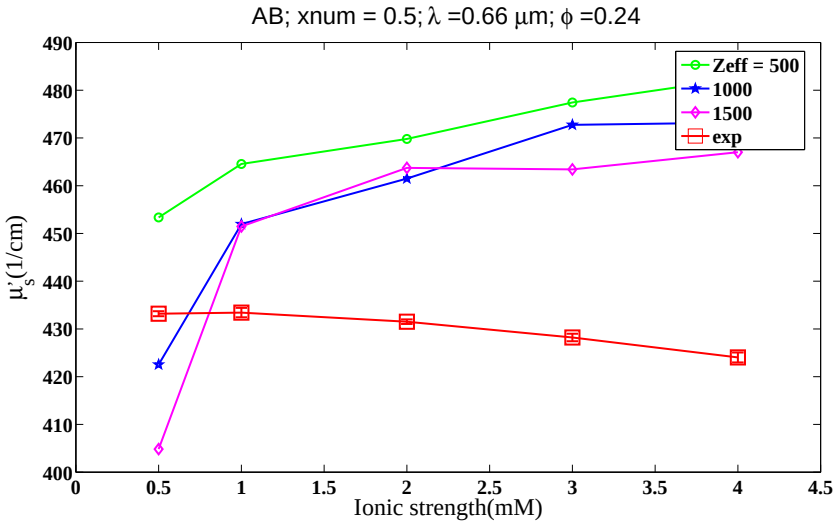

(a) $\lambda = 660$

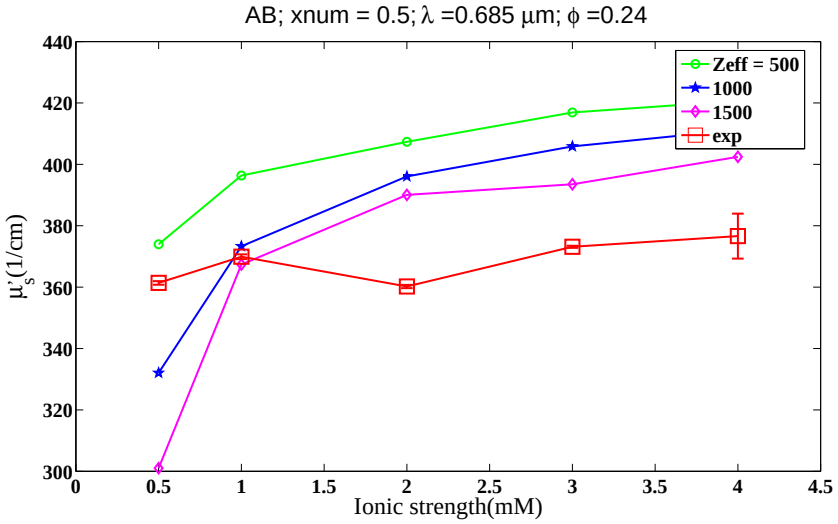

(b) $\lambda = 685$

Fig. 71.: Isotropic scattering coefficient measurements versus ionic strength of a bidisperse mixture of polystyrene latexes. Open squares connected with solid lines are experimental measurements and points connected with solid lines are numerical solution of the OZ equation with Yukawa potential and HNC closure. The particle sizes are $\sigma = 144nm$ and $\sigma = 223nm$, at a volume fraction of $\phi = 0.24$, $x_{num} = 0.5$ and ionic strengths of 0.5,1,2,3 and 4mM at (a)$\lambda = 660$,(b)$\lambda = 685$, (c)$\lambda = 785$ and (d)$\lambda = 828$nm.

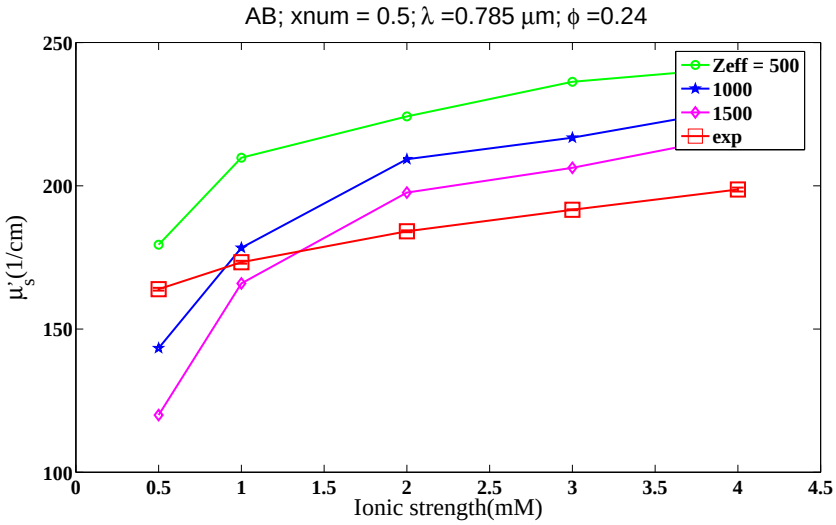

(c) $\lambda = 785$

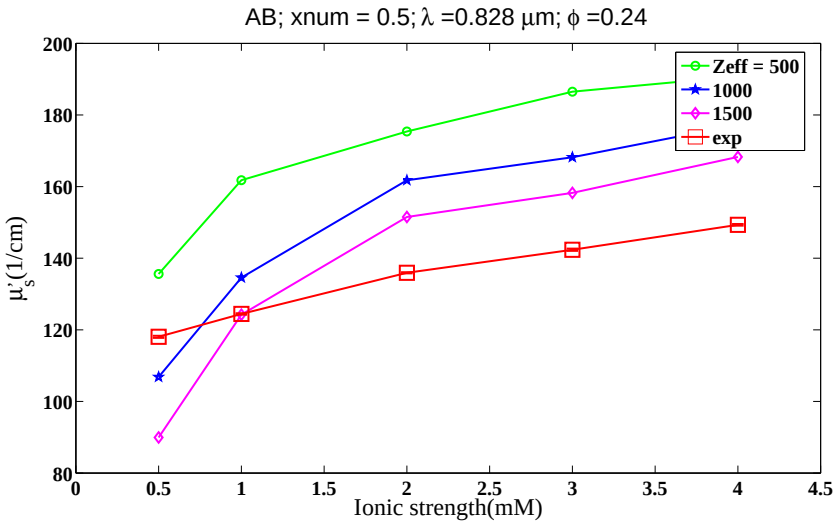

(d) $\lambda = 828$

Fig. 71.: Continued.

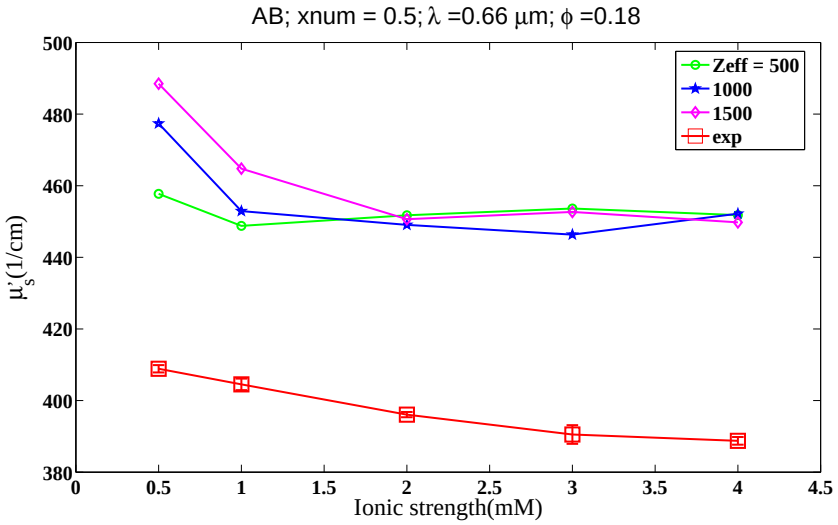

(a) $\lambda = 660$

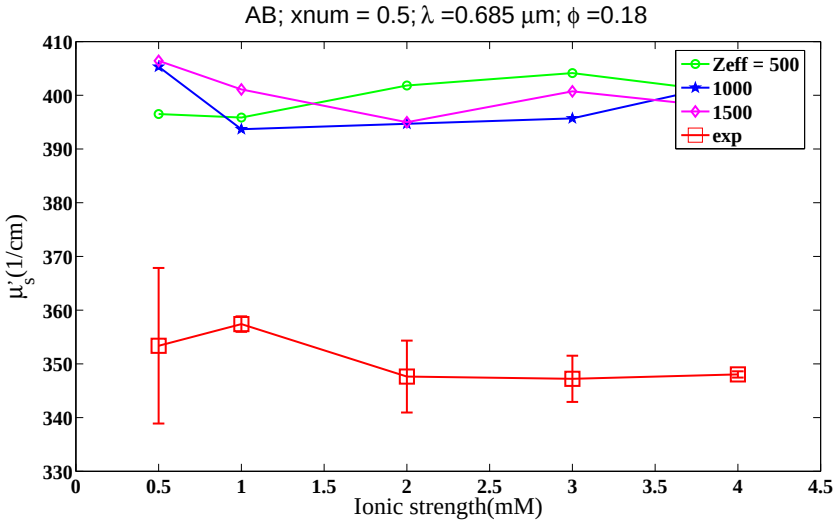

(b) $\lambda = 685$

Fig. 72.: Isotropic scattering coefficient measurements versus ionic strength of a bidisperse mixture of polystyrene latexes. Open squares connected with solid lines are experimental measurements and points connected with solid lines are numerical solution of the OZ equation with Yukawa potential and HNC closure. The particle sizes are $\sigma = 144nm$ and $\sigma = 223nm$, at a volume fraction of $\phi = 0.18$, $x_{num} = 0.5$ and ionic strengths of 0.5,1,2,3 and 4mM at (a)$\lambda = 660$,(b)$\lambda = 685$, (c)$\lambda = 785$ and (d)$\lambda = 828$nm.

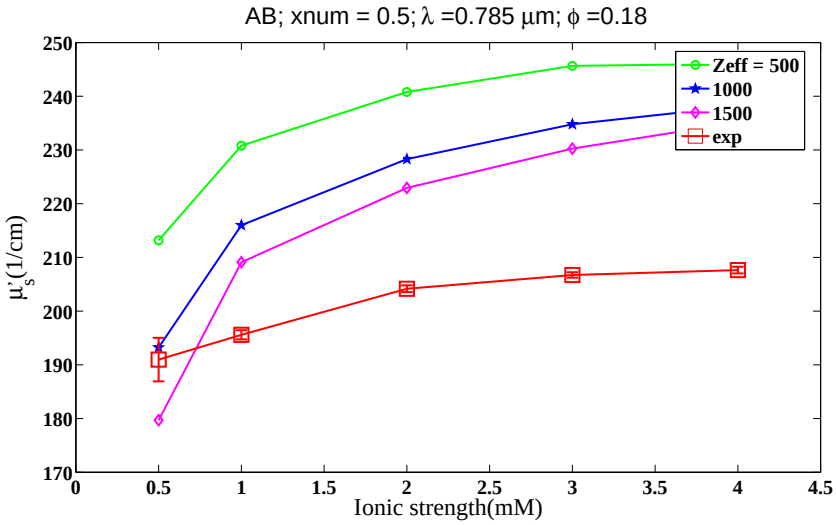

(c) $\lambda = 785$

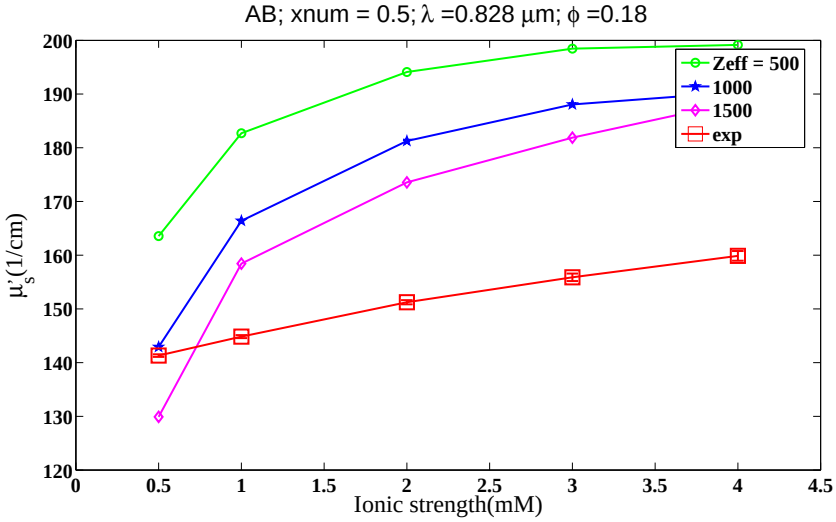

(d) $\lambda = 828$

Fig. 72.: Continued.

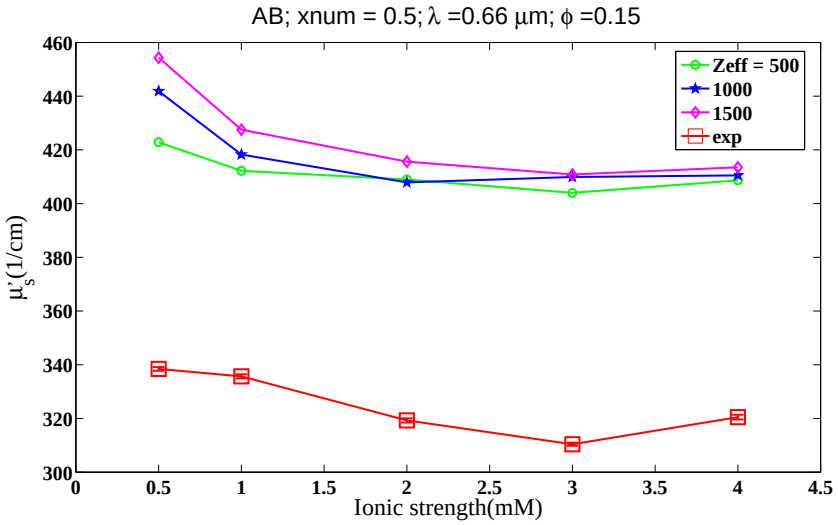

(a) $\lambda = 660$

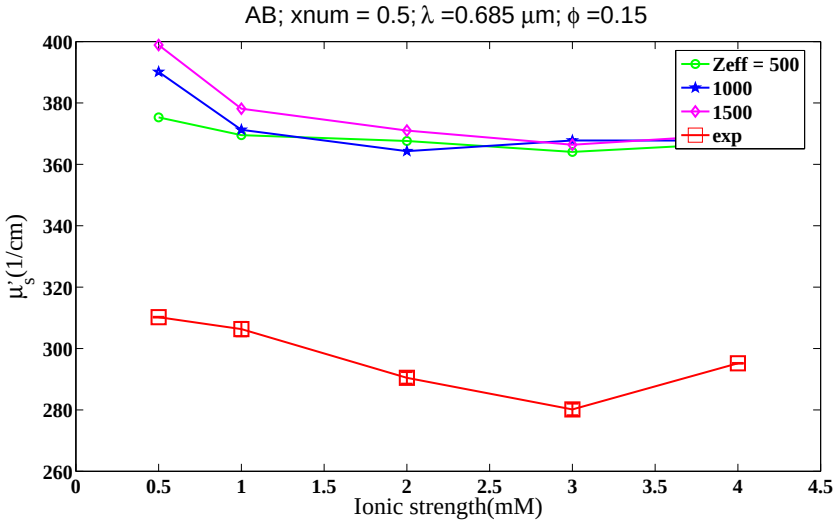

(b) $\lambda = 685$

Fig. 73.: Isotropic scattering coefficient measurements versus ionic strength of a bidisperse mixture of polystyrene latexes. Open squares connected with solid lines are experimental measurements and points connected with solid lines are numerical solution of the OZ equation with Yukawa potential and HNC closure. The particle sizes are $\sigma = 144nm$ and $\sigma = 223nm$, at a volume fraction of $\phi = 0.15$, $x_{num} = 0.5$ and ionic strengths of 0.5,1,2,3 and 4mM at (a)$\lambda = 660$,(b)$\lambda = 685$, (c)$\lambda = 785$ and (d)$\lambda = 828$nm.

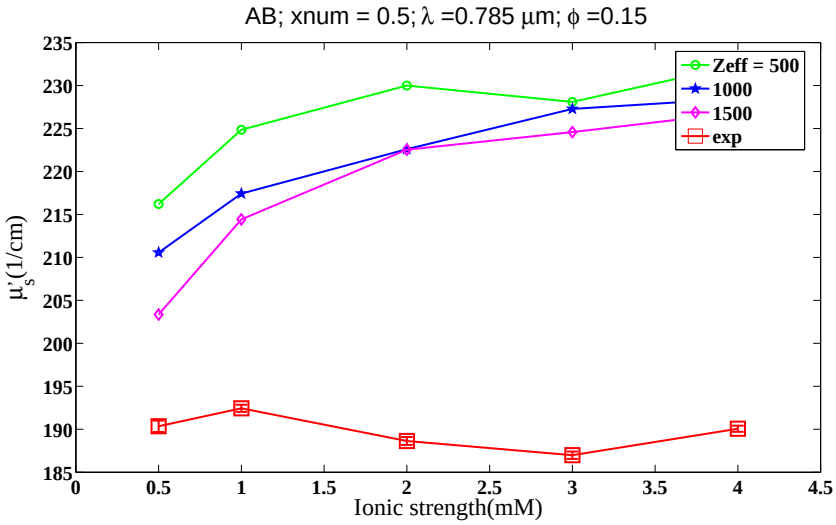

(c) $\lambda = 785$

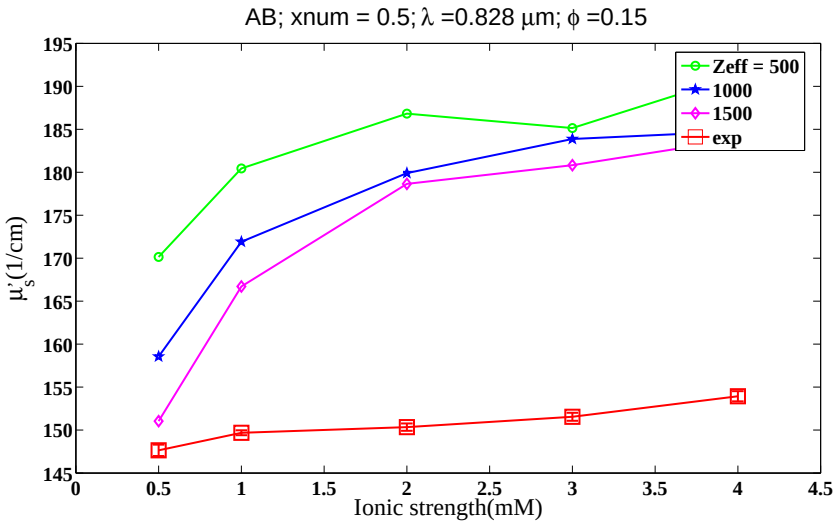

(d) $\lambda = 828$

Fig. 73.: Continued.

Figures 74, 75 and 76 depict the model comparisons with the experimental data for a number ratio of particles of 0.75. The isotropic scattering coefficient data is plotted versus the ionic strength of the dispersion. The comparisons are provided for a larger number of effective charge values, as the OZ equations were found to converge for this number ratio at higher charge values.

The trends among the experimental data are found to be close to model predictions for lower volume fractions of $\phi = 0.18$ and $\phi = 0.15$. The experimental data were found to have fluctuations at certain wavelengths as the ionic strength was changed. Upon observation of the wavelengths of 660 and 685nm, the same samples show close similarity in the experimental data, which implies the correctness of the experiment. The fluctuations are attributed to the various zones of the partial structure factor being explored by the experiment i.e. a range of partial structure factors explored by the wave vector values. The peaks of the structure factor being explored are those of the higher diameter particle as well as the lower size particle. Also the concentration of the higher diameter particle is the highest in this case and at lower wavelengths there is an increasing probability of the experimental data being beyond the first peak of the structure factor from models.

The convolution of the trends obtained from the smaller sized particle as well as the higher diameter particle may also lead to increasing fluctuations observed in the experimental data.

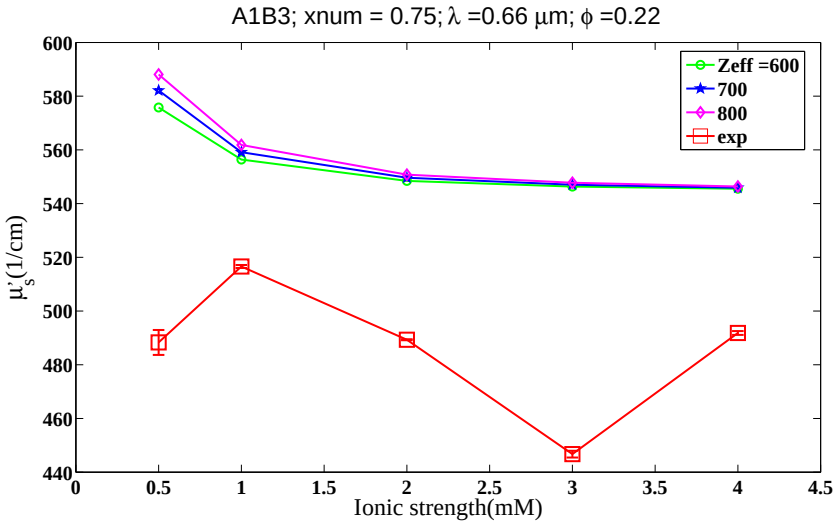

(a) $\lambda = 660$

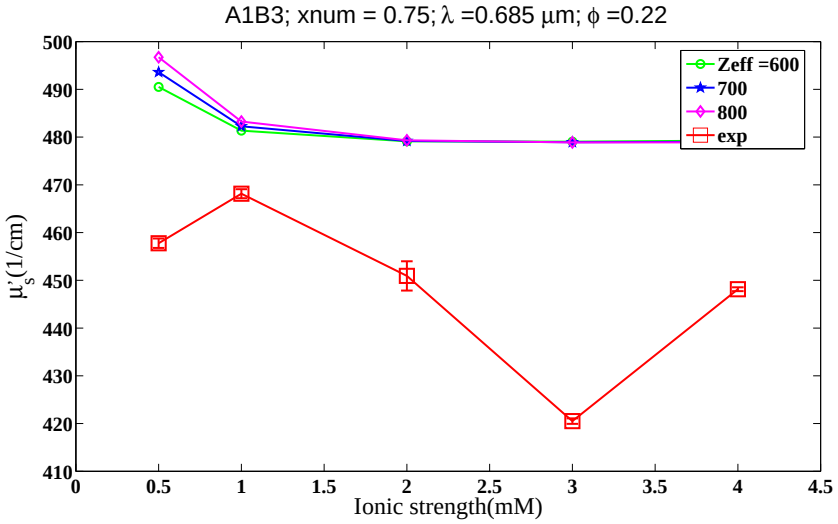

(b) $\lambda = 685$

Fig. 74.: Isotropic scattering coefficient measurements versus ionic strength of a bidisperse mixture of polystyrene latexes. Open squares connected with solid lines are experimental measurements and points connected with solid lines are numerical solution of the OZ equation with Yukawa potential and HNC closure. The particle sizes are $\sigma = 144nm$ and $\sigma = 223nm$, at a volume fraction of $\phi = 0.22$, $x_{num} = 0.75$ and ionic strengths of 0.5,1,2,3 and 4mM at (a)$\lambda = 660$,(b)$\lambda = 685$, (c)$\lambda = 785$ and (d)$\lambda = 828$nm.

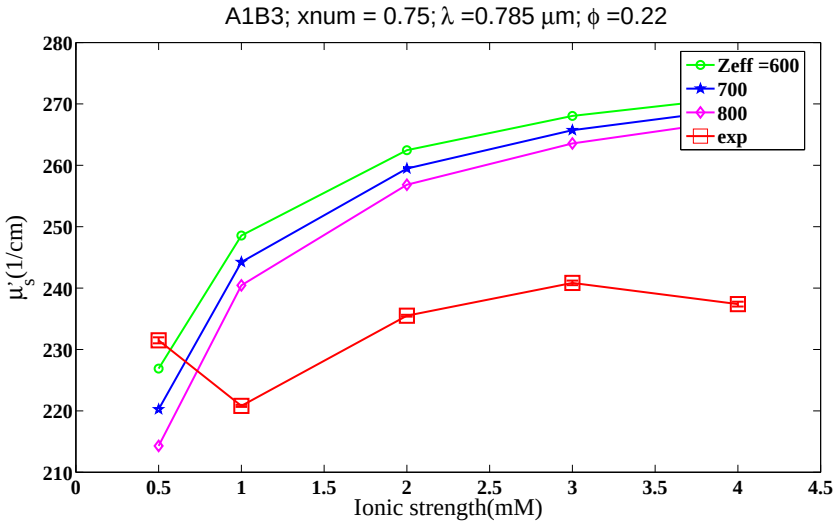

(c) $\lambda = 785$

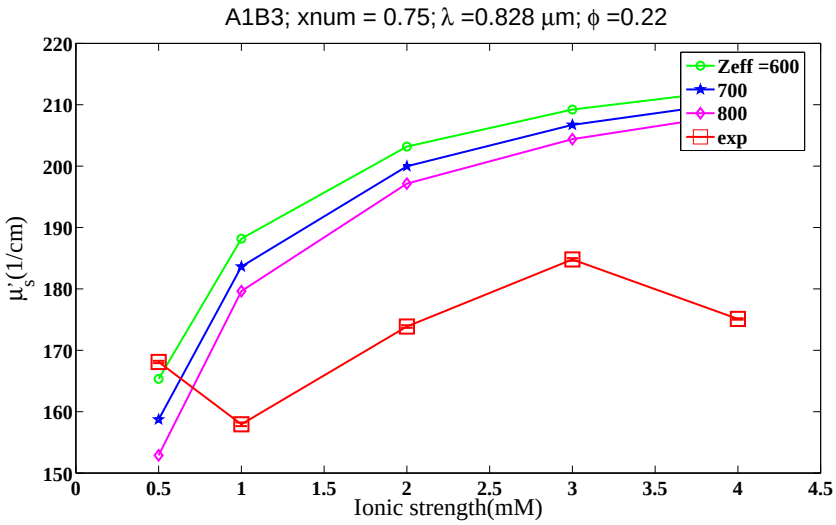

(d) $\lambda = 828$

Fig. 74.: Continued.

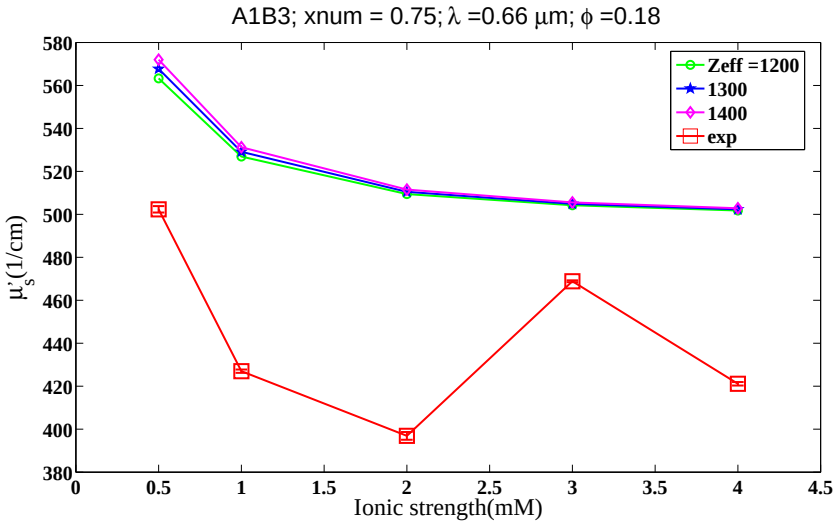

(a) $\lambda = 660$

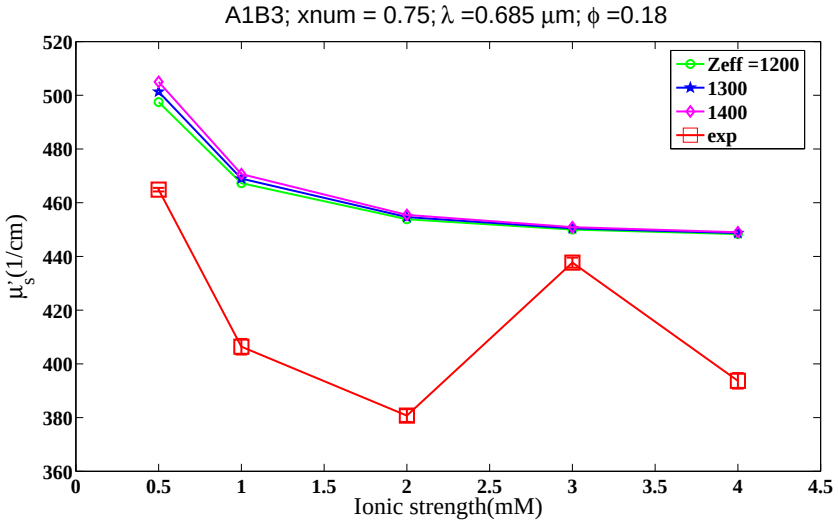

(b) $\lambda = 685$

Fig. 75.: Isotropic scattering coefficient measurements versus ionic strength of a bidisperse mixture of polystyrene latexes. Open squares connected with solid lines are experimental measurements and points connected with solid lines are numerical solution of the OZ equation with Yukawa potential and HNC closure. The particle sizes are $\sigma = 144nm$ and $\sigma = 223nm$, at a volume fraction of $\phi = 0.18$, $x_{num} = 0.75$ and ionic strengths of 0.5,1,2,3 and 4mM at (a)$\lambda = 660$,(b)$\lambda = 685$, (c)$\lambda = 785$ and (d)$\lambda = 828$nm.

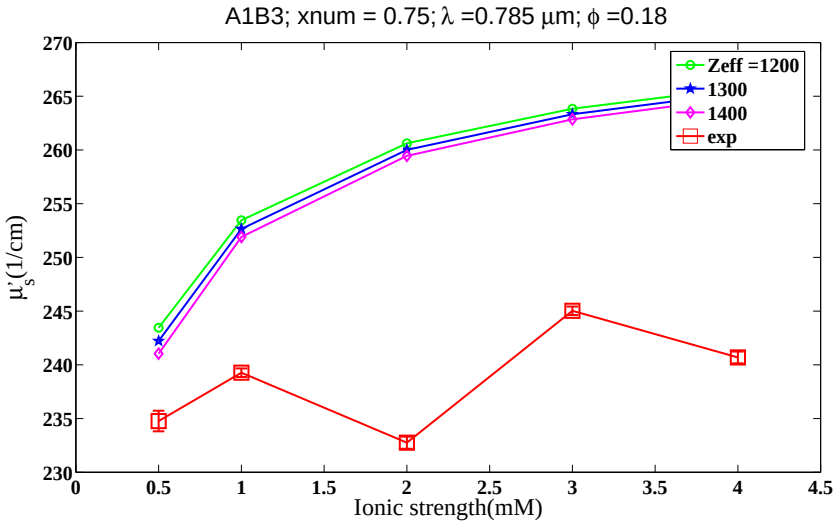

(c) $\lambda = 785$

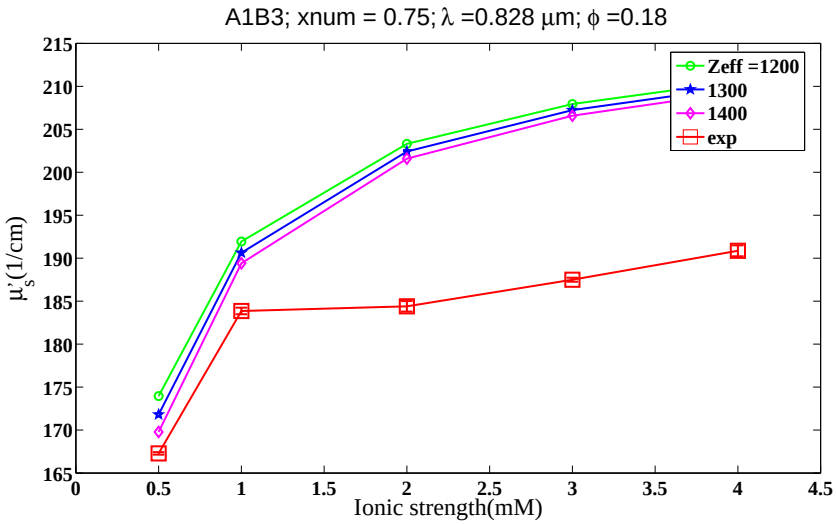

(d) $\lambda = 828$

Fig. 75.: Continued.

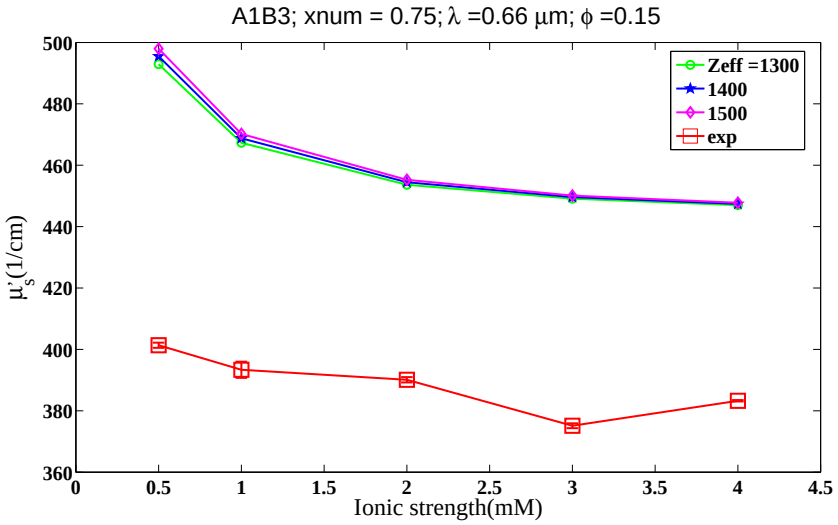

(a) $\lambda = 660$

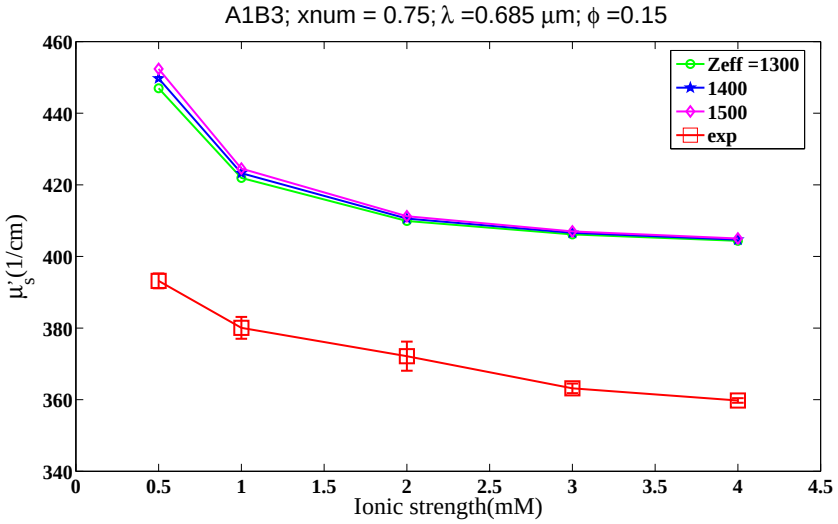

(b) $\lambda = 685$

Fig. 76.: Isotropic scattering coefficient measurements versus ionic strength of a bidisperse mixture of polystyrene latexes. Open squares connected with solid lines are experimental measurements and points connected with solid lines are numerical solution of the OZ equation with Yukawa potential and HNC closure. The particle sizes are $\sigma = 144nm$ and $\sigma = 223nm$, at a volume fraction of $\phi = 0.15$, $x_{num} = 0.75$ and ionic strengths of 0.5,1,2,3 and 4mM at (a)$\lambda = 660$,(b)$\lambda = 685$, (c)$\lambda = 785$ and (d)$\lambda = 828$nm.

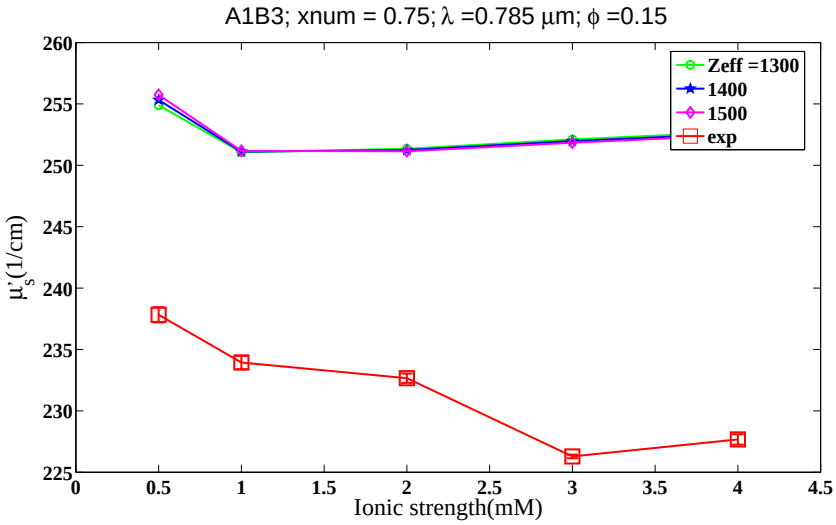

(c) $\lambda = 785$

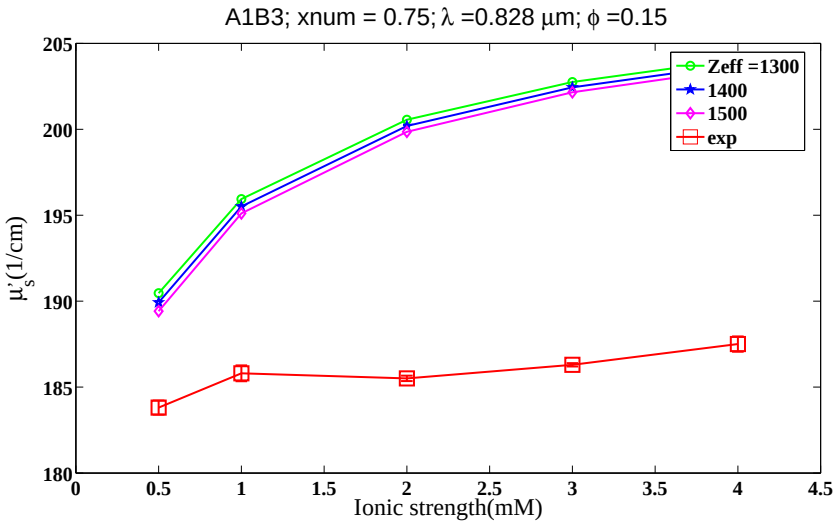

(d) $\lambda = 828$

Fig. 76.: Continued.

F. Summary

Frequency domain photon migration measurements are found to be sensitive to changing ionic strengths in colloidal dispersions, as well as changes in the medium with respect to the size of the particles. The data found from experiment are found to have similar trends with model predicted data and the differences observed can be due to incorrect refractive indices or the models inaccuracy to predict changes in the structure.

The experiments on dense bidisperse dispersions at high concentrations are first of their kind and the recovery of essential parameters from the experimental data by inversion techniques needs better solvers for the OZ equations. The effective charge values on the particles are found to increase with increasing ionic strength, as can be observed from the isotropic scattering coefficients. Even though at this stage the effective charge values are not recovered by inversion techniques, the possibility of obtaining the effective charge values from inversion techniques was not ruled out. The technique of global optimization and finding the global minimum may be used to obtain the size and the charge values for the bidisperse mixture.

CHAPTER IX

FUTURE WORK

1. Better, faster solvers for the Ornstein Zernike equations and include polydispersity in numerical solutions to understand the effects on the isotropic scattering coefficient.

2. Thermodynamic calculations for mixtures and compare with available macroscopic measurement techniques such as osmotic pressure and rheological measurements, which can be correlated with isotropic scattering data from Frequency Domain Photon Migration measurements.

3. Include attractive forces in the simulations and predict structure factors for attractive potential systems, and hence a complete representation of the DLVO potential.

4. Recovery of particle sizes for bimodal distributions of particles and use of Bspline basis functions to eliminate the use of known distributions to represent particle size polydispersity.

5. Estimation of refractive indices from commercial instruments to accurately represent sample details in problems.

6. Absorption properties to be modelled for multiwavelength measurements.

7. Incorporate Ewald summation techniques to correct or check for any discrepancies with results obtained from truncation of potential.

CHAPTER X

SUMMARY AND CONCLUSIONS

This research work summarizes the possible ways of obtaining the structure factors for concentrated dispersions, where interactions play an important role in particle positional correlations. Monte Carlo simulations provided the structure factors of concentrated dispersions to the highest volume fractions and charge values of the particles. Corresponding numerical solutions of the Ornstein Zernike equations, were found to be exactly similar to the results found from Monte Carlo simulations, for cases of Yukawa potentials and closure models of Hypernetted Chain and Percus Yevick. The Ornstein Zernike equations were found to be less stable and do not converge for very high volume fractions and charge values. Consequently Monte Carlo simulations were resorted to for a solution. Analytical solutions of the Ornstein Zernike equations, using the Mean Spherical Approximation were found to be inaccurate when compared for monodisperse dispersions and no solution could be obtained for bidisperse dispersions.

We show FDPM measurements to be sensitive to changing electrostatic interactions, at low ionic strengths of dispersions, in monodisperse as well as bidisperse dispersions.

For the case of monodisperse dispersions the changes in the isotropic scattering coefficient with changing ionic strength were found to be sensitive and accurate with the available models of predicting the isotropic scattering coefficient. For the dense dispersions particle diameter $\sigma = 144$ nm, the isotropic scattering coefficient increased with ionic strength, consistent with predictions from forward models of the isotropic scattering coefficient. For dense dispersions particle diameter $\sigma = 223$ nm, we found that at 660 and 685nm wavelengths isotropic scattering coefficient decreased as the

ionic strength of the dispersion increased and at wavelengths of 785 & 828nm, the trend was reversed. The isotropic scattering coefficients are found to be appreciably different from model predictions. The differences are attributed to refractive indices as parameters for computing μ_s, and possible over predictions of structure changes from structure factor models.

FDPM measurements have shown sensitivity to changing ionic strengths in bidisperse dispersions, and the isotropic scattering coefficients displayed similar trends as those predicted by the OZ solution of the HNC closure and HSY potential. The variation in trends with ionic strength in the dispersions was captured effectively with model predictions, and the discrepancy at lower wavelengths is attributed to incorrect refractive indices, and over predictions of structure from forward models. The fluctuations in the isotropic scattering coefficients, observed for A1B3 mixtures may be due to the mixed regions of the structure factor being explored, and the presence of two different sized particles in the dispersions. There is consistency among the experimental results at two different wavelengths and hence the measurement data cannot be ruled out to have artifacts. Polydispersity could be modelled using a distribution of particles and the methodology for bidisperse mixtures with binary Yukawa potential and HNC closure or from MC simulations using a distribution of particles. The variation in isotropic scattering coefficient data could be highly dependent upon the amount of polydispersity of the dispersion.

Polydisperse dispersions at high ionic strengths, have been modelled with the polydisperse Percus Yevick Hard Sphere models, and the experimental data from seven different wavelengths were modelled using the PYHS theory. The particle size distribution was obtained for dense dispersions, using experimental measurements and nonlinear inversion techniques, by which the global optimum was sought through the use of genetic algorithms. The volume fraction of the dispersions was also kept

as unknown and a range of values was specified for the global minimization routines. The particle size distribution was recovered accurately in comparison with dynamic light scattering measurement, which obtains the particle size distribution for dilute dispersions of particles, and the recovered volume fractions were found to be close to those obtained from evaporation measurements.

The characterization methods developed for FDPM measurements may help to determine the effective charge on the particles within dense dispersions, or at best reveal a range of values for the effective charge. The current algorithms for solving the OZ equations can work in real time for monodisperse dispersions and for a few number ratios of particles in bidisperse dispersions, enabling forward comparisons and future inverse analysis.

REFERENCES

[1] J. Lewis, "Colloidal processing of ceramics," *Journal of American Ceramic Society*, vol. 83, no. 10, pp. 2341–2359, 2000.

[2] A. Rogach, A. Susha, F. Caurso, G. Sukhorukov, A. Kornowski, S. Kershaw, H. Mohwald, A. Echymuller, and H. Weller, "Nano and microengineering: Three dimensional colloidal photonic crystals prepared from submicrometer-sized polystyrene latex spheres pre-coated with luminescent polyelectrolyte/nanocrystal shells," *Advanced Materials*, vol. 12, no. 5, pp. 333–337, 2000.

[3] V. Tohver, J. Smay, A. Braem, P. Braun, and J. Lewis, "Nanoparticle halos: A new colloid stabilization mechanism," *Proceedings of the National Academy of Sciences*, vol. 98, no. 16, pp. 8950–8954, 2001.

[4] J. Smay, J. Cesarano III, and J. Lewis, "Colloidal inks for directed assembly of 3-d periodic structures," *Langmuir*, vol. 18, pp. 5429–5437, 2002.

[5] W. Lee, A. Chan, M. Bevan, J. Lewis, and P. Braun, "Nanoparticle-mediated epitaxial assembly of colloidal crystals on patterned substrates," *Langmuir*, vol. 20, pp. 5262–5270, 2004.

[6] R. Langer, "New methods of drug delivery," *Science*, vol. 249, no. 4976, pp. 1527–1533, 1990.

[7] W. Russel, D. Saville, and W. Schowalter, *Colloidal Dispersions*. New York, NY: Cambridge University Press, 1989.

[8] K. Milton, *The Scattering of Light and Other Electromagnetic Radiation*. New York, NY: Academic Press, 1969.

[9] C. Bohren and D. Huffman, *Absorption and Scattering of Light by Small Particles*. New York, NY: John Wiley and Sons, 1983.

[10] H. Van De Hulst, *Light Scattering by Small Particles*. New York, NY: Dover Publication, 1981.

[11] Y. Huang and E. Sevick-Muraca, "Validating the assumption to the interference approximation by use of measurements of absorption efficiency and hindered scattering in dense dispersions," *Applied Optics*, vol. 43, no. 4, pp. 814–819, 2004.

[12] R. Hunter, *Foundations of Colloid Science Vol 2*. New York, NY: Oxford Science Publications, 1986.

[13] J. Mendez-Alcaraz and R. Klein, "Depletion forces in colloidal mixtures," *Physical Review E*, vol. 61, no. 4, pp. 4095–4099, 2000.

[14] R. Castaneda-Priego, A. Rodriguez-Lopez, and J. Mendez-Alcaraz, "Depletion forces in two dimesional colloidal mixtures," *Journal of Physics: Condensed Matter*, vol. 15, pp. S3393–S3409, 2003.

[15] S. Asakura and F. Oosawa, "Interaction between particles suspended in solutions of macromolecules," *Journal of Polymer Science*, vol. 33, p. 183, 1958.

[16] R. Ottewill, "Colloidal dispersions," *Faraday Discussions of the Chemical Society*, vol. 90, pp. 1–15, 1990.

[17] T. Tadros and A. Hopkinson, "Use of viscoelastic measurements for investigating the stability/flocculation of concentrated dispersions," *Faraday Discussions of the Chemical Society*, vol. 90, pp. 41–55, 1990.

[18] R. Buscall, J. Goodwin, M. Hawkins, and R. Ottewill, "Viscoelastic properties of concentrated latices," *Journal of chemical society, Faraday transactions 1*, vol. 78, pp. 2873–2887, 1978.

[19] J. Brady, "The rheological behavior of concentrated colloidal dispersions," *Journal of Chemical Physics*, vol. 99, no. 1, pp. 567–581, 1993.

[20] J. Goodwin and R. Ottewill, "Properties of concentrated colloidal dispersions," *Journal of Chemical Society. Faraday Transactions*, vol. 87, no. 3, pp. 357–369, 1991.

[21] D. Oxtoby, "New perspectives on freezing and melting," *Nature*, vol. 347, pp. 725–730, 1990.

[22] D. Quemada and C. Berli, "Energy of interaction in colloids and its implications in rheological modeling," *Advances in Colloid and Interface Science*, vol. 98, pp. 51–85, 2002.

[23] R. Ottewill, A. Parentich, and R. Richardson, "Osmotic pressure measurements on strongly interacting poymer colloid dispersions," *Colloids and Surfaces: Physicochemical and Engineering Aspects*, vol. 161, pp. 231–242, 2000.

[24] M. Kotlarchyk and S. Chen, "Analysis of small angle neutron scattering spectra from polydisperse interacting colloids," *Journal of Chemical Physics*, vol. 79, no. 5, pp. 2461–2469, 1983.

[25] L. Cannavacciuolo, C. Sommer, J. Pedersen, and P. Schurtenberger, "Size, flexibility, and scattering functions of semiflexible polyelectrolytes with excluded volume effects: Monte Carlo simulations and neutron scattering experiments," *Physical Review E*, vol. 62, no. 4, pp. 5409–5419, 2000.

[26] J. Brunner-Popela and O. Glatter, "Small-angle scattering of interacting particels. I. Basic principles of a global evaluation technique," *Journal of Applied Crystallography*, vol. 30, pp. 431–442, 1997.

[27] B. Weyerich, J. Brunner-Popela, and O. Glatter, "Small-angle scattering of interacting particels. II. Generalized indirect fourier transformation under considerations of the effective structure factor for polydisperse systems," *Journal of Applied Crystallography*, vol. 32, pp. 197–209, 1999.

[28] A. Guinier and G. Fournet, *Small-angle scattering of X-Rays*. New York, NY: John Wiley, 1955.

[29] C. Robertus, W. Philipse, J. Joosten, and Y. Levine, "Solution of the percus-yevick approximation of the multicomponent adhesive spheres system applied to the small angle x-ray scattering from microemulsions," *Journal of Chemical Physics*, vol. 90, no. 8, pp. 4482–4490, 1989.

[30] B. Berne and R. Pecora, *Dynamic Light Scattering*. New York, NY: Dover Publications, 1976.

[31] C. Johnson and D. Gabriel, *Laser Light Scattering*. New York, NY: Dover Publications, 1981.

[32] J. Duderstadt and L. Hamilton, *Nuclear Reactor Analysis*. New York, NY: Wiley Publications, 1976.

[33] J. Fishkin and E. Gratton, "Propagation of photon-density waves in strongly scattering media containing an absorbing semi-infinite plane bounded by a straight edge," *J. Opt. Soc. Am. A*, vol. 10, no. 1, pp. 127–139, 1993.

[34] A. Ishimaru, "Theory and application of wave propagation and scattering in random media," *Proceedings of the IEEE*, vol. 65, no. 7, pp. 1030–1061, 1977.

[35] M. Patterson, B. Chance, and B. Wilson, "Time resolved reflectance and transmittance for the non-invasive measurement of tissue optical properties," *Applied Optics*, vol. 28, pp. 2331–2336, 1989.

[36] A. Ishimaru, *Wave Propagation and Scattering in Random Media*. New York, NY: Academic Press, 1978.

[37] D. Weitz and D. Pine, *Diffusing- Wave Spectroscopy in Dynamic Light Scattering:The method and some applications, Monographs on the physics and the chemistry of materials, 49*. Oxford, UK: Clarendon Press, 1995.

[38] A. Ishimaru, "Optical multiple scattering by particles," *Part. Part. Sys. Charact.*, vol. 11, pp. 183–188, 1994.

[39] X. Qiu, X. Wu, J. Xue, D. Pine, D. Weitz, and P. Chaikin, "Hydrodynamic interactions in concentrated suspensions," *Physical Review Letters*, vol. 65, no. 4, pp. 516–519, 1990.

[40] P. Kaplan, A. Dinsmore, A. Yodh, and D. Pine, "Diffuse-transmission spectroscopy: A structural probe of opaque colloidal mixtures," *Physical Review E*, vol. 50, no. 6, pp. 4827–4835, 1994.

[41] R. Garg, R. Prud'homme, I. Aksay, F. Liu, and R. Alfano, "Optical transmission in highly concentrated dispersions," *Journal of Optical Society of America A*, vol. 15, no. 4, pp. 932–935, 1998.

[42] P. Saulnier, M. Zinkin, and G. Watson, "Scatterer correlation effects on photon transport in dense random media," *Physical Review B*, vol. 42, pp. 2621–2623,

1990.

[43] P. Wolf, G. Maret, E. Akkermans, and R. Maynard, "Optical coherent backscattering by random media: An experimental study," *Journal of Physics France*, vol. 49, pp. 63–75, 1988.

[44] P. Wolf, G. Maret, E. Akkermans, and R. Maynard, "Theoretical study of coherent backscattering of light by disordered media," *Journal of Physics France*, vol. 49, pp. 77–98, 1988.

[45] Z. Sun, Y. Huang, and E. Sevick-Muraca, "Precise analysis of frequency domain photon migration measurement for characterization of concentrated colloidal suspensions," *Review of Scientific Instruments*, vol. 73, no. 2, pp. 383–393, 2002.

[46] J. Fishkin, T. Peter, A. Cerussi, S. Fantini, M. Franceschini, and E. Gratton, "Frequency-domain method for measuring spectral properties in multiple-scattering media: Methemoglobin absorption spectrum in a tissue like phantom," *Applied Optics*, vol. 34, no. 7, pp. 1143–1155, 1995.

[47] Z. Sun, C. Tomlin, and E. Sevick-Muraca, "Investigation of particle interactions in concentrated colloidal suspensions using frequency domain photon migration: Monodisperse system," *Journal of Colloid and Interface Science*, vol. 245, pp. 281–291, 2002.

[48] S. Banerjee, R. Shinde, and E. Sevick-Muraca, "Probing static structure of colloid-polymer suspensions with multiply scattered light," *Journal of Colloid and Interface Science*, vol. 209, pp. 142–153, 1999.

[49] R. Shinde, G. Balgi, S. Banerjee, S. Richter, J. Reynolds, J. Pierce, and

E. Sevick-Muraca, "Investigation of static structure factor in dense suspensions by use of multiply scattered light," *Applied Optics*, vol. 38, no. 1, pp. 197–204, 1999.

[50] A. Dukhin and P. Goetz, "Acoustic spectroscopy for concentrated polydisperse colloids with high density contrast," *Langmuir*, vol. 12, pp. 4987–4997, 1996.

[51] A. Dukhin and P. Goetz, "Acoustic spectroscopy for concentrated polydisperse colloids with low density contrast," *Langmuir*, vol. 12, pp. 4998–5003, 1996.

[52] A. Dukhin and P. Goetz, "Acoustic and electroacoustic spectroscopy," *Langmuir*, vol. 12, pp. 4336–4344, 1996.

[53] R. Hunter, "Recent developments in the electroacoustic characterisation of colloidal suspensions and emulsions," *Colloids and Surfaces A*, vol. 141, no. 1, pp. 37–65, 1998.

[54] M. Allen and D. Tildesley, *Computer Simulation of Liquids*. New York, NY: Oxford Science Publications, 1987.

[55] M. Gillan, "A new method of solving the liquid structure integral equations," *Molecular Physics*, vol. 38, no. 6, pp. 1781–1794, 1979.

[56] J. Herrera, P. Cummings, and H. Ruiz-Estrada, "Static structure factor for simple liquid metals," *Molecular Physics*, vol. 96, no. 5, pp. 835–847, 1999.

[57] Y. Rosenfeld, "Ewald method for simulating Yukawa systems," *Molecular Physics*, vol. 88, no. 5, pp. 1357–1363, 1996.

[58] A. Giacometti, D. Gazzillo, G. Pastore, and T. Das, "A numerical study of binary Yukawa model in regimes characteristic of globular proteins in solution," *Physical Review E*, vol. 71, no. 3, pp. 031108–031108–10, 2005.

[59] J. Salacuse, A. Denton, and P. Egelstaff, "Finite-size effects in molecular dynamics simulations: Static structure factor and compressibility. I Theoretical method," *Physical Review E.*, vol. 53, no. 3, pp. 2382–2389, 1996.

[60] J. Salacuse, A. Denton, P. Egelstaff, M. Tau, and L. Reatto, "Finite-size effects in molecular dynamics simulations: Static structure factor and compressibility. II application to a model krypton fluid," *Physical Review E.*, vol. 53, no. 3, pp. 2390–2401, 1996.

[61] J. Salacuse and P. Egelstaff, "Finite-size effects in molecular dynamics simulations: Intermediate scattering function and the velocity of sound. III theory and application to a model krypton fluid," *Physical Review E.*, vol. 64, pp. 051201–1–051201–10, 2001.

[62] N. Ashcroft and D. Langreth, "Structure of binary liquid mixtures. I*," *Physical Review*, vol. 156, no. 3, pp. 685–692, 1967.

[63] R. Hunter, *Foundations of Colloid Science Vol 1.* New York, NY: Oxford Science Publications, 1986.

[64] D. Frenkel, R. Vos, C. Kruif, and A. Vrij, "Structure factors of polydisperse systems of hard spheres: A comparison of Monte Carlo simulations and percusyevick theory," *Journal of Chemical Physics*, vol. 84, no. 8, pp. 4625–4630, 1986.

[65] F. Lado, "Numerical fourier transforms in one, two and three dimensions for liquid state calculations," *Journal of Computational Physics*, vol. 8, pp. 417–433, 1971.

[66] M. Lotfollahi and H. Modarress, "Solving integral equations for binary and

ternary systems," *Journal of Chemical Physics*, vol. 116, no. 6, pp. 2487–2492, 2002.

[67] G. Abernethy and M. Gillan, "A new method of solving the HNC equation for ionic liquids," *Molecular Physics*, vol. 39, no. 4, pp. 839–847, 1980.

[68] L. Lloyd, *Molecular Thermodynamics of Non Ideal Fluids*. Oxford, UK: Butterworth Heinemann, Butterworths series in Chemical Engineering, 1988.

[69] E. Kuwana and E. Sevick-Muraca, "Flourescence lifetime spectroscopy for ph sensing in multiply scattering media with dyes exhibiting multi-exponential decay kinetics," *Biophysical Journal*, vol. 83, pp. 1165–1176, 2002.

[70] Y. Gong and K. Nakashima, "Characterization of polystyrene latex surfaces by conductometric titration, Rhodamine 6G adsorption, and electrophoresis measurements," *Langmuir*, vol. 16, pp. 8546–8548, 2000.

[71] Y. Gong and K. Nakashima, "A novel method to determine the effective charge of polystyrene latex particles in aqueous dispersion," *Langmuir*, vol. 17, pp. 2889–2892, 2001.

[72] M. Labib and A. Robertson, "The conductometric titration of latices," *Journal of Colloid and Interface science*, vol. 77, no. 1, pp. 151–161, 1980.

[73] J. Stone-Masui and A. Watillon, "Characterization of surface charge on polystyrene surfaces," *Journal of Colloid and Interface Science*, vol. 52, no. 3, pp. 479–503, 1975.

[74] M. Wilkinson, J. Hearn, and P. Steward, "The cleaning of polymer colloids," *Advances in Colloid and Interface Science*, vol. 81, pp. 77–165, 1999.

[75] T. Allen, *Particle Size Measurement*. New York, NY: Kluwer Academic Publishers, 1997.

[76] G. Elicabe and L. Garcia-Rubio, "Latex particle size distribution from turbidimetric measurements," *Polymer Characterization, Advances in Chemistry Series*, vol. 227, pp. 83–104, 1990.

[77] H. Frock, "Particle-size determination using angular light - scattering," *ACS Sym Series*, vol. 146-160, p. 332, 1987.

[78] M. Jones, B. Curry, M. Brewster, and K. Leong, "Inversion of light-scattering measurements for particle size and optical constants: Theoretical study," *Applied Optics*, vol. 33, no. 18, pp. 4025–4034, 1994.

[79] D. Horne and C. Davidson, "Application of diffusing wave spectroscopy to particle sizing in concentrated dispersions," *Colloids and Surfaces A*, vol. 77, pp. 1–8, 1993.

[80] F. Scheffold, "Particle sizing with diffusing wave spectroscopy," *Journal of dispersion science and technology*, vol. 23, no. 5, pp. 591–599, 2002.

[81] Z. Sun, C. Tomlin, and E. Sevick-Muraca, "Approach for particle sizing in dense polydisperse colloidal suspension using multiple scattered light," *Langmuir*, vol. 17, pp. 6142–6147, 2001.

[82] D. McClements, "Principles of ultrasonic droplet size determination in emulsions," *Langmuir*, vol. 12, no. 14, pp. 3454–3461, 1996.

[83] F. Alba, G. Crawley, J. Fatkin, D. Higgs, and P. Kippax, "Acoustic spectroscopy as a technique for the particle sizing of high concentration colloids, emulsions and suspensions," *Colloids and Surfaces A*, vol. 153, pp. 495–502, 1999.

[84] K. Alexander, G. Storti, and M. Morbidelli, "Particle sizing in colloidal dispersions by ultrasound. model calibration and sensitivity analysis," *Langmuir*, vol. 15, pp. 2338–2345, 1999.

[85] V. Meeren, M. Statsny, J. Vanderdeelen, and L. Baert, "Particle sizing of concentrated emulsions using fibre optic quasi-elastic light scattering," *Colloids and Surfaces A: Physicochemical and Engineering Aspects*, vol. 76, pp. 125–133, 1993.

[86] H. Dhadwal, R. Ansari, and W. Meyer, "A fiber-optic probe for particle sizing in concentrated suspension," *Review of Scientific Instruments*, vol. 62, no. 12, pp. 2963–2968, 1991.

[87] C. Urban and P. Schurtenberger, "Characterization of turbid colloidal suspensions using light scattering techniques combined with cross-correlation methods," *Journal of Colloid and Interface Science*, vol. 207, pp. 150–158, 1998.

[88] P. Segre, W. Megen, P. Pusey, K. Schatzel, and W. Peters, "Two-colour dynamic light scattering," *Journal of Modern Optics*, vol. 42, no. 9, pp. 1929–1952, 1995.

[89] Z. Sun and E. Sevick-Muraca, "Inversion algorithms for particle sizing with photon migration measurement," *AIChE J*, vol. 47, p. 148, 2001.

[90] Y. Huang, Z. Sun, and E. Sevick-Muraca, "Assessment of electrostatic interactions in dense colloidal suspensions with multiply scattered light," *Langmuir*, vol. 18, pp. 2048–2053, 2002.

[91] M. Gerkin and G. Faris, "High-precision frequency-domain measurements of the optical properties of turbid media," *Optics Letters*, vol. 24, no. 14, pp. 930–932, 1999.

[92] A. Yodh, P. Kaplan, and D. Pine, "Pulsed diffusing-wave spectroscopy: High resolution through nonlinear optical gating," *Physical Review B*, vol. 42, no. 7, pp. 4744–4747, 1990.

[93] A. Tarantola, *Inverse Problem Theory and Methods for Model Parameter Estimation*. Philadelphia, PA: SIAM, 2005.

[94] A. Tarantola and B. Valette, "Generalized non linear inverse problems solved using the least squares criterion," *Reviews of Geophysics and Space Physics*, vol. 20, no. 2, pp. 219–232, 1982.

[95] A. Tarantola and B. Valette, "Inverse problems quest for information," *Journal of Geophysics*, vol. 50, pp. 159–170, 1982.

[96] K. Mosegaard and A. Tarantola, "Monte Carlo sampling of solutions to inverse problems," *Journal of Geophysical Research*, vol. 100, no. B7, pp. 12431–12447, 1995.

[97] R. Sanchez and N. McCormick, "Numerical evaluation of optical single-scattering properties using multiple-scattering inverse transport methods," *Journal of Quantitative Spectroscopy and Radiative Transfer*, vol. 28, no. 3, pp. 169–184, 1982.

[98] D. Ligon, J. Gillespie, and P. Pellegrino, "Aerosol properties from spectral extinction and backscatter estimated by an inverse Monte Carlo method," *Applied Optics*, vol. 39, no. 24, pp. 4402–4410, 2000.

[99] Z. Sun and E. Sevick-Muraca, "Investigation of particle interactions in dense colloidal suspensions using frequency domain photon migration: Bidisperse systems," *Langmuir*, vol. 18, pp. 1091–1097, 2002.

[100] E. Sevick-Muraca, E. Pierce, H. Jiang, and J. Kao, "Photon migration measurement of latex size distribution in concentrated suspensions," *AIChE J.*, vol. 43, p. 655, 1997.

[101] G. Balgi, J. Reynolds, R. Mayer, R. Cooley, and E. Sevick-Muraca, "Measurements of multiply scattered light for online monitoring of changes in size distribution of cell debris suspension," *Biotechnology Progress*, vol. 15, pp. 1106–1114, 1999.

[102] H. Jiang, G. Marquez, and L. Wang, "Particle sizing in concentrated suspensions by use of steady-state, continuous-wave photon-migration techniques," *Optics letters*, vol. 23, no. 5, pp. 394–396, 1998.

[103] D. Goldberg, *Genetic Algorithms in Search, Optimization and Machine Learning*. Boston, MA: Addison-Wesley Pub Co, 1989.

[104] M. Ye, S. Wang, Y. Lu, T. Hu, Z. Zhu, and X. Yiqian, "Inversion of particle-size distribution from angular light scattering data with genetic algorithms," *Applied Optics*, vol. 38, no. 12, pp. 2677–2685, 1999.

[105] G. Stell and L. Blum, "Polydisperse systems I: Scattering function for polydisperse fluids of hard or permeable spheres," *Journal of Chemical Physics*, vol. 71, no. 1, pp. 42–46, 1979.

[106] A. Yu and N. Standish, "A study of particle size distributions," *Powder Technology*, vol. 62, pp. 101–118, 1990.

[107] C. Houck, J. Joines, and M. Kay, "A genetic algorithm for function optimization: A matlab implementation," *ACM transactions on mathematical software, http://ie.ncsu.edu/mirage/GAOToolbox/gaot/*, 1995.

[108] Z. Michalewicz, D. Logan, and S. Swaminathan, "Evolutionary operators for continuous convex parameter spaces," *Proceedings of the Third Annual Conference on Evolutionary Programming, World Scientific Publishing, River Edge, NJ*, pp. 84–97, 1994.

[109] Y. Huang, V. Yuwono, and E. Sevick-Muraca, "Modification of electrostatic interaction by Rhodamine 6G adsorption on polystyrene latex as assessed by frequency domain photon migration," *Langmuir*, vol. 18, pp. 9192–9197, 2002.

[110] Y. Huang and E. Sevick-Muraca, "Characterization of pigment particle absorption efficiencies using frequency domain photon migration," *Analytical Chemistry*, vol. 75, pp. 6958–6962, 2003.

[111] Y. Huang and E. Sevick-Muraca, "Assessment of small-angle and angle-averaged structure factor for monitoring electrostatic colloidal interactions using multiply scattered light," *Journal of Colloid and Interface science*, vol. 251, pp. 434–442, 2002.

[112] E. Verwey and J. Overbeek, *Theory of the Stability of Lyophobic Colloids.* Amsterdam: Elsevier, 1948.

[113] C. Hoheisel and R. Zhang, "Structure and phase-separation behavior of Yukawa mixtures studied by the Mean-Spherical Approximation and computer calculations ," *Physical Review A*, vol. 43, no. 10, pp. 5332–5335, 1991.

[114] D. Cebula, J. Goodwin, G. Jeffrey, R. Ottewill, A. Parentich, and R. Richardson, "Properties of concentrated polystyrene latex dispersions," *Faraday Discussions of the Chemical Society*, vol. 76, pp. 37–52, 1983.

[115] P. Pusey and W. Megen, "Phase behaviour of concentrated suspensions of nearly hard colloidal spheres," *Nature*, vol. 320, pp. 340–342, 1986.

[116] B. Tata, "Colloidal dispersions and phase transitions in charged colloids," *Current Science*, vol. 80, no. 8, pp. 948–958, 2001.

[117] S. Auer and D. Frenkel, "Crystallization of weakly charged colloidal spheres: A numerical study," *Journal of Physics: Condensed Matter*, vol. 14, pp. 7667–7680, 2002.

[118] F. Azhar, M. Baus, J. Ryckaert, and E. Meijer, "Line of triple points for hard core Yukawa fluid: A computer simulation study," *Journal of Chemical Physics*, vol. 112, no. 11, pp. 5121–5126, 2000.

[119] M. Robbins, K. Kremer, and G. Grest, "Phase diagram and dynamics of Yukawa systems," *Journal of Chemical Physics*, vol. 88, no. 5, pp. 3286–3312, 1988.

[120] E. Sirota, H. Ou-Yang, S. Sinha, P. Chaikin, J. Axe, and Y. Fujii, "Complete phase diagram of a charged colloidal system: A synchrotron x-ray scattering study," *Physical Review Letters*, vol. 62, no. 13, pp. 1524–1527, 1989.

[121] J. Dhont, S. Smits, and H. Lekkerkerker, "A time resolved static light scattering study on nucleation and crystallization in a colloidal system," *Journal of Colloid and Interface Science*, vol. 152, no. 2, pp. 386–401, 1992.

[122] T. Palberg, "Crystallization kinetics of repulsive colloidal spheres," *Journal of Physics: Condensed Matter*, vol. 11, pp. R323–R360, 1999.

[123] T. Ohtsuki, S. Mitaku, and K. Okano, "Studies of ordered monodisperse latexes. II theory of mechanical properties," *Japanese Journal of Applied Physics*, vol. 17, no. 4, pp. 627–635, 1978.

[124] M. Shigeki, T. Ohtsuki, K. Enari, A. Kishimoto, and K. Okano, "Studies of ordered monodisperse latexes. I shear ultrasonic measurements," *Japanese Journal of Applied Physics*, vol. 17, no. 2, pp. 305–313, 1978.

[125] M. Brunner, C. Bechinger, W. Strepp, V. Lobaskin, and H. Grunberg, "Density-dependent pair interactions in 2D colloidal suspensions," *Europhysics Letters*, vol. 58, no. 6, pp. 926–932, 2002.

[126] H. Versmold, U. Wittig, and W. Hartl, "Colloid particle charge determination via the structure factor S(Q)," *Journal of Chemical Physics*, vol. 95, no. 24, pp. 9937–9940, 1991.

[127] W. Hartl and H. Versmold, "Liquid-like ordered colloidal suspensions: The influence of the particle concentration," *Journal of Chemical Physics*, vol. 88, no. 11, pp. 7157–7161, 1988.

[128] A. Yethiraj and A. Blaaderen, "A colloidal model system with an interaction tunable from hard sphere to soft and dipolars," *Nature*, vol. 421, pp. 513–517, 2003.

[129] C. Royall, M. Leunissen, and A. Blaaderen, "A new colloidal model system to study long-range interactions quantitatively in real space," *Journal of Physics: Condensed Matter*, vol. 15, pp. S3581–S3596, 2003.

[130] J. Crocker and D. Grier, "Methods of digital video microscopy for colloidal studies," *Journal of Colloid and Interface science*, vol. 179, pp. 298–310, 1996.

[131] A. Larsen and D. Grier, "Like-charge attractions in metastable colloidal crystallites," *Nature*, vol. 385, pp. 230–233, 1997.

[132] U. Gasser, E. Weeks, A. Schofield, P. Pusey, and D. Weitz, "Real-space imaging of nucleation and growth in colloidal crystallization," *Science*, vol. 292, pp. 258–262, 2001.

[133] A. Blaaderen and P. Wiltzius, "Real-space structure of colloidal hard-sphere glasses," *Science*, vol. 270, no. 5239, pp. 1177–1179, 1995.

[134] N. Verhaegh and V. Blaaderen, "Dispersions of Rhodamine-labeled silica spheres: Synthesis, characterization, and flourescence confocal scanning laser microscopy," *Langmuir*, vol. 10, pp. 1427–1438, 1994.

[135] I. Piirma, *Emulsion Polymerization*. New York, NY: Academic Press, 1982.

[136] S. Alexander, P. Chaikin, P. Grant, G. Morales, and P. Pincus, "Charge renormalization, osmotic pressure, and bulk modulus of colloidal crystals: Theory," *Journal of Chemical Physics*, vol. 80, no. 11, pp. 5776–5781, 1984.

[137] L. Belloni, M. Drifford, and P. Turq, "Counterion diffusion in polyelectrolyte solutions," *Chemical Physics*, vol. 83, pp. 147–154, 1984.

[138] E. Trizac, M. Aubouy, and L. Bocquet, "Analytical estimation of effective charges at saturation in poisson-boltzmann cell models," *Journal of Physics: Condensed Matter*, vol. 15, pp. S291–S296, 2003.

[139] E. Trizac, L. Bocquet, M. Aubouy, and H. Grunberg, "Alexander's prescription for colloidal charge renormalization," *Langmuir*, vol. 19, pp. 4027–4033, 2003.

[140] D. Nikolov and C. Ivanov, "Optical plastic refractive measurements in the visible and near infrared regions," *Applied Optics*, vol. 99, no. 13, pp. 2067–2070, 2000.

[141] J. Gilchrist, A. Chan, E. Weeks, and J. Lewis, "Phase behavior and 3d structure of strongly attractive microsphere-nanoparticle mixtures," *Langmuir*, vol. 21, no. 24, pp. 11040–11047, 2005.

[142] R. Ottewill, H. Hanley, A. Rennie, and G. Straty, "Small-angle neutron scattering studies on binary mixtures of charged particles," *Langmuir*, vol. 11, pp. 3757–3765, 1995.

[143] N. Lutterbach, H. Versmold, V. Reus, L. Belloni, and T. Zemb, "Charge-stabilized liquid like ordered binary colloidal suspensions. 1. ultra-small-angle x-ray characterization," *Langmuir*, vol. 15, pp. 337–344, 1999.

[144] N. Lutterbach, H. Versmold, V. Reus, L. Belloni, T. Zemb, and P. Lindner, "Charge-stabilized liquid like ordered binary colloidal suspensions. 2. partial structure factors determined by small-angle neutron scattering," *Langmuir*, vol. 15, pp. 345–352, 1999.

[145] P. Kaplan, A. Yodh, and D. Pine, "Diffusion and structure in dense binary suspensions," *Physical Review Letters*, vol. 68, no. 3, pp. 393–396, 1992.

[146] J. Hoye and L. Blum, "Solution of the Ornstein-Zernike equation with Yukawa closure for a mixture," *Journal of Statistical Physics*, vol. 19, no. 4, pp. 317–324, 1978.

[147] J. Hoye and L. Blum, "Solution of the Yukawa closure of the Ornstein-Zernike equation," *Journal of Statistical Physics*, vol. 16, no. 5, pp. 399–413, 1977.

[148] L. Blum, "Solution of the Ornstein-Zernike equation for a mixture of hard ions and Yukawa closure," *Journal of Statistical Physics*, vol. 22, no. 6, pp. 661–672, 1980.

[149] M. Ginoza, "Mean Spherical Approximation solution of Ornstein-Zernike equation in a charged hard sphere system with screened coulombic interactions," *Journal of the Physical Society of Japan*, vol. 54, no. 8, pp. 2783–2785, 1985.

[150] M. Ginoza, "Solution of the Ornstein-Zernike equation for a mixture of hard spheres with Yukawa closure: The case of factorizable coefficients," *Journal of the Physical Society of Japan*, vol. 55, no. 1, pp. 95–101, 1986.

[151] M. Ginoza and M. Yasutomi, "Analytical model of the static structure factor of a colloidal dispersion: Interaction polydispersity effect," *Molecular Physics*, vol. 93, no. 3, pp. 399–404, 1998.

[152] M. Ginoza and M. Yasutomi, "Static structure factor for a colloidal dispersion with size and charge polydispersities: Mean spherical approximation model in hard-sphere Yukawa fluids," *Physical Review E*, vol. 59, no. 2, pp. 2060–2066, 1999.

[153] O. Vazquez, J. Herrera, and L. Blum, "Static structure factor and thermodynamic properties of a binary Yukawa mixture," *Physica A*, vol. 325, pp. 319–332, 2003.

[154] S. Petris, J. Stankovich, D. Chan, and R. Ottewill, "Modeling the structure of charged binary colloidal dispersions," *Langmuir*, vol. 19, pp. 1121–1126, 2003.

[155] E. Arrieta, C. Jedrzejek, and K. Marsh, "Numerical MSA solution for binary Yukawa mixtures," *Journal of Chemical Physics*, vol. 86, no. 6, pp. 3607–3625, 1987.

[156] R. Krause, B. D'Aguanno, J. Mendez-Alcaraz, G. Nagele, R. Klein, and R. Weber, "Static structure factors of binary suspensions of charged polystyrene

spheres: Experiment against theory and computer simulation," *Journal of Physics: Condensed matter*, vol. 3, pp. 4459–4475, 1991.

[157] J. Mendez-Alcaraz, B. D'Aguanno, and R. Klein, "The structure of binary mixtures of charged colloidal suspensions," *Physica A*, vol. 178, pp. 421–443, 1991.

[158] G. Zerah, "An efficient newton's method for the numerical solution of fluid integral equations," *Journal of Computational Physics*, vol. 61, pp. 280–285, 1985.

[159] P. Salgi and R. Rajagopalan, "Polydispersity in colloids: Implications to static structure and scattering," *Advances in Colloid and Interface Science*, vol. 43, pp. 169–288, 1993.

[160] Z. Sun and E. Sevick-Muraca, "Investigation of structure factors in dense colloidal suspensions using frequency domain photon migration: Polydisperse systems," *Journal of Colloid and Interface Science*, vol. 270, pp. 329–336, 2004.

[161] S. Dali, J. Rasmussen, Y. Huang, R. Roy, and E. Sevick-Muraca, "Particle sizing in dense suspensions using multiwavelength frequency-domain photon migration measurements," *AIChE*, vol. 54, no. 4, pp. 1116–1124, 2005.

[162] A. Vrij, "Influence of polydispersity on the light scattering of concentrated dispersions of spherical particles," *Chemical Physics Letters*, vol. 53, no. 1, pp. 144–147, 1978.

[163] A. Vrij, "Mixtures of hard spheres in the percus-yevick approximation. light scattering at finite angles," *Journal of Chemical Physics*, vol. 71, no. 8, pp. 3267–3270, 1979.

[164] W. Griffith, R. Triolo, and A. Compere, "Analytical structure function of a polydisperse percus-yevick fluid with schulz(gamma) distributed diameters," *Physical Review A*, vol. 33, no. 3, pp. 2197–2200, 1986.

[165] S. Auer and D. Frenkel, "Suppression of crystal nucleation in polydisperse colloids due to increase of the surface free energy," *Nature*, vol. 413, no. 18, pp. 711–713, 2001.

[166] P. Bolhius and D. Kofke, "Monte Carlo study of freezing of polydisperse hard spheres," *Physical Review E*, vol. 54, no. 1, pp. 634–643, 1996.

[167] S. Heimer and D. Tezak, "Structure of polydispersed colloids characterized by light scattering and electron microscopy," *Advances in Colloid and Interface Science*, vol. 98, pp. 1–23, 2002.

[168] B. Aguanno and R. Klein, "Structural effects of polydispersity in charged colloidal dispersions," *Journal of Chemical Society Faraday Transactions*, vol. 87, no. 3, pp. 379–390, 1991.

[169] K. Ng, "Hypernetted chain solutions for the classical one-component plasma up to $\gamma = 7000$," *Journal of Chemical Physics*, vol. 61, no. 7, pp. 2680–2689, 1974.

[170] P. Beurten and A. Vrij, "Polydispersity effects in the small-angle scattering of concentrated solutions of colloidal spheres," *Journal of Chemical Physics*, vol. 74, no. 5, pp. 2744–2748, 1981.

[171] N. Wagner, R. Krause, A. Rennie, B. Aguanno, and J. Goodwin, "The microstructure of polydisperse, charged colloidal suspensions by light and neutron scattering," *Journal of Chemical Physics*, vol. 95, no. 1, pp. 494–508, 1991.

APPENDIX A

ANALYTICAL EXPRESSIONS FOR THE STRUCTURE FACTORS: HARD SPHERE

The analytical static structure factors are provided for monodisperse hard sphere Percus Yevick fluid, bidisperse Percus Yevick fluid and in the Mean Spherical Approximation (MSA) for the monodisperse Yukawa fluid.

Static structure factor: Monodisperse PYHS

$$\begin{aligned}\frac{1}{S(Q)} &= 1+\frac{24\phi}{x^3}\{a(\sin x - x\cos x)\\ &+ b[(\frac{2}{x^2}-1)x\cos x + 2\sin x - 2/x]\\ &+ \frac{\phi a}{2}[\frac{24}{x^3}+4(1-\frac{6}{x^2})\sin x\\ &- (1-\frac{12}{x^2}+\frac{24}{x^4})x\cos x]\}\end{aligned} \tag{A.1}$$

where $x \equiv Q\sigma$; $\phi = \frac{\pi\rho\sigma^3}{6}$; $a = (1+2\phi)^2(1-\phi)^{-4}$ and $b = -3\phi(\phi+2)^2/2(1-\phi)^4$

Static structure factor: Bidisperse PYHS

$$g_{11} = [(1+\frac{\eta}{2}) + \frac{3\eta_2}{2}(\alpha-1)](1-\eta)^{-2}$$

$$g_{22} = [(1+\frac{\eta}{2}) + \frac{3\eta_1}{2}(\frac{1}{\alpha}-1)](1-\eta)^{-2}$$

$$g_{12} = [(1+\frac{\eta}{2}) + \frac{3}{2}\frac{1-\alpha}{1+\alpha}(\eta_1-\eta_2)](1-\eta)^{-2}$$

$$\beta_1 = \sigma_1 b_1 = -6[\eta_1 g_{11}^2 + \frac{\eta_2}{4}(1+\alpha)^2\alpha g_{12}^2]$$

$$\beta_2 = \sigma_2 b_2 = -6[\eta_2 g_{22}^2 + \frac{\eta_1 \alpha^{-3}}{4}(1+\alpha)^2 g_{12}^2]$$

$$\sigma_2 b = -3(1+\alpha)[\frac{\eta_1 g_{11}}{\alpha^2} + \eta_2 g_{22}]g_{12}$$

$$\beta_{12} = \sigma_1 b = -3\alpha(1-\alpha)(\alpha^{-2}\eta_1 g_{11} + \eta_2 g_{22})g_{12}$$

$$\gamma_1 = \sigma_1^3 d = [\eta_1 a_1 + \alpha^3 \eta_2 a_2]$$

$$a_1 = \frac{\partial(\beta\rho')}{\partial\eta_1}$$

$$a_2 = \alpha^{-3}\frac{\partial(\beta\rho')}{\partial\eta_2}$$

where $(\beta\rho')$ is the reduced function

$$(\beta\rho') = \{(\eta_1 + \alpha^3\eta_2)(1+\eta+\eta^2) - 3\eta_1\eta_2(1-\alpha)^2 \times [1+\eta_1+\alpha(1+\eta_2)]\}(1-\eta)^{-3}$$

The expressions for a_1 and a_2 are found to reduce as follows

$$\begin{aligned}
a_1 &= -(1 + 2\eta_1 - 2\eta_2 + 3\eta_1^2 - 2\eta_1\eta_2 + \eta_2^2 - 2\alpha^3\eta_2 \\
&+ 2\eta_1\eta_2\alpha^3 - \eta_2^2\alpha^3 + 3\alpha\eta_2 - 3\eta_2^2\alpha + 12\eta_1\eta_2\alpha \\
&+ 3\alpha^2\eta_2 + 6\eta_2^2\alpha^2 - 6\eta_1\eta_2\alpha^2)/(-1+\eta_1+\eta_2)^3 \\
&+ 3(\eta_1 + \eta_1^2 - 2\eta_1\eta_2 + \eta_1^3 - \eta_1^2\eta_2 + \eta_1\eta_2^2 \\
&+ \alpha^3\eta_2 - 2\eta_1\eta_2\alpha^3 + \eta_2^2\alpha^3 + \alpha^3\eta_2\eta_1^2 - \eta_1\eta_2^2\alpha^3 \\
&+ \alpha^3\eta_2^3 + 3\eta_1\eta_2\alpha - 3\eta_1\eta_2^2\alpha + 6\eta_1^2\eta_2\alpha + 3\eta_1\eta_2\alpha^2 \\
&+ 6\eta_1\eta_2^2\alpha^2 - 3\eta_1^2\eta_2\alpha^2)/(-1+\eta_1+\eta_2)^4 \qquad \text{(A.2)}
\end{aligned}$$

$$
\begin{aligned}
a_2 &= (-(-2\eta_1 - \eta_1^2 + 2\eta_1\eta_2 + \alpha^3 - 2\eta_1\alpha^3 + 2\alpha^3\eta_2 + \alpha^3\eta_1^2 - 2\eta_1\eta_2\alpha^3 + 3\eta_2^2\alpha^3 \\
&+ 3\alpha\eta_1 - 6\eta_1\eta_2\alpha + 6\eta_1^2\alpha + 3\alpha^2\eta_1 + 12\eta_1\eta_2\alpha^2 - 3\eta_1^2\alpha^2)/(-1+\eta_1+\eta_2)^3 \\
&+ 3(\eta_1 + \eta_1^2 - 2\eta_1\eta_2 + \eta_1^3 - \eta_1^2\eta_2 + \eta_1\eta_2^2 + \alpha^3\eta_2 - 2\eta_1\eta_2\alpha^3 \\
&+ \eta_2^2\alpha^3 + \alpha^3\eta_2\eta_1^2 - \eta_1\eta_2^2\alpha^3 + \alpha^3\eta_2^3 3\eta_1\eta_2\alpha - 3\eta_1\eta_2^2\alpha + 6\eta_1^2\eta_2\alpha + 3\eta_1\eta_2\alpha^2 \\
&+ 6\eta_1\eta_2^2\alpha^2 - 3\eta_1^2\eta_2\alpha^2)/(-1+\eta_1+\eta_2)^4)/\alpha^3 \qquad \text{(A.3)}
\end{aligned}
$$

The expressions for the direct correlation functions are obtained as follows

$$
\begin{aligned}
-n_1 C_{11}(y) &= -\frac{24\eta_1}{\alpha^3 y^3}\{a_1(\sin\alpha y - \alpha y\cos\alpha y) + \frac{\beta_1}{\alpha y}[2\alpha y\sin\alpha y - (\alpha^2 y^2 - 2)\cos\alpha y - 2] \\
&+ \frac{\gamma_1}{\alpha^3 y^3}[(4\alpha^3 y^3 - 24\alpha y)\sin\alpha y - (\alpha^4 y^4 - 12\alpha^2 y^2 + 24)\cos\alpha y + 24]\} \quad \text{(A.4)}
\end{aligned}
$$

To obtain $-n_2 C_{22}(y)$, η_1 is replaced by η_2, αy by y, β_1 by β_2, and γ_1 by $\alpha^{-3}\gamma_1$. The fourier transform of $C_{12}(r)$ is written as

$$
\begin{aligned}
-n_1^{\frac{1}{2}} n_2^{\frac{1}{2}} C_{12}(y) &= 3(1-\alpha)^3 \frac{\eta x^{1/2}(1-x)^{1/2}}{x + (1-x)\alpha^3} a_1 \frac{\sin y_\lambda - y_\lambda \cos y_\lambda}{y_\lambda^3} + 24\eta \frac{x^{1/2}(1-x)^{1/2}\alpha^3}{x + (1-x)\alpha^3} \\
&\times [P_1 + P_2 + P_3] \qquad \text{(A.5)}
\end{aligned}
$$

$$
\begin{aligned}
P_1 &= \frac{\sin y_\lambda}{y_1^4}\{\beta_{12}[2y_1\cos y_1 + (y_1^2 - 2)\sin y_1] + \frac{\gamma_{12}}{y_1}[(3y_1^2 - 6)\cos y_1 + (y_1^3 - 6y_1)\sin y_1] \\
&+ \frac{\gamma_1}{y_1^2}[(4y_1^3 - 24y_1)\cos y_1 + (y_1^4 - 12y_1^2 + 24)\sin y_1]\} \qquad \text{(A.6)}
\end{aligned}
$$

$$
\begin{aligned}
P_2 &= \frac{\cos y_\lambda}{y_1^4}\{\beta_{12}[2y_1\sin y_1 + (y_1^2 - 2)\cos y_1 - 2] + \frac{\gamma_{12}}{y_1}[(3y_1^2 - 6)\sin y_1 - (y_1^3 - 6y_1)\cos y_1] \\
&+ \frac{\gamma_1}{y_1^2}[(4y_1^3 - 4y_1)\sin y_1 - (y_1^4 - 12y_1^2 + 24)\cos y_1 + 24]\} \qquad \text{(A.7)}
\end{aligned}
$$

$$P_3 = \frac{a_1}{y_1}\{\cos y_\lambda(\frac{\sin y_1 - y_1\cos y_1}{y_1^2} + \frac{1-\alpha}{2\alpha}\frac{1-\cos y_1}{y_1}) + \sin y_\lambda(\frac{\cos y_1 + y_1 \sin y_1 - 1}{y_1^2} + \frac{1-\alpha}{2\alpha}\frac{\sin y_1}{y_1})\} \quad \text{(A.8)}$$

$$y_\lambda = K\lambda = \frac{1}{2}y(1-\alpha)$$

$$\gamma_{12} = 4\lambda d\sigma_1^2 = 2\gamma_1\left(\frac{1-\alpha}{\alpha}\right)$$

Static structure factor: Polydisperse PYHS

The expressions for partial structure factors S_{ij} for a polydisperse hard sphere system are given by:

$$S_{ij}(q) = \delta_{ij}(q) - 2\sqrt{n_i n_j}\frac{Z_2 Z_3 + Z_1 Z_4}{q^3(X^2+Y^2)} \quad \text{(A.9)}$$

where q is the magnitude of the scattering wave vector, n_i and n_j are the number densities of hard spheres with diameters d_i and d_j respectively.

For $d_{ij} = (d_i + d_j)/2$

$$Z_1 = Y\sin(qd_{ij}) - X\cos(qd_{ij}) \quad \text{(A.10)}$$

$$Z_2 = X\sin(qd_{ij}) + Y\cos(qd_{ij}) \quad \text{(A.11)}$$

$$Z_3 = \frac{\pi}{\triangle}\left(2 + \xi_3\frac{\pi}{\triangle}\right) + qR_4 \quad \text{(A.12)}$$

$$Z_4 = \frac{\pi}{\triangle}\left(2d_{ij} + \frac{1}{2}d_i d_j \xi_2\frac{\pi}{\triangle}\right) + qR_4 \quad \text{(A.13)}$$

Here $\triangle = 1 - \frac{\pi}{6}\xi_3$ and $\xi_n = \sum_l n_l d_l^n$. The parameters X, Y, R_3 and R_4 are given by

$$X = 1 - \frac{2\pi}{\triangle}(1 + \frac{\pi\xi_3}{2\triangle})\sum_k n_k x_2(d_k) - \frac{2\pi}{\triangle}\sum_k n_k d_k x_1(d_k)(1 + \frac{\pi\xi_2 d_k}{4\triangle}) - \frac{1}{2}(\frac{\pi}{\triangle})^2 \sum_{k,l} n_k n_l [x_1(d_k)x_1(d_l) - y_1(d_k)y_1(d_l)](d_k - d_l)^2 \quad \text{(A.14)}$$

$$Y = -\frac{2\pi}{\triangle}(1 + \frac{\pi\xi_3}{2\triangle})\sum_l n_l y_2(d_l) - \frac{2\pi}{\triangle}\sum_k n_k d_k y_1(d_k)(1 + \frac{\pi\xi_2 d_k}{4\triangle}) - \frac{1}{2}(\frac{\pi}{\triangle})^2 \sum_{k,l} n_k n_l [x_1(d_k)y_1(d_l) + x_1(d_l)y_1(d_k)](d_k - d_l)^2 \quad \text{(A.15)}$$

$$R_3 = \left(\frac{\pi}{\triangle}\right)^2 \sum_k n_k (d_k - d_i)(d_k - d_j) y_1(d_k) \quad \text{(A.16)}$$

$$R_4 = \left(\frac{\pi}{\triangle}\right)^2 \sum_k n_k (d_k - d_i)(d_k - d_j) x_1(d_k) \quad \text{(A.17)}$$

where x_1, x_2, y_1, and y_2 are given by:

$$x_1(d) = q^{-2}[\cos(qd) - 1] \quad \text{(A.18)}$$

$$x_2(d) = q^{-3}[qd - \sin(qd)] \quad \text{(A.19)}$$

$$y_1(d) = q^{-2}[qd - \sin(qd)] \quad \text{(A.20)}$$

$$y_2(d) = q^{-3}[\cos(qd) + 0.5q^2d^2 - 1] \quad \text{(A.21)}$$

APPENDIX B

ANALYTICAL EXPRESSIONS FOR THE STRUCTURE FACTORS: MSA YUKAWA

The static structure factor for the monodisperse Hard sphere Yukawa model has been given by Herrera *etal*. The original paper has typographical errors and have been correctly presented by Dr. Yingqing Huang in his PhD dissertation, and is provided in this appendix.

Parameter definition

$e_o = 1.60 \times 10^{-19}$	electron charge (Coulomb)
$k_B = 1.38 \times 10^{-23}$	Boltzmann constant (Joule/Kelvin)
$N_A = 6.023 \times 10^{23}$	Avogadro Number (per mole)
$\epsilon = 8.85 \times 10^{-12}$	Electric Permittivity of Vacuum (C^2/Jm)
$\epsilon_r = 78.54$	Dielectric Constant
T	Temperature (K)
κ	Inverse Debye Length
σ	Mean Particle Size
z_{eff}	Effective surface charge
θ	Scattering Angle
η	Volume Fraction
λ	Wavelength
m	Refractive index of the suspending fluid

Calculation of the static structure factor S(k)

$L_B = \frac{e_o^2}{4\pi\epsilon\epsilon_r k_B T}$	Bjerrum Length
$\epsilon_o = \frac{z_{eff}^2 L_B}{\sigma(1+z/2)^2}$	Dimensionless Coupling Energy
$q = \frac{m}{4\pi\lambda}\sin(\theta/2)$	Scattering Vector
$k = q\sigma$	Dimensionless Scattering Vector

$$z = \kappa\sigma$$

$$\eta_1 = 1 - \eta$$

$$\eta_2 = 1 + 2\eta$$

$$\eta_3 = \frac{\eta_2}{\eta_1}$$

$$\eta_4 = 2 + \eta$$

$$\eta_5 = 3\eta$$

$$\eta_6 = 6\eta$$

$$\phi_o = \frac{1-exp(-z)}{2}$$

$$\phi_1 = \frac{1}{z^3}\left[1 - \frac{z}{2} - \left(1 + \frac{z}{2}\right)exp(-z)\right]$$

$$\xi_o = z - (2+z)\phi_o + \xi_1(\eta_3 + \tfrac{z}{2})\tfrac{1}{z}$$

$$\xi_1 = 2z\phi_o - \frac{12\eta\phi_1 z^2}{\eta_1}$$

$$\xi = \xi_1\gamma + \xi_o$$

The roots of the following equation are used to obtain the value of the parameter γ

$$\gamma(\gamma+1) = \frac{\eta_6\epsilon}{\xi^2} \tag{B.1}$$

The root of this equation which leads to any physically meaningful results is the positive root, and can be easily identified. Here, the parameter ϵ indicates the interaction potential at contact.

$$\alpha_o = \eta_6 \frac{2+z}{\eta_1 z^2}$$

$$\alpha_1 = \eta_6 \frac{2\eta_2 + z\eta_4}{(\eta_1 z)^2}$$

$$A = \frac{1}{\eta_1}[\eta_3(1+2\gamma) + 2z\gamma(\gamma+1)]$$

$$B = \frac{1}{\eta_1}[1 - 2\gamma(1+2\gamma+2\frac{\eta_3}{z})]$$

$$C = \frac{1}{\eta_5}[-\gamma exp(z)(\xi_1\gamma + \xi_o)]$$

$$D = \frac{\gamma}{\eta_5}(-\alpha_o + z\alpha_1\gamma - z\gamma) - C$$

$$R_1 = k\cos k + k - 2\sin k$$

$$R_2 = \cos k - 1$$

$$R_3 = \frac{k\cos k + z\sin k}{z^2 + k^2}$$

$$R_4 = \frac{z}{z^2 + k^2}$$

$$R = 1 - \eta_6 \left[\frac{AR_1}{k^3} + \frac{BR_2}{k^2} - \frac{R_3 z D exp(-z)}{k} + (D+C)R_4 \right]$$

$$T_1 = k\sin k - 2 + k - 2\sin k$$

$$T_2 = \sin k - k$$

$$T_3 = \frac{z\cos k - k\sin k}{z^2 + k^2} - \frac{1}{z}$$

$$T_4 = \frac{k}{z^2 + k^2}$$

$$T = -\eta_6 \left[\frac{AT_1}{k^3} + \frac{BT_2}{k^2} + \frac{T_3 z Dexp(-z)}{k} + (D + C)T_4 \right]$$

$$S(k) = \frac{1}{R^2 + T^2} \tag{B.2}$$

where $S(k)$ is the structure factor at the dimensionless scattering vector $k = q\sigma$

Reference:

1. J.N.Herrera, P.T.Cummings, and H.Ruiz-Estrada, "Static structure factor for simple liquid metals," Molecular Physics 96(5),835-847 (1999).

2. Yingqing Huang, PhD Dissertation, "Characterization of Dense suspensions using frequency domain photon migration", Texas A & M Univeristy, 2004

VITA

SARABJYOT SINGH DALI

EDUCATION **B.Tech.** Chemical Engineering,
Indian Institute of Technology, Kharagpur, India, 2001
Ph.D. Chemical Engineering,
Texas A&M University, College Station, TX 77843

PEER REVIEWED PUBLICATIONS

- Sarabjyot S. Dali, John Rasmussen, Yingqing Huang, Ranadhir Roy, and Eva M. Sevick-Muraca, "Determination of particle size in dense suspensions using multi-wavelength frequency domain photon migration measurements," *AIChE Journal*, 51(4), 1-12, 2005.

- Tianshu Pan, Sarabjyot S. Dali, and Eva M. Sevick-Muraca, "Evaluation of photon migration using a two speed model for characterization of packed powder beds and dense particulate suspensions," *Optics Express*, 13(10), 3600-3618, 2005.

- Sarabjyot S. Dali, John Rasmussen, Yingqing Huang, Feng Liang and Eva M. Sevick-Muraca, "Modeling and study of dense monodisperse charged lattices using frequency domain photon migration measurements." (*In preparation*)

- Sarabjyot S. Dali and Eva M. Sevick-Muraca, "Modeling and study of dense bidisperse charged lattices using frequency domain photon migration measurements." (*In preparation*)